The Role of Magnetic Fields Across Different Scales in the Early Stages of Star Formation

Janik Karoly

A thesis submitted in partial fulfilment
of the requirements for the degree of
Doctor of Philosophy

Jeremiah Horrocks Institute for Mathematics, Physics and Astronomy
University of Central Lancashire

October 2024

Declaration

Type of Award: Doctor of Philosophy

School: Engineering and Computing

The work presented in this thesis was carried out at the Jeremiah Horrocks Institute for Mathematics, Physics and Astronomy, University of Central Lancashire.

I declare that while registered as a candidate for the research degree, I have not been a registered candidate or enrolled student for another award of the University or other academic or professional institution.

I declare that no material contained in the thesis has been used in any other submission for an academic award. Data and analysis used in this thesis that are not my own are clearly cited in the text.

I further declare that all of the work in this thesis is my own original research carried out under the supervision of Professor Derek Ward-Thompson, with the following exceptions:

I reduced the SCUBA-2/POL-2 data presented in Chapter 3 using methods developed by myself (see Chapter 2) in coordination with Dr. David Berry and the JCMT BISTRO SCUBA-2/POL-2 Data Reduction Team, of which I am a member. All of the Herschel and Planck data used are archival. The HARP data used are from the archive and then I further reduced them using standard reductions available from the JCMT. All of the data analysis is my own original work. The analysis in Chapter 3 has been published in The Astrophysical Journal (2023, vol. 952 issue 1, id. 29), in a paper that I am the first author of and written entirely by me but in collaboration with members of the BISTRO Survey who offered comments.

Similarly, I reduced all of the SCUBA-2/POL-2 data presented in Chapter 4 using standard JCMT/POL-2 data reduction methods and those presented in Chapters 2 and 3. The sources were/are worked on by other members of the BISTRO Survey on the Prestellar Cores Tiger Team (of which I am a member), but all analysis and reductions presented here is my own. Work pertaining to L183 has been published prior to the start of my PhD in an article in The Astrophysical Journal (2020, vol. 900 issue 2, id. 181) that I am first author on. However, the L183 data presented in Chapter 4 has been re-reduced from the raw data and the analysis is new. Work pertaining to L1495A has been published in The Astrophysical Journal (2023, vol. 946 issue 2, id. 62) in a paper that I am the second author on, but I was the one to reduce the data and the analysis presented here was worked on by myself as well, and any further analysis is my own.

Similarly, I reduced the SCUBA-2/POL-2 data presented in Chapter 5 using standard JCMT/POL-2 data reduction methods. The NH_3 data from the SWAG Survey were provided to me by Dr. Jürgen Ott, a member of the survey. All analysis of the SWAG data presented is original and my own. All of the data analysis is my own original research. I am the head of the BISTRO Survey Galactic Center Tiger Team and oversee the distribution of data and the work being done. Many of the sources discussed in this chapter are being worked on by members of the group, but any analysis or reductions I present are my own.

Chapter 6 includes analysis of previously published data. Where this happens, it is explicitly stated and proper references are given. In some cases the data have been provided from the paper authors, in other cases I have re-reduced the data. All analysis in Chapter 6 is original and my own.

I declare that no material contained in the thesis has been used in any other submission for an academic award and is solely my own work.

No proof-reading service was used in the compilation of this thesis.

Janik Karoly

October 2024

Abstract

We investigate the role of magnetic fields in the early stages of star formation and across a variety of scales. We start by focusing on a nearby molecular cloud Lynds 43 and investigating the magnetic field in relation to the density structure, the outflow of a protostellar object and its role compared to turbulent motions and gravity. We then expand this analysis towards other nearby, low-mass star forming regions. We focus primarily on the magnetic field strength and its orientation to the cores and other density structures, as well as its role compared to turbulent motions and gravity. We then move two orders of magnitude further away to the Central Molecular Zone where we investigate the role of the magnetic field in shaping the large-scale kinematics of the region, specifically how it can help inform an orbital model for the material within the CMZ. We also calculate magnetic field strengths of individual clouds and investigate the overall contribution of the magnetic field and also how it relates to the density structures of the individual clouds.

In L43, we find an evolutionary gradient along the isolated filament that L43 is embedded within, with the most evolved source closest to the Sco OB2 association. One of the protostars drives a CO outflow that has created a cavity in the dust structure to the southeast. We find a magnetic field that appears to be aligned with the cavity walls of the outflow. We also find a magnetic field strength of $\sim$160$\pm$30 μG in the main starless core and up to $\sim$90$\pm$40 μG in the more diffuse, extended region. These field strengths give magnetically super- and sub-critical values respectively and both are found to be roughly trans-Alfvénic. When we extend some of this

analysis to other nearby low-mass star forming regions, we find that many of the evolved cores are already magnetically super-critical and have field strengths in the range of 30–130 μG. We do not find any preferential alignment of the magnetic fields with either the core orientation or the large-scale magnetic field.

In the CMZ we find that the magnetic field follows a proposed orbital model in the western half, but not as well in the eastern half. The eastern half is significantly more confusing with both gas kinematics and the amount of material there which could be affecting the magnetic field we observe. Our proposed orbit is continuous in position-velocity space except for a gap in continuity between roughly Sgr A* and the 'Brick,' a known chaotic area where open ends of an orbit may be crossing. We also find that the clouds in the CMZ have large magnetic field strengths, on the order of mG, and a majority are sub-Alfvénic and magnetically sub-critical. This suggests a strong influence of the magnetic field within the molecular clouds of the CMZ.

We finally bring all of the sources together to investigate overall trends based on the magnetic field information. We assume that as clouds start to become gravitationally bound, material can then be dragged across magnetic field lines, hence altering their orientation. We find that there is not a single magnetic field strength versus column density relation that explains differing orientations between small-scale magnetic fields in cores and the large-scale magnetic field around it. In the CMZ, we also find that the magnetic field is preferentially perpendicular to the density structure in a majority of the clouds. Compared to conclusions from nearby star-forming regions, this would suggest that the magnetic field is now at the stage of helping to feed material onto central hubs from which star formation may occur. We also find that different modes of star-formation have distinct magnetic field patterns that are common across a variety of sources.

Contents

List of Tables

List of Figures

Acknowledgements

I would like to thank my supervisor first and foremost, Derek Ward-Thompson, for believing in me to carry out this research and complete the PhD. For reading my thesis and educating me on how bass ackwards my writing could be. Thank you to my second supervisor Jason Kirk for always being available to chat about the most basic science questions to ensure I wasn't barking up the wrong tree or overthinking things. Thank you also to my third supervisor Kate Pattle who was instrumental in advising me on any and all SCUBA-2/POL-2 questions, whether it be science/analysis, observations or data reduction.

I would like to thank my parents who believed in me to achieve this level of higher education and who didn't put up too much of a fuss about having me move halfway around the world to do it. I would also like to thank my grandparents and whole family who always offered unconditional support and encouragement.

I would like to thank Robert Schlichting who oversaw my initial serious interest in Astrophysics while at Cleveland High School and pushed me further along my physics path. I would furthermore like to thank Dr Kristin Kulas for giving me the opportunity to pursue a summer astrophysics research project while at Santa Clara University and opening up countless opportunities. And then a massive thank you to Drs. B-G Andersson and Archana Soam who were my summer research mentors and to this day are still close colleagues and friends who have advised me throughout the PhD and with future choices.

I will also be forever grateful to Patrick Holden for setting up the Moses Holden

Fellowship at UCLan which funded my PhD journey.

And finally to the other post-graduate students and faculty in the JHI who made it an enjoyable and friendly environment over the last three and a half years. Especially Alexia Lopez who made every attempt to keep me focused and on track as an office buddy but couldn't always keep me from quacking about.

Chapter 1

Introduction

1.1 Current Understanding of Star Formation

Astronomy is often referred to as the 'oldest science.' This is in part due to the fact that it is a science that can be done with our eyes and the 'lab' for this science is the endless night sky above us. While early civilizations may have been misled about believing that stars were fixed to a heavenly sphere with us as the center of our universe, there was still enough insight to identify those distant points of light to be stars similar to our own Sun. If astronomy is the oldest science, and stars were the visible data points for this science, then one of the oldest questions must be: 'how did they get there?' More importantly, or more close-to-home, how did our Sun get here and ultimately, how did we get here? But to understand the birth of our star, we would have to look 4.6 billion years back into the past, or, we can look to the environment around us and investigate regions which we think will create stars like our Sun.

Our understanding of the process of star formation has made leaps and bounds over the past century. Much of the original science of stars was observations of stars already there, determining their distance, properties and age among other things. While nebulae were observed since the 1600s, their relation to the birth (and death) of stars was not really posited until the late 1800s and early 1900s when Jeans (1902) investigated the stability of a nebula, finding when it might contract and collapse, giving us the eventual Jean's Mass and Length.

Now, with the advent of infrared and submillimeter telescopes, the rest of the galaxy and the universe is visible to us and we can see some of the matter hidden in the optical - the interstellar medium (ISM) - namely the gas and dust that sits between stars. The collapse of gas and dust clouds to form stars from the interstellar medium is still not entirely understood. One missing piece in this process is the role of magnetic fields. Great strides have been made in recent years to answer this question with our ability to observe and measure magnetic fields, as well as inject them into simulations. However, for the most part, we continue to rely on plotting lines over pretty images and calling it science.

1.2 The Interstellar Medium

The ISM is broadly the material between the stars in a galaxy. In our own galaxy, it is made up primarily of 70% hydrogen, 28% helium and 2% heavier elements such as oxygen, carbon and nitrogen (Ward-Thompson & Whitworth, 2011). A vast majority, nearly 99%, is in the gas phase with the rest being dust or micron-scale material. The ISM is considered to be a three phase system (McKee & Ostriker, 1977). The three phase ISM is shown in Figure 1.1 and consists of a hot, ionized medium (HIM) at $\sim 10^5$ K and $\sim 10^{-3}$ cm^{-3}, the warm, neutral H I (and a separate ionized, H II surrounding) medium (WNM) at $\sim 10^{3-4}$ K and $\sim 10^{-1}$ cm^{-3} and the cold neutral medium (CNM) at $\sim 10^{1-2}$ K and $\sim 10^{1-2}$ cm^{-3}.

The large scale of the ISM is a diffuse, inhomogenous hot ionized medium that is heated by supernovae via expanding waves/shocks when massive, young stars die (McKee & Ostriker, 1977; Tielens, 2005). The ionization is near unity for this medium and the shocked gas is extremely hot ($T \geq 10^6$ K; Tielens, 2005) due to the energetic nature of supernovae. The cooling time of the HIM is significant ($\geq 10^6$ yrs; Tielens, 2005), so much of the ISM is in this phase (70–80%; McKee & Ostriker, 1977). Within this hot ionized medium is the CNM which are cold, dense clouds that are almost entirely neutral and which are formed where the gas has cooled between shocks. Surrounding those clouds is the warm interstellar layer which is less dense and slightly warmer. That shell is further divided into two regions, the ionized outer shell and the neutral inner shell. The UV emission of young OB stars can also heat the hot interstellar medium but the timescales are much shorter than the supernovae heating so the OB stars are primarily thought to contribute to the warm ionized medium (Tielens, 2005).

The cold neutral medium is where molecular clouds are formed and where much of the molecular hydrogen (H_2) is found. These molecular clouds are the sites of future star formation and will be discussed in more detail below. The cold neutral medium can be broken down into three components, with a cool H I component, a diffuse H_2 component and a dense H_2 component (Draine, 2010).

1.2.1 The Large Scale ISM

As mentioned above, the largest scale in the ISM is technically the HIM because it is the most prevalent, with a filling factor of 70–80%. However, it is not the most mass-heavy component and is certainly not where stars form. While it is ~30 times larger in volume, it is nearly five orders of magnitude less dense. In the regions between the HIM shocks, where the ISM has been allowed to cool and is shielded by the warm medium, molecular clouds form, the first stage in star formation.

1.2.1.1 Molecular Clouds

Molecular clouds are so named due to their composition being primarily molecular gas. They are also often called 'dark clouds' or infrared dark clouds (IRDCs)

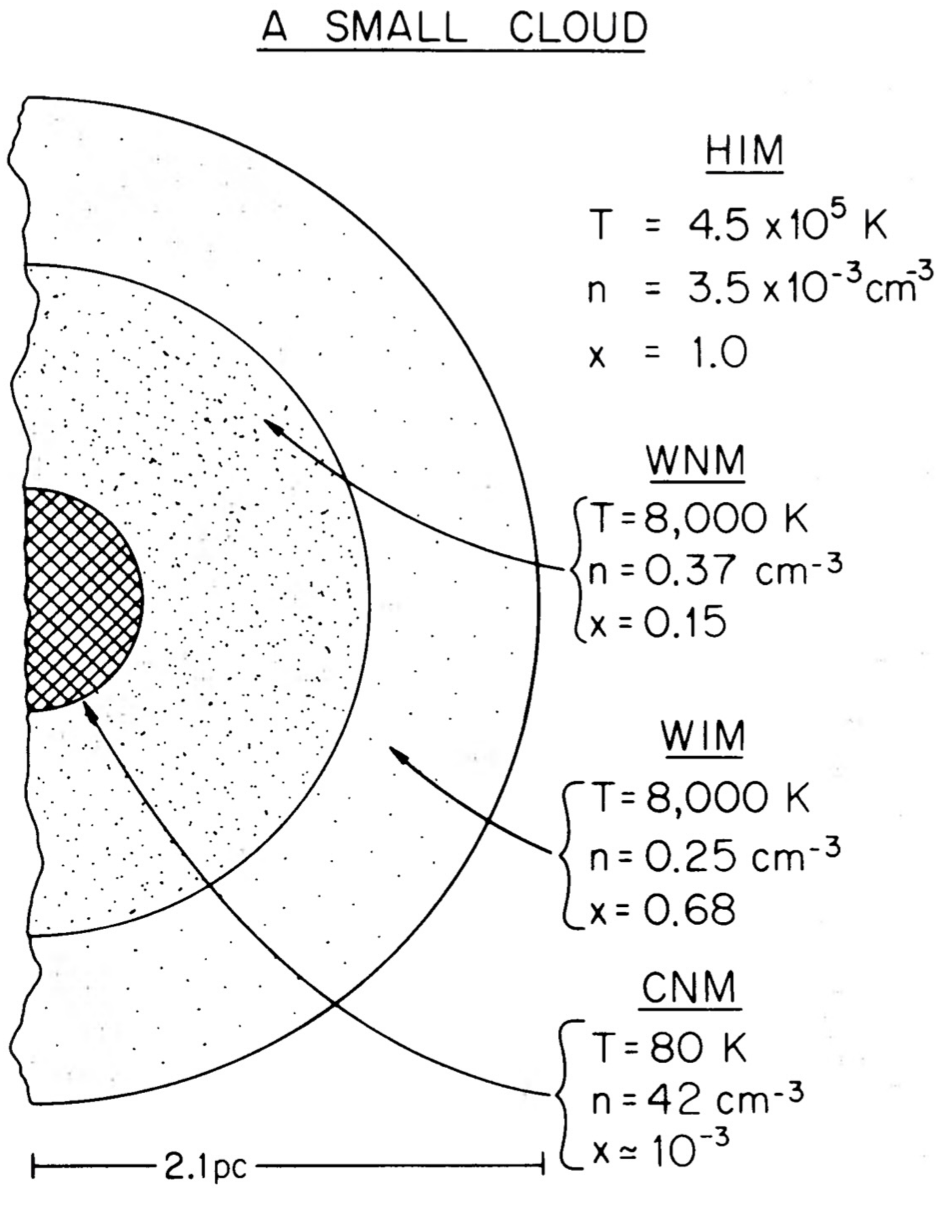

Figure 1.1: The three phase interstellar medium as defined by McKee & Ostriker (1977). The figure was also adopted from McKee & Ostriker (1977). T is the temperature, n is the hydrogen volume density and x is the ionization fraction (n_e/n).

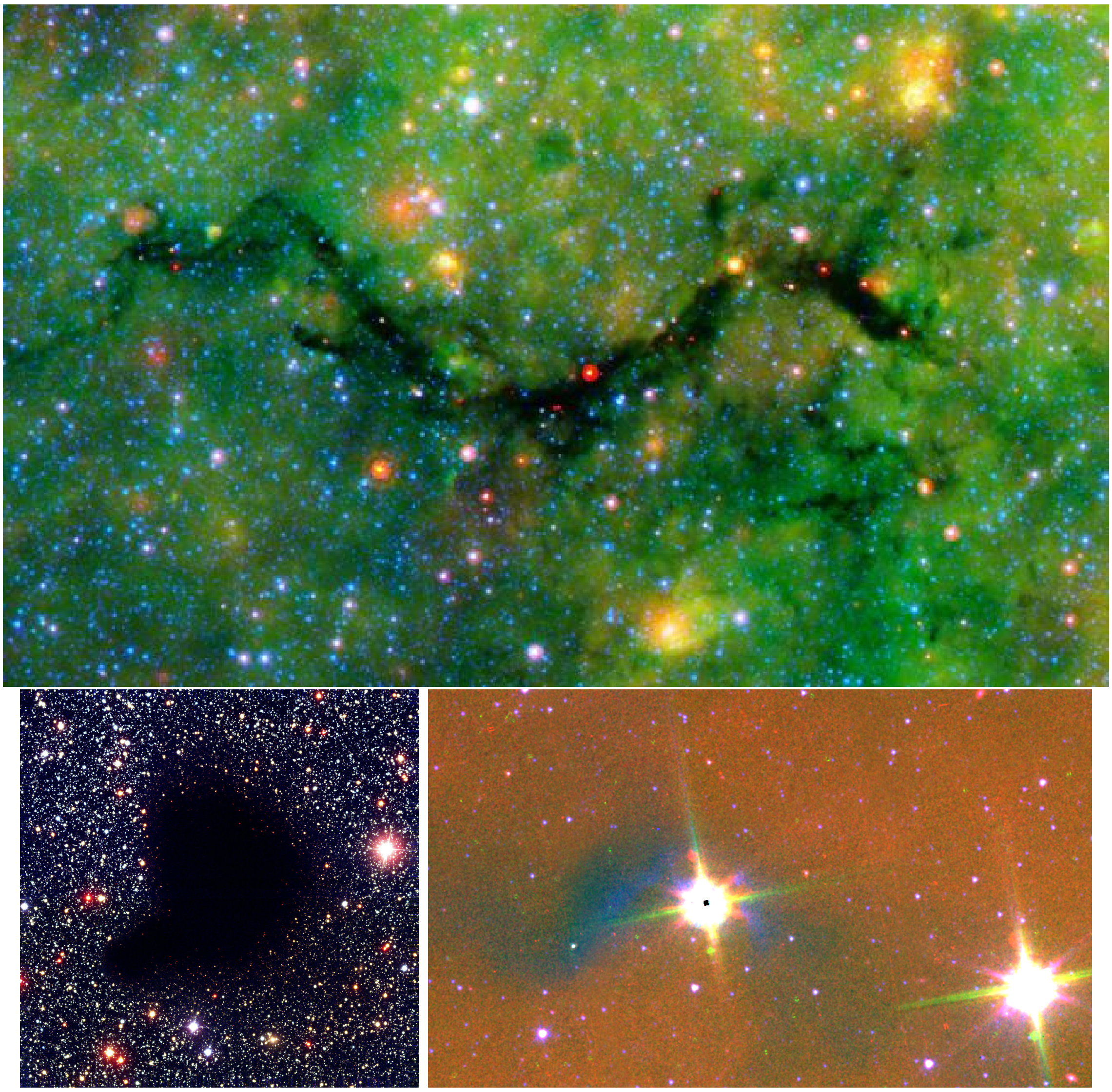

Figure 1.2: Examples of molecular clouds across different size scales exhibiting their 'dark' nature. *Upper:* The IRDC G11.11-0.12 cloud as seen with the IRAC and MIPS cameras on *Spitzer* (Credit: NASA, JPL-Caltech/S. Carey (SSC/Caltech)). The width of the image is approximately 72 pc. *Lower left:* Barnard 68 is an isolated dark core (Credit: ESO; VLT/ANTU and FORS1) with a radius of $\approx$0.08 pc. *Lower right:* The IRDC Lynds cloud 43 as seen with *Spitzer* again. There are two embedded protostars which are the bright regions. The background stars are blue-ish point sources. The width of the image is approximately 0.4 pc.

because their dense structures block out background starlight and they appear as dark regions in optical/NIR images (see Figure 1.2). However, in the infrared and submillimetre–millimetre, these clouds are very bright. They block the background light due to the inclusion of 'dust' in the cloud, normally silicates and carbon compounds, which are micron to sub-micron in size and absorb the background light. Though the dust only makes up $\sim$1% of molecular clouds (Ward-Thompson & Whitworth, 2011), it is sufficient to block the background light. The dust also aids in the formation of molecular gas by acting as a catalyst to allow for the formation of molecular gas on the grain surfaces and by blocking UV radiation which would destroy molecules.

These molecular clouds are generally $\sim 10^{1-5}$ cm^{-3} from their diffuse edges into their dense interiors, and in the range of 10–50 K with the colder material in the denser regions. The molecular clouds are so cold because the dust also blocks a significant amount of UV light which would normally heat the cloud. They can vary in mass, where some molecular clouds may only form a single core and be on the order $\sim M_\odot$, while others such as Sagittarius B2 in the Galactic Center can be up to 10^7 $M_\odot$ but also slightly higher gas temperatures in the range of 60–100 K (Schwörer et al., 2019). Molecular clouds can also either be filamentary in nature or contain filamentary structures within them.

1.2.1.2 Filamentary Structures

With the launch of the ESA *Herschel* Space Telescope, the interstellar medium and specifically the molecular clouds within were seen in a new light. *Spitzer* had previously found some filamentary structures in our galaxy (see upper panel of Figure 1.2), observed as long, dark 'snakes' on a starry background, but for *Herschel* which operated at 70, 160, 250, 350 and 500 μm, filaments shone brightly. Additionally, because *Herschel* was a space telescope, it was not limited to observing small angular structures (due to atmosphere variability which ground-based observatories suffer from) and instead it saw the whole, large-scale structure of molecular clouds. Figure 1.3 shows two famous molecular clouds that have long filaments, the Taurus Molecular Cloud (TMC) complex and the Orion Molecular Cloud (OMC) complex.

Once a handful of filaments were found, they were soon found everywhere (André et al., 2014). These filaments were also found to have a characteristic width of 0.1 pc (Arzoumanian et al., 2011) but ranged in length from structures within clouds up to kilo-parsec sized objects. They were identified as very active sites of star formation and their interaction with magnetic fields has previously been studied in the infrared and submillimeter in great detail (e.g. Soler et al., 2013; Planck Collaboration et al., 2016b). It is believed that filaments are able to funnel material along their length into cores which form within the filaments (Hacar et al., 2023), although these cores can form in a variety of environments within the filament (Seifried & Walch, 2015). Magnetic fields can help initially form the filament (Hacar et al., 2023) and further accrete matter onto the filament, with field lines perpendicular to filaments in diffuse regions, so material falls along the lines onto the filament and then parallel in the dense regions where the flow of material is dominant (Planck Collaboration et al., 2016b; Arzoumanian et al., 2021, and see Section 1.2.3 for further discussion). This accretion signature is also seen in velocity gradients which are perpendicular to the main axis of the filament (Kirk et al., 2013; Palmeirim et al., 2013).

The formation of cores within filaments is well-documented, with more than 75% of prestellar cores lying within dense filaments (André, 2017). Filaments are turbulent and so over time, supersonic compressions can create local over-densities in the filament which can further accrete material and therefore seed fragmentation (Hacar et al., 2023). There are two dominant modes of gravitational instabilities leading to cores in filaments (Hacar et al., 2023). The first is edge fragmentation, where a filament of finite length experiences enhanced collapse at the ends of the

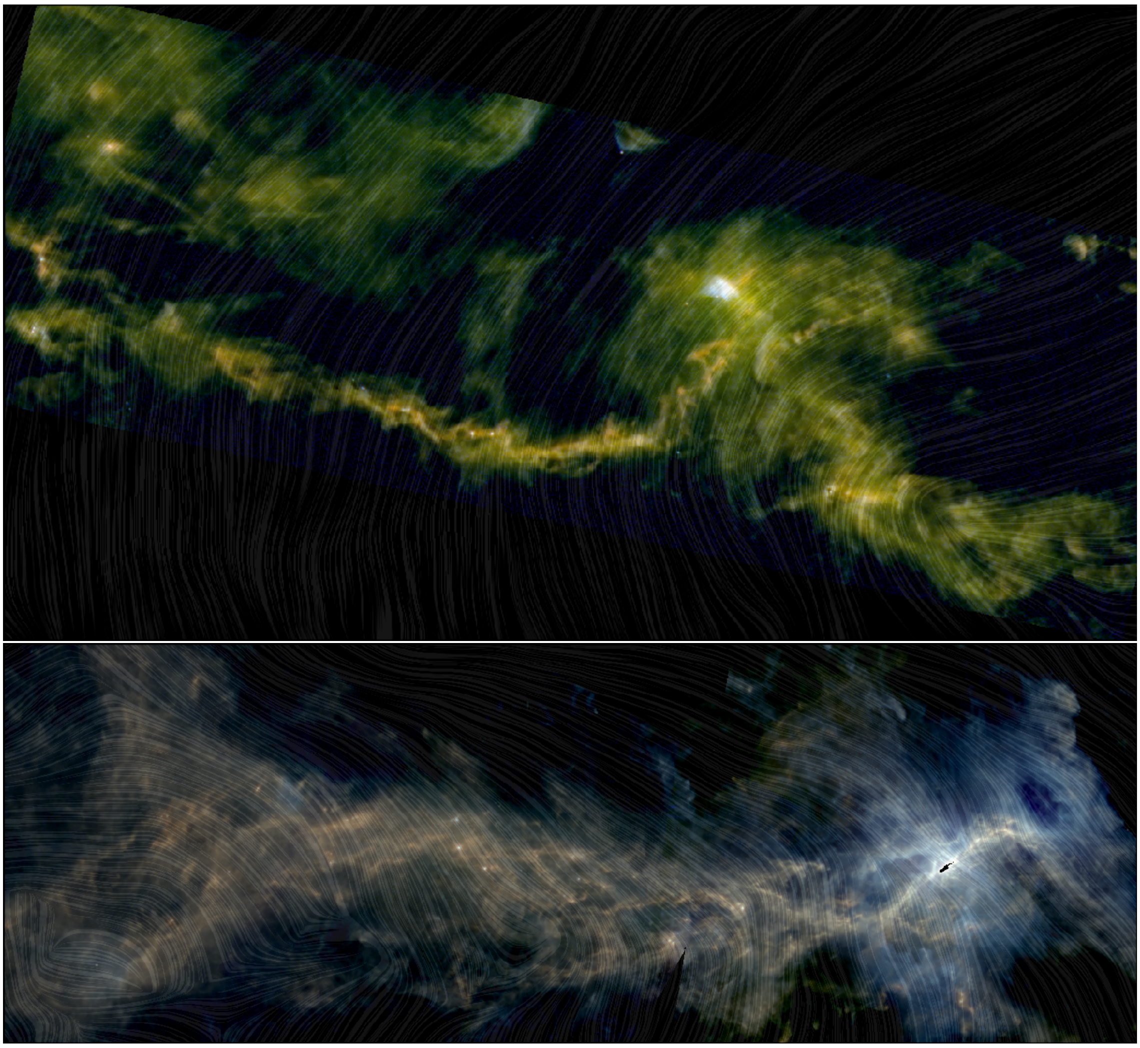

Figure 1.3: Herschel observations of Taurus (upper) and Orion A (lower) Molecular Cloud complexes. The overlaid texture shows the magnetic field orientation derived from Planck observations. Both regions are highly filamentary. Both images were taken from the European Space Agency website (credit: ESA/Herschel/Planck; J. D. Soler, MPIA).

filament due to gravitational focusing (Bastien, 1983; Pon et al., 2012; Clarke & Whitworth, 2015). The timescale for this collapse is just the free fall time scale modified by the aspect ratio of the filament (Equation 18 of Hacar et al., 2023), though the onset of the collapse should occur and be observed earlier (Seifried & Walch, 2015). Despite this expected early onset, very few filaments are observed to have clear indications of this edge fragmentation (Yuan et al., 2020, and references therein).

Instead, fragmentation in filaments seem to arise more commonly from density perturbations and supercritical line masses (Seifried & Walch, 2015), which occur on comparable or faster time scales than the edge fragmentation (Hacar et al., 2023). If perturbations are larger than a critical values of λ_{crit}=3.93 $R_{\rm flat}$ (where $R_{\rm flat}$ is the filament's (inner) flat radius from the Plummer-like profile), then hydrostatic filaments can fragment to form cores equally spaced with masses $\sim M_{\rm Jeans}$ (Hacar et al., 2023). The separation of the cores is given by an unstable mode $\lambda_{\rm max}$ which is two times the λ_{crit} value (Larson, 1985; Inutsuka & Miyama, 1992). Comparing Equations 18 and 19 of Hacar et al. (2023), it can be seen that the fragmentation time for this method will generally be much less than edge on fragmentation unless the filament has an aspect ratio close to unity, at which point it is more ellipsoidal/spheroidal. However, the constant separation of the cores by $\lambda_{\rm max}$ is not often seen (e.g. Mattern et al., 2018). Instead, the fragmentation spacing may be hierarchical (Hacar et al., 2023). Here, there would be smaller chains of cores consistent with Jeans fragmentation that are embedded within larger clumps in the filament. These larger clumps have spacings determined by large-scale, gravitationally-unstable modes of the filaments (Teixeira et al., 2016) or turbulent modes (Seifried & Walch, 2015). The turbulent modes lead to another form of fragmentation, which is due to turbulent motions in supersonic filaments which seed the fragment locations (Seifried & Walch, 2015).

André (2017) also noted that the observed prestellar core formation threshold is approximately equal to the line-mass threshold where filaments become gravitationally unstable, fragmenting along their length (Inutsuka & Miyama, 1992). This observationally supports the theoretical expectation for the gravitational instability of isothermal gas cylinders (André, 2017).

1.2.2 The Small Scale ISM

Inside molecular clouds and filaments lie regions where the birth of stars is taking place. It generally starts in areas of over-densities which are theorized to be either seeded by turbulence or fed by filaments and over time may become starless cores. Those starless cores may then become prestellar cores as they exceed their Jeans mass and reach a point where a star is likely to be born from that individual core. This can happen in very isolated regions or in a massive molecular cloud where clusters may be born.

Starless cores form the first stage in the eventual life cycle of a star. Before any fusion occurs or before anything starts collapsing, enough material must come together to overcome internal pressures. Starless cores refer only very broadly to overdensities and the subset of starless cores which are gravitationally unstable are called prestellar cores

Prestellar cores are the time in a core's evolution where it is gravitationally bound and it evolves towards a higher degree of central condensation, but no protostar has actually been formed. Prestellar cores, unlike some starless cores, are destined to become stars. Starless cores are brightest in the far-infared to submillimeter regime which indicates they are cold, and indeed temperatures in prestellar cores will generally range from ∼7–15 K (Ward-Thompson & Whitworth, 2011). Previously, an additional criterion was set for prestellar cores which was that they were dense enough (10^4 cm^{-3}) to have NH_3 detected which is a high-density gas tracer (Benson

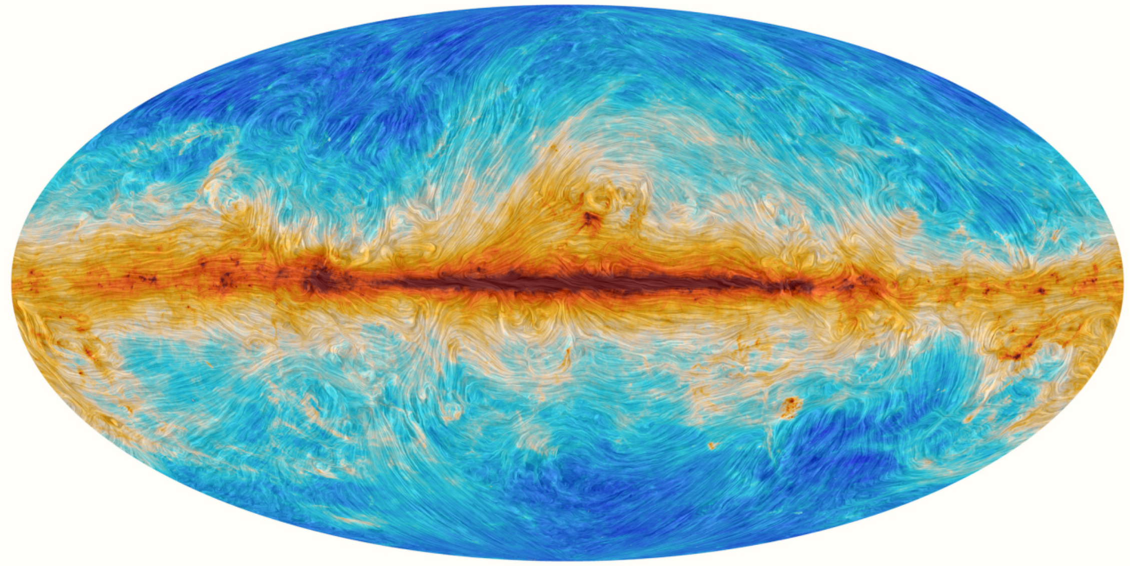

Figure 1.4: Observation of the magnetic field in molecular clouds within the Milky Way as observed by Planck at 353 GHz (Planck Collaboration et al., 2016b).

& Myers, 1989).

1.2.3 Interaction of the ISM and the Magnetic Field

Magnetic fields (B-fields) are known to be prevalent throughout the interstellar medium (ISM) and thread through molecular clouds (see Figure 1.4; Planck Collaboration et al., 2016b). Multiple simulations have demonstrated that turbulence and magnetic fields often play a role in the formation of filaments and molecular clouds (Federrath, 2015), and although the magnetic field does not appear to dominate as heavily over gravity or turbulence as first thought, it has a non-negligible influence (Hennebelle & Inutsuka, 2019; Krumholz & Federrath, 2019).

The ISM is well approximated by a flowing, electrically-conducting fluid and so magnetic fields interact with it, especially in the diffuse material where it is fully ionized. Here the material is well coupled to the field due to flux freezing, where the magnetic field is constrained to move with the fluid or control the movement of the fluid. Moving forward, this assumption is almost always made, with the exception of instances where gravity is sufficiently strong to collapse across magnetic field lines, something referred to as 'ambipolar diffusion.' In molecular clouds however, most of the material is molecular and therefore neutral and not highly ionized. We can however still assume the magnetic field plays a role because cosmic ray (CR) ionization is able to ionize some of the material, even up to high densities (Padovani, Galli & Glassgold, 2009; Padovani et al., 2018). The ionization of molecular clouds formed primarily of H_2 occurs from a variety of mechanisms and cosmic ray particles, including, but not limited to, CR proton impact, CR electron impact and CR electron capture ionization (for a full list, see Table 1 of Padovani, Galli & Glassgold, 2009). This ionized material is then still well coupled to the field lines.

1.2.3.1 Ambipolar Diffusion

Ambipolar diffusion is originally a concept in plasma physics with regards to the diffusion of positive and negative (hence ambipolar) ions and electrons where the charged particles are coupled to each other due to electric fields created when, for example, electrons diffuse faster than the ions (Simon, 1955). In astrophysics, ambipolar diffusion generally refers to the diffusion of neutral particles across magnetic field lines (Mouschovias, 1979). As mentioned above, the ISM is at least partially ionized, from diffuse down to dense molecular clouds, and is threaded with a magnetic field. These ions in the molecular clouds, generally H^+, H_2^+ and electrons (Padovani, Galli & Glassgold, 2009), are tightly coupled to the magnetic field line. The ions are also coupled to the surrounding neutral medium via collisions (Mouschovias, 1979). In the absence of any coupling, the neutral material would not feel the magnetic field and it could undergo regular gravitational collapse. However, being coupled with the ions now makes it more difficult for the neutrals to flow across the magnetic field line. Ambipolar diffusion is the eventual diffusion of these neutrals across the magnetic field lines as they become decoupled from the ions. This diffusion will be further driven by pressure gradients or gravitational acceleration (Ward-Thompson & Whitworth, 2011).

This sort of magnetic field regulated collapse is shown in Figure 1.5. Initially the material in the diffuse medium flows along the magnetic field lines as in panel a. Then zooming in on a forming core, again the magnetic field influences the material to flow along the field lines, creating this ellipsoid shape in panel c. At this point, the gravitational acceleration will be large in the semi-major axis direction and so some diffusion of neutrals across the magnetic field lines occurs. With the diffusion of the neutrals across the magnetic field lines, a dense core builds up. This will distort the magnetic field by pinching it along the inward collapse and the 'classic' sign of this occurring is the hourglass magnetic field shape, similar to what is seen in panel d of Figure 1.5. This assumes that the increased gravitational potential of the formed dense core attracts the ions as well, and these drag the field lines. This has been spotted observationally before (Girart, Rao & Marrone, 2006) and will be shown in Section 4.3.1. Ambipolar diffusion has also been observed through differences in ion and neutral velocity spectra (Li et al., 2010).

Ambipolar diffusion has been difficult to implement in magnetohydrodynamic (MHD) simulations because it is a non-ideal MHD effect. On large scales, magnetic fields and turbulent flows are well-coupled and ideal MHD can be assumed (Li et al., 2010). However, on individual cloud scales, the ambipolar diffusion process plays a significant role (Li et al., 2010). In the last decade, ambipolar diffusion has been added to MHD codes (Masson et al., 2016; Cui & Bai, 2021; Sadanari et al., 2023; Zier, Springel & Mayer, 2024) and it was found that it plays an important role in regulating disk properties, such as size, preventing catastrophic amplification of the magnetic field strength and influencing the magnetic field and rotation axis orientation (Masson et al., 2016).

1.2.3.2 Simple Model of Star Formation and Ambipolar Diffusion

Figure 1.5 shows the general process described above from the filament down to the core, assuming a strong and dynamically important magnetic field. In panel a, a filament is formed by material falling along magnetic field lines and the magnetic field is perpendicular to the diffuse material. Once the filament is dense enough, on the smaller scale in panel b, the material is now flowing along the filament towards an overdensity. In this dense region, the magnetic field is now parallel to the dense structure, dragged along by the flow of material towards the over-density. Within the molecular core, the material is again falling along the field lines into the individual molecular core such as predicted in the strong field model. In this case the core starts to contract along the field lines. Panel c zooms in on the core, where infall of material along the field lines has created a compressed core with the magnetic field parallel to the minor axis. Now the density and mass of the core is enough that gravity starts to pull inward and drag the magnetic field lines. Panel d then shows the end result which is a molecular core undergoing collapse but with an hourglass magnetic field orientation.

The magnetic field also has a fundamental dependence on density, regardless of importance in the cloud evolution. Typically, the magnetic field scales with volume density as $B \propto n^{\kappa}$. In the event of a gravitationally-bound, isothermal, spherical cloud symmetrically collapsing, κ is $\approx$2/3 (Mestel, 1966). This assumes strict flux-freezing, which at cloud scales will still be valid, but as discussed above, at core scales, ambipolar diffusion must be considered. In practice, as discussed later in Section 1.6.2, the magnetic field seems to follow a two step relation where κ=0 up to a critical density and therefore shows no dependence on the density, and then it becomes $\approx$2/3 beyond the critical density (Crutcher & Kemball, 2019). This suggests that as the cloud collapses, the magnetic field strength is actually amplified due to the compression of the field lines.

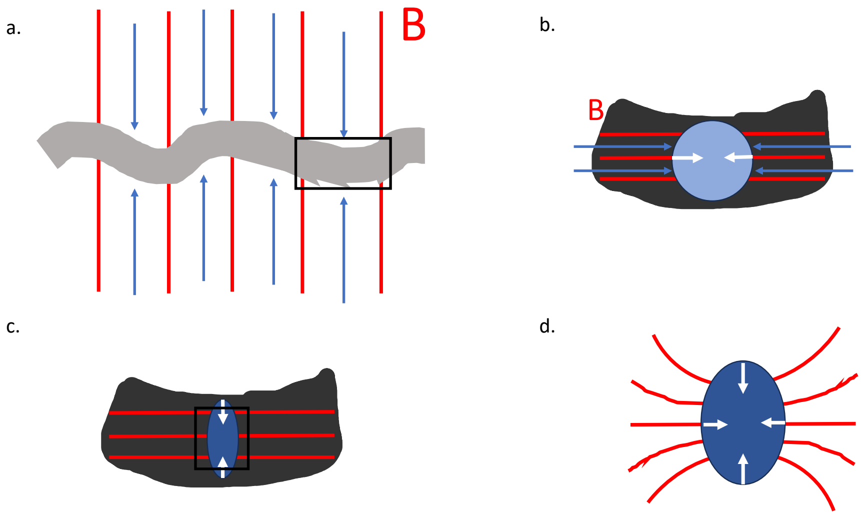

Figure 1.5: A cartoon illustrating the theoretical path to star formation which includes magnetic fields as dynamically important. Magnetic fields are shown in red, the filament in shades of grey, the molecular core and general infall of material in blue and motion of infall shown with white arrows. For the filament and the molecular core, darker grey and darker blue, respectively, indicate higher densities. A description of the cartoon is given in the text.

1.3 Fundamental Processes of Star Formation

Gravity and thermal motions of the gas have long been accepted as the two fundamental factors in star formation. Gravity is an inward force that would cause material to collapse and eventually form a star, while the thermal effects are an outward pressure, supporting a cloud against collapse. Once a molecular cloud is gravitationally bound, it could in principle collapse on the free-fall time scale which is given by

$$t_{ff} = \sqrt{\frac{3\pi}{32G\rho}} \,, \tag{1.1}$$

where ρ is the density of the cloud (Ward-Thompson & Whitworth, 2011). However, if all of the clouds that are gravitationally bound were to collapse on the order of that free-fall time scale, the star formation rate would be $10\times$ greater than what is observed (Zuckerman & Evans, 1974). Therefore, it could be suggested that fewer clouds are gravitationally bound or that, perhaps more realistically, there are more forces relevant to the evolution of the material.

Two other processes which are known to exist at all scales in the ISM and molecular clouds, namely the action of magnetic fields and turbulence, are also thought to play a role. There are two schools of thought with regard to these processes (Crutcher, 2012). One is that star formation is completely magnetically controlled, where magnetic fields provide sufficient support against collapse until clouds eventually undergo ambipolar diffusion and overpower the magnetic field, hence forming a star, but on a much longer timescale than without the magnetic field (Crutcher, 2012). The other school of thought is that the magnetic field is negligible and that star formation is controlled by non-thermal turbulent motions in the ISM and molecular clouds. Once turbulence has dissipated in molecular cores, they can then begin to collapse (Crutcher, 2012). In reality, star formation is not a simple process and is most likely affected by all of the above processes: gravity, thermal and non-thermal motions and the magnetic field.

Turbulence in the ISM has been well-observed across all scales. It is theorized to create many of the gravitational instabilities that eventually go on to form molecular clouds and cores at different scales. However, at some point turbulence does dissipate or lose out to gravity because stars do form. It can also be included in the Virial Theorem where the virial parameter of a molecular cloud can be given as

$$\alpha = \frac{5\sigma_v^2 R}{3GM} , \tag{1.2}$$

where σ_v^2 is the line-of-sight velocity dispersion (thermal and non-thermal), R is the radius of the cloud and M is the mass of the cloud. In the event that α=1, the cloud is considered to be in virial equilibrium, whereas if α is <1, it is unstable to collapse and conversely stable if α >1. A magnetic energy term can also be included in the Virial Theorem and so help determine the virial equilibrium of a cloud (Ward-Thompson & Whitworth, 2011). If we assume the magnetic contribution to be the dominant support of the cloud, we can calculate the virial parameter of the cloud to be

$$\alpha_B = \frac{5}{9}\frac{B^2 R^4}{GM^2} , \tag{1.3}$$

where B is the magnetic field strength. Again, if α_B is =1, >1 or <1, the cloud is in virial equilibrium, is gravitationally stable (this time due to magnetic influence) or is gravitationally unstable to collapse respectively.

While turbulence can be one of the main supports against gravitational collapse (Federrath & Klessen, 2012), the dissipation timescale for the turbulent energy is also shorter than the age of the clouds, ∼1 Myr (Mac Low, 1999) versus ∼20–30 Myr (Larson, 1981) respectively. This suggests that additional support mechanisms must be in place, or that turbulent energy is continuously re-injected into the cloud. This can happen due to stellar feedback and supernovae, the expansion of H II regions or molecular outflows.

Magnetic fields can provide additional support against collapse where turbulence may not be able to do so or dissipates away with no re-injection. As discussed above, magnetic fields are theorized to support against gravitational collapse across field lines due to the coupling of neutrals and ions. However, this support does not last forever and eventually, as can be seen in Figure 1.5, if there is sufficient material the collapse eventually occurs. The predicted hourglass of the magnetic field lines is considered a clear indicator of ambipolar diffusion, but it has only been seen in a few cores (e.g. Girart et al., 2012).

As mentioned above, the whole star formation process is a multi-scale process with the magnetic field and turbulence playing roles across all scales. Magnetic fields and turbulence most likely also affect each other where strong magnetic fields can result in anisotropic turbulence which can seed structure formation (Pattle et al., 2023) as well as help prevent the dissipation of turbulence (Brandenburg & Lazarian, 2013). With the interplay of magnetic fields and turbulence, one process will not always dominate, which is why we likely do not see many cores showing the hourglass morphology. Instead we see more cores with the field lines parallel to the minor axis (Basu, 2000) such as the initial condition of a strong-field model, but the process afterwards may be more complicated with thermal, turbulent and magnetic energies all contributing.

1.3.1 Theorized Modes of Star Formation

Stars are known to form in all sorts of environments. The requirements are that there is enough material to collapse and eventually form a dense core, but this material can accumulate and collapse in a variety of ways. Seo et al. (2019) suggested three general modes for star formation, fast, slow and isolated, which are shown in Figure 1.6. This model arose after a study was performed in the Taurus Molecular Cloud complex, specifically in the extended filament system known as B211/B213/L1495A which is the extended arm east-west arm in the upper panel of Figure 1.3

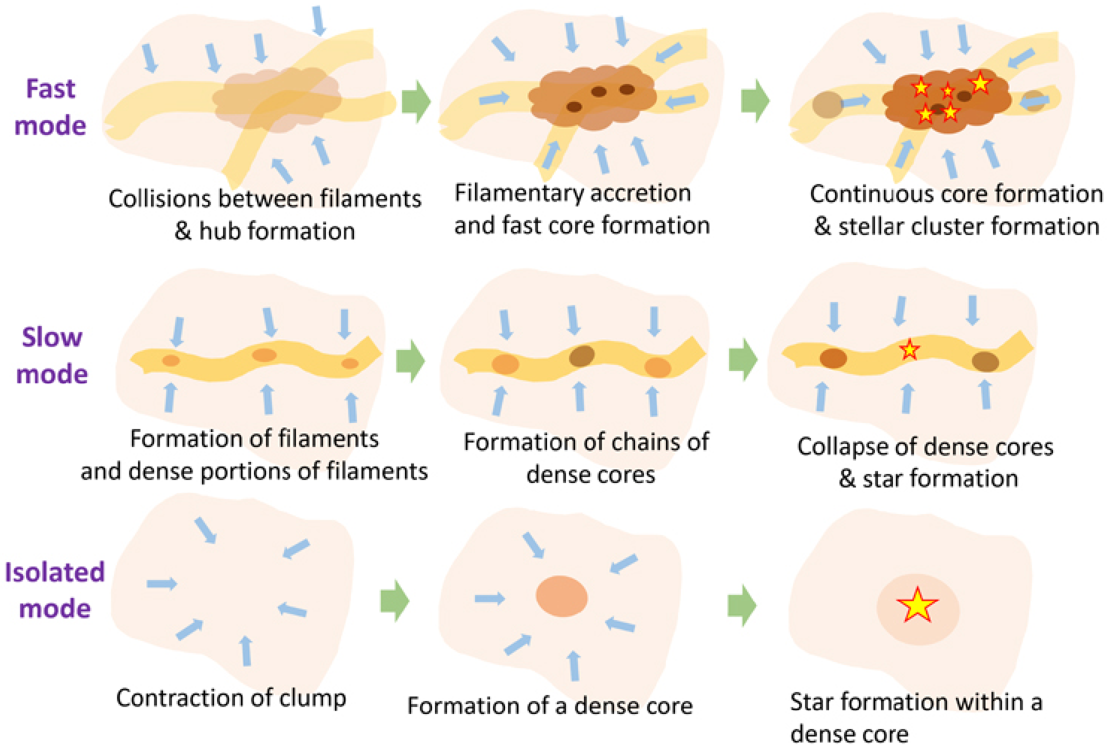

Figure 1.6: The cartoon star formation model taken from Seo et al. (2019). These are the three modes of star formation observed in the Taurus Molecular Cloud.

The fast mode of star formation is one that can lead to the formation of clusters (Seo et al., 2019). In this fast mode, filaments feed a central hub or central filament, accreting material until a dense region is formed where core formation can take place. Enough mass is centrally located that numerous cores and eventually stars can form, hence the clustering, or perhaps, a high-mass core and star can form. This sort of star formation has been observed in regions such as Monoceros R2 (Hwang et al., 2022) and NGC 6334 (Arzoumanian et al., 2021).

The slow mode proposed by Seo et al. (2019) was suggested due to the observation of a number of dense cores within the Taurus filament. Some of the dense cores were gravitationally bound while some were confined by the pressure of the surrounding filament. However, the eventual formation of a star does not seem to be influenced by any large scale nature of the filament. The large scale flow of the filament is important for creating the dense cores and 'feeding them' but not eventual star formation (Seo et al., 2019). Some work has been done in additional cores in the B213 (Eswaraiah et al., 2021) and L1495A (Ward-Thompson et al., 2023) filament areas, especially looking at the magnetic field within these cores.

The final mode of star formation, the isolated mode, was limited to just one core in the region. However, as will be discussed later in Chapter 4, this sort of core evolution is seen throughout the ISM (Karoly et al., 2020; Lin et al., 2024; Karoly et al., 2023), though a majority of dense cores are still embedded within filaments (André et al., 2010) as opposed to quiescent environments.

1.3.2 Protostars

Once a prestellar core has become gravitationally unstable, it begins to isothermally collapse due to the core's ability to freely radiate away the increase in gravitational energy, hence maintaining a constant temperature (Ward-Thompson & Whitworth, 2011). Once it has reached a stage where it can support itself against gravity with

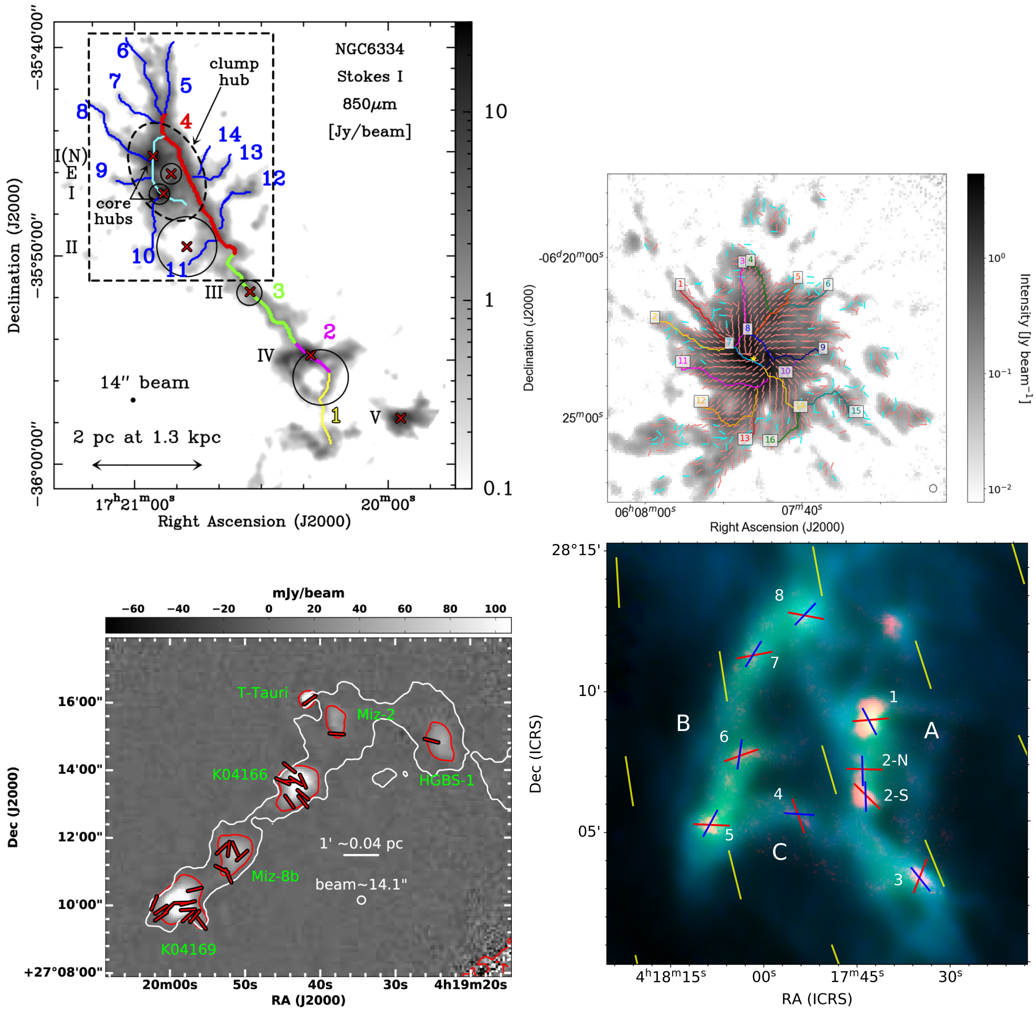

Figure 1.7: *Upper row:* NGC 6334 (left; Arzoumanian et al., 2021) and Monoceros R2 (right; Hwang et al., 2022) illustrating the fast mode. The colored extended lines show identified filaments and in Monoceros R2, the small pink and blue lines show the magnetic field. *Lower row:* B213 (left; Eswaraiah et al., 2021) and L1495A (right; Ward-Thompson et al., 2023) illustrating the slow mode of star formation. Here the red lines in both images are the magnetic field orientations. In L1495A, the yellow lines are the large-scale magnetic field and the blue lines are local filament orientation.

its own internal pressure, it is said to be a hydrostatic object (Ward-Thompson & Whitworth, 2011) and it is often surrounded by a gaseous envelope (often referred to as the 'first core' stage; Larson, 1969; Stamatellos et al., 2007). It is at this stage that the hydrostatic object becomes optically thick due to the increasing gas envelope density, then the increase in gravitational energy is not easily radiated away and so the luminosity of the object decreases (Ward-Thompson & Whitworth, 2011). Then the central object accretes material from the surrounding envelope. At this point it releases some of the accreted material in aligned and oppositely directed outflows called bipolar outflows. The outflows are thought to carry away excess angular momentum from the infalling matter (Ward-Thompson & Whitworth, 2011) and can also affect the surrounding material (such as if the protostar is still well-embedded in the molecular cloud). For a further discussion on outflows and their relation with magnetic fields, see the following Section 1.3.2.1. Once the object has accreted enough mass, it will become a pre-main-sequence star whose luminosity is chiefly from collapse and accretion and eventually a main-sequence star once hydrogen fusion begins.

1.3.2.1 Magnetic Fields and Protostellar Outflows

Initially, the magnetic field in a star-forming core will look similar to panel d of Figure 1.5. In this scenario, the pinching of the magnetic field in the center is often where an accretion disk is formed (Girart, Rao & Marrone, 2006). This can also be seen in Figure 1 of Tsukamoto et al. (2023) where the ALMA dust continuum elongation is parallel to the axis along which the magnetic field is pinched. This figure also shows the observed bipolar outflows that come from these young stellar objects. Figure 1.8 shows the theoretical evolution of the magnetic field along the lifetime of the protostar (Machida, 2017). The key magnetic field observables that this produces is the pinched magnetic field prior to and just after the first core

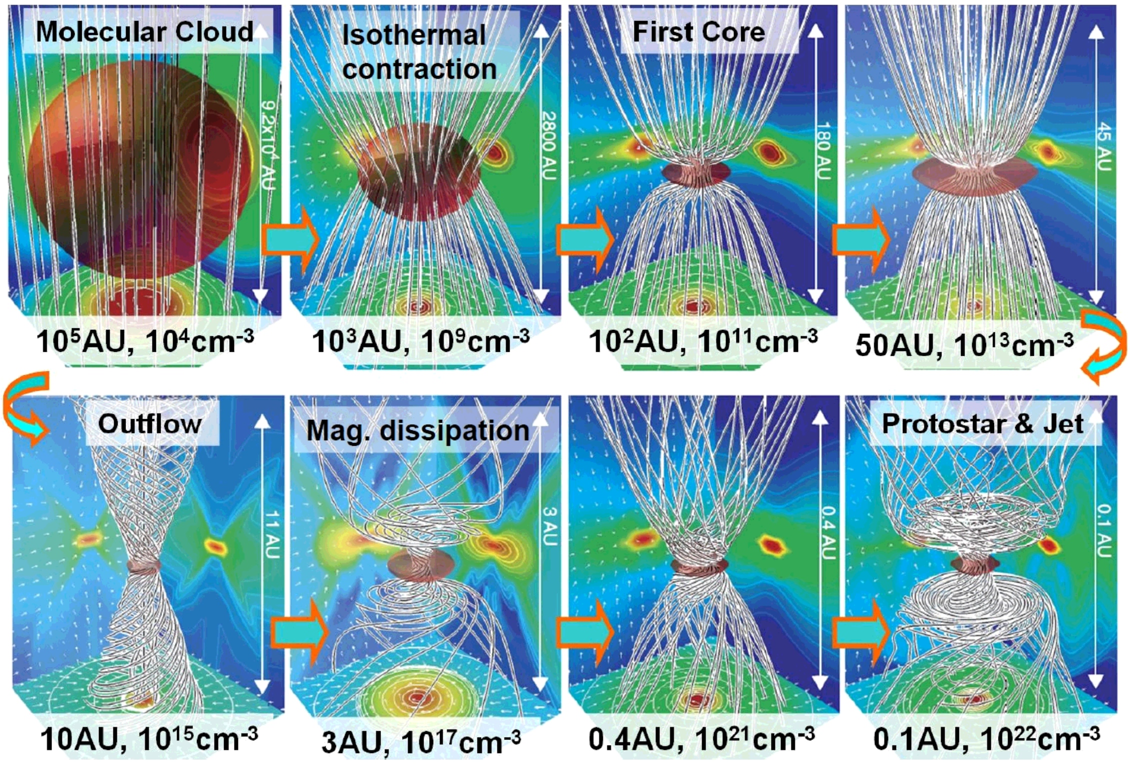

Figure 1.8: Figure 1 from Machida (2017) showing the magnetic field along the stages towards the formation of a protostar.

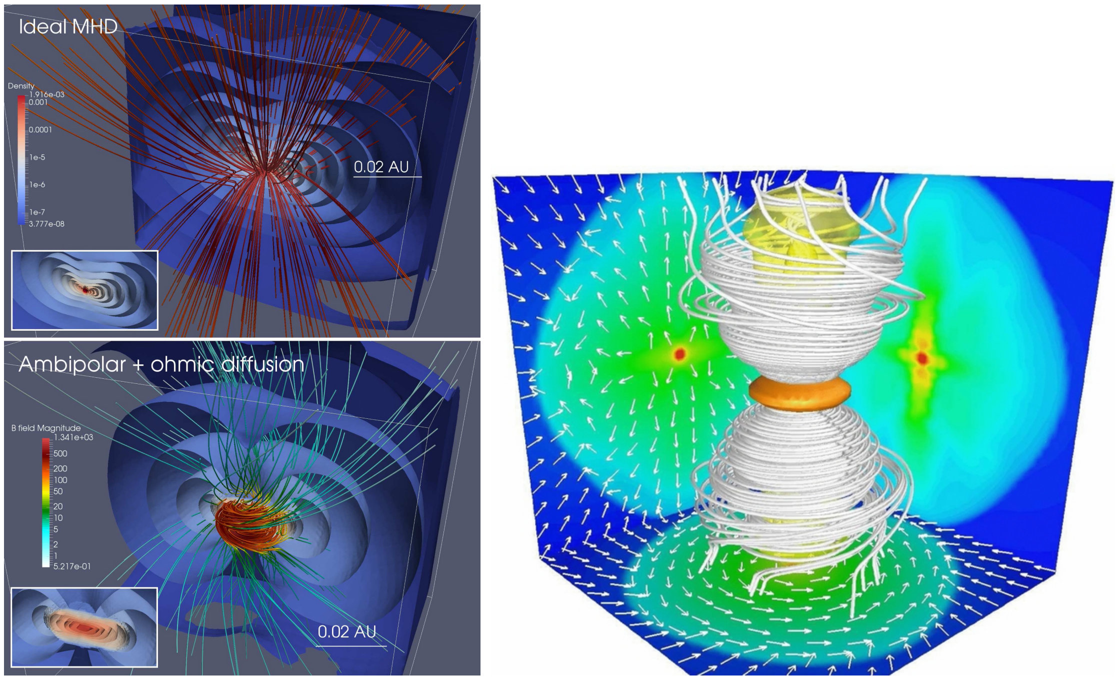

Figure 1.9: *Left:* Figure 4 from Vaytet et al. (2018) showing the magnetic field in a forming protostar simulated with ideal MHD (Upper) and non-ideal MHD (Lower). *Right:* Figure 23 from Tomida et al. (2013) showing the magnetic field in white lines, gas with velocity $>3\,\mathrm{km\,s^{-1}}$ is shown in yellow. The high density inner region ($\rho > 10^{-5}\,\mathrm{g\,cm^{-3}}$) is shown with the orange surface. The white arrows show direction of fluid.

formation and then once the outflow has started, the magnetic field is wound up from the core/disk. The magnetic fields are also wound up in the outflows which shows that there is this initial transfer of angular momentum, from the core scale outwards, mainly by the magnetocentrifugal mechanism (Blandford & Payne, 1982). This is also seen in the radiation MHD (RMHD) simulations of Tomida et al. (2013, see right panel of Figure 1.9) which also take into account some non-ideal effects.

The magnetic field plays a variety of roles in the protostellar evolution. As already mentioned, it plays a role in removing angular moment from the disk via magnetocentrifugal mechanisms. This is often known as magnetic braking (Tsukamoto et al., 2023). If there was no role of magnetic fields, the angular momentum of the core would continue to increase, flattening out the structure into a large disk. With the removal of angular momentum by the magnetic field, large disks do not form. Conversely, with a very strong magnetic field, a very insignificant disk would form (see upper left panel of Figure 1.9). A weaker magnetic field would still allow disks to form which can be reconciled with disk structures seen in protostars (e.g. Yen et al., 2017).

The magnetic field plays an initial role in the formation of the core, but once gravitational collapse has begun, ambipolar diffusion is needed to prevent amplification of the magnetic field strength to such a degree that it would prevent further collapse. This can be seen in the left panel of Figure 1.9. In the ideal MHD scenario, magnetic field strengths are much higher since ambipolar diffusion is not taken into account and so there is no decoupling of neutrals and ions. So when the core collapses, it drags in the magnetic fields with it, amplifying the magnetic flux as the same flux tubes are now threading a smaller volume. The strong magnetic field has suppressed the gas rotation and so there is no twisting of the magnetic field (Tsukamoto et al., 2023). In the non-ideal MHD simulation, ambipolar diffusion is allowed and so neutrals drift inwards, decoupled from the magnetic field and therefore not amplifying its strength. Then the core rotation is able to twist the weaker magnetic field (here also shown by blue lines rather than the red lines in the ideal MHD simulation panel). The twisting of the magnetic field also helps to drive the jets and outflows from the core (Tsukamoto et al., 2023). The disk structure is also more extended.

1.3.2.2 Expected Magnetic Field Observations

The observed magnetic field would vary for these sources based on inclination angle. Viewed directly edge on, if there was dust swept up by the outflow into outflow cavity walls, we would expect to see east/west plane-of-sky magnetic fields (observed by dust polarization) in the plane above and below the source, but would not see it on the edges where they field would be along the line-of-sight. We would also expect to see a pinched field on the envelope scale in the protostar if we assume ideal MHD, but a toroidal magnetic field at the disk scale. Whereas for non-ideal MHD (see Figure 1.9) we would expect the magnetic field around the envelope to begin to look toroidal, as well as the field at the disk scale. If the outflow were inclined towards us, and again, dust was swept up by the outflow creating cavity walls, then we would see magnetic fields aligned with the cavity walls. This would be from the plane-of-sky projection of the wrapped up magnetic field around the outflow. This has been seen at larger scales in Karoly et al. (2023, and see Chapter 3) and at smaller, ALMA scales in Hull et al. (2017); Hull et al. (2020); Lyo et al. (2021); Pattle et al. (2022). Magnetic fields have also been observed in disks, where a toroidal field is seen (Segura-Cox et al., 2015; Lee et al., 2018), or a more complicated mixture of toroidal and poloidal is seen (Stephens et al., 2014), though care must be taken to avoid polarization produced by self-scattering in larger dust grains (Stephens et al., 2017).

1.3.2.3 Classification of Protostars

Protostars go through a 4 stage process, divided into Class 0, I, II and III (André, 1994). Class 0 is the youngest stage of the protostar and was discovered by the James Clerk Maxwell Telescope (Andre, Ward-Thompson & Barsony, 1993). The stages of protostars are often identified by their infrared spectral index α which is given by

$$\alpha = \frac{\mathrm{d}log(\lambda F_\lambda)}{\mathrm{d}log\lambda} \ , \tag{1.4}$$

where λ and F_λ are the wavelength and flux density at the wavelength. The spectral index is just the slope of a spectral energy density plot generally taken between 2.2

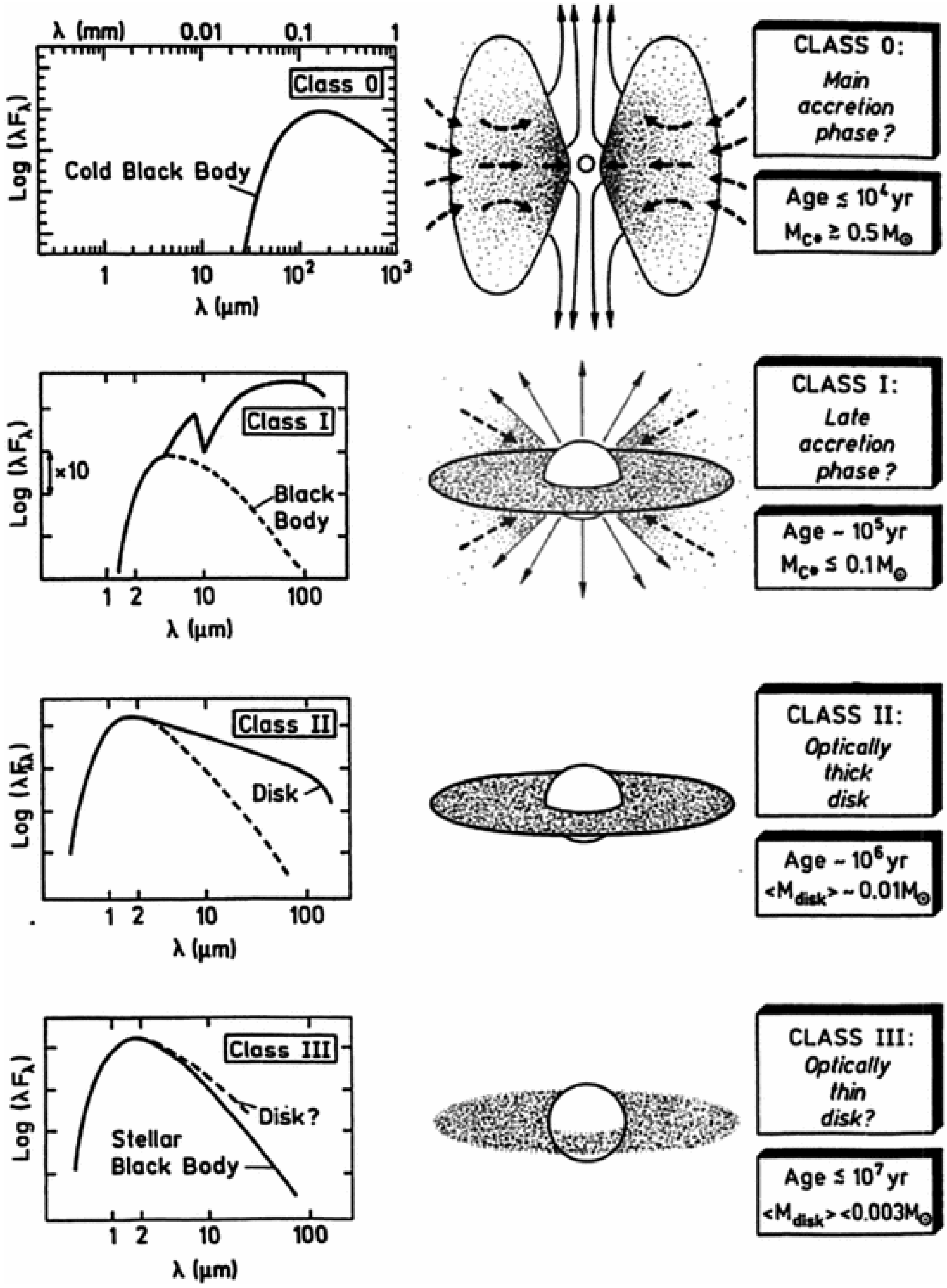

Figure 1.10: The evolutionary sequence of protostars, detailing the Classes 0–III Andre & Montmerle (1994).

and 20–25 μm (Wilking, Lada & Young, 1989) which is the infrared range of the spectral energy density curve.

Class 0 objects are generally protostars where the surrounding gas envelope is still more massive than the hydrostatic core embedded inside (Andre, Ward-Thompson & Barsony, 1993). This is then the main accretion phase for the protostar and hence a stage at which large, energetic bipolar outflows are produced and they are often characterized by no near-infrared (<10 μm) emission but strong submillimeter emission (André, 1995). Class I protostars are when the accretion phase has slowed considerably but the protostar is still embedded and hence it still has a significant infrared excess and so $\alpha >0$ (Wilking, Lada & Young, 1989). Class II protostars are those which are generally considered classical T Tauri stars and are now brighter in luminosity having begun radiating from Kelvin-Helmholtz contraction and still have a significant disc. Much of the accretion at this stage has ended. The spectral index of Class II sources is $0> \alpha >-2$ (Wilking, Lada & Young, 1989). Class III protostars have only a slight infrared excess, due to the residual disc, and are approaching the main sequence and typically have a spectral index of <-2 (Wilking, Lada & Young, 1989).

1.4 Magnetic Fields in Relation to other Star Formation Processes

Magnetic fields are subject to the influence of numerous processes in molecular clouds. Gravity and turbulence are two factors which can affect the magnetic field structure and strength (Hennebelle & Inutsuka, 2019), but its relation to the thermal pressure of the cloud must also be considered. Additionally, protostellar outflows have been known to either affect, or be affected by, magnetic fields, as seen by many instances of the magnetic fields tracing outflows (see Hull et al., 2017; Hull et al., 2020; Lyo et al., 2021; Pattle et al., 2022). This phenomenon, along with stellar winds and general stellar feedback, can also inject turbulence into molecular clouds, at which point it again competes with the local magnetic field. We can often calculate the energy budget of a core, which can also include the energy of protostellar jets or stellar winds.

In general, we can calculate the magnetic energy in a cloud using

$$E_{\rm B}(\rm J) = 10^{-20}\frac{\rm B^2(\mu G^2)V(m^3)}{2\mu_o(N\,A^{-2})} \tag{1.5}$$

where B is the magnetic field strength in μG (as measured in the plane-of-sky), V is the volume of the region in m^3 and μ_o is the permeability of free space, giving us the magnetic energy in Joules (see Equation 4.74 of Ward-Thompson & Whitworth, 2011). This gives an approximation of the magnetic energy budget and can then be compared to gravitational and thermal and non-thermal kinetic energies.

1.4.1 Gravity

In the early stages of a core's evolution, the magnetic field can provide some support against gravitational collapse (see panels b to c in Figure 1.5). At some point however, the core becomes massive enough that it could overcome the magnetic support and begin to collapse. To determine this in molecular clouds and cores, the parameter mass-to-flux ratio (λ) is used (Crutcher, 2004).

λ compares the critical value for the mass, $\mathrm{M}_{B_{\rm crit}}$, which can be supported by the magnetic flux through a flux tube Φ, such that $\mathrm{M}_{B_{\rm crit}} = \Phi/2\pi\sqrt{G}$ (Nakano & Nakamura, 1978) to the observed mass and flux values. If the column density N and magnetic field strength B can be measured, the observed value for the ratio between mass and flux is $(M/\Phi)_{\rm obs}$=mNA/BA and then the mass-to-flux ratio λ is,

$$\lambda = \frac{(M/\Phi)_{\rm obs}}{(M/\Phi)_{\rm crit}} = 7.6\times 10^{-21}\frac{N_{\rm H_2}(\rm cm^{-2})}{B_{\rm pos}(\mu G)} \tag{1.6}$$

where m=2.8 m_{H}, N_{H_2} is the molecular hydrogen column density and B_{pos} is the plane-of-sky magnetic field strength (Crutcher, 2004). To the same order, this mass-to-flux ratio value can also be derived from the magnetic virial parameter (Equation 1.3). Setting the mass in that equation to be the critical mass and substituting $N\pi m_{\mathrm{H}} \sim M/R^2$, we can rearrange to get a similar parameter which is $\sim$5$\times$10^{-21} N_{H_2} / B.

When $\lambda < 1$, the magnetic field is strong enough to support against gravity; this is referred as the "magnetically sub-critical" regime. Alternatively, if $\lambda > 1$, then the magnetic field is insufficient by itself to oppose gravity, and the cloud is instead "magnetically super-critical".

In Figure 1.5, panel b shows a magnetically sub-critical core, panel c shows a magnetically trans-critical core (*lambda* $\sim$1, the transition phase between sub- and super-critical) and then finally panel d shows a magnetically super-critical core. This follows the general observation which is that the envelopes of molecular cores/clouds are generally sub-critical whereas the cores transition towards magnetically super-critical at higher densities (Crutcher, 2012).

1.4.2 Turbulence or Non-thermal Motions

In the gas, the non-thermal motions are approximated from the 1-D line-of-sight velocity dispersion. Magnetic fields can generate turbulence via Alfvén waves where Alfvén waves are either transverse or torsional waves in the magnetic field lines and have a velocity v_{A}, given by

$$v_{\mathrm{A}} = \frac{B}{\sqrt{4\pi\rho}} \, , \tag{1.7}$$

where B is the magnetic field strength and ρ is the gas density. Alfvén waves travel along magnetic field lines and their restoring force is the magnetic tension. The oscillations can impart non-thermal motions to the ions and hence to the neutral gas, seeding turbulence.

The Alfvénic Mach number is given by

$$\mathcal{M}_{\rm A} = \frac{\sigma_{\rm NT}}{v_{\rm A}} \propto \sqrt{\frac{E_{K,NT}}{E_B}} \ , \tag{1.8}$$

where $\sigma_{\rm NT}$ is the one-dimensional non-thermal velocity dispersion of the gas and $v_{\rm A}$ is the Alfvén velocity of the magnetic field and $E_{K,NT}$ and E_B are respectively the non-thermal kinetic energy and the magnetic energy. Since $\mathcal{M}_{\rm A}$ is approximately a relation between the non-thermal kinetic energy and magnetic energy, this metric can determine the relative influence of the two. $\mathcal{M}_{\rm A}$ <1 suggests the magnetic field is more important than turbulent motions (sub-Alfvénic) while $\mathcal{M}_{\rm A}$ >1 means the turbulent motions are more important (super-Alfvénic).

1.4.3 Thermal Motions

The magnetic potential energy can also be compared to the thermal energy of the plasma. In general, molecular clouds and cores are very cold, in the range of 10–50 K. The thermal-to-magnetic energy ratio is given by the plasma beta value

$$\beta = \frac{E_{K,T}}{E_B} = \frac{nk_BT}{10^{-20}B^2/2\mu_0} \ , \tag{1.9}$$

where $E_{K,T}$ is the thermal kinetic energy, n is the column density in m^{-3}, T is the temperature in Kelvin, k_B is the Boltzmann constant, B is the magnetic field strength in μG and μ_0 is the magnetic permeability in units of N A^{-2}.

If we consider a molecular cloud of order 10^3 cm^{-3}, at 20 K and with a magnetic field strength of 150 μG, the plasma beta value calculated using Equation 1.9 is 0.003. Values of β less 1 indicate a magnetically-dominated system. In the ISM and cold molecular clouds, we generally disregard the comparison between thermal energy and magnetic potential energy because of the low β value. As mentioned above, magnetic field strength in the denser regions of molecular clouds is thought to go as $n^{0.5}$, in which case the β value is only temperature dependent and the low β assumption continues to hold.

1.5 Magnetic Field in MHD Simulations of Low-Mass Star Formation

In Sections 1.3.2.1 and 1.2.3.1, we have already discussed recent advances in MHD simulations, particularly in the context of non-ideal MHD simulations (those that account for effects such as ambipolar diffusion) and resolved protostar simulations. The suite of MHD simulations available are far more expansive than these two special cases. Codes such as ATHENA++ (Stone et al., 2008, 2020), RAMSES (Teyssier, 2002; Masson et al., 2012) and SILCC (Walch et al., 2015) are sophisticated MHD simulation packages.

Beginning at larger scales in low-mass star formation, many simulations look at how the magnetic field evolves during the formation of filaments (where low-mass cores may form) or individual molecular clouds. Simulations with SLICC (Girichidis et al., 2018) show that at lower gas densities, the magnetic field follows the volume density scaling (see Section 1.2.3.2) with $\kappa \approx 2/3$, suggesting that flux-freezing holds. Then κ becomes $\approx 1/4$, which indicates that material is flowing along the magnetic field lines, suppressing any compressional effect (Girichidis et al., 2018). This would indicate a magnetic field that is initially parallel to the material but that will soon become perpendicular as material builds up in a ridge perpendicular to the magnetic field. Significantly less molecular clouds are formed in the simulations with a magnetic field than without. In addition, they find clouds to form initially magnetically sub-critical and then transition to super-critical within 30-40 Myr (Girichidis et al., 2018). Seifried et al. (2020) also see a transition of magnetic fields being parallel to structures to then becoming perpendicular at column densities of $\sim 10^{21-21.5}\,\mathrm{cm}^{-2}$.

On the filament scale, Seifried & Walch (2015) found that magnetic fields perpendicular to filaments cannot stabilize supercritical filaments, but magnetic fields parallel to the filament elongation stabilize the filament from radial collapse and maintain the characteristic 0.1 pc filament width. Beattie & Federrath (2020) find that in sub- to trans-Alfvénic simulations (with a Mach number <4), the anisotropies in column density are aligned with the magnetic field, while when the Mach number is >4, the high density filaments are perpendicular to the magnetic field. Wurster, Bate & Price (2019) also find this relation between filaments and magnetic field orientation. Based on these different simulations, it would seem that the evolution of the magnetic field may differ in regions and be dependent on the formation of the filament if there are some filaments with preferentially parallel magnetic fields. Observationally, the transition towards perpendicular orientation to high density filaments is more commonly seen (Soler et al., 2013; Planck Collaboration et al., 2016b).

Going down further in scale to individual cores (such as those which might form in filaments, see Section 1.2.1.2), Masson et al. (2016) used the non-ideal MHD extension of RAMSES (Masson et al., 2012) to investigate the effect of the magnetic field and non-ideal MHD conditions on formation of the first Larson core (the 'First Core' in Figure 1.8). They define the Larson core at a density of $\sim 10^{-13}\,\mathrm{g\,cm^{-3}}$ and when the gas is optically thick enough to stop radiative cooling (Larson, 1969; Masson et al., 2016). They find that the mass of the Larson core remains similar between the non-ideal MHD and ideal MHD model, but that the magnetic field strength and morphology vary. The magnetic field strength is less in the non-ideal MHD case and its morphology is not as pinched as the ideal MHD case. This is due to the ambipolar diffusion in the non-ideal MHD where neutrals have decoupled from the magnetic field and flux-freezing is not as strong. This also hinders the braking mechanism since the magnetic flux is not increasing as drastically (Masson et al., 2016). They also find that any initial misalignment of the magnetic field and the rotation axis does not affect the non-ideal MHD results, with ambipolar diffusion effects still dominating the resulting magnetic field morphology.

In Section 1.3.2.1 we reviewed what these simulations show in protostars. To summarize, they show a magnetic field which is toroidal around a conical shell from the outflow. Within the disk, the magnetic field is toroidal when considering non-ideal MHD effects. There is still slight pinching to the magnetic field and a poloidal component will be seen at the disk where the outflows are being launched from.

Simulations which consider non-ideal MHD effects show that from large-scale down to small-scale, the magnetic field plays a role in the evolutionary track of a stellar object. To begin with it is governed largely by ideal MHD effects, where flux-freezing still occurs, and the material falls along magnetic fields lines, forming dense ridges which are then perpendicular to the magnetic field lines. Then once the core is formed within these ridges, the magnetic field will be slightly pinched inwards, though not as significantly if not considering ambipolar diffusion. Then once a protostar is formed and outflows are launched, the magnetic field orientation helps funnel the outflow outwards and remove angular momentum from the disk. This appears as a magnetic field wrapped around the outflow and toroidal in the disk.

1.6 Observational Techniques of Magnetic Fields

Magnetic fields in our own galaxy can be observed through a variety of techniques, including, but not limited to, dust polarization (Hall, 1949; Hiltner, 1949; Andersson, Lazarian & Vaillancourt, 2015), the Zeeman effect (Zeeman, 1897; Crutcher & Kemball, 2019), spectral line polarization (Goldreich-Kylafis effect; Goldreich & Kylafis, 1981, 1982) and Faraday rotation (Cooper & Price, 1962). We primarily use dust polarization measurements due to the relative ease of observation, but we compare with Zeeman observations where possible. Localized Faraday rotation is difficult to use in our own galaxy due to significant foreground contamination, though there are some novel methods being introduced (see Tahani et al., 2018), while the Goldreich-Kylafis effect suffers from a $\pm 90^o$ degeneracy in the magnetic field direction (Goldreich & Kylafis, 1981).

1.6.1 Interstellar Dust Polarization

The most widely used method of probing interstellar (and occasionally galactic) magnetic fields is the measurement of interstellar dust polarization (Hall, 1949; Hiltner, 1949). The morphology of the plane-of-sky (POS) component of the mean magnetic field (averaged along the line of sight) in the interstellar medium can be directly inferred from the polarization of dust thermal **emission** at far-infrared (FIR) and sub-millimetre (sub-mm) wavelengths (see Andersson, Lazarian & Vaillancourt, 2015, and references therein). At optical and near-infrared (NIR) wavelengths, the magnetic field can be inferred from the polarization of dust **extinction**. In the FIR to sub-mm regime, the polarized emission is expected to be perpendicular to the plane-of-sky magnetic field orientation due to the alignment of interstellar dust grains with magnetic fields through Radiative Alignment Torques (RATs) (Lazarian & Hoang, 2007; Andersson, Lazarian & Vaillancourt, 2015). In the optical to NIR, the polarized emission is expected to be parallel to the plane-of-sky magnetic field. This is because at optical/NIR wavelengths, the light is absorbed by the dust grains and the maximum absorption happens along the semi-major axis and so the transmitted polarization is parallel to the semi-minor axis which is parallel to the magnetic field. Therefore the polarization vector is parallel to the magnetic field. In the FIR/sub-mm regime, the radiation comes from thermal emission of the dust grains and the maximum emission happens along the semi-major axis and hence the polarization vector is parallel to the semi-major axis. Since the semi-minor axis is aligned with the magnetic field, the polarization vector must be rotated by 90° to infer the magnetic field direction.

As wavelength increases, the depth into which we can observe molecular clouds increases as well. Because NIR and optical polarization rely on extinction polarimetry, they can only probe diffuse regions and therefore more generally trace the large-scale magnetic fields. The dense molecular clouds which harbor star formation are too optically thick for extinction polarimetry and that is where we rely on FIR-mm emission polarimetry. The thermal emission of the dust grains occurs in the FIR-mm regime and so generally FIR-mm polarization traces the smaller-scale magnetic field within molecular clouds. These molecular clouds can have volume densities up to 10^{5-6} cm^{-3} and temperature around 10-15 K and so rely largely on cosmic ray ionization to heat the grains (so they can thermally re-radiate).

The limitation of this method of observations is that only the 2-D POS magnetic field component is observed. There is also no direct measurement of the magnetic field strength with dust polarization. There have been a variety of methods to try and estimate the magnetic field strength from dust polarization observations. These are introduced later in the thesis but all essentially stem from the Davis-Chandrasekhar-Fermi method (DCF Davis, 1951; Chandrasekhar & Fermi, 1953).

In this thesis, we primarily use 850 μm polarization observations obtained with the POL-2 polarimeter at the JCMT (see Chapter 2). Unless explicitly stated otherwise, the 'half-vectors' shown in the figures will represent the magnetic field direction, i.e. the polarization vectors have been rotated by 90^o. The term 'half-vectors' is used here due to the 180^o ambiguity in the direction of polarization vectors (i.e. the vectors do not have an arrow head, 45^o is the same as 225^o).

1.6.1.1 Radiative Alignment Torque Theory

The inference of POS magnetic fields from polarization observations requires that interstellar dust grains align with the local magnetic field. The currently accepted theory for the alignment is the radiative alignment torque (RAT) theory (Lazarian & Hoang, 2007; Andersson, Lazarian & Vaillancourt, 2015).

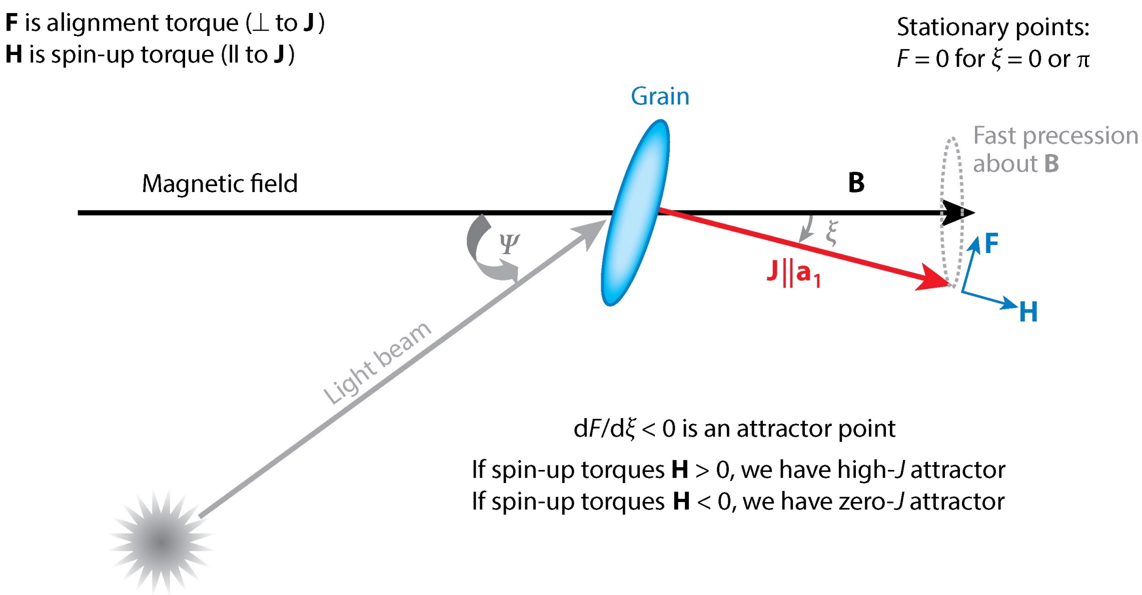

Figure 1.11: A simplified cartoon of RAT from Andersson, Lazarian & Vaillancourt (2015). The grain is modelled as an ellipsoid and is being spun up by radiation incident on it with an angle of Ψ to the B-field. The grain's spin axis J is parallel to the axis of maximum inertia a_1 after internal alignment. It is precesseing around the magnetic field, B, with an angle ξ. The alignment torque F will be 0 when the grain's spin axis is parallel to the magnetic field and hence the grain will be aligned (this is a stationary point).

RAT theory predicts that irregular sized grains (though often approximated as an ellipsoid) are spun up by angular momentum transfer from photons which have a wavelength less than twice the grain's effective radius. Once the grain is spun up, if it is paramagnetic (such as silicates), it exchanges some of its rotational energy for spin-flips in the solid (Barnett effect; Barnett, 1915; Purcell, 1979) which creates some charge separation and causes the angular momentum of the grain to align with the grain's axis of maximum inertia (in an ellipsoid, the semi-minor axis). With the rotation and charge separation, the grain is magnetized, specifically parallel to the axis of rotation (the semi-minor axis). Now that the grain is magnetized and has a magnetic moment, it precesses around the local magnetic field via Larmor precession (Dolginov & Mitrofanov, 1976). With continued radiative torques, the grain eventually aligns with the local magnetic field with the semi-minor axis parallel to the magnetic field which is a stationary point and hence the grain will remain aligned (Lazarian & Hoang, 2011), until its next collision with another grain, after which the whole process repeats. RAT theory has been well-tested, primarily by observations confirming various theoretical requirements that other grain alignment mechanisms cannot explain. In addition, the alignment of grains is a phenomenon that has been demonstrated in the laboratory (Abbas et al., 2004).

1.6.2 Zeeman Effect

The Zeeman effect is considered to be the 'gold standard' of magnetic field observations because it directly measures magnetic field strength. A general review of the Zeeman effect is given by Crutcher & Kemball (2019). It was first definitively detected in the diffuse, extended ISM in the 21 cm hyperfine line of H I by Verschuur (1968). H I is the 'easiest' species to detect the Zeeman effect in and only many years later was it then detected in molecules, specifically OH and CN. The Zeeman effect is simply the splitting of a spectral line when the particle is interacting with a magnetic field. The frequency of the spectral line is shifted by

$$\nu = \nu_0 \pm \frac{\mu_B B}{h} \ , \tag{1.10}$$

where ν is the shifted frequency, ν_0 is the unshifted frequency of that spectral line, μ_B=$e\hbar/2m_e$ is the Bohr magneton (9.27×10^{-28} J G^{-1}), $\hbar$ is the reduced Planck's constant and B is the magnetic field strength. Since the splitting magnitude is proportional to the B-field strength, the B-field strength is directly recoverable. The most sensitive species to the Zeeman effect are those with odd numbers of electrons (Crutcher & Kemball, 2019). Theoretically, with full observation of Stokes I, Q, U and V, information of the whole B-field (line-of-sight and plane-of-sky) is recoverable, though instruments are currently not sensitive enough and only the line-of-sight B-field information is gathered.

Some of the most important work that has come from the Zeeman observations is the general scaling law of the magnetic field and the number density (see Figure 1.12). It was observed that up until some density n_0 the magnetic field strength was a constant B_0 with increasing number density and afterwards it increased as $B_0(\frac{n}{n_0})^\alpha$ where n_0 is $\approx$300 cm^{-3} and α is 0.65$\pm$0.05 (Crutcher & Kemball, 2019). B_0 is found to be 10–20 μG which agrees well with interstellar magnetic field strengths. When plotting Zeeman measurements against N_H (hydrogen column density), the transition from constant to increasing B happens at $\sim$10^{22} cm^{-2} (Crutcher & Kemball, 2019) which agrees well with the transition column density found in Planck Collaboration et al. (2016b) as mentioned above in Section 1.2.3. Assuming the transition points in n_H and N_H are the same, this indicates the transition occurs for clouds in the diameter range 0.1–1 pc, sizes which are not unusual for molecular cores.

However, the Zeeman effect is very time-consuming to observe and it can be difficult to observe line-tracers in the densest of star-forming cores.

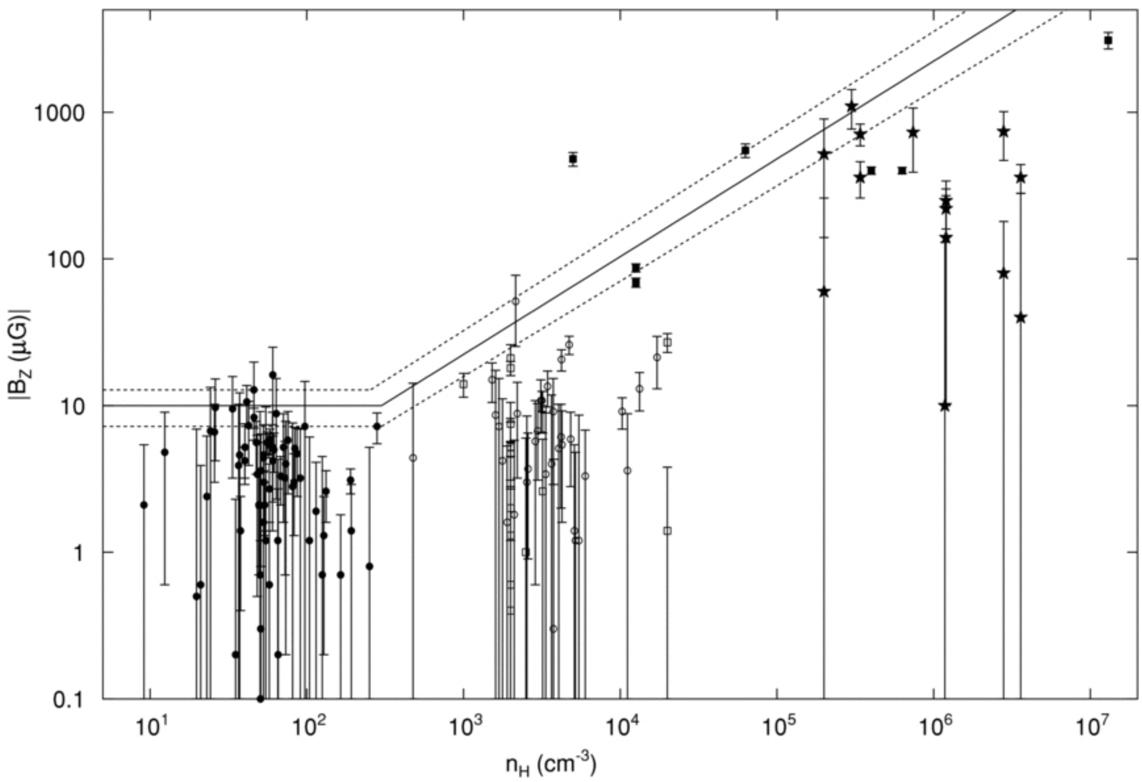

Figure 1.12: Figure 1 from Crutcher et al. (2010) showing the relationship between line-of-sight magnetic field strength (probed with H I, OH and CN) and hydrogen volume density (where n(H) is either n(H_I) or 2n(H_2)). Filled cirlces indicate H_I diffuse clouds, open circles and squares are dark clouds, filled squares and stars are molecular clouds. The plotted solid line shows the most probable model and the dotted lines show acceptable ranges in model parameters.

1.6.3 Spectral Line Polarization and Faraday Rotation

Two other methods for observing magnetic fields are spectral line polarization due to the Goldreich-Kylafis (G-K) effect and Faraday rotation.

Faraday rotation is the rotation of the plane of polarization due to the propagation of that polarized light through a magnetized medium that is populated with electrons. The plane of polarization rotation is due to the moving electrons (moving due to the electric field of the propagating radiation) creating a magnetic field which is in addition the local magnetic field of the medium and hence creating a net magnetic field which affects the left- and right- circular polarization differently and so a net rotation in linear polarization is seen. The amount of rotation is given by

$$\Delta\psi = \lambda^2(0.812 \int n_e \vec{B} \cdot \vec{dl}) = \lambda^2 \mathrm{RM} \ , \tag{1.11}$$

where $\Delta\psi$ is the amount of rotation in radians, λ is the wavelength, n_e is electron volume density of the magnetized region and $\vec{B}$ and $\vec{dl}$ are the magnetic field strength and path length respectively. The value RM is the rotation measure which the magnetic field is derived from given some assumed electron density. The polarization angle will be different at different wavelengths which allows a rotation to be calculated for each wavelength and a plot of $\Delta\psi$ versus λ^2 will then yield the RM value. Since the path length is along the line-of-sight, the magnetic field strength and direction (as indicated by the sign) is in the line-of-sight as well. Pulsars and extragalactic sources are often the targets for Faraday rotation measurements, where the rotation of the polarization from those objects at different wavelengths can yield a RM value. Then, once the electron number density is known, a magnetic field strength and direction can be inferred.

The G-K effect is the linear polarization of emission lines and was first predicted by Goldreich & Kylafis (1981, 1982). In the presence of a magnetic field, the rotational levels of the molecule are split into magnetic sub-levels and if these are unequally populated, there is a net polarization of the emission line. It is a particularly useful tool because it theoretically allows for a third-dimension measurement of the magnetic field, in velocity space.

Both of these methods are very difficult to perform observationally in dense molecular clouds, though for different reasons. Faraday rotation has been successfully used to probe galactic scale magnetic fields and ionized regions in the ISM (due to high n_e), but it is difficult to use in dense molecular clouds due to significant foreground contamination and low free electron density (initially thought to be near zero) in dense regions. There are novel methods being introduced and investigated such as building a model of the foreground contamination from pointings immediately around the target (an on-off method; Tahani et al., 2018) which have produced sensible results, though it is still largely untested. It assumes the source of electrons in the dense regions is cosmic ray ionization, an assumption which is now thought to be valid (Padovani, Galli & Glassgold, 2009; Padovani et al., 2018). However it relies on existing catalogs of RM values and the characterization of the electron volume density is still difficult.

The G-K effect, though generally well-understood, remains difficult to observe, particularly in achieving polarization detections above the instrumental polarization level (e.g. Forbrich et al., 2008). However it has been performed in some cases, particularly in the circumstellar envelopes of AGB stars (e.g. Girart et al., 2012; Huang et al., 2020). Additionally, it suffers from a $\pm 90^o$ degeneracy in the magnetic field direction which complicates interpretation.

1.7 B-fields In STar-forming Region Observations

The B-fields In STar-forming Region Observations (BISTRO) survey is a large program at the James Clerk Maxwell Telescope (JCMT) which has had three successfully accepted bids for time (Project IDs: M16AL004, M17BL011 and M20AL018).

These three bids have been named 'BISTRO-1,' 'BISTRO-2' and 'BISTRO-3.' Each generation of BISTRO builds on the previous generation's work, but all with the ultimate goal of determining what the effect of the magnetic field is on star formation.

With the instalment of a polarimeter on the James Clerk Maxwell Telescope (see Chapter 2), BISTRO-1 followed up many targets from the Gould Belt Survey (Ward-Thompson et al., 2007) which studied nearby star-forming regions of relatively low mass, but that could be well-resolved by the JCMT at approximately thousands to tens of thousands of AU. BISTRO-1 set forth the three axes that the next two generations would seek to fill out, the mass/size, evolutionary and resolution scale axes.

BISTRO-2 pushed the mass/size scale and evolutionary scale axes to new points by observing intermediate distance ($\sim$1–2 kpc) and intermediate- to high-mass star-forming regions. These regions would now be resolved more at the filament and molecular cloud scale ($\sim$1 pc) and the evolutionary focus shifted from individual stars/cores to the whole star forming regions.

BISTRO-3 has pushed all scales to their extremes. It has targeted very nearby, individual, low-mass star-forming cores, getting high resolution observations of the earliest stages of individual star formation, the prestellar cores. On the other end of the axes, the Galactic Center was also observed where JCMT resolves cloud-scale magnetic fields and where the molecular clouds are massive but undergoing lower-than-expected star formation. In addition, a series of high mass protostellar objects were observed.

1.8 Thesis Outline

The work is presented as follows. Chapter 2 discusses the observations and data reduction associated with the results presented. This focuses primarily on the JCMT and its SCUBA-2 and POL-2 instruments. Then Chapter 3 is an in-depth study of the magnetic field in L43 which is a nearby, isolated but complex star forming region. Chapter 4 builds on the results of Chapter 3 and considers other molecular clouds observed with BISTRO, discussing the various modes of star formation (fast, slow and isolated) and the effect of the magnetic field. Chapter 5 then moves far away from nearby star-forming regions to the Galactic Centre where we demonstrate a large-scale dependence of the material on the magnetic field, showing the global field structure, and more global laws of star formation will be discussed. Chapter 6 brings together Chapter 3–5 in the context of discussing the magnetic field in different modes of star formation and evaluating critical column densities in star formation. Finally, conclusions are presented and future work is discussed.

Chapter 2

Instrumentation, Observations and Data Reduction

2.1 The James Clerk Maxwell Telescope

The James Clerk Maxwell Telescope (JCMT) is a 15 m dish telescope operated by the East Asian Observatory (EAO) but the UK and Ireland are partner institutions with certain universities providing some funding. It sits on the summit of Mauna Kea at 4092 m on the island of Hawai'i. The JCMT is a 15 meter radio dish mounted on a alt-azimuth mount. The design of the telescope is Cassegrian-Nasmyth with the tertiary mirror able to rotate to direct the light to different instruments. The JCMT operates between 0.45 and 3.49 mm (666–86 GHz) which is made possible by its location on the summit of Mauna Kea and favorable weather patterns. Observations towards the higher frequencies are generally quite difficult from Earth due to the atmosphere absorbing most of the light in that wavelength range. Despite JCMT's location, it is still quite difficult to observe at 450 μm. This can be seen in Figure 2.2 and Table 2.1, where transmission is much lower at 450 μm (666 GHz) than at 850 μm (353 GHz).

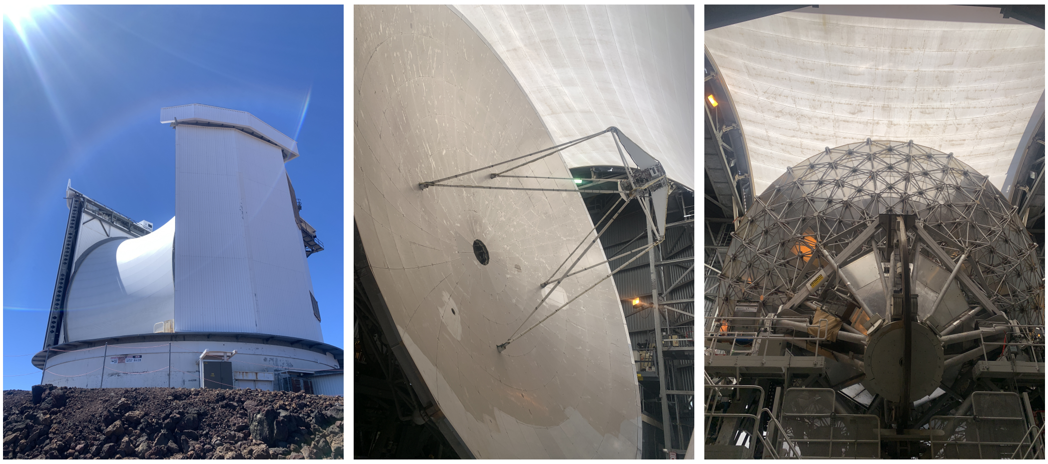

Figure 2.1: *Left:* The JCMT as seen from the outside with its doors open. The GORE-TEX™ wind blind can be seen in the front. *Center:* The 15-m dish of the JCMT. The secondary mirror can be seen on its four legs and the hole to the tertiary mirror is seen in the center. *Right:* The dish as seen from behind. The main cabin is in the center and SCUBA-2/POL-2 is to the left and HARP to the right. Pictures from Janik Karoly.

CHAPTER 2

There are three primary instruments on the JCMT. The Submillimetre Common-User Bolometer Array 2 (SCUBA-2), the Heterodyne Array Receiver Program (HARP) and Nāmakanui. Nāmakanui is an in-cabin instrument while SCUBA-2 and HARP are out-of-cabin alongside the telescope. The data presented in this thesis come primarily from SCUBA-2 and its associated polarimeter POL-2. Some supplementary data will come from HARP, but it is all archival and simple mosaicking steps were taken with reduced data products rather than any in-depth data reduction. SCUBA-2 operates simultaneously at 450 and 850 μm (666 and 353 GHz respectively). HARP can be tuned between 325 and 375 GHz, while Nāmakanui has receivers which can operate at 86, 230 and 345 GHz. The specifications, operation and data reduction for SCUBA-2/POL-2 will be discussed in detail below.

The JCMT categorizes the site conditions using five weather bands. It defines the weather bands based on a value τ_{225} which is the atmospheric opacity at 225 GHz as measured by instruments on the summit. The value τ_{225} is determined using the equation

$$\tau_{225} = 0.04\text{PWV} + 0.017\,, \tag{2.1}$$

where PWV is the measurable precipitable water vapor in millimeters. The PWV is measured by a radiometer at 225 GHz at the Sub-Millimeter Array (SMA) observatory (formerly located at the Caltech Submillimeter Observatory) which is next to the JCMT on the summit and by an in-cabin, line-of-sight radiometer at 183 GHz at the JCMT. The values at 183 GHz are converted to 225 GHz to compare directly with the SMA values, and then the opacity can further be converted to opacity at 353 and 666 GHz (Holland et al., 2013; Mairs et al., 2021) for the purpose of calculating extinction values (see Section 2.3). The weather bands for the JCMT are defined in Table 2.1. Polarimetry observations can only be done in Bands 1 and 2. Observing total intensity with SCUBA-2 can by done in Bands 1 through 3, though as can be seen in Table 2.1, transmission at 450 μm in Band 3 is very low, so only

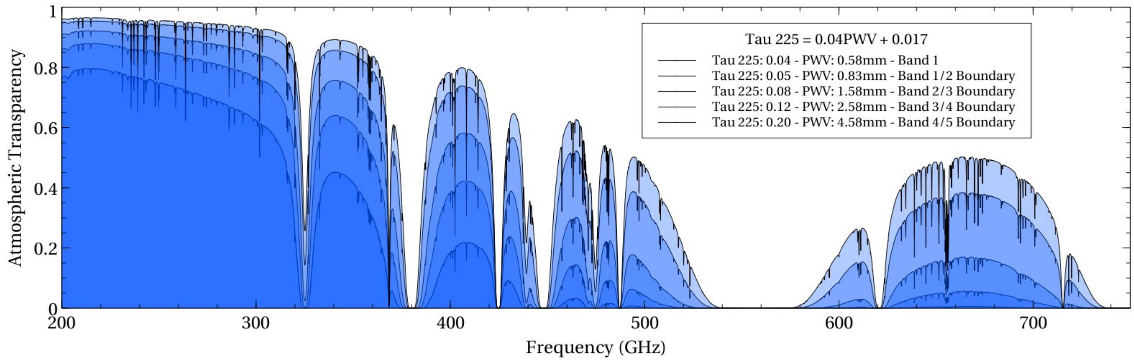

Figure 2.2: The atmospheric transmission at JCMT is shown vs frequency. The transmissions at the weather band boundaries are plotted to demonstrate how transmission drops off with increasing PWV. Band 1 weather is shown as the lightest blue and the Band 4/5 boundary is the darkest blue. This image was taken from the JCMT website (`https://www.eaobservatory.org/jcmt/observing/weather-bands/`).

the brightest objects will be observable. HARP and Nāmakanui are generally used to observe in Bands 4 and 5 where bright spectral lines, particularly those at longer wavelengths can still be observed, however they can be used in any weather bands.

2.1.1 SCUBA-2

The Submillimetre Common-User Bolometer Array 2 (SCUBA-2) on the JCMT is a dual-band, 10,000 pixel bolometer camera. In total it has eight 32×40 sub-arrays with four dedicated to the 850 μm band and four to the 450 μm band. The pixels are superconducting transition edge sensors (TESs; Irwin (1995)) and it was one of the first detectors to incorporate TESs, which allowed imaging cameras to be scaled up from hundreds of pixels to now thousands to tens of thousands. This was further aided by the development of Superconducting Quantum Interference Device (SQUID) amplifiers which allowed for a multiplexed readout system (de Korte et al., 2003). Though it is in total a 10,000 pixel camera, due to its age only ≈60% are in

Band	τ_{225}	PWV (mm)	trans.^{850} (%)	trans.^{450} (%)
1	<0.05	<0.83	82	28
2	0.05–0.08	0.83–1.58	77	19
3	0.08–0.12	1.58–2.58	67	7
4	0.12–0.2	2.58–4.58	53	2
5	>0.2	>4.58	45	0.5

Table 2.1: A table showing the different weather parameters for the observing bands of JCMT. The approximate transmission at both 850 (trans.^{850}) and 450 μm (trans.^{450}) is given as well. Transmission values are taken from the EAO JCMT website (`https://www.eaobservatory.org/jcmt/observing/weather-bands/`).

operation (see Figure 9 of Holland et al. (2013) for an example of the loss of pixels).

The optical path for SCUBA-2 can be seen in Figure 2.3. After reflection from the secondary mirror unit, the tertiary mirror which sits in the cabin reflects the light through a series of mirrors (C1–C3) which move the focal plane through the bearing tube and out to the side of the dish towards where SCUBA-2 is set up. Two more mirrors (N1 and N2) send the light path into the SCUBA-2 instrument, through the main window which is at room temperature and into the optics box where three more mirrors direct the light into the 1 K box which houses the focal plane units (FPUs). Within the optics box and the 1 K box, the light passes through a series of thermal blocking, low-pass, high-pass and bandpass filters. It is within this box that the dichroic is placed which splits the light between 450 and 850 μm. This array of filters and their associated temperatures can be seen in Figure 2.4.

At 850 μm, the half-power bandwidth of the bandpass filters is 85 μm (35 GHz) and at 450 μm it is 32 μm. At 850 μm, the half-power bandwidth corresponds to a frequency range of ≈336–372 GHz which encompasses the ^{12}CO (3-2) line at 345.796 GHz (867 μm). This means that 850 μm flux observations may be

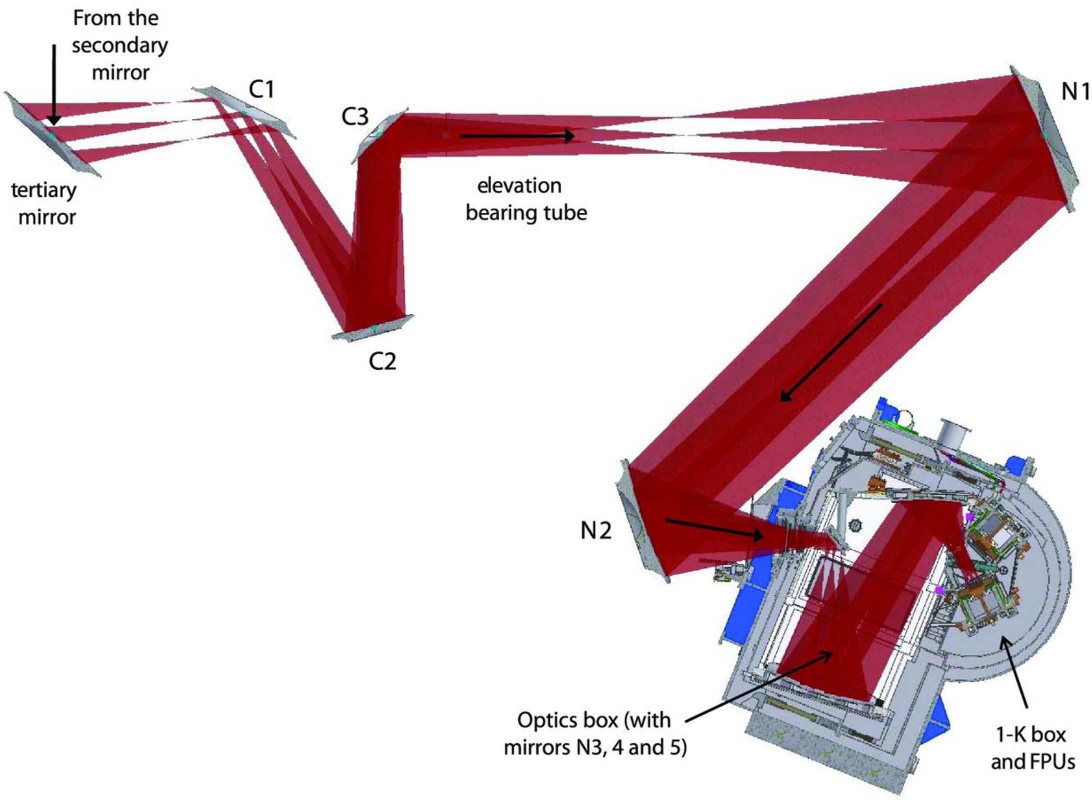

Figure 2.3: The optical path for the SCUBA-2 instrument. Light comes in from the secondary mirror at the top. The 1 K box houses the sub-arrays. Taken from Figure 2 of Holland et al. (2013).

contaminated by ^{12}CO (3-2) flux. There is an established process for cleaning the 850 μm maps (Parsons et al., 2018), which will be used when ^{12}CO (3-2) data is available and is discussed in more detail later in Section 3.3.3. The effective resolution of SCUBA-2 is $9\farcs6$ at 450 μm and $14\farcs1$ at 850 μm (Holland et al., 2013). This was re-estimated in Mairs et al. (2021) to be $\sim14\farcs4\pm0\farcs3$, which was empirically measured from the historical observations reviewed in that article. When modeling the full beam as a two-component beam, consisting of the main beam and an error, or secondary, beam, Mairs et al. (2021) calculate an effective FWHM of $8\farcs6\pm1\farcs3$ at 450 μm and $12\farcs6\pm1\farcs9$ at 850 μm from a two-component Gaussian fit. Moving forward, an effective FWHM beam width of $14\farcs1$ will be used.

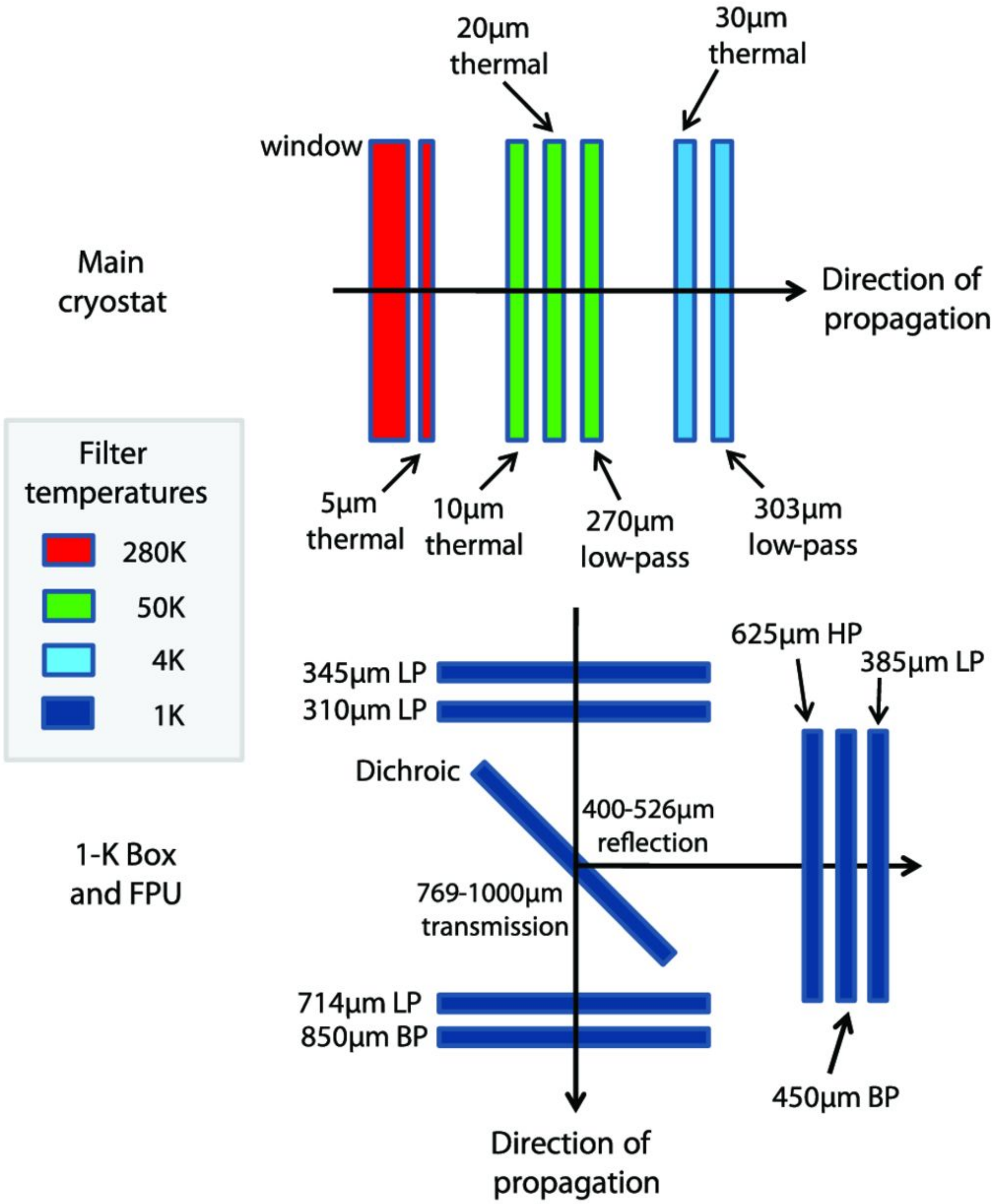

Figure 2.4: This figure shows all of the components within the SCUBA-2 cabin (the blue box seen in Figure 2.6). Here 'LP' and 'HP' correspond to low-pass and high-pass filters. The dichroic which splits the 450 and 850 μm can be seen as well. The detectors sit at the end of the arrows in the 1 K box and are cooled further to 50 mK. Taken from Figure 4 of Holland et al. (2013).

The SCUBA-2 detectors have 40 rows and 32 columns of active bolometers. There is a 41st row which is a 'dark row' and contains no TESs but has a SQUID element. This row is used to investigate common-mode noise for each column (Holland et al., 2013) which is generally atmospheric signal which is constant across the bolometers. Because each bolometer needs to read an independent signal, they need to be thermally isolated. This is done by etching the bolometers after the superconducting material is deposited (see Figure 2.5). There is also a small heater circuit for each bolometer (see upper right of Figure 2.5) which is used to supply a known amount of radiation which is used when flat-fielding at the beginning of observations.

Though the bolometers are individual and thermally isolated, they sit on a multiplexer wafer which allows the rows to be read out one by one. Each pixel has its own 'first stage' SQUID which can be seen in the lower Figure 2.5 diagram labeled as SQ1. Each of the columns are coupled to a secondary SQUID (SQ2) via a summing coil. SQUIDs are very sensitive magnetometers and are used to read and amplify the output signal of the TESs. In practice, at any one time, 39 of the rows in the sub-array are turned off and only one is active. That row will measure the amount of incoming radiation and then will shut off, the next row will turn on and use the previous row as a starting point and then try to measure the incoming radiation at its location. The rows are cycled through at a rate of 12 kHz and once an image of the sub-array is made with power for each pixel, they are stacked on top of each other at a rate of 200 Hz (Holland et al., 2013).

The method of measuring incident radiation or power is with biasing. Essentially, the incoming radiation will strike the thermal absorbers which are coupled to the TESs which will change the temperature of the TES super-conductor which will in turn alter the resistance of the super-conductor by moving it above its critical

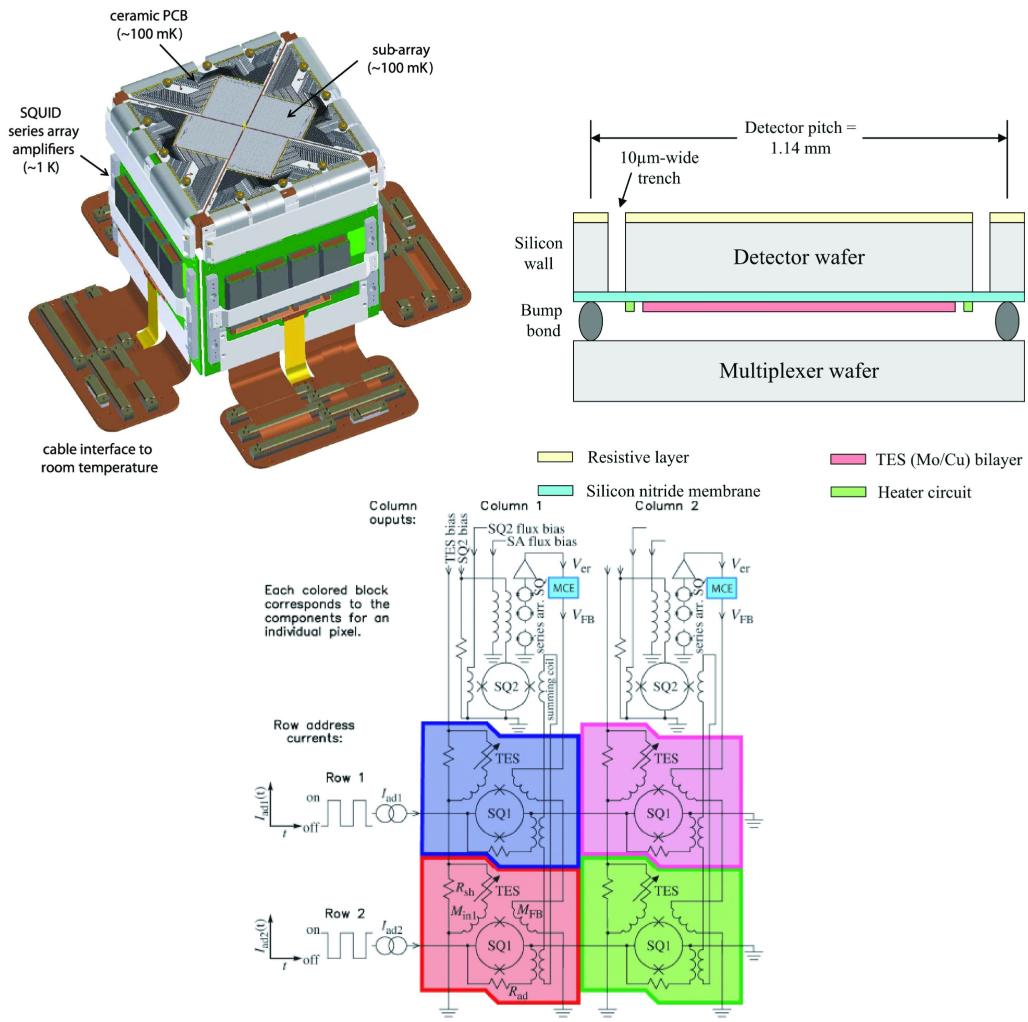

Figure 2.5: All three images taken from Holland et al. (2013). *Upper Left:* The focal plane unit for SCUBA-2 with the four sub-arrays and other key components labelled. *Upper Right:* A simplified schematic of a single bolometer on SCUBA-2 with main components labelled. The multiplexer wafer contains the SQUID amplifier circuitry. *Lower:* An example circuit diagram of a 2×2 array (as opposed to the 40×32 SCUBA-2 array). SQ1 are the first-stage SQUIDs coupled to the TES bolometer and the SQ2 are the second stage squid used to amplify the signal. The I_{ad} current is sued to switch on/off the rows.

Wavelength, Date Range	FCF_{peak} (Jy beam^{-1} pW^{-1})	FCF_{arcsec} (Jy arcsec^{-2} pW^{-1})
450 μm, Pre 2018 Jun 30	531±93	4.61±0.60
450 μm, Post 2018 Jun 30	472±76	3.87±0.53
850 μm, Pre 2016 Nov 19	525±37	2.25±0.13
850 μm, 2016 Nov 19–2018 Jun 30	516±42	2.13±0.12
850 μm, Post 2018 Jun 30	495±32	2.07±0.12

Table 2.2: Flux Calibration Factors over the lifetime of SCUBA-2. They were obtained between 087:00 and 17:00 (UTC). The table is replicated from Mairs et al. (2021).

temperature and stop it super-conducting. With a set voltage across the super-conductor, this change in resistance will cause a change in current. The current itself is fed into a loop around a SQUID. With the change in current, there is an induced magnetic field which affects the signal of the SQUID. The readout is looking for a null signal from the SQUID, so a current is fed to a separate loop to oppose and cancel the output signal of the SQUID. Once a null signal is found, the amount of current supplied is measured, providing a total power.

The output from SCUBA-2 provides data in ‘instrumental units’ of picoWatts (pW). To convert from the instrumental units to astronomical units, the observatory provides a Flux Conversion Factor (FCF) which takes the data from pW to either Jy beam^{-1} or Jy arcsec^{-2}. This FCF is based on standard point sources such as Uranus. There was recent work done by Mairs et al. (2021) to go back through the last decade of archival calibrator observations and re-estimate the FCF. The FCF table from Mairs et al. (2021) is given below. Most of the data presented here was taken post-June 2018 and so will be using the FCF of 495 Jy beam^{-1} pW^{-1}.

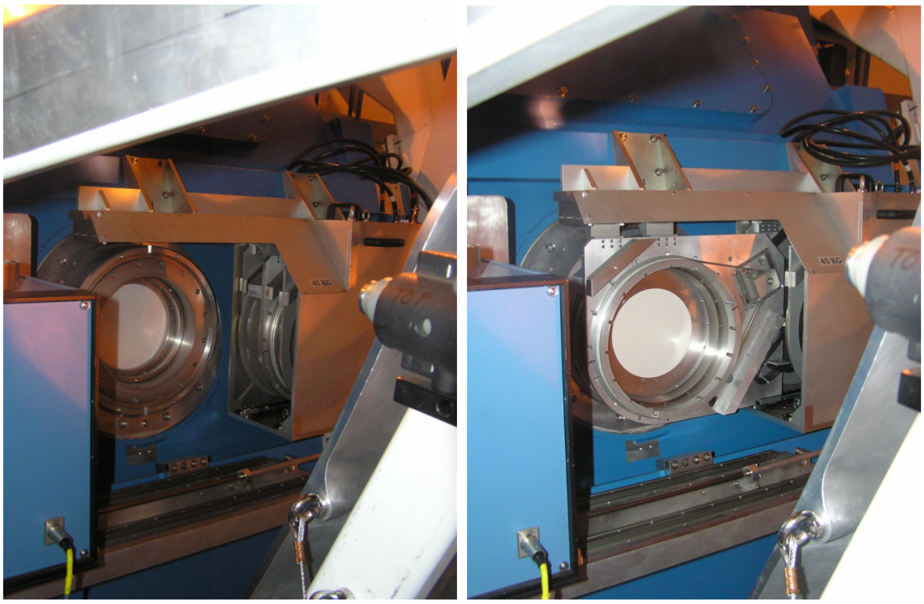

Figure 2.6: *Left:* The window to SCUBA-2 can be seen. POL-2 is tucked away to the right, out of the beam. *Right:* POL-2 is now inserted in the beam, in front of the SCUBA-2 window. Both images taken from the EAO POL-2 Data Reduction Cookbook (`https://starlink.eao.hawaii.edu/docs/sc22.htx/sc22ch2.html`).

2.1.2 POL-2

SCUBA-2 has an associated polarimeter called POL-2. The polarimeter sits on an arm which can be adjusted to place the polarimeter directly in front of the window to SCUBA-2. POL-2 is a linear polarimeter and its design follows a schematic like that shown in Figure 2.7. POL-2 consists of a half-wave plate (HWP) and a wire-grid polarizer which acts as the fixed analyzer. There is an initial wire-grid polarizer before the HWP but it is only used in the beam for testing.

The HWP rotates the plane of polarization of incoming polarized radiation. The HWP has a preferred axis which means it passes light that is polarized parallel to its axis while delaying the perpendicular polarized light by half a wavelength. The net polarization vector that passes through the HWP is such that the HWP preferred axis bisects the incoming polarization vector and the net polarization vector.

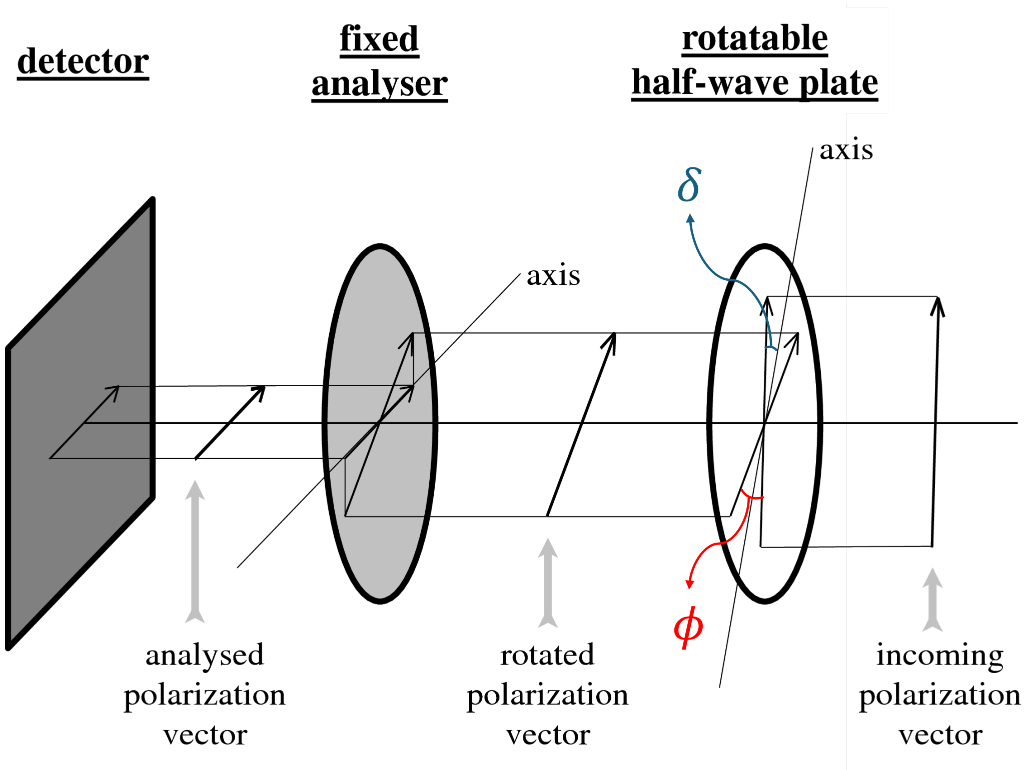

Figure 2.7: The typical optical components of a single-beam polarizer such as POL-2. Schematic taken from the POLPACK Cookbook (`https://starlink.eao.hawaii.edu/docs/sun223.htx/sun223se3.html`). See the text for definitions of the angles ϕ and δ.

Figure 2.8: The three components of POL-2 are slightly separated to show them individually. The HWP is shown in the middle between the two wire-grid analyzers. Image taken from the EAO POL-2 Data Reduction Cookbook (`https://starlink.eao.hawaii.edu/docs/sc22.htx/sc22ch2.html`).

Another way to think of it is that it rotates the polarization vector by an angle ϕ which is 2δ where δ is then the angle between the incoming polarization vector and the HWP axis (see Figure 2.7). Once the polarized light has been rotated, it passes through the fixed analyzer which allows light polarized parallel to its axis to pass through to the detector.

The HWP is itself rotated so its axis rotates as well and with it, the throughput plane of polarization. The fixed analyzer does as the name suggests and remains fixed. The rotation of the HWP then gives data in a time-series where the polarization properties vary with HWP rotation which itself varies with time.

Since POL-2 is only designed as a linear polarimeter, it does not measure or characterize the Stokes V parameter which is used to describe the circular polarization of the radiation. This leaves POL-2 measuring just the Stokes I, Q and U parameters. Stokes I is the total intensity of the polarized radiation. Stokes Q is the radiation that is polarized perpendicular or parallel to the reference plane. Stokes U is the radiation that is polarized $\pm 45°$ to the reference plane. From these parameters, the linearly polarized intensity (PI) and polarization angle (θ) can be calculated as

$$PI^2 = Q^2 + U^2 \;, \tag{2.2}$$

and

$$\theta = \frac{1}{2} tan^{-1} \frac{U}{Q} \,, \tag{2.3}$$

where percent polarization p is calculated as p = $100 \times PI/I$.

The JCMT has a GORE-TEX$^{\mathrm{TM}}$ membrane installed (see Figure 2.1). This membrane can contribute to instrumental polarization (IP), along with a variety of other causes. The IP contributes to the total PI and can also change polarization angle. The team at JCMT has constructed an IP model which attempts to correct for the various sources of IP.

The standard practice is to take a bright and unpolarized point source and measure the polarization. Uranus is the standard unpolarized source for the JCMT and it is what helped construct the older IP model (Friberg et al., 2018). POL-2 measures Uranus to exhibit roughly 1.5% polarization which demonstrates that there is some incoming polarized light not from the astronomical source. It should also be noted that the IP at JCMT is elevation dependent.

The current (as of 2019 August) IP model (Friberg et al., 2018) estimates the IP in a different manner to better model the IP at 450 μm. This different method is consistent with the previous IP model at 850 μm. The current method uses very bright extended sources that have good characterization of the Stokes I, Q and U parameters. The data are reduced with no IP correction model applied so that the IP is still present within the map. The data are reduced using the standard POL-2 reduction pipeline which is discussed later in Section 2.3 though omitting the parameter *skyloop* since observations and their IP need to be considered independently. Once the reductions are done, each Stokes Q and U map is scaled by the Stokes I map from that observation to account for variations in FCF for each observation.

Then at each pixel which falls within the astronomical signal mask, the Stokes Q and U value from each observation is plotted in a scatter plot. The plotted Q and U points should be scattered around a circle with a radius of PI where the true Q and U value is the center of the circle. The distance of each (Q, U) point from the center is therefore a measure of the IP in that observation.

Then the Stokes Q and U values are given by

$$Q = Q_m - I \times PI_Q \ , \tag{2.4}$$

and

$$U = U_m - I \times PI_U \ , \tag{2.5}$$

where Q_m and U_m are the measured values and I is the total intensity multiplied then by either PI_Q or PI_U which are the factors coming from the IP model.

2.1.3 POL-2 Scanning Mode

Observations with POL-2 are performed using a modified SCUBA-2 DAISY mode (Holland et al., 2013) optimized for POL-2 (Friberg et al., 2016) called POL2_CVDAISY, where CV means 'constant velocity.' Due to the fact that Stokes Q and U are generally much fainter than Stokes I (which is all SCUBA-2 detects on its own), the scan speed of the POL2_CVDAISY mode is slower ($8''$ s^{-1} vs $155''$ s^{-1}) than its SCUBA-2 CVDAISY counterpart. This is to allow good Q and U values to be accurately determined. In addition, the HWP must make a full rotation (which takes 0.5 s) at each position before moving on, so the scan speed needs to be slower to allow this to happen.

The SCUBA-2 DAISY mode is meant for small-field observations, generally small and compact sources. The reason is that it produces a central $3'$ region with uniform coverage, with noise and exposure time increasing and decreasing respectively to the edge of the map (see Figure 2.9). The other SCUBA-2 mode commonly available, the PONG scan pattern, creates a uniform $30'$ field, but the exposure time at any given position in the map is generally only ∼0.014 of the total exposure time, while for the DAISY mode, that central $3'$ region is ∼0.25 of the total exposure time (Holland et al., 2013). As mentioned above, this additional exposure time helps to accurately determine Stokes Q and U values, something which SCUBA-2 does not need to do.

The POL2_CVDAISY mode has a scan speed of $8''$ s^{-1} with a HWP rotation frequency of 2 Hz. The data reduction pipeline will split up the time stream into

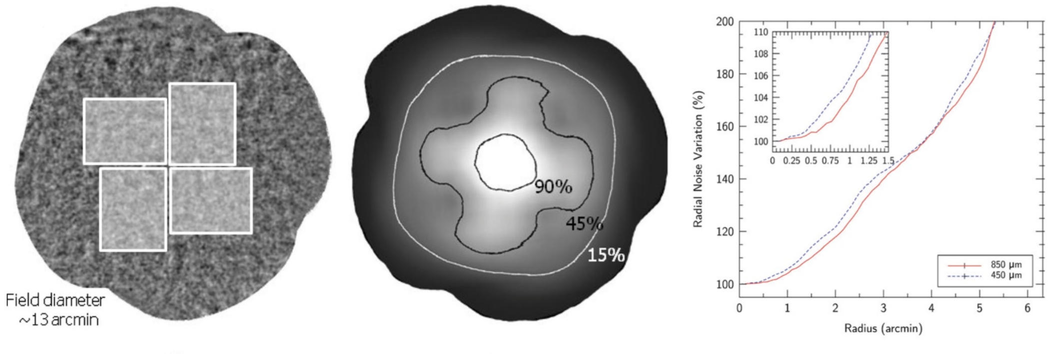

Figure 2.9: Figure taken from the upper panel of Figure 12 in Holland et al. (2013). On the left, the configuration of the four sub-arrays of SCUBA-2 is shown overlaid on a typical size DAISY map. The central image shows the exposure time percentages relative to the peak exposure time value. The right plot shows how quickly the noise variation grows as you move to the edges of the map.

shorter segments which it will then determine a value of Stokes Q and U from. The length of this shorter segment is the time of a single HWP rotation, so 0.5 seconds. With a scan speed of $8'' \mathrm{~s}^{-1}$, this corresponds to $4''$ on the sky for one segment which is the accepted pixel size of the POL-2 data reduction (see Section 2.3).

2.2 SCUBA-2/POL-2 Observations

All observations with SCUBA-2/POL-2 were conducted with the POLCV_DAISY POL-2 observing mode which is described in Section 2.1.3. Targets that were a part of BISTRO were observed for a set amount of time (generally ≈14 hours) in order to achieve a uniform noise level across the sources and sufficient signal-to-noise to detect polarization in fainter objects.

2.2.1 BISTRO-3

The observations presented in this thesis were taken from 2020 February and are currently ongoing as part of the BISTRO large survey program (Project ID: M20AL018; see Section 1.7) in its third generation of observations, 'BISTRO-3'. The observations were proposed as 27 repeats of $\sim$31 minutes to give approximately 14 hours of observing time for each target. The goal was to observe all targets to a depth of $\sim$1.5 mJy/beam, a similar depth as those in the first two generations of observations, 'BISTRO-1' and 'BISTRO-2'.

2.2.1.1 Prestellar Cores

There were originally a set of six prestellar cores to observed by BISTRO-3. Those six cores are listed in Table 2.3. After a handful of observations of FeSt 1-457, it was determined to be too faint. The cores which have been observed to date are L1544, L1498, L43 and L1517B. Of these, only L43 and L1544 are fully complete, with 27/27 observations complete. Freed up time also allowed BISTRO-3 to complete observations of L1495A which was originally a BISTRO-2 source with only 9 of 20 observations completed. L1495A is also now complete with a total of 20 observations each approximately 41 minutes for a similar $\approx$14 hours of integration time (this was the observing plan from BISTRO-2).

Similar to FeSt 1-457, L1498 is extremely faint. Initial reductions of the POL-2 data show no Stokes I emission and similarly, no Stokes Q and U, though it was detected using the previous polarimeter and camera, SCUPOL (Kirk, Ward-Thompson & Crutcher, 2006), and also in Stokes I with SCUBA-2. The observations with SCUBA-2 are able to obtain deeper sensitivities, but the source should have still been visible in Stokes I with POL-2. For example, L1517B which has a similar peak flux density is observable with POL-2, though it is also very faint and has low signal-to-noise polarization vectors.

Table 2.3: List of the prestellar cores observed in BISTRO-3 with their predicted flux density and 3-σ polarization level

Source	R.A. (J2000)	Dec. (J2000)	Peak FD (mJy/beam)	3-σ (%)	Completed Observations[a]
L1544	05:04:17	+25:10:48	314	1.4	27
L1498	04:11:00	+24:58:00	140	3.2	9
L43	16:34:29	-15:47:11	369	1.2	27
L1517B	04:55:20	+30:38:04	136	3.3	13
FeSt 1-457	17:35:45	-25:33:12	180	2.5	–
L1495A[b]	04:17:43	+28:08:38	$\sim$125	3.6	11[c]

a. Out of 27 proposed observations.

b. L1495A was originally a 'BISTRO-2' source but was not fully observed. It is a series of prestellar cores and was completed as part of 'BISTRO-3.'

c. Out of 11 from 'BISTRO-3.'

Work was done by Sheng-Jun Lin (a postdoctoral fellow at ASIAA) to attempt to extract the Stokes I signal. We successfully proposed for SCUBA-2 time at the JCMT to obtain supplemental data for L1498. With this SCUBA-2 data, we tried to use it as a mask to guide the pipeline to where the emission was. This method was successful in previous work he had done on L1512 (Lin et al., 2024) and was again successful with L1498. The work I present later in Chapter 4 follows this method, but all the reduction has been done by myself. Dr. Lin is actively working on the project, but we are waiting for further observations. All analysis on this source I will present is my own, but is preliminary. The same is true for L1517B and L1544 which are both sources led by other members of the BISTRO survey, but the work presented here is my own reductions and analysis.

2.2.1.2 The Central Molecular Zone

The initial proposed set of sources for the Galactic Centre/Central Molecular Zone were the 20 km s^{-1} complex, The Brick (G0.253+0.016), Clouds E/F and Sagittarius B2. Early on in observations, I reduced the data from the Galactic Centre and it soon became apparent that these sources were incredibly bright, with very high signal to noise measurements in polarization. It was determined that the originally planned 27 repeats would be wasteful and the sensitivity did not need to be so high. While this would end the uniform depth/sensitivity of all BISTRO sources (i.e. not going down to a σ=1.5 mJy beam^{-1} in all fields), it would free up observing time.

With the additional observing time, I proposed to the BISTRO team that we redistribute this time around the Central Molecular Zone (CMZ) and attempt to create a mosaic of the CMZ from one side to the other. Having previously arrived at an integration time of 4 hours for each of the original 'BISTRO-3' sources, we limited the integration time for each new proposed field to 4 hours in order to attempt to create a uniform mosaic across the CMZ. In practice this is not possible without many more pointings because of the POL-2 scanning mode as described in Section 2.1.3. The noise not equally well-characterized across the whole field since we are limited to the inner $3'$ for uniform noise and up to $6'$ for 'trustworthy' coverage (Holland et al., 2013; Arzoumanian et al., 2021).

We settled on the addition of 10 new pointings in the CMZ. These are shown in Figure 2.10 as black circles and listed in Table 2.4. To achieve the uniform coverage, we use some PI data which was accessed from the CADC archive. We use data from project ID: M17AP074 around the 20 and 50 km s^{-1} clouds which can be seen with the lime green circles in Figure 2.10. The other PI data is from project ID: M20AP023 which observed the dust ridge, Sagittarius C and the pointing coincident with Field 3 (see Figure 2.10). The pointings from M20AP023 are shown as blue and red circles in Figure 2.10.

Using the SCUBA-2 ITC (integration time calculator) on the JCMT Hedwig website, we can calculate the expected 850 μm sensitivity for 4 hours of integration time in Band 2 weather and assuming $12''$ pixel sizes for the final polarization vectors. This is done by varying the declination of the source. For a declination of -28°, using the POL-2 CVDAISY mapping, we would achieve a sensitivity in the range of 2.851–3.742 mJy beam^{-1}, so we use the mean value 3.275 mJy beam^{-1}. This sensitivity is used to calculate the 3-σ detection in Table 2.4 for Fields 1–10. The peak flux density values for Field 1–10 are taken from Parsons et al. (2018). For the original BISTRO-3 fields, the flux density values are taken from the BISTRO-3 proposal and the 3-σ values are calculated using the map sensitivity of 3.275 mJy beam^{-1}.

2.3 Data Reduction

To reduce the data, we used the Submillimetre User Reduction Facility (SMURF) package (Chapin et al., 2013) from the Starlink software (Currie et al., 2014). The

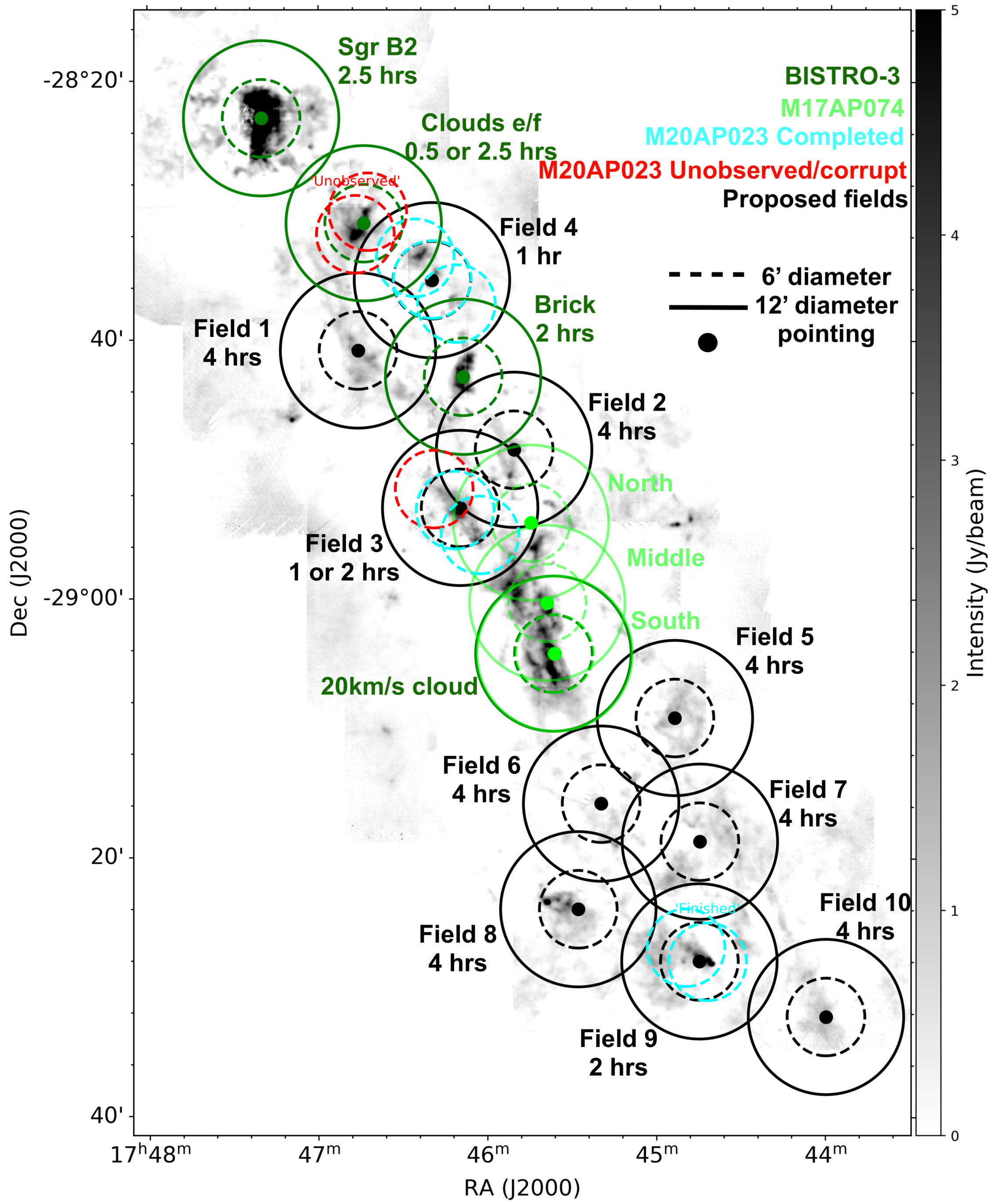

Figure 2.10: Background is the 850 μm dust emission from SCUBA (Price et al., 2001). Overlaid are the 4 original pointings from BISTRO-3 as dark green circles. Light green circles correspond to data from project M17AP074. Cyan and red circules correspond to data from project M20AP023 where red circles were unobserved or data was corrupted. Each of the pointings has the 6′ region defined and then the larger 12′ region which shows the approximate size of a map.

Table 2.4: List of the CMZ fields observed in BISTRO-3 with their predicted flux density, 3-σ polarization level and their number of completed observations. Field numbers correspond to the circles in Figure 2.10

Source	R.A. (J2000)	Dec. (J2000)	Peak FD (mJy/beam)	3-σ (%)	Completed Observations[a]
20 km s^{-1} Cloud	17:45:38	-29:04:30	6066	0.2	8
The Brick	17:46:10	-28:43:00	4225	0.2	8
Clouds E/F	17:46:45	-28:31:10	5115	0.2	8
Sgr B2	17:47:20	-28:23:07	131737	0.007	8
Field 1	17:46:46	-28:40:50	1292	0.8	3
Field 2	17:45:51	-28:48:30	2090	0.5	5
Field 3	17:46:10	-28:53:00	2378	0.4	0[b]
Field 4	17:46:20	-28:35:24	5765	0.2	0[c]
Field 5	17:44:54	-29:09:12	1024	1.0	3
Field 6	17:45:20	-29:15:50	882	1.1	3
Field 7	17:44:45	-29:18:45	903	1.1	8
Field 8	17:45:28	-29:24:00	9161	0.1	5
Field 9	17:44:45	-29:28:00	6032	0.2	4[d]
Field 10	17:44:00	-29:32:15	625	1.6	4

a. Out of 8 proposed observations.

b. Out of 4. This field is supplemented by data from M20AP023.

c. Out of 2. This field is supplemented by data from M20AP023.

d. Out of 4. This field is supplemented by data from M20AP023.

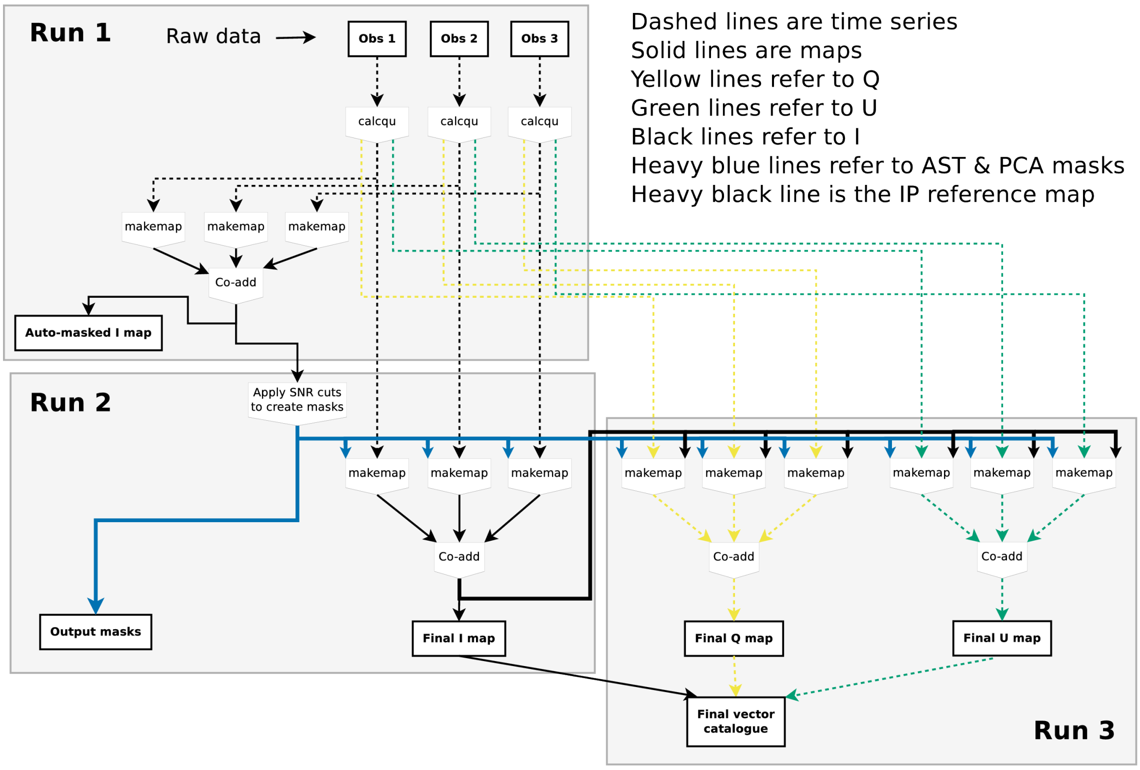

Figure 2.11: An overall flow chart for the POL-2 data reduction pipeline. In practice Run 2 and Run 3 are run at the same time with the same command, but the data are reduced in the order of Stokes I, Q, U. The additional parameters of *skyloop* and *mapvar* that are discussed in Section 2.3.3 will be used at the *makemap* and Co-add steps respectively. The figure is taken from Figure 3.1 of the POL-2 Data Reduction Cookbook (`https://starlink.eao.hawaii.edu/docs/sc22.htx/sc22ch23.html`).

SMURF package contains the data reduction routine for SCUBA-2/POL-2 observations named *pol2map*[1].

pol2map is a command which calls various other commands such as *calcqu* and *makemap* (see Sections 2.3.2 and 2.3.3 for a description of these two commands). It is built to use the SCUBA-2 command *makemap* but with additional steps to deal with polarization data. It runs in three distinct steps, though the last two steps are generally combined. Those steps are outlined in Sections 2.3.2 and 2.3.3. The general flow of *pol2map* is shown in Figure 2.11 while the flow of *makemap* is shown in Figure 2.12.

The SCUBA-2/POL-2 map maker creates astronomical maps by solving for the astronomical signal amongst a variety of noise sources using the maximum-likelihood technique, where the time-series data is expressed as the true map of the sky with some noise. Then that expression is inverted in order to estimate the map as a weighted combination of variables to decrease the variance in the map, solving until a threshold is reached (Chapin et al., 2013). The inversion is very computationally intensive (Chapin et al., 2013) so a compromise was achieved for SCUBA-2/POL-2 data where it is assumed that both low-frequency, non-white noise can be modelled and that astronomical signal can be identified and removed iteratively and so only white noise remains which can be calculated as a scalar rms and hence give a good characterization of the noise distribution. Bolometer cameras like SCUBA-2 are inherently limited by white photon and phonon noise from the instrument and ambient backgrounds, henceforth 'white noise.' The other non-white noise is typically low-frequency and comes from sources that produce slow variations in the background such as thermal variations in the cryostat and most notably, interference from the atmosphere. The frequency at which this noise is comparable to the white noise level is called the '$1/f$ knee' (Chapin et al., 2013). This low-frequency noise, as discussed

[1]http://starlink.eao.hawaii.edu/docs/sun258.htx/sun258ss73.html
http://starlink.eao.hawaii.edu/docs/sc22.htx/sc22.html

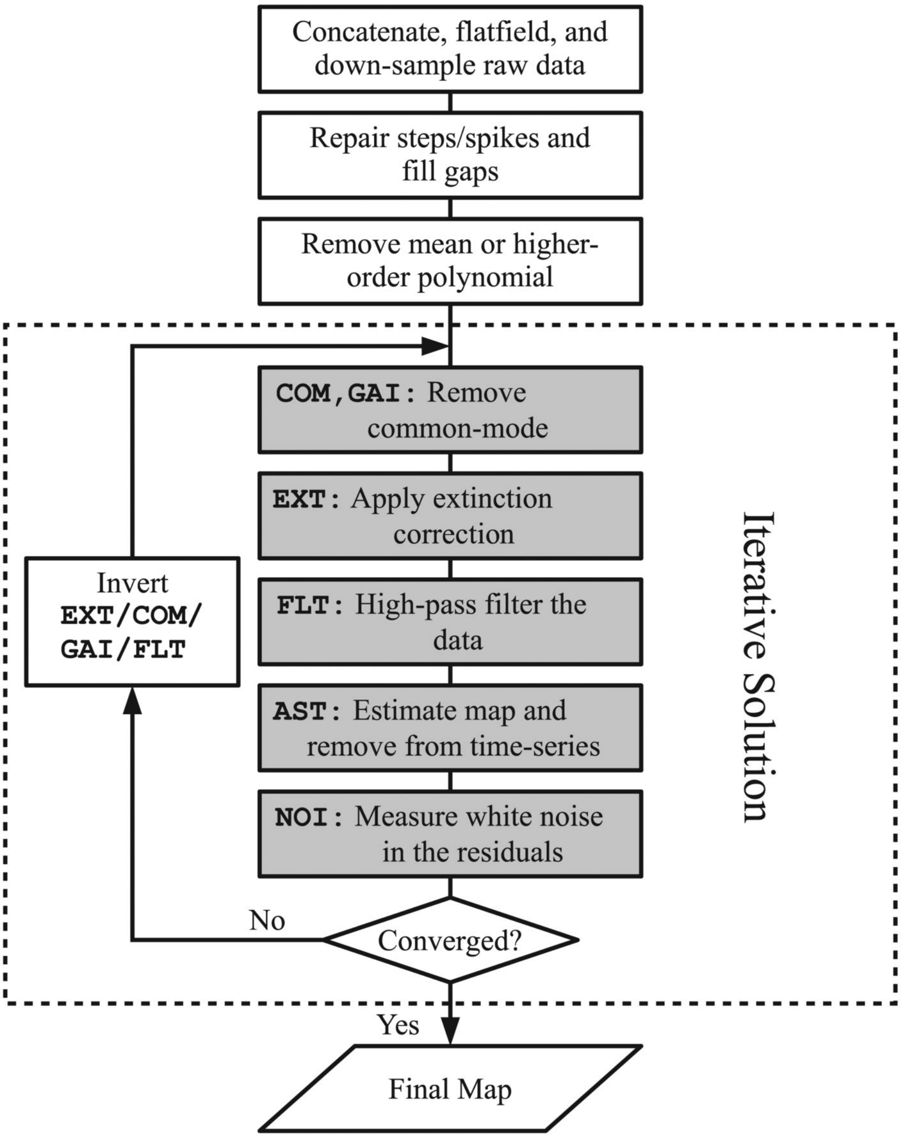

Figure 2.12: A general flow chart of the SCUBA-2 map maker command *makemap*. The POL-2 data reduction command, although called *pol2map*, calls *makemap* and so follows a similar flow chart but includes PCA masking. This flow chat is taken from Figure 2 of Chapin et al. (2013).

later, is largely correlated across all bolometers in time. If all the low-frequency noise was successfully removed, the map would be 'white noise limited' and have a noise level of NEFD/$\sqrt{t}$ which is the noise equivalent flux density (NEFD; white noise level of a bolometer in 1 second of integration) divided by the square root of the integration time in a map pixel.

2.3.1 Signal Modelling

The signal from a bolometer is modelled as

$$b_i(t) = f_i[e(t)a_i(t) + n_i(t)] \ , \tag{2.6}$$

where $b_i(t)$ is the signal of the $i-th$ bolometer, f_i is a scale factor which scales the terms in brackets from their delivered power in units of pW to the digitized unit of the bolometer (determined from flat-fielding), $e(t)$ is the time varying extinction (as discussed in Section 2.1 and further discussed below), $a_i(t)$ is the time-varying astronomical signal due to scanning the telescope and $n_i(t)$ is a source of noise, both white and non-white. That source of noise can be further broken down into many components,

$$n_i(t) = n_i^w(t) + g_i n^c(t) + n_i^f(t) \ , \tag{2.7}$$

where $n_i^w(t)$ is uncorrelated white noise, $n^c(t)$ is the correlated/common-mode signal with a scale factor g_i for each bolometer and $n_i^f(t)$ is the remaining noise (mainly low frequency) in excess of the white noise level that either has no correlation or a complicated correlation between bolometers (and so is not included with the common-mode signal).

In order for the map-maker to create a map from the time-streams, it iterates for a variable number of iterations until it has converged. In each iteration, there are a series of models which are applied in order to remove the various sources of noise as estimated by Equation 2.7 in the data and extract the true astronomical signal ($a_i(t)$) and characterization of noise. The order of this can be seen in Figure 2.12, within the dashed box. In order for the map-maker to converge, the map-based convergence statistic, $M_{\rm c}$ must be below 0.05, i.e. on average map pixels change by less than 5% of the estimated map rms. $M_{\rm c}$ is given by

$$M_{\rm c}^j = \frac{1}{N}\sum_i \frac{|m(x_j, y_j) - m(x_{j-1}, y_{j-1})|}{\sqrt{v(x_j, y_j)}} \ , \tag{2.8}$$

where j tracks the iterations and i indexes the N number of pixels. $m(x, y)$ is the pixel brightness as estimated by the weighted average of the bolometer data samples ($b_i(t)$, see Equation 2.6) that land inside that pixel (any bolometer at any point in time). The weights are set to $(1/\sigma^w)^2$ which is the estimated inverse variance expected from the bolometer white noise levels. $v(x, y)$ is the value from the variance map where the variance for each pixel is calculated from the scatter in the weighted samples falling in the pixel, so

$$v(x, y) = \frac{\sum_j w_j \sum_j w_j b_j - (\sum_j w_j b_j)^2}{N_j(\sum_j w_j)^2} \ , \tag{2.9}$$

where j here tracks the number of bolometer samples falling in the pixel (x, y) and b are the bolometer data values and w is again the weights as defined above.

The total signal observed by the array can be broken down into four main components which are each iteratively modelled throughout the mapmaking routine (see Figure 2.12):

1. `AST` - the astronomical signal which is the signal originating from the source of interest, $a_i(t)$ in Equation 2.6

2. `COM` - the common-mode signal, a signal which is common across all bolometers and is taken as the average signal from all bolometers at each time-step, $n^c(t)$ in Equation 2.7

3. `FLT` - low-frequency $1/f$ noise, $n_i^f(t)$ in Equation 2.7

4. `NOI` - the white noise of the detector, $n_i^w(t)$ in Equation 2.7

The `GAI` and `EXT` model correct for the gain and extinction of each bolometer and are given by g_i in Equation 2.7 and $e(t)$ in Equation 2.6 respectively.

SCUBA-2 (and POL-2) data are dominated at frequencies less than ∼2 Hz by highly correlated signals (Chapin et al., 2013). Much of this signal is a common-mode signal and is easy to model and remove by just subtracting the average signal from all bolometers at each time-step. The primary source of the common-mode signal is the atmosphere which is common across all bolometers and is exceptionally bright. Removing the `COM` signal is the first step and it must be very robust to ensure no atmospheric signal contaminates the astronomical signal. This requirement is what ultimately limits SCUBA-2's ability to observe extended structure because the map maker will confuse that large-scale structure as common-mode signal in the `COM` model and remove it. The faint extended structure is also much fainter than the atmospheric signal (Chapin et al., 2013). The size scale which is cleaned by the `COM` model can be controlled with a parameter in the reduction. This step assumes that there is no spatial variation in the atmosphere across the array footprint which is the case due to the quick scanning speed and modelling of the `COM` signal at each time-slice. The `COM` model is also useful because it can be used to calculate the `GAI` model which is the gain/offset for each bolometer. This is done by comparing the bolometer time-series with the common-mode signal and fitting it with a least-squares linear fit to determine a gain (Chapin et al., 2013). In this stage, any bolometers which depart radically from the common mode are also flagged as bad and omitted from the final map (Chapin et al., 2013).

After the common mode signal is removed, there is still a residual correlated signal that is difficult to model. First the data is corrected for extinction (`EXT`) which is done using a multiplicative factor, derived from the PWV values discussed in Section 2.1. This is done in the iterative step to decrease the impact of small errors which have the opportunity to be amplified in the final map (Chapin et al., 2013).

Then the `FLT` model takes the FFT of the bolometer time-series data and applies a series of filters. In this step, the maximum recoverable angular scale can be defined as well as a frequency filter cut-off. Large-scale structures not removed with the `COM` model might still be present in the data and if it is not real astronomical signal, then it is $1/f$ noise (large angular scales correspond to low frequencies). Therefore, defining the maximum recoverable angular scale influences what $1/f$ signal is removed. The `FLT` model is generally used simply as a high-pass filter in order to remove residual noise after the `COM` cleaning (Chapin et al., 2013).

The next step is to then estimate the astronomical signal and remove it via the `AST` model. The map estimation occurs by using a nearest-neighbour resampling of the data onto a grid. The standard pixel size for SCUBA-2/POL-2 reductions can be controlled with the 'pixsize' parameter, but is by default $4''$ (this is further discussed in Section 2.3.4). The brightness for each pixel is determined by the weighted average of bolometer samples which fall into that pixel. For the first step, the weight is set to 1, but in later steps, it is $(1/\sigma^w)^2$ where σ^w is determined from the previous iteration's `NOI` model. In this step, the variance map is also estimated, with the variance value for each pixel determined by Equation 2.9. Once the signal map has been estimated, it is projected into the time domain in order to remove from Equation 2.6.

The final step (`NOI` model) is to measure the white noise levels for each bolometer now that the time-series have been cleaned of correlated and noncorrelated non-white noise and astronomical signal. The white noise level for each bolometer, as mentioned above, is approximated with a single, non-time-varying variance σ^{w2}. This is done by calculating the power spectral density of the bolometer and getting an average white noise level from the 2–10 Hz region, a clean region between the $1/f$ knee and the high-frequency line features for typical bolometer data (Chapin et al., 2013).

Once all these steps have been completed, the removed noise models are inverted back into the time stream data (except for the astronomical signal) and the map-maker runs again to model and remove the noise. Once it does this, the astronomical signal is added back in and then re-calculated. This happens until the map-based convergence statistic, $M_{\rm c}$, is less than 0.05, or the map-maker decides it cannot reach that level given the number of allowed iterations (this can be set in the configuration of the data reduction). The map-based convergence statistic is calculated on the astronomical signal map, so once the changes in the astronomical signal map fall below the threshold, the map-maker has converged.

2.3.1.1 PCA modelling

When reducing POL-2 data, an additional modelling step called the `PCA` model (stands for Principle Component Analysis; PCA) is used. For just SCUBA-2, the background is removed using just the common-mode model which ignores any spatial variations in the background, focusing just on the time domain. In reality, the IP acts on the large sky background (relative to astronomical signal) and therefore gives large background values of Stokes Q and U. If the IP was constant across the focal plane it could potentially be removed with the common-mode model, but it is not constant, meaning there is spatial variations in the Stokes Q and U background. The spatial variation in this background is seen within the JCMT beam lobes (Friberg et al., 2016) where the JCMT secondary (error) beam size is $49\farcs1$ (Mairs et al., 2021). No model has been produced for the beam varying IP or the focal plane IP (Friberg et al., 2016) and the current IP model is only elevation dependent (see Section 2.1.2). This is why PCA is necessary to remove the additional background fluctuations. It is also required when using a slow scan speed where the atmosphere will fluctuate quicker than the scanning speed (which is the case for POL-2 scans) and create non-common fluctuations (hence not removable by the common-mode model) across the map which are then smoothed out by the PCA.

The `PCA` map step goes between the `GAI` and `EXT`, so is done after the initial common-mode model is removed. The PCA step is applied on each bolometer time-stream and it identifies the strongest time-dependent components present in multiple bolometers which are assumed to represent spatially varying background signal and then removes them. The assumption here is that the astronomical signal will not be time-varying. For star-forming regions, this assumption is especially valid over the span of minutes to hours of the observations. The areas that the PCA runs on are determined by a signal-to-noise cut of the data, identifying areas that are believed to have astronomical signal and those regions are masked out, leaving the PCA to run on the background. The number of PCA components to remove is also specified using the parameter `pca.pcathresh`. The default for the reduction is a value of 50 for step 1 and a value of 150 for step 2 (see Sections 2.3.2 and 2.3.3). If the map maker cannot successfully converge in an upper limit of iterations, it will attempt to lower the PCA threshold. One issue with PCA is that it will remove some astronomical signal as well. However, since that signal remains in the time-streams, it may be possible to recover later with more iterations of the map-maker (Chapin et al., 2013).

2.3.2 Step 1: Separation of time-streams and initial Stokes I map

In the first step, the command *calcqu* is called to separate the raw bolometer time-streams into Stokes I, Q and U time-streams. These Stokes I, Q and U time-stream data are stored in a directory for subsequent map-making runs. From one observing block at the JCMT, a series of N-Dimensional Data Format (NDF) time-stream files are created for each sub-array and each wavelength which contain a time-series of bolometer signals and HWP positions. These are the raw time-series files that are input into *calcqu*, which takes care of flat-fielding, cleaning and ultimately concatenating the raw time-series and then separating them into the three Stokes parameters based on the intensities and HWP positions. The data are also down-sampled to 2 Hz so that there are two samples of Stokes I, Q and U values per second. Some of the cleaning that happens in this step removes large spikes in the data as well as large steps (which may have been caused by cosmic rays, for example) by interpolating between the beginning and end of the step/spike to fill the gap. These steps would normally be done by the *makemap* command as seen in Figure 2.12, but in *pol2map* they are performed by *calcqu*. The other key difference is the down-sample to 2 Hz. While this does match the HWP frequency, it is also partially constrained by the scanning speed. In order to fully sample the Gaussian beam, a pixel size of 4–5$''$ is needed (assuming a 14$.''$1 beam) and with the low scan speed of $8''s^{-1}$ for POL2_CVDAISY, that gives a sample rate of 2 Hz for a 4$''$ pixel, which is the standard pixel size of the data reduction pipeline.

Once the raw data have been separated into Stokes I, Q and U time-stream, the command *makemap* (Chapin et al., 2013) is then called to create an initial Stokes I map from the Stokes I time-streams. This initial Stokes I map is made following the steps seen in Figure 2.12 and described above in Section 2.3. Each of the observation blocks are solved independently and then are co-added to produce a single Stokes I map. When the co-add is complete, each observation then builds a pointing model comparing its pointing to the co-add. This pointing model is used in the next step.

2.3.3 Step 2: Final Stokes *I*, *Q* and *U* maps and vector catalog

The SCUBA-2/POL-2 data reduction routine makes use of masks for some of the modelling steps outlined in Section 2.3.1. Here, a 'mask' is just a spatial map which identifies regions of interest to either include or omit from the modelling routines. In some data reduction routines for interferometry, these masks can be defined by the user, but here the masks are defined by a signal-to-noise cut to help find where astronomical signal exists.

The Stokes I map from the first step is used to create an `AST` and `PCA` mask at a fixed signal-to-noise ratio which can be set by the user. These masks are used as a guess to mask where the astronomical signal is and we refer to these as the auto-generated masks. The `AST` mask is used to define background regions that are forced to zero after each iteration in order to prevent growth of spurious structures in the map. The `PCA` mask is used to define regions that are excluded from the Principle Component Analysis which removes correlated large-scale noise components from the bolometer time-streams. The second step of the reduction creates the final Stokes I, Q and U maps and a polarization half-vector catalog. The term half-vector is used to signify that the polarization vectors do not have a direction, i.e. 40° is the same as 220° and so vector angles are only given over the range -90° to 90°, measured east of north. The Stokes I, Q and U maps are solved for and created sequentially with the Stokes I map created first in order to use it as the IP reference map. The final Stokes I, Q and U maps are created using a similar map-making method as mentioned in Section 2.3.1 and 2.3.2 but with a key difference, which is the parameter *skyloop*.

In standard reductions, such as that described in Section 2.3.2, *makemap* is run on each observation separately until each converges and then the final map is created as a co-add of the individual maps. When *skyloop* is used, it instead processes each observation under a single iteration of *makemap*. So instead of running *makemap* for 20 iterations on 20 individual observations (i.e. 400 times), it will run *makemap* for 20 iterations, with each iteration involving solving for all 20 observations in parallel, and comparing them with each other. *Skyloop* improves the recovery of fainter, extended emission in the map by doing this iteration of individual observations in parallel. At each iteration, *skyloop* creates either the Stokes I, Q or U map using a method which tries to minimize instabilities of the map-making algorithm within the `AST` mask, therefore allowing better characterization of fainter, more extended structure. When using *skyloop*, convergence often requires many more iterations than simply using *makemap*. In addition, *skyloop* combines all observations at the end of each iteration, so any spurious growth of large-scale structures in a single iteration is suppressed when averaging with other iterations since they will be independent.

Another optional parameter to use in the reduction is *mapvar*. *Mapvar* controls how the variances in the final co-added maps are calculated. The default method for calculating variances is to simply propagate the variances of each individual map which were created by *makemap* (see Section 2.3 and Equation 2.9). When using *mapvar*, the variances are instead calculated from the spread of pixel data values between individual observation maps. *Mapvar* is only a better characterization of the noise then when there are a sufficient number of individual observations (a minimum of 10 observations is advised[2]). The variances from *mapvar* will tend to be larger due to residual uncorrected pointing errors and low-level artificial extended structures that develop within the source region defined by the AST mask (which vary from observation to observation, hence increasing variance).

We corrected for instrumental polarization in the Stokes Q and U maps based on the final Stokes I map and the "August 2019" IP polarization model[3].

[2]https://starlink.eao.hawaii.edu/docs/sc22.htx/sc22ch3.html

[3]https://www.eaobservatory.org/jcmt/2019/08/new-ip-models-for-pol2-data/

To further increase the S/N of polarization half-vectors and attempt to account for the JCMT beam size, they are often binned to a resolution of 12–14″. The polarization half-vectors are also debiased using an asymptotic estimate (AS) as described in Wardle & Kronberg (1974) to remove statistical bias in regions of low S/N (see Equation 2.10).

The polarization intensity (PI) of light is generally given by Equation 2.2 and the polarization fraction is just the PI divided by intensity, I. The values for the debiased polarization fraction P_{deb} are calculated from

$$P_{deb} = \frac{1}{I}\sqrt{Q^2 + U^2 - \sigma^2}\ , \tag{2.10}$$

where I, Q, and U are the Stokes parameters, and $\sigma^2 = (Q^2\sigma_Q^2 + U^2\sigma_U^2)/(Q^2 + U^2)$ where σ_Q, and σ_U are the uncertainties for Stokes Q and U. The uncertainty δP of the polarization degree was obtained using

$$\delta P_{deb} = \sqrt{\frac{(Q^2\delta Q^2 + U^2\delta U^2)}{I^2(Q^2 + U^2)} + \frac{\delta I^2(Q^2 + U^2)}{I^4}}\ , \tag{2.11}$$

with δI being the uncertainty for the Stokes I total intensity.

The other debiasing method that can be used is introduced by Plaszczynski et al. (2014); Montier et al. (2015) and is referred to as the 'modified asymptotic estimator' (MAS). It accounts for the occasions where Equation 2.10 is undefined, when $Q^2 + U^2 < \sigma^2$ and the polarization is calculated by

$$P_{deb}^{mas} = \frac{1}{I}[PI - 0.5\sigma^2(1 - e^{-(PI/\sigma)^2})/PI]\ . \tag{2.12}$$

The polarization position angles θ, measured from North to East in the sky projection (North is 0°), are calculated using Equation 2.3.

The corresponding uncertainties in θ were calculated using

$$\delta\theta = \frac{1}{2}\frac{\sqrt{Q^2\delta U^2 + U^2\delta Q^2}}{(Q^2 + U^2)} \times \frac{180°}{\pi}\ . \tag{2.13}$$

The plane-of-sky orientation of the magnetic field is inferred by rotating the polarization angles by 90° which assumes that the polarization is caused by elongated dust grains aligned perpendicular to the magnetic field (see Section 1.6.1.1).

2.3.4 Use of 8 Arcsecond Pixels

Standard reductions of SCUBA-2/POL-2 observations are done with a 4″ pixel size (e.g. Pattle et al., 2021). Nearly all of these reductions have been done on bright, high S/N sources. As we approach the limit of the POL-2 polarimeter, we can explore the use of larger pixel sizes to attempt to boost the S/N in these extended, low-surface-brightness sources. The use of different pixel sizes in reductions of JCMT SCUBA-2 data has been explored before, such as in the Gould Belt Survey (Ward-Thompson et al., 2007) where originally 6″ (see Sadavoy et al., 2013) and 3″ (see Mairs et al., 2015) pixels were used with the latter being chosen in order to recover small scale structure. The current default SCUBA-2/POL-2 pixel size of 4″ was picked in order to properly sample the Gaussian beam and allow the mapmaking algorithm to converge in a reasonable time (Chapin et al., 2013), as well as to avoid smoothing due to larger pixels. However, with faint sources such as starless cores, we need to investigate the potential of using larger pixel sizes.

One issue with using larger pixels is that the larger pixel size tends to produce masks that cover a larger area of the sky. Doubling the pixel size from 4″ to 8″ typically causes the number of bolometer samples falling in each pixel to increase by a factor of four, thus increasing the S/N of each pixel value by a factor near to two (since the variance goes as 1/N, see Equation 2.9). Since each mask is defined by a fixed S/N cut-off, this causes a larger fraction of the map to be covered by the mask. An increase in the size of the `AST` mask is potentially problematic, as it can encourage the growth of artificial large-scale structures within the masked areas (see Chapin et al., 2013). Distinguishing such artificial structures from real astronomical signal requires care.

Our solution to this problem is to re-use the 4″ pixel auto-generated masks when creating externally masked maps with 8″ pixels, rather than using new masks based on the auto-masked 8″ maps. This method is outlined in Figure 2.13. The smaller 4″ masks will then restrict the growth of artificial extended structures giving us more confidence in the remaining extended structure. To do this, we run the entire reduction using the standard 4″ pixel size (Step 1 and left side Steps 2/3 in Figure 2.13). We then regrid the `AST` and `PCA` masks from that reduction to 8″ (Step 1.5 in Figure 2.13) using the command *compave* from the KAPPA package (Currie & Berry, 2014). We then run the second step of the reduction using the regridded `AST` and `PCA` masks to create the externally masked Stokes I, Q and U maps as well as the polarization vector catalogs, using a pixel size of 8″ (right side Steps 2/3 in Figure 2.13).

We tested this method on the molecular cloud L43 (see Chapter 3). This resulted in a molecular cloud that looked similar to the original 4″ reduction but with better S/N and therefore more polarization half-vectors (vector catalog increased from 98 vectors to 133 vectors at the same S/N cut). This is the reduction presented later in that chapter.

As a further check, we performed a Jackknife Test by dividing our observations into two populations and comparing the Stokes I, Q and U maps from both populations. We saw a more significant difference between the populations when using the auto-masked 8″ maps. This difference occurred mainly in the areas where emission was present in the 8″ maps but not present in the 4″ maps, raising further doubt as to the validity of the new extended emission in the auto-masked 8″ maps. Any differences seen in 8″ reduction done using the regridded masks were the same as differences seen in 4″ reduction, just smoothed due to larger pixel sizes.

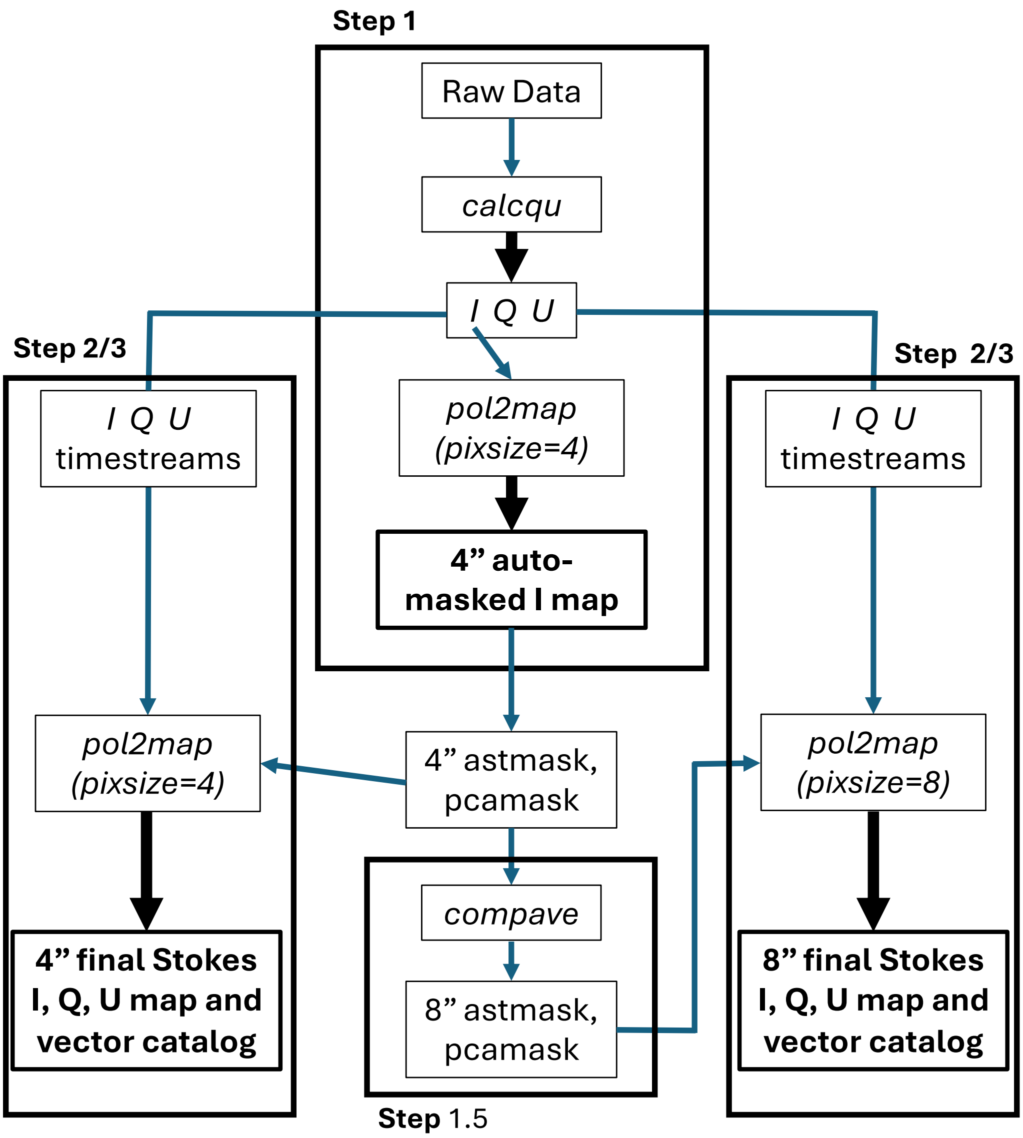

Figure 2.13: A somewhat simplified flowchart of Figure 2.11 showing the 8″ method. Step 1 and the left Step 2/3 is the same as in Figure 2.11. The addition of Step 1.5 is showing where the masks are regridded and then used in the right Step 2/3 which is ran with a pixel size of 8″ and is the 'regridded' 8″ reduction mentioned in the text. In the text where we mention 'auto-masked 8″ maps' or '8″ auto-generated masks', this refers to running Step 1 with pixsize=8 which gives an 8″ auto-masked I map instead which is then used to make the 'astmask' and 'pcamask' (eliminating Step 1.5) used in running Step 2/3.

2.3.4.1 8″ Stokes *I* maps

Our initial concern over using a reduction that made use of auto-generated masks from an initial 8″ Stokes *I* map was that the emission was much more extended than in the 4″ maps. We do not expect to recover much large-scale flux due to inherent limitations with SCUBA-2/POL-2 data reduction and observing through the atmosphere (see Section 2.3.1). SCUBA-2 is fundamentally unable to measure flux on size scales larger than the array size due to the need to distinguish between atmospheric and astrophysical signal (see Section 2.3.1 and Holland et al., 2013; Chapin et al., 2013), and POL-2 is even more restricted due to its small map size and slow mapping speed (Friberg et al., 2016). There are detailed discussions of SCUBA-2 large-scale flux loss compared to *Herschel* (a space observatory operating at comparable wavelengths 70–500 μm) in Sadavoy et al. (2013) and Pattle et al. (2015), and detailed discussion of the role of masking in SCUBA-2 data reduction in Mairs et al. (2015) and Kirk et al. (2018). The lower left and lower central panels of Figure 2.15 demonstrate the additional large-scale flux we see when using auto-generated 8″ masks, where the contours from the Stokes *I* continuum created using the regridded 4″ masks are plotted over the Stokes *I* continuum resulting from reducing the data using the auto-generated 8″ masks. The background map for both even and odd groups clearly shows emission beyond the extent of the drawn contours.

However, it can also be seen that this extended emission that we see from the contours aligns well with the SPIRE 250 μm image, as mentioned in Section 2.3.4. It can be seen from Figure 2.14 that the 250 μm dust emission extends further to the east from where the 850 μm contours end and follows the same shape that we see from the 8″ emission in Figure 2.15. We also see this dust morphology in all the *Herschel* bands meaning there is real extended astronomical signal in those areas, signal that JCMT could theoretically observe. However, it does not follow that

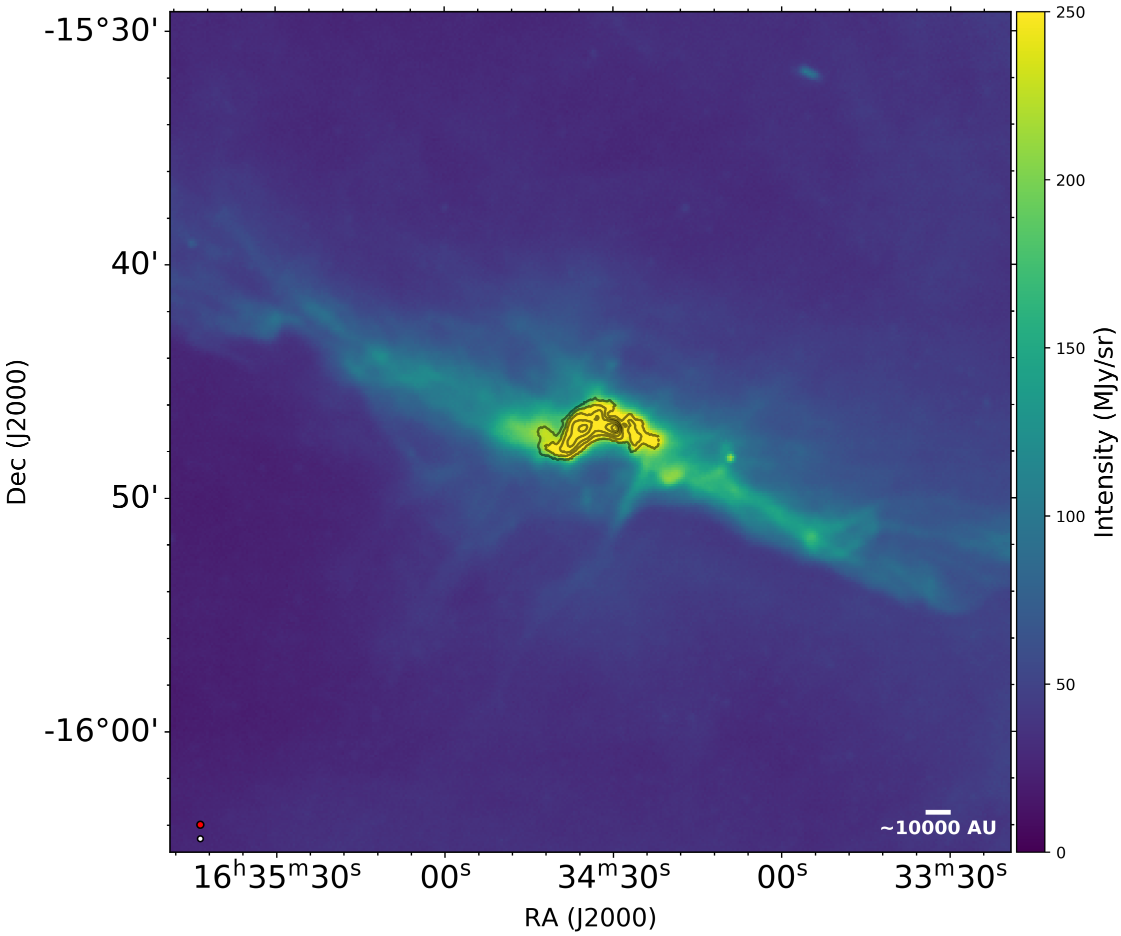

Figure 2.14: The background is the 250 μm dust map observed with *Herschel*/SPIRE. Black contours of the 850 μm SCUBA-2/POL-2 Stokes I emission are overlaid. These data come from the standard 4″ reduction. The extended emission to the east and west of the 850 μm contours can clearly be seen in the 250 μm data.

the SCUBA-2/POL-2 Stokes I data (from auto-generated $8''$ mask maps) in these regions is well-characterized because *Herschel* is able to observe extended structure and JCMT is not expected to or is expected to lose this structure in the data reduction process (see Section 2.3.1). This poor characterization of that extended emission is shown by the lower right panel of Figure 2.15.

As mentioned in Section 2.3.4, to further investigate this, we performed a Jackknife Test on the data, We divided the 26 observations into two groups, which we have designated as 'even' and 'odd'. We divided the observations by just alternating between 'even' and 'odd' when the observations were ordered by date of observation. In each group, we then reduced the observations using the normal method described in Sec.2.3 with both $4''$ pixels and with $8''$ pixels. Then for each group we reduced the observations using the new method (see Sec. 2.3.4), where we regridded the masks from the $4''$ reduction in each group to $8''$ and used those masks when running an $8''$ reduction instead of using the auto-generated $8''$ masks.

Figure 2.16 shows the results of the Jackknife Test in Stokes I maps for the reduction method presented in this work. Figure 2.15 then shows the results of the Jackknife Test, but using the $8''$ pixel auto-generated masks. The upper rows in Figures 2.15 and 2.16 are the same and shows the Stokes I map from a standard $4''$ reduction. All of the figures have the same grey scale and the difference map is the odd map subtracted from the even map. Stokes Q and U emission is very weak in starless cores and so little difference was seen between the two methods.

In Figure 2.16, there is some difference seen between the 'even' and 'odd' maps with the normal $4''$ reduction, but this same difference can be seen in the regridded $8''$ reduction, just slightly blurred due to the larger pixel sizes. The difference is most likely due to the group selection and would change with different grouping. However, in Figure 2.15, the difference in the auto-generated $8''$ mask reduction is very different from the $4''$ reduction. Additionally, the difference is seen in the

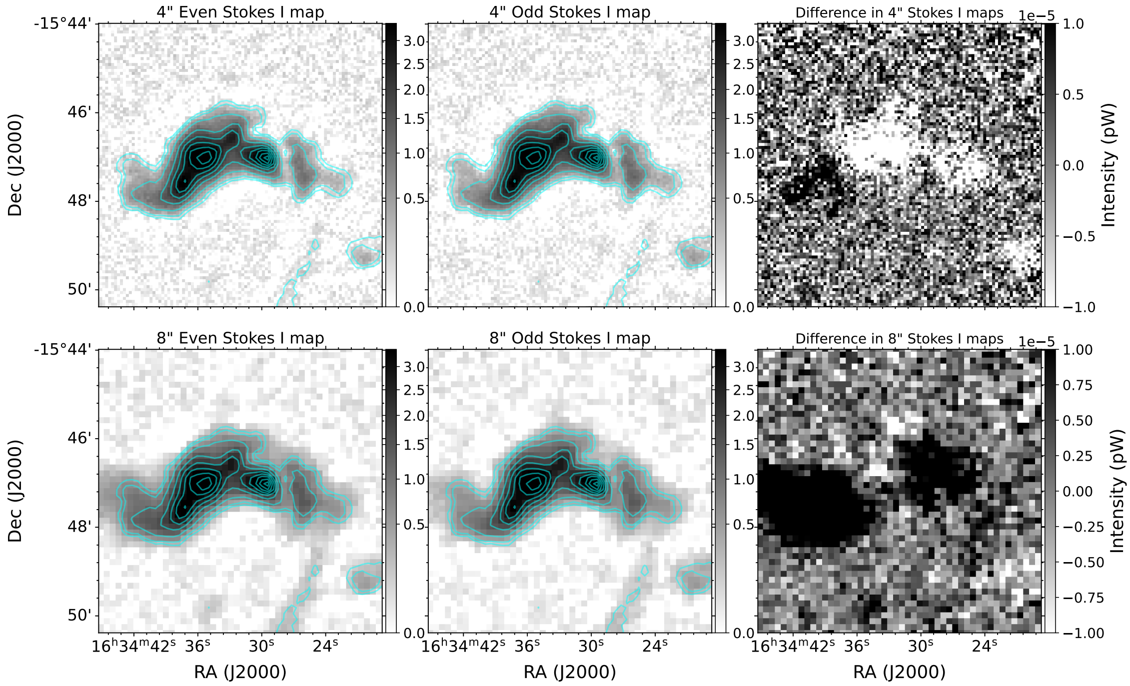

Figure 2.15: Results of the Jackknife Test for the data reduction technique using the auto-generated 8″ masks when reducing with 8″ pixels. Top row shows the 4″ Stokes I maps from the even and odd groups as well as the difference between the groups. The grey scales on the even and odd maps are $\times 10^{-4}$ pW.

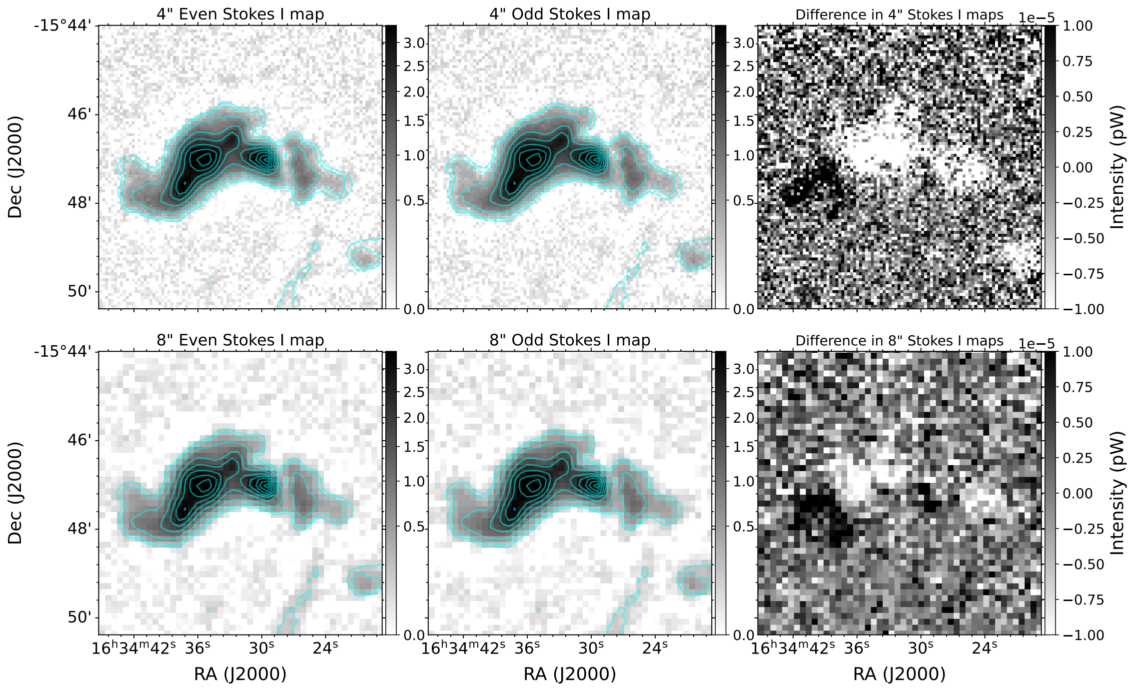

Figure 2.16: Results of the Jackknife Test for the data reduction technique presented in Section 2.3.4. Top row shows the 4″ Stokes I maps from the even and odd groups as well as the difference between the groups. Bottom row are the 8″ Stokes I maps and the difference between them. The grey scales are the same as Figure 2.15.

areas of extended emission that appear in the normal 8″ reductions but not in the 4″ reduction (as traced by the contours). This difference is why we raise concerns with blindly increasing the value of the *pixsize* parameter in the data reduction and potentially producing artificial structures. A different Jackknife Test grouping may yield a different residual map, or one that is not so severely different. Future reduction tests can be conducted to determine if it is a selection effect or in fact growth of non-astronomical signal.

In the 8″ maps, a different FCF was used from the standard ones in Table 2.2. We do use the values from Table 2.2 and still multiply by the 1.35 factor needed when POL-2 is used, but we further multiplied by a factor of 1.12 to account for the 8″ pixels. This extra factor was determined from SCUBA-2 calibration plots[4].

2.4 Supplemental Data and Observations

2.4.1 CO Observations

We used archival observations of the CO J = 1-0 line carried out with the Berkeley Illinois Maryland Array (BIMA) 10 antenna interferometry array. The CO J = 1-0 data were obtained from Lee et al. (2002) and details of the observations and data reduction can be found therein. The BIMA observations have a synthesized beam size at ≈115 GHz of 12.″8×12.″8, similar to that of JCMT.

We also used archival observations of the CO J = 3-2 line carried out with HARP, on the JCMT, to remove the CO contribution in L43 (see Chapter 3). This is discussed further in Section 3.3.3. The data were accessed from the Canadian Astronomy Data Centre database[5] (Project ID: M07AU11) and were downloaded as reduced spectral cubes which were then mosaicked using the PICARD recipe

[4]https://www.eaobservatory.org/jcmt/instrumentation/continuum/scuba-2/calibration/
[5]https://www.cadc-ccda.hia-iha.nrc-cnrc.gc.ca/en/jcmt/

MOSAIC_JCMT_IMAGES[6].

2.4.2 NH_3 Observations

NH_3 (3-3) observations were kindly given to us by Jürgen Ott on behalf of the Survey of Water and Ammonia in the Galactic Center (SWAG) team (Krieger et al., 2017). The data were obtained with the Australia Telescope Compact Array (ATCA) and followed up a previous map made with Mopra single-dish observations. The velocity data has been binned to a resolution of $\sim$2 km s^{-1} with an increase in signal-to-noise of $\approx$2.2. The beam size of the NH_3 observations is $26.0'' \times 17.7''$, but the maps are reduced onto $3''$ pixels.

[6] http://www.starlink.ac.uk/docs/sun265.htx/sun265ss15.html

Chapter 3

Lynds 43

3.1 Overview

This chapter is work that was published in Karoly et al. (2023). It provides an in-depth look at one of the prestellar cores observed in BISTRO-3, Lynds 43. This chapter also introduces analysis techniques and serves as a template for analysis that will be used later in Chapters 4 and 5. A comparison of this source with other sources presented in Chapters 4 and 5 follows in Chapter 6. The chapter starts with an overview of Lynds 43, then follows with results about the cloud characteristics and magnetic field information and then finally a discussion about how the magnetic field interacts with the molecular cloud.

The data reduced in this section were collected as part of the BISTRO-3 survey at the JCMT (Project ID: M20AL018). The data were reduced as outlined in Sections 2.3 and 2.3.4. The ^{12}CO J=3-2 HARP data used were downloaded from the CADC archive (Project ID: M07AU11) and were downloaded as reduced spectral cubes that were then mosaicked using the PICARD recipe MOSAIC_JCMT_IMAGES[1]. We also used archival observations of the ^{12}CO J=1–0 line carried out with the Berkely Illinois Maryland Array (BIMA) 10 antenna interferometry array. The ^{12}CO

[1]http://www.starlink.ac.uk/docs/sun265.htx/sun265ss15.html

J=1–0 data were obtained from Lee et al. (2002), and details of the observations and data reduction can be found therein. BIMA has a similar beam size to that of JCMT at 12″ at this frequency.

3.2 Lynds 43

L43 is a nearby molecular cloud in the northern region of the Ophiuchus star-forming region (see Figure 3.1) at 120–125 pc which is the mean distance to the Ophiuchus complex. This is derived from a value of 125±25 pc using photometric distances (de Geus, de Zeeuw & Lub, 1989) and a value of $120.0^{+4.5}_{-4.2}$ pc from VLBA nonthermal radio observations (Loinard et al., 2008). As can be seen in Figure 3.1, L43 is an isolated dense core with a visual extinction >30 mags. It contains a sub-millimetre bright starless core (Ward-Thompson et al., 2000) to the east and to the west an embedded young stellar object (YSO), IRAS 16316-1450, a T Tauri star (Herbst & Warner, 1981) originally classified as a Class II source currently transitioning from a protostar to a main-sequence star (Andre & Montmerle, 1994). However, Chen et al. (2009) and Yoon et al. (2021) have more recently classified it as a Class I source based on Spitzer and spectral line data respectively. IRAS 16316-1450 is most commonly known as red nebulous object (RNO) 91 (Cohen, 1980), although this technically refers to the reflection nebula with which the YSO is associated (Hodapp, 1994). The YSO is also associated with an extended, asymmetrical and bipolar CO outflow (Lee et al., 2002, and see Figure 3.2) and HCO^+, N_2H^+ and CS emission (Lee & Ho, 2005). The CO outflow is detected in the ^{12}CO J = 1-0, 2-1 and 3-2 transitions, but there is no detection in the higher transitions (Yang et al., 2018). The CO J = 1-0 outflow is shown in Figure 3.2. The J = 2-1 transition is plotted in Figure 1 of Bence et al. (1998). All three of the transitions show a very dominant southern outflow, although the HARP CO J = 3-2 data shows a smaller northern lobe as well (see Figure 3.3).

Another YSO, named RNO 90 (Cohen, 1980, also known as V1003 Oph) sits further to the west, $\sim$0.2 pc away from RNO 91 (see Figure 3.2), and is also classified as a T Tauri star (Herbst & Warner, 1981) but is a much more evolved source, with an age of 2-6 Myr (Garufi et al., 2022) and a protoplanetary disk (e.g. Pontoppidan et al., 2010). It sits at a distance of 114.7–116.7 pc (Gaia Collaboration et al., 2021; Bailer-Jones et al., 2018) suggesting that this star sits either in the foreground of the L43 molecular cloud or perhaps the filament where they are embedded is inclined towards us so that RNO 90 is closer than the dense core (both assume a distance to the dense sub-millimetre core L43 similar to the mean distance of the larger Ophiuchus region, $\approx$120 pc). The presence of a reflection nebula for both RNO 90 and 91 suggests they do sit just in front of or are partially embedded in the filament/molecular cloud (Herbst & Warner, 1981). The reflection nebula traces the material at the head of the outflow cavity, where the protostar is illuminating the dust (see Figure 4 of Mathieu et al., 1988). L43 is therefore a unique environment which consists of an older T-Tauri star, a younger Class I protostar and a starless core within a very isolated filament and molecular cloud, and with an evolutionary gradient from southwest to northeast.

Figure 3.2 shows the dense starless core with green contours as observed by JCMT at 850 μm, which is embedded within a longer more diffuse filament seen by *Herschel*. This isolated filament, seen also in Figure 3.1 is oriented at $\approx 67°$ E of N. *Planck* polarization observations also show a large-scale magnetic field roughly parallel to the filament, although curving slightly to the south. The magnetic field of the starless core was previously observed using the predecessor to POL-2, SCUPOL, by Ward-Thompson et al. (2000) and a magnetic field strength in the core was calculated to be $\approx$160 μG using the SCUPOL observations and the DCF method (Crutcher et al., 2004, see Section 3.3.6 for details on the DCF method). Additionally, Ward-Thompson et al. (2000) suggested that the magnetic field might be affected by the outflow of the RNO 91 source, although the entire molecular cloud was not observed and RNO 91 was on the very edge of the SCUPOL observations. The southern, blue-shifted lobe of the CO outflow from RNO 91 (Lee et al., 2002) is seen in Figure 3.2 where RNO91 and 90 are also both labelled.

3.3 Results

3.3.1 850 μm Dust Morphology

Figure 3.2 shows the 850 μm dust contours in green overlaid on the *Herschel* SPIRE 250 μm where the 850 μm dust traces the densest part of the filament. The filament does continue to the east and west but this may be more extended structure and is therefore lost by SCUBA-2/POL-2. The 850 μm dust traces the northern edge of the CO outflow cavity which is discussed in the next section. The 850 μm emission is peaked in the main starless core (L43) and then the dust region surrounding RNO 91.

Figure 3.4 shows the column density map which is discussed later in Sec. 3.3.3 but it has the 850 μm dust contours overlaid with more levels to better show the emission structure. In the main starless core, the densest emission peaks toward the centre, but then there are two lobes that extend to the northwest and southeast. A small peak can be seen in southeast lobe in Figure 3.4. We do not have resolved kinematic or significant magnetic field data between these three areas (the centre part and the two lobes) so it is not possible to tell if they are fragmenting. However the 850 μm emission shows structure suggesting these could be on the way to fragmentation.

We can model these three regions as Bonnor-Ebert spheres (Ebert, 1955; Bonnor, 1956) and estimate their critical BE masses. We take the sound speed $c_{\rm s}$ to be $\sim$0.19 km s^{-1} which was calculated assuming a dust temperature of 12.1 K (Planck Collaboration et al., 2016c). The critical BE mass can be calculated using the

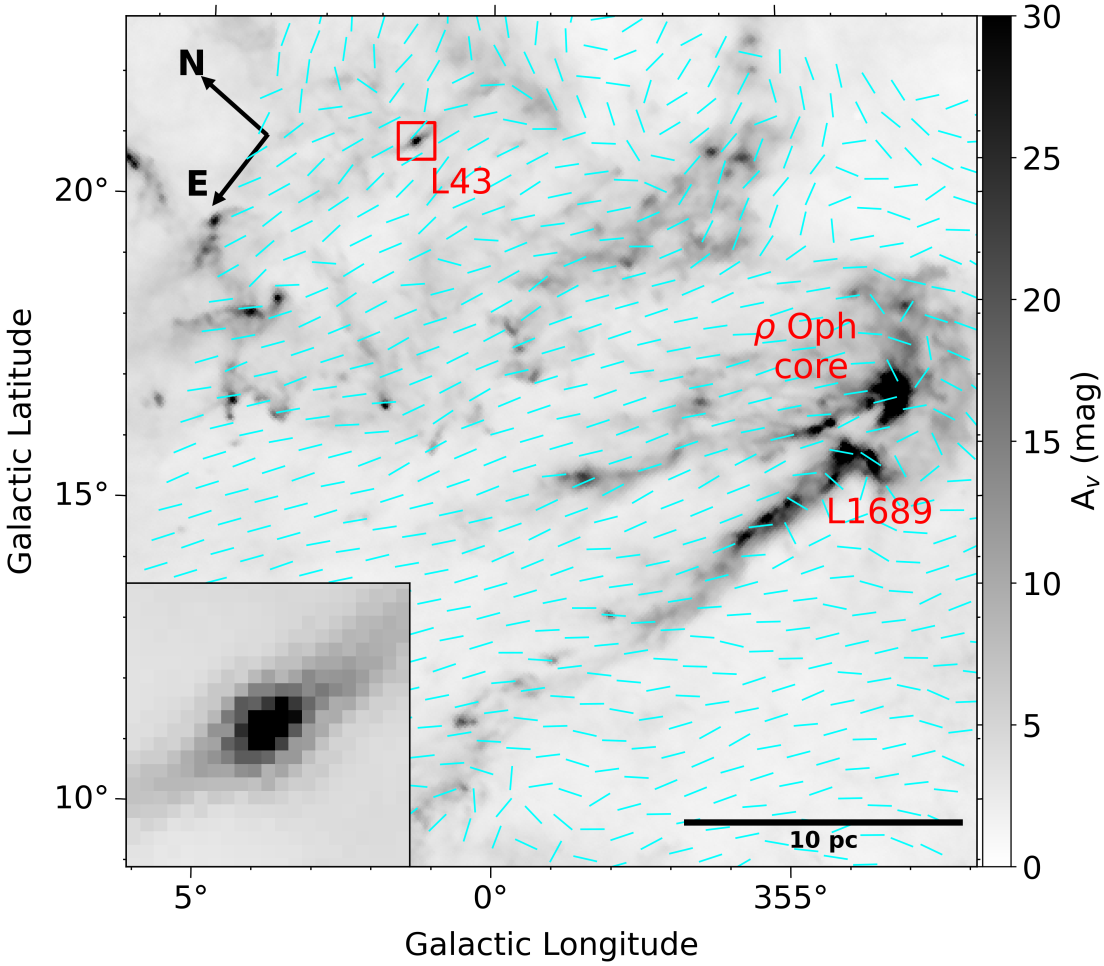

Figure 3.1: An extinction map of the Ophiuchus region made from Planck dust emission maps (Planck Collaboration et al., 2016a). The inset is a zoomed in picture of the red box labeled L43. The rotated red box in the inset shows the region plotted in Figure 3.2 in the J2000 coordinate system. The well known clouds of the ρ Oph core (also known as L1688) and L1689 are labelled as a reference. The cyan vectors overlaid show the magnetic field as inferred from Planck dust polarization observations at 353 GHz (Planck Collaboration et al., 2016b), smoothed to 30′ resolution.

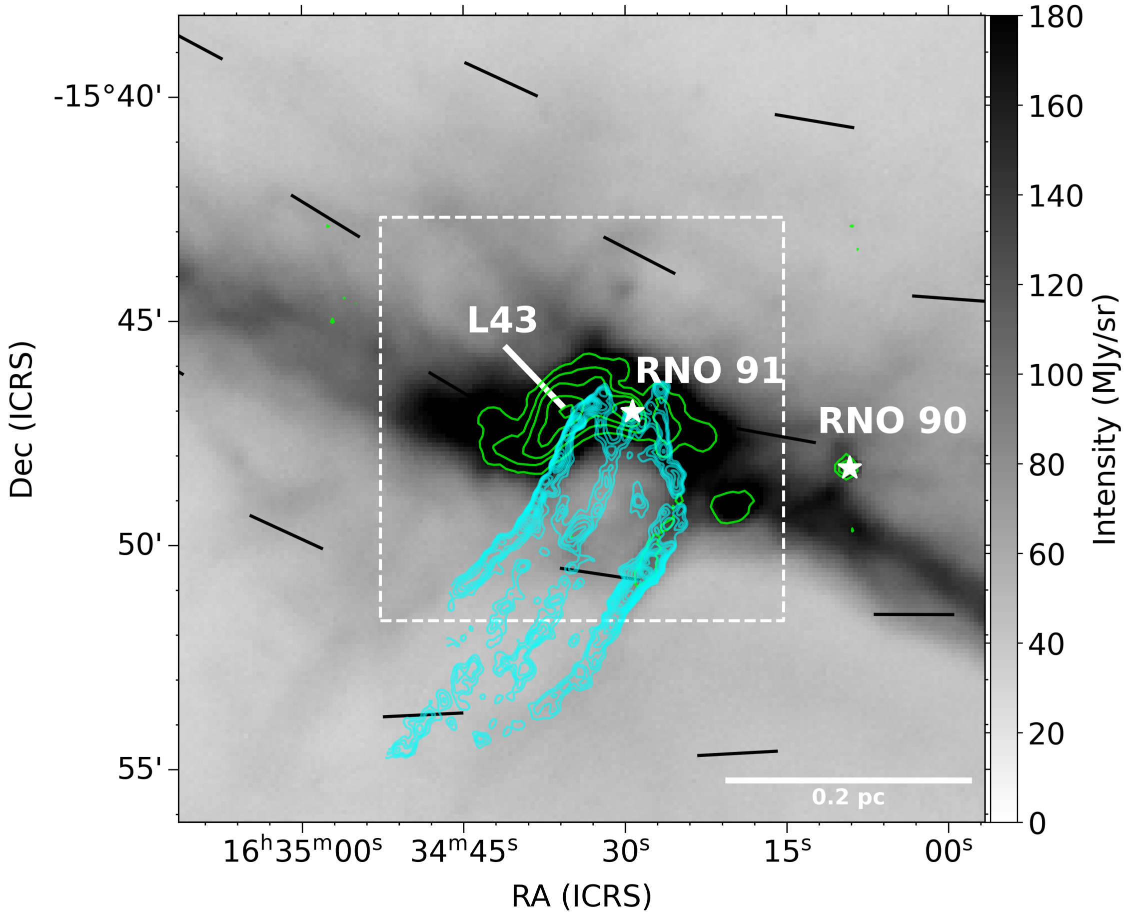

Figure 3.2: *Herschel* SPIRE 250 μm dust continuum map with SCUBA-2/POL-2 850 μm dust continuum green contours from this work. Planck B-field vectors are overlaid in black and are all normalized to a single length and over-sampled at every $5'$. The two embedded YSOs are labelled. Additionally, the CO J=1-0 emission from RNO 91 (Lee et al., 2002) is shown in cyan which was integrated from 0.5 to -5 km s^{-1}. The white dashed box shows the area of interest that is plotted in later figures

relation (Eq 3.9, Bonnor, 1956),

$$M_{\mathrm{BE,crit}} = 3.3\frac{c_{\mathrm{s}}^2}{G}R_{\mathrm{crit}} \ , \tag{3.1}$$

where G is the gravitational constant and R_{crit} is the critical radius of the core. We estimate R_{crit} from the observed flux structure (visualized using the contours in Figure 3.4 where the two lobes either end can be seen and using the contour line at 150 mJy/beam to trace the circular shape) and use it to also calculate total flux for total mass estimates. Values for R_{crit} are given in Table 3.1 along with locations of the three potentially fragmenting regions in the submillimeter core (NW, Main and SE). The estimated critical BE masses of the two lobes are $M_{\mathrm{BE,crit}}^{\mathrm{NW}}$ ~0.21 $\mathrm{M}_\odot$ and $M_{\mathrm{BE,crit}}^{\mathrm{SE}}$ ~0.20 $\mathrm{M}_\odot$ for the northwest and southeast lobes respectively. For the central (main) peak, the estimated critical BE mass is $M_{\mathrm{BE,crit}}^{\mathrm{main}}$ ~0.32 $\mathrm{M}_\odot$.

We can estimate the total mass from the 850 μm dust emission using the relation from Hildebrand (1983),

$$M_{\mathrm{TOT}} = \frac{F_\nu D^2}{\kappa_\nu B_\nu(T_{\mathrm{d}})} \ , \tag{3.2}$$

and see also Ward-Thompson & Whitworth (2011), where

$$\kappa_\nu = \kappa_o \left(\frac{\nu}{\nu_o}\right)^\beta \ , \tag{3.3}$$

and F_ν is the total measured flux density at the observed frequency ν, $B_\nu(T_{\mathrm{d}})$ is the Planck function for a dust temperature T_{d}, and κ_ν is the monochromatic opacity per unit mass of dust and gas. We use T_{d}=10 K from temperature maps we derived with SED fitting (see Section 3.3.3). κ_ν ~0.0125 $\mathrm{cm^2\,g^{-1}}$ assuming $\kappa_o = 0.1\,\mathrm{cm^2\,g^{-1}}$, $\nu_o = 10^{12}$ Hz (Beckwith et al., 1990) and β=2. We should note that κ_ν can have a systematic uncertainty of up to 50% (Roy et al., 2014).

Assuming a distance of 125 pc, we estimate total masses from the 850 μm dust emission of $M_{\mathrm{TOT}}^{\mathrm{NW}}$ ~0.14 $\mathrm{M}_\odot$ and $M_{\mathrm{TOT}}^{\mathrm{SE}}$ ~0.17 $\mathrm{M}_\odot$ for the northwest and southeast lobes respectively and $M_{\mathrm{TOT}}^{\mathrm{main}}$ ~0.53 $\mathrm{M}_\odot$ for the main core. This suggests that if they are indeed fragmented, the central part of the starless core may be undergoing gravitational collapse (i.e. $M_{TOT}^{main}/M_{BE,crit}^{main} > 1$) while the two smaller lobes are not, rather than a coherent collapse of the whole core. All of the masses are summarized in Table 3.1.

We also estimated the envelope mass from the 850 μm dust emission of the two T-Tauri sources RNO 90 and RNO 91 using Eq. 3.2. We find a total estimated envelope mass for RNO 90 of M_{TOT}^{RNO90}=0.05±0.02 $M_{\odot}$ assuming a distance of 115.7±1 pc and a radius of 14.4″. This is orders of magnitude greater than the dust mass of the disk as seen by ALMA which is closer to $2\times10^{-5}\,M_{\odot}$ (Garufi et al., 2022), but we do not resolve this structure and are more likely seeing the remaining dusty envelope. For RNO 91, we estimate a total mass from the 850 μm dust emission of M_{TOT}^{RNO91}=∼0.48±0.24 $M_{\odot}$ assuming a distance of 125 pc and that the dusty envelope is an ellipse with dimensions 32.0×18.0″ rotated 60° East of North. This estimated total mass value is in good agreement with Young et al. (2006) who found a mass of 0.3±0.1 $M_{\odot}$. Assuming just a uniform sphere of radius 15.6″, we get an estimated total mass of 0.215±0.109 $M_{\odot}$.

3.3.2 Outflow of RNO 91

As mentioned in Section 3.2, there is a weak CO outflow driven by the embedded Class I protostar in RNO 91. The southern outflow traces the southern edge of the L43 starless core and forms a limb-brightened U shape (Lee et al., 2002), which is seen in all transitions. The southern outflow is heavily blue-shifted, indicating the outflow is tilted towards us, potentially by up to 60° (Lee & Ho, 2005). Weintraub et al. (1994) finds that RNO 91 is not very deeply embedded in the L43 molecular cloud and rather sits nearer to us than the main submillimetre starless core.

However, a very clear dust cavity can be seen in Figure 3.2 which the outflow traces nearly perfectly. This dust cavity sits along the filament, and it appears that the filament has been disrupted by the outflow, as material is cleared to the

Table 3.1: Mass estimates of L43 sub-cores

	SMM core sources			Protostellar sources	
	NW Lobe[a]	Main[a]	SE Lobe[a]	RNO 90	RNO 91[a]
RA (J2000)	16:34:32.73	16:34:35.33	16:34:37.16	16:34:09.29	16:34:29.57
DEC (J2000)	-15:46:31.0	-15:46:58.72	-15:47:32.2	-15:48:14.9	-15:46:58.6
$R_{\rm crit}$ ($''$)	12.8	19.6	12.0	–	–
R ($''$)	–	–	–	14.4	32.0×18.0 (60°)
$M^{\rm b}_{\rm BE,crit}(M_\odot)$	0.21	0.32	0.20	–	–
$M^{\rm c}_{\rm TOT}(M_\odot)$	0.14	0.53	0.17	0.05(0.02)	0.48(0.24)

$R_{\rm crit}$ is the critical radius of the object as described in Sec. 3.3.1 used to estimate critical BE masses. R is the observed radius of the source as based on the flux distribution. For RNO 91 we have listed the semi-major and semi-minor axes of the ellipse with the position angle (E of N) in parentheses.

a. Distance to source taken to be 125 pc (see Sec. 3.2)

b. See Equation 3.1

c. See Equation 3.2

south and potentially pushed north to form the kink in the filament, though there is not much redshifted CO emission to the north. This morphology of the dust in the filament suggests some sort of interaction with or influence by the outflow. This does contradict the above claim that the source is not deeply embedded. The 850 μm dust emission also shows this U-shaped bend to the south, suggesting even the densest part of the filament is affected by, or was initially affected by, the outflow. Bence et al. (1998) did suggest that the outflow has been weakened over time by a UV radiation field, so the current outflow we observe may not be the original morphology or strength.

One possibility then is that the source was previously embedded and cleared out the dust cavity we see including along the LOS so that it presently sits in the foreground of the dense filament. This was also suggested by Mathieu et al. (1988) who determined that RNO 91 was once associated with the dense molecular core, but has since blown through the dense gas with the outflow. They also suggest that the outflow energy is only coupled with a small fraction of the core mass. So the majority of the dense starless core L43 is undisturbed, though as discussed later, our observations of the magnetic field suggest that we are either only tracing affected foreground dust or that the outflow has influenced some of the dense material.

Regardless, the fact that the dust appears to be heavily influenced by the outflow suggests we must be careful in our analysis of the magnetic field which is traced by the dust. A more in-depth discussion of the interaction of the outflow with the magnetic field and potential CO emission or polarization contribution is presented in Section 3.4.2.

3.3.3 Dust Column Density

Figure 3.3 shows the ^{12}CO (J = 3-2) outflow from RNO 91 spatially overlaps with the Stokes I emission. As mentioned in Section 2.1.1, the bandpass filter allows in flux from the ^{12}CO (J = 3-2) line. We attempt to 'correct' the 850 μm Stokes I maps by removing potential contamination. We follow the method of Parsons et al. (2018) using the HARP data mentioned in Section 3.1. We use the regular 4″ Stokes I map because this correction method is best-characterised for 4″ maps before and for the purposes of fitting the black-body spectrum, we do not require the increase in signal-to-noise that is helpful for our polarization vectors. The contributions to total intensity from CO is ∼5–10%, getting up to ∼20% directly around RNO 91. We should note that the reduction produced slight negative bowling to the north of the L43 emission, though not in a region of any emission.

We then use archival *Herschel* Photodetector Array and Camera Spectrometer (PACS) 160 μm, SPIRE 250, 350 and 500 μm dust emission maps[2], along with the JCMT 850 μm dust emission map from this work to create a column density map (see Figure 3.4). We filter the *Herschel* maps in order to remove the large-scale structure that SCUBA-2/POL-2 is not sensitive to. We follow the method from Sadavoy et al.

[2]from http://archives.esac.esa.int/hsa/whsa/

(2013) and Pattle et al. (2015) of introducing the *Herschel* maps into the Stokes I timestream and repeating the reduction process from Section 2.3.3, using $4''$ pixels. We then subtract the original 850 μm only SCUBA-2/POL-2 Stokes I emission from the map which included the *Herschel* maps in the reduction and the resulting map was the filtered *Herschel* map.

We then fit the five maps with a modified black-body (Hildebrand, 1983)

$$F_{\nu} = \mu_{\mathrm{H}_2} m_{\mathrm{H}} N_{\mathrm{H}_2} B_{\nu}(T_{\mathrm{d}}) \kappa_{\nu} \,, \tag{3.4}$$

where again F_{ν} is the measured flux density at the observed frequency ν, $B_{\nu}(T_{\mathrm{d}})$ is the Planck function for a dust temperature T_{d}, μ_{H_2} is the mean molecular weight of the hydrogen gas in the cloud, m_H is the mass of an hydrogen atom, N_{H_2} is the column density, and κ_{ν} is the dust opacity (see Eq. 3.3). We use a value of 2.8 for μ_{H_2}, and κ_{ν} was calculated for each frequency observed using Equation 3.3, where β is the emissivity spectral index of the dust and is taken to be 1.8 (an approximate value in starless cores, Schnee et al., 2010; Shirley et al., 2005; Sadavoy et al., 2013), and we again assume $\kappa_o = 0.1\,\mathrm{cm}^2\,\mathrm{g}^{-1}$ and $\nu_o = 10^{12}$ Hz (Beckwith et al., 1990). We used temperature values from previously derived dust temperature maps using just the non-filtered SPIRE maps and 850 μm maps. In both solving for the temperature maps and now the column density maps, we convolved the data at 160, 250, 350 and 850 μm to the largest resolution which was at 500 μm with a resolution of $\approx 35''$ and then regridded all of the maps to the 850 μm map grid. Then we were able to do our pixel-by-pixel fitting.

The column density map is shown in Figure 3.4. We see column densities in the main starless core on the order of $10^{22.8}\,\mathrm{cm}^{-2}$ which is $\sim 6 \times 10^{22}\,\mathrm{cm}^{-2}$, with a maximum column density of $\sim 3 \times 10^{23}\,\mathrm{cm}^{-2}$

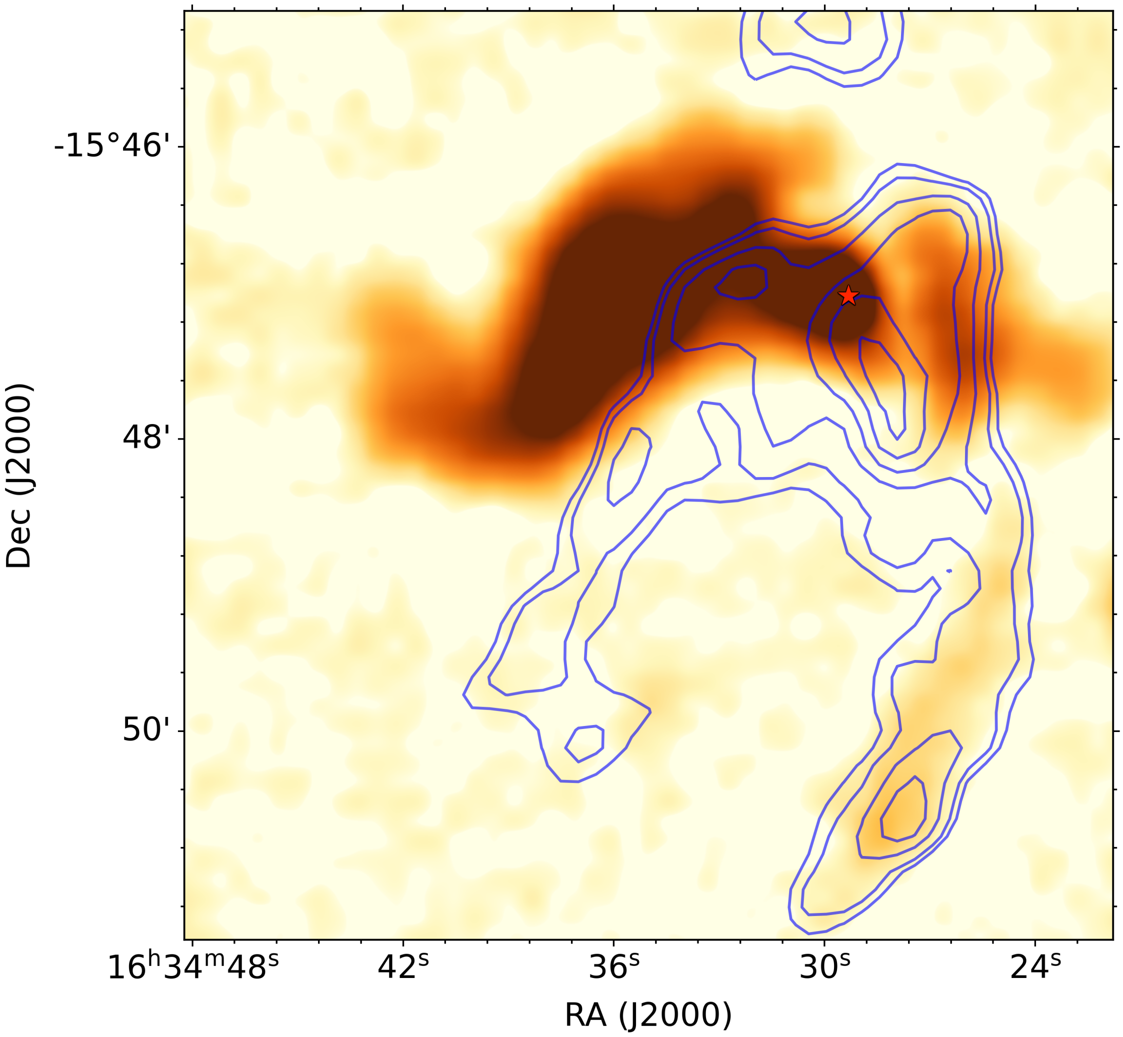

Figure 3.3: HARP ^{12}CO J=3-2 emission plotted in blue contours (integrated from -11.2 to -19.5 km s^{-1}) over the 850 μm dust emission. The location of RNO 91 is shown with a red star. The overlap with some of the dust emission is evident and these regions showed some level of CO contamination when attempting to remove CO emission from the dust emission as outlined in Section 3.3.3.

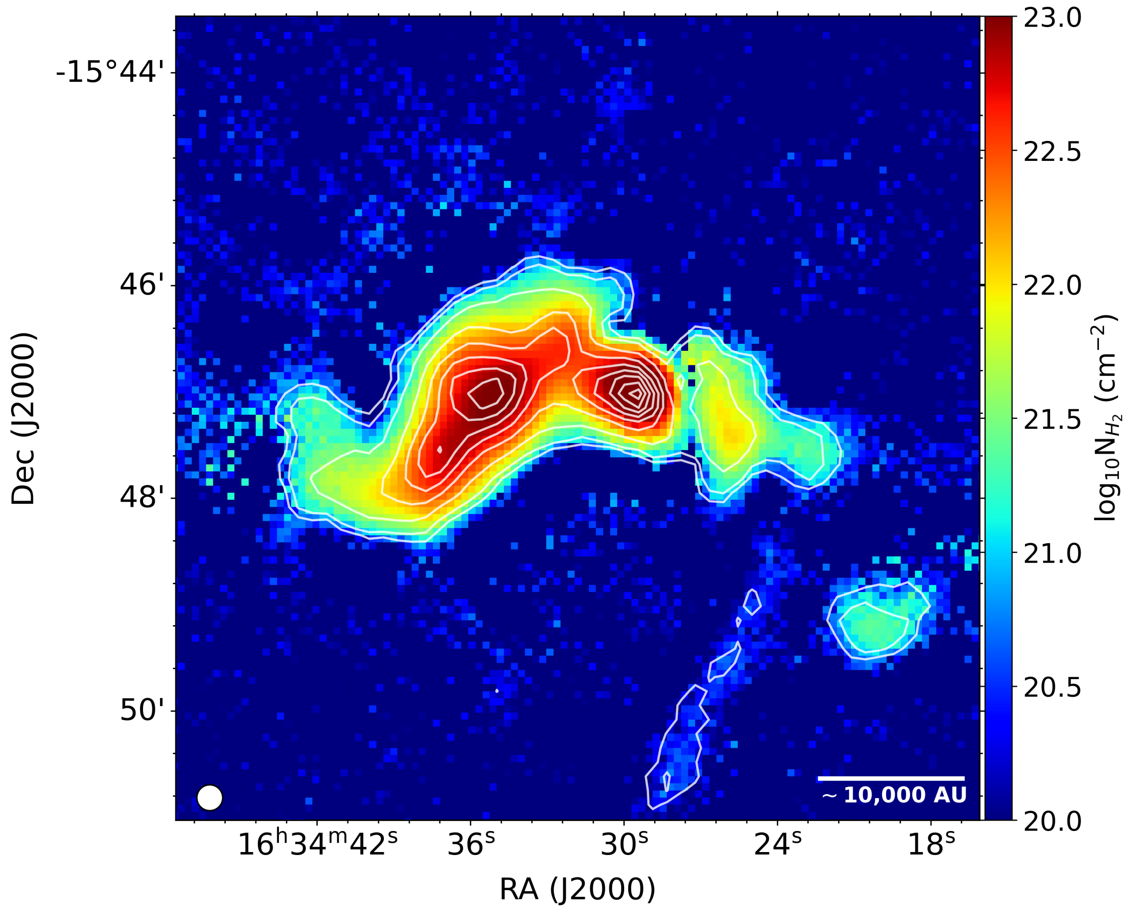

Figure 3.4: Molecular hydrogen column density map calculated from filtered PACS 160 μm, SPIRE 250, 350 and 500 μm and SCUBA-2/POL-2 850 μm maps, with 850 μm contours overlaid at [10, 20, 50, 100, 150, 200, 250, 300, 350] mJy beam^{-1}. The method for calculating the H_2 column density is described in Section 3.3.3.

3.3.4 Polarization Properties of the Starless Core

In Figure 3.6 we plot polarization fraction versus intensity of the non-debiased polarization half-vectors in L43. We focus only on the central $3'$ diameter region of L43 (centered at RA=16h:34m:34s, Dec=-15^{o}47$'$11$''$) as this is where the exposure and noise are roughly uniform and is where the dense molecular cloud is. A very clear decrease in polarization fraction can be seen towards the regions of high intensity. Within starless cores, this depolarization occurs in the highest density regions, due to some combination of field tangling and the loss of grain alignment at high enough A_V's ($\approx$20 mag) as predicted by RAT theory (Andersson, Lazarian & Vaillancourt, 2015). A common method to study the grain alignment efficiency in molecular clouds is to determine the relationship between polarization efficiency and visual extinction, where polarization fraction and total intensity can be substituted for those two quantities respectively at submillimetre wavelengths (see Pattle et al. 2019 and references therein).

The relationship between polarization and intensity should follow a power law, $p \propto A_V^{-\alpha}$, where an α of 1 indicates a loss of alignment and an α of 0 would indicate perfect alignment. We follow the methods of Pattle et al. (2019) and use the Ricean fitting technique to fit the data. This method fits the mean of the Rice distribution (Rice, 1945) to the non-debiased polarization data, using Equation 21 of Pattle et al. (2019). This is the black line in Figure 3.6. We get α=0.83$\pm$0.06 for the 12$''$ vectors and see an obvious offset from the null (the grey dashed line in Figure 3.6) which would indicate we retain some alignment. The null hypothesis corresponds to α=1. Additionally, the ordered polarization geometry suggests that we are continuing to trace the magnetic field to high A_V's. We performed the Ricean fitting for polarization vectors binned from 8$''$ up to 32$''$ and see α values from 0.89 to 0.70 respectively.

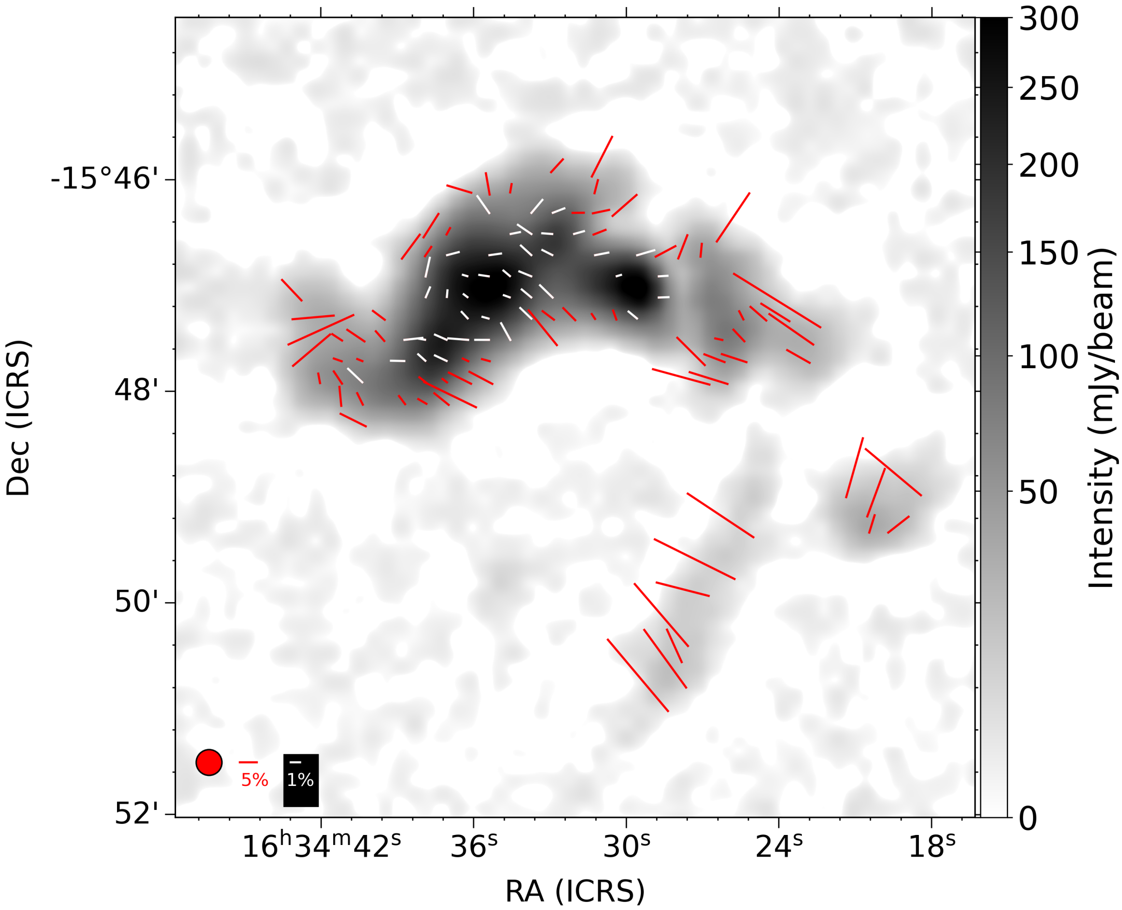

Figure 3.5: The polarization half vectors are plotted as red lines and scaled by the percentage polarization. Vectors plotted in white have P<2% and are scaled three times larger than the red vectors. Scale vectors are shown in the bottom left of the image next to the JCMT beam size. The plotted vectors are binned to 12″ and have a S/N cut of $I/\delta_I > 10$ and $p/\delta_p > 2$ applied. The clear decrease in percentage polarization towards the areas of high intensity (and therefore high extinction or column density) can be seen.

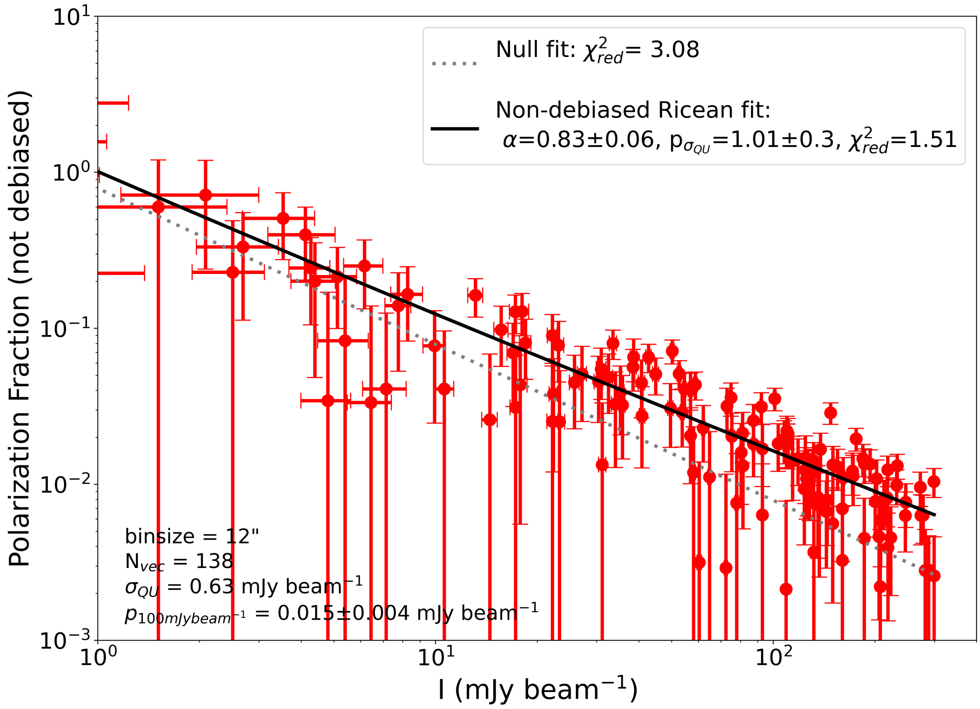

Figure 3.6: A plot of polarization fraction versus Stokes I intensity of non-debiased polarization vectors in the inner $3'$ area of the map. The vectors are binned to $12''$ and the only selection criteria is Stokes $I > 0$. The null fit is plotted as a grey dashed line, while the Ricean fit is plotted as a black solid line. The α value for the Ricean and reduced-χ^2 values are given for both fits in the legend.

3.3.5 Magnetic Field Morphology

The vectors chosen for analysis have a S/N cut of $I/\delta_I > 10$ and $p/\delta_p > 2$. A S/N cut of $p/\delta_p > 2$ can be quite poor in polarization so we must proceed with caution with those vectors. In Figure 3.7 we plot the lower S/N vector distribution (dashed histogram) and the higher S/N vectors with $p/\delta_p > 3$ (solid histogram). Within most of the molecular cloud, the two S/N cuts agree well with the lower S/N vectors following the same orientation as the higher S/N vectors. The polarization angle distributions follow the same shape between the two S/N cuts and they agree well with that found by Matthews et al. (2009) in the SCUPOL legacy survey (blue histogram). Using the lower S/N cut we get more data points to then use when calculating magnetic field strength (see Sec. 3.3.6) which could increase the spread of the position angles but can also increase the statistical confidence in the calculated dispersion.

We also performed a 2-sample Kolmogorov–Smirnov (KS) test on the different polarization angle distributions. The first KS test compared the distribution from Matthews et al. (2009, 40 vectors) with our $p/\delta_p > 2$ distribution (117 vectors). The second KS test compared the $p/\delta_p > 2$ distribution with the $p/\delta_p > 3$ distribution (60 vectors). For the first KS test, we obtain a KS test statistic of 0.15 and p-value of 0.44. For the second KS test, we obtain a KS test statistic of 0.09 and a p-value of 0.83. For the two tests, assuming a 95% confidence level, the threshold KS test statistic would be 0.25 and 0.22 respectively (calculated from $c(\alpha)\times\sqrt{(n+m)/(n\times m)}$ where n and m are the number of points in the two distributions and $c(\alpha)$ is a factor depending on the confidence level, here 1.36 for a confidence level of 95%). In both tests, the KS test statistic is lower than their respective threshold values and the p-values are both above the null value of 0.05. So for both comparisons, we cannot reject the null hypothesis and so we can conclude that the two distributions being compared did come from the same initial distribution.

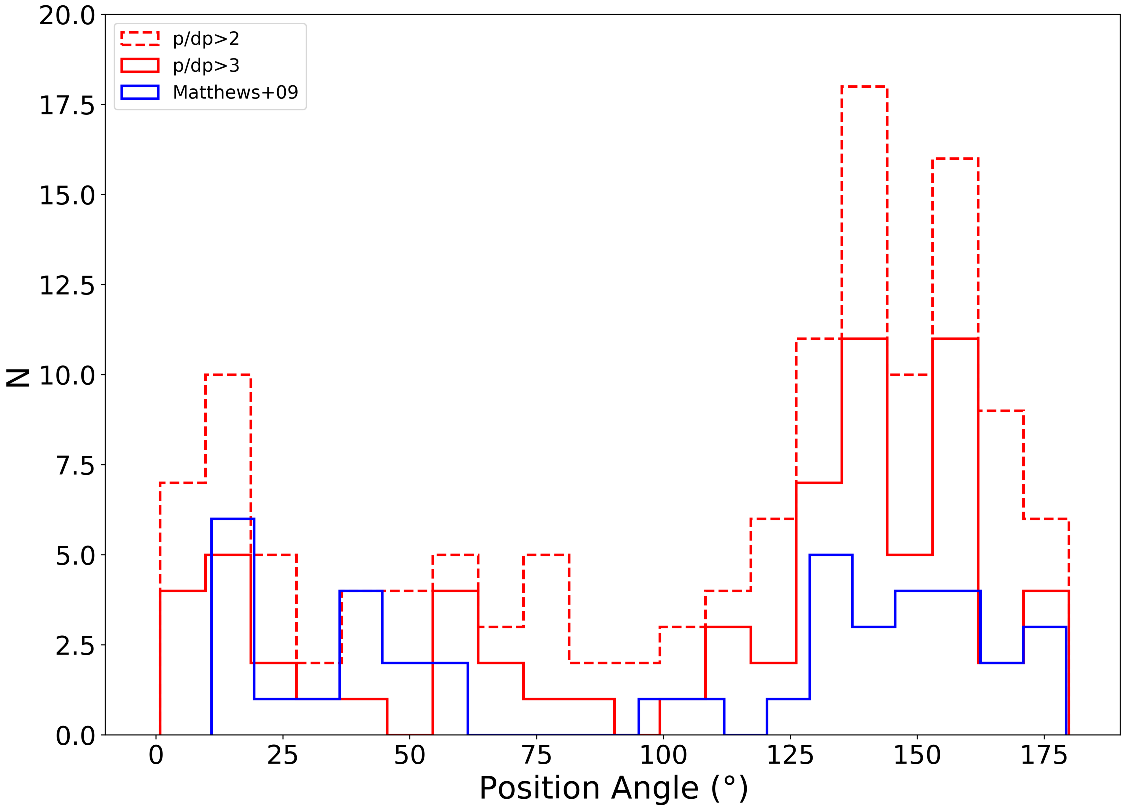

Figure 3.7: The distribution of the position angles of polarization half-vectors rotated by 90° to infer the magnetic field orientation. The dashed line distribution has a S/N cut of $I/\delta_I > 10$ and $p/\delta_p > 2$. The solid red line distribution has a stricter $p/\delta_p > 3$ S/N cut applied. The B-field position angle distribution from Matthews et al. (2009) are plotted in blue. The vector populations between the two S/N cuts appear consistent and they also agree with the previous SCUPOL (Matthews et al., 2009) observations (see Section 3.3.5 for the two K-S tests). This suggests that the lower S/N vectors still trace the magnetic field.

As can be seen in Figure 3.7, there is no clear single morphology of the magnetic field and it instead must be considered as either randomized or a multiple-component field. There is a rather distinct peak around 150° with then more random distribution of angles towards the lower magnetic field polarization angles. Some of this distribution at lower polarization angles is smaller structured field components in other parts of the molecular cloud, such as a component at around 60° in the dense core. As will be discussed later in Section 3.4.2, we suspect that the magnetic field is partially influenced by the CO outflow from RNO 91. This was discussed as well in Ward-Thompson et al. (2000) where they suggested the western edge of the field they observed was being influenced by RNO 91. With the more sensitive POL-2 observations and a larger FOV, we can actually see the overlap of the CO emission with some of the magnetic field vectors.

We split the magnetic field inferred from the 850 μm polarized emission of L43 into three parts, the two labeled regions seen in Figure 3.8 and then the magnetic field vectors which spatially (in the plane-of-sky) overlap with the CO outflow or are nearby and follow the same orientation. We list the mean field orientation, $\langle\theta_{\mathrm{B}}\rangle$, and standard deviation from a Gaussian fit of the magnetic field position angle distributions in Table 3.2. Regions 1 and 2 show different magnetic field orientations, although both are rather scattered. Region 2 which corresponds to the northern half of the starless core has a magnetic field that has an average orientation of 63° E of N which is roughly parallel to the filament (≈67°) and *Planck* magnetic field orientations (≈60°). It also lies roughly perpendicular to the local core elongation axis which is something seen across starless and prestellar cores (see Pattle et al., 2023, for a recent review). This is further discussed in the context of the region's evolution in Section 3.4.3. There is more scatter towards the center of the region, which is what causes the spread we see in the position angles, but the structured component can be seen on either side.

Region 1 has a slightly more coherent magnetic field structure that is orientated $\approx$140° E of N, nearly perpendicular to the filament direction and parallel to the CO outflow. Considering it is still near to the CO outflow and is a less dense region, the magnetic field could still be influenced by the CO outflow, or we are simply seeing another component of the complex magnetic field. The mean field orientation of the vectors spatially overlapping with the CO outflow is 146° which is well aligned with the outflow direction which we have taken to be $\sim$150$\pm$10° due to it curving slightly.

We also detect a few B-field vectors in the dust envelope of RNO 90 and in a very diffuse 'blob', isolated to the west. RNO 90 is shown in the inset of Figure 3.8 and the magnetic field is orientated roughly north-south. The magnetic field in the diffuse blob to the west appears to still follow the large-scale *Planck* field, something that has been seen in diffuse cores (Ward-Thompson et al., 2023) and other isolated starless cores (L1689B, Pattle et al., 2021). The fact that this more diffuse region still follows the *Planck* field while Region 1 does not suggests that Region 1 may indeed be, or have been, affected by the outflow.

3.3.6 Magnetic Field Strength

We estimated the magnetic field strength in L43 using the Davis-Chandrasekhar-Fermi (DCF) method (Davis, 1951; Chandrasekhar & Fermi, 1953). The DCF method (see Eq. 3.7) assumes that the geometry of the mean magnetic field is uniform in each region. It then assumes that deviations from this uniformity are Alfvénic such that the deviations are due to non-thermal gas motions. The Alfvénic Mach number of the gas (see Section 1.4) is given by

$$\mathcal{M}_{\mathrm{A}} = \frac{\sigma_{\mathrm{NT}}}{v_{\mathrm{A}}} = \frac{\sigma_{\theta}}{Q} \, , \tag{3.5}$$

where the non-thermal deviations are quantified by a dispersion in magnetic field position angles, σ_θ. $\sigma_{\rm NT}$ is the one-dimensional non-thermal velocity dispersion of the gas and Q is a correction factor that accounts for variations of the magnetic field on scales smaller than the beam and along the line-of-sight where 0< Q <1 (Ostriker, Stone & Gammie, 2001). $v_{\rm A}$ is the Alfvén velocity of the magnetic field, which is given by Equation 1.7. Rearranging Equation 3.5 and using the definition for Alfvén velocity from Equation 1.7,

$$v_{\rm A} = Q\frac{\sigma_{\rm NT}}{\sigma_\theta} = \frac{B}{\sqrt{4\pi\rho}} \ , \tag{3.6}$$

where B is the magnetic field strength and ρ is the gas density. Since the dispersion in position angles, σ_θ, is for plane-of-sky (POS) observations we can only calculate the plane-of-sky magnetic field strength, B_{pos}, which is then given by

$$B_{pos} \approx Q\sqrt{4\pi\rho}\frac{\sigma_{\rm NT}}{\sigma_\theta} \tag{3.7}$$

This can then be simplified to

$$B_{\rm pos}(\mu{\rm G}) \approx 18.6\,{\rm Q}\sqrt{{\rm n(H_2)(cm^{-3})}}\frac{\Delta {\rm v_{NT}(km\,s^{-1})}}{\sigma_\theta({\rm degree})} \tag{3.8}$$

Typically Q is taken to be 0.5 (see Ostriker, Stone & Gammie, 2001; Crutcher et al., 2004) but we will consider a range of Q values, 0.28< Q <0.62 from Liu, Zhang & Qiu (2022) (see their Table 3) to obtain upper and lower limits of the B-field strength. Then $n({\rm H_2})$ is the volume density of molecular hydrogen where $n({\rm H_2})$=$\rho/\mu_{\rm H_2}m_{\rm H}$ and $\mu_{\rm H_2}$=2.8 and $m_{\rm H}$ is the mass of hydrogen. Δ $\rm v_{NT}$ is the FWHM of the non-thermal gas velocity calculated by $\Delta\ {\rm v_{NT}} = \sigma_{\rm NT}\sqrt{8{\rm ln}2}$. As mentioned above, σ_θ is the dispersion of the position angles of the magnetic field vectors, which we calculated using an angular dispersion function as discussed later in this section. It should be noted that Crutcher et al. (2004) finds on average $B_{pos}/B \approx \pi/4$, but since this is a general statistical correction, we do not use this when calculating the magnetic field strength. This method of calculating the magnetic field strength has been found to generally overestimate the field strength, but without direct Zeeman measurements, it is currently thought to be the best option when using dust polarization measurements.

We can then rewrite Equations 3.5 and 3.6 as

$$\mathcal{M}_{\mathrm{A}} = 1.74 \times 10^{-2}\sqrt{2}\,\frac{\sigma_\theta(\mathrm{degree})}{Q}\ , \tag{3.9}$$

and

$$v_{\mathrm{A}}(\mathrm{km\,s^{-1}}) = 24.2\mathrm{Q}\,\sqrt{2}\,\frac{\Delta \mathrm{v_{NT}}(\mathrm{km\,s^{-1}})}{\sigma_\theta(\mathrm{degree})}\ , \tag{3.10}$$

respectively. We have also included a $\sqrt{2}$ factor in Equations 3.9 and 3.10 which is suggested by Heiles & Troland (2005) to account for the velocity line width assumptions, specifically converting the 1-D line-of-sight velocity measurements to an approximate value suitable for estimating the POS magnetic field strength.

We calculated the magnetic field strength in Regions 1 and 2 (shown in Fig. 3.8) using Equation 3.8. We treated the regions as ellipses with semi-major and semi-minor axes a and b (see Table 3.2), and assumed the depth of those regions to be the geometric mean, $c = \sqrt{ab}$. We used column density values from Figure 3.4 to calculate the volume density, n(H_2), in each region. We used N_2H^+ (1-0) velocity line profiles from Caselli et al. (2002a), which have a resolution of $\sim$0.063 km s^{-1}. We corrected them to account for the thermal component (since Eq. 3.8 uses non-thermal velocity line widths) which was calculated using the excitation temperature, T_{ex}=7±1 K (also from Caselli et al., 2002a), giving 0.35±0.02 km s^{-1}. It should be noted, the velocity line profile observations are from the main starless core (Region 1). These observations do not necessarily extend to Region 2, but we do not have observations of Region 2 specifically so elect to use the same line width value as Region 1. Line widths of other tracers in the main starless core vary with some larger than and some smaller than the 0.35 km s^{-1} value we use (see Chen et al.,

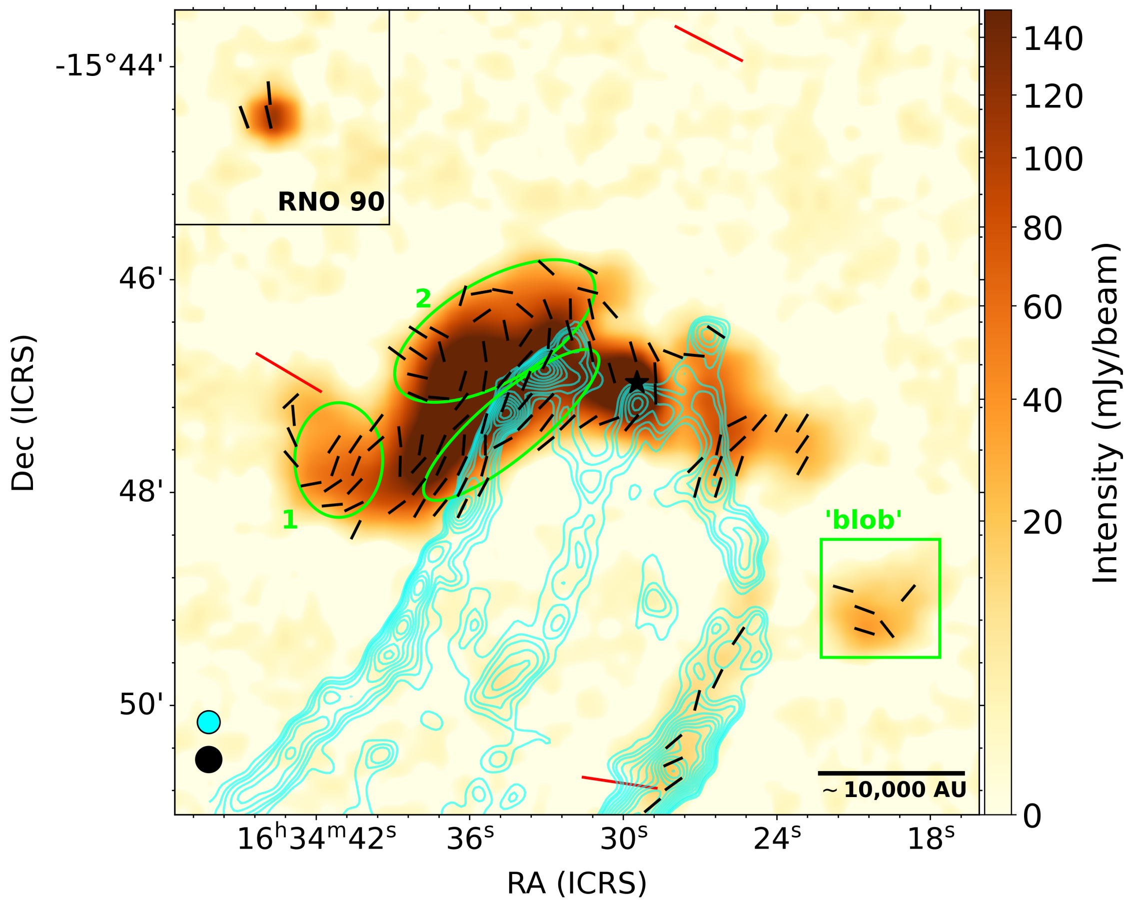

Figure 3.8: Magnetic field half-vectors are plotted in black with a uniform length over the 850 μm dust emission map. Planck vectors are the larger red vectors. The CO outflow continuum discussed in Sec. 3.3.2 is plotted with blue contours. Regions 1 and 2 are labeled and the ellipses drawn are listed in Table 3.2. The third ellipse shows the area of the cloud we used to calculate column and volume densities for the outflow vectors. We also label the dust 'blob' to the west and RNO 90 is shown in the upper left corner. The BIMA and JCMT beam sizes are shown in the lower left in blue and black respectively.

2009), but N_2H^+ (1-0) traces dense regions of molecular clouds which should coincide with the depths we are observing at 850 μm as well. There are also NH_3 observations of the starless core from Jijina, Myers & Adams (1999) and Fehér et al. (2022), with a spread of line width values from 0.273 km s^{-1} (HFS fitting from Fehér et al., 2022) to 0.718 km s^{-1} (Gaussian fitting from Fehér et al., 2022) and then 0.32 km s^{-1} (Jijina, Myers & Adams, 1999). Considering the largest line width, the B-field strength could be up to two times larger.

We determined the dispersion of position angles in each region using the angular dispersion function (Hildebrand et al., 2009, see their Equations 1 and 3). This assumes that there is a large-scale structured field and a smaller turbulent or random component. We assume that the length scales we are observing with JCMT/POL-2 (ℓ) are greater than the turbulent correlation length and much smaller than the large-scale field (such as Planck). While the former statement may be more difficult to accurately determine, the latter is true in our situation as we see a very structured large-scale B-field from Planck (see Fig. 3.2) with no variations in the region we are looking at (admittedly a single Planck beam nearly covers the whole region). The contribution of both the turbulent and large-scale components to the angular dispersion of B-field vectors $\langle\Delta\Phi^2(\ell)\rangle^{1/2}$ is given by the terms b and $m\ell$ respectively and the relation (Hildebrand et al., 2009),

$$\langle\Delta\Phi^2(\ell)\rangle_{tot} \simeq b^2 + m^2\ell^2 + \delta_\theta^2(\ell) \ , \tag{3.11}$$

where $\delta_\theta^2(\ell)$ is the additional contribution to the dispersion from measurement uncertainties (see Eq. 2.13). In each region we calculated $\langle\Delta\Phi^2(\ell)\rangle_{tot}$ and then fit Eq. 3.11 to determine values for m and b. The plots are seen in Fig. 3.10 where the best-fit parameters are shown as well. In all three regions, limiting the fitting to the first 3 bins (36″) provides the best fit (as determined by χ^2 <1), though for the outflow region, extending the fit to 48″ still provided χ^2 <1. For this region we

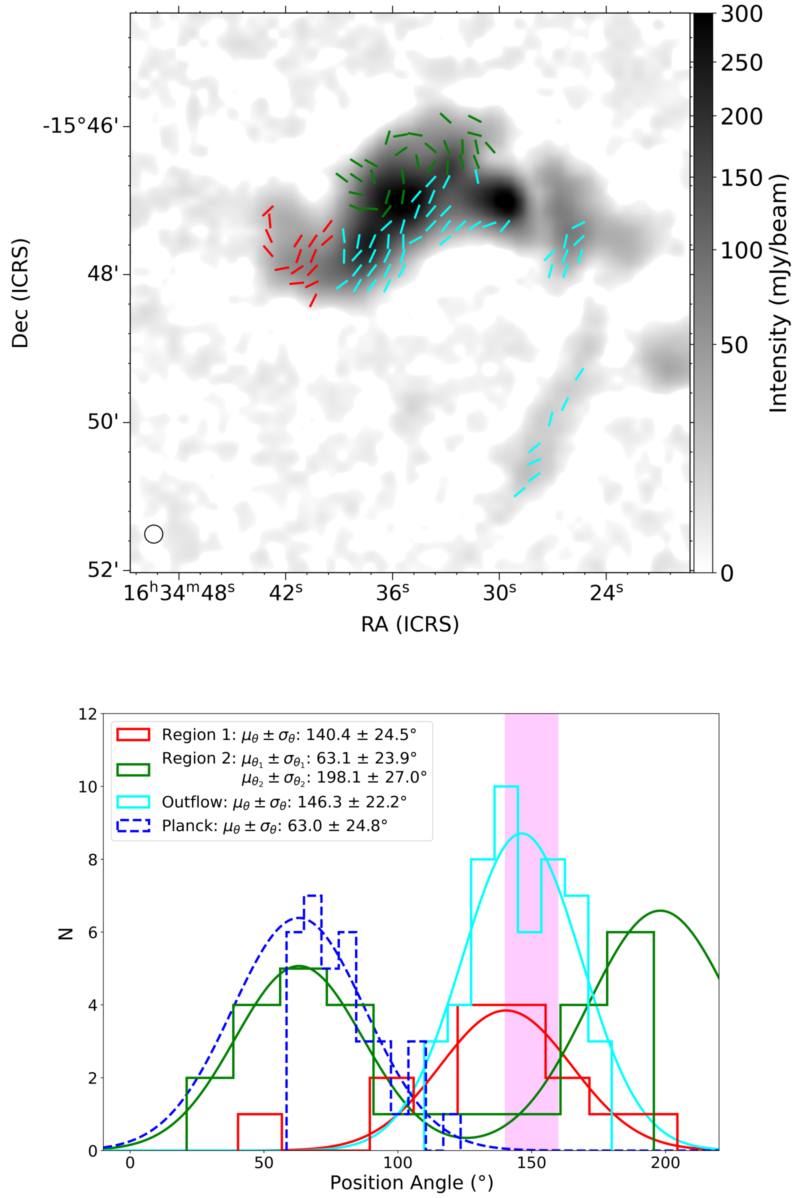

Figure 3.9: *Upper:* The magnetic field vectors are plotted as uniform length lines with different colors corresponding to the different regions identified in Figure 3.8. The cyan vectors are those overlapping with the outflow, the red vectors correspond to Region 1 and the green vectors with Region 2. *Lower:* A histogram showing the distribution of the vector position angles shown in the different regions in the upper image. The colors match the same regions as above. The Planck vectors are plotted as a dark blue peak. The outflow orientation is shown as a purple region centered at ∼150 with a width of ±10° due to the curve. When a Gaussian is fit to the distribution, the mean and standard deviation are given in the legend.

then take the mean of the b values from both fits (14.2 for $36''$ and 13.7 for $48''$) to get $b \approx 14.0 \pm 1.5$. Generally we see the dispersion slowly increase with distance (Hildebrand et al., 2009; Hwang et al., 2023, and see top panel of Fig. 3.10) but in the bottom two panels of Fig. 3.10 we see the dispersion growing and then at a large distance, suddenly drop again. In the case of Region 2 (bottom panel of Fig. 3.10) the distance this happens at, $\sim 120''$, is the distance between the two structured components mentioned in Sec. 3.3.5, further justifying a structured field approximately oriented at 56° and parallel with the Planck field and the filament direction. The dispersion in magnetic field position angles, σ_θ, can then be calculated by

$$\sigma_\theta = \frac{b}{\sqrt{2 - b^2}} \frac{180^o}{\pi} \ , \tag{3.12}$$

where b (in radians) is found from the angular dispersion function fit (see Hildebrand et al., 2009, and Fig 3.10).

The magnetic field strength in Regions 1 and 2 is ~40–90 μG and ~70–160 μG respectively. All the values calculated when considering the magnetic field strength are listed in Table 3.2. In our situation, the difference in magnetic field strength between regions is due to variations in density and angular dispersion of the vectors since we use a constant velocity line width value across the region. For example, despite the larger σ_θ in Region 2, it is also denser which is what increases the magnetic field strength and makes it comparable, if not greater than, the magnetic field in Region 1. We calculate an upper and lower bound for each of our magnetic field strengths based on the variation in Q of $0.28 < Q < 0.62$ (Liu, Zhang & Qiu, 2022). The value in Region 2 is approximately that found by Crutcher et al. (2004), although they treated the region as a sphere and had a smaller dispersion angle of 12°. We find a slightly larger column and volume density, by a factor of ~1.3.

The magnetic field strength calculated for the outflow is ~120-260 μG. However, we note that this value may be severely overestimated and its use for interpretation

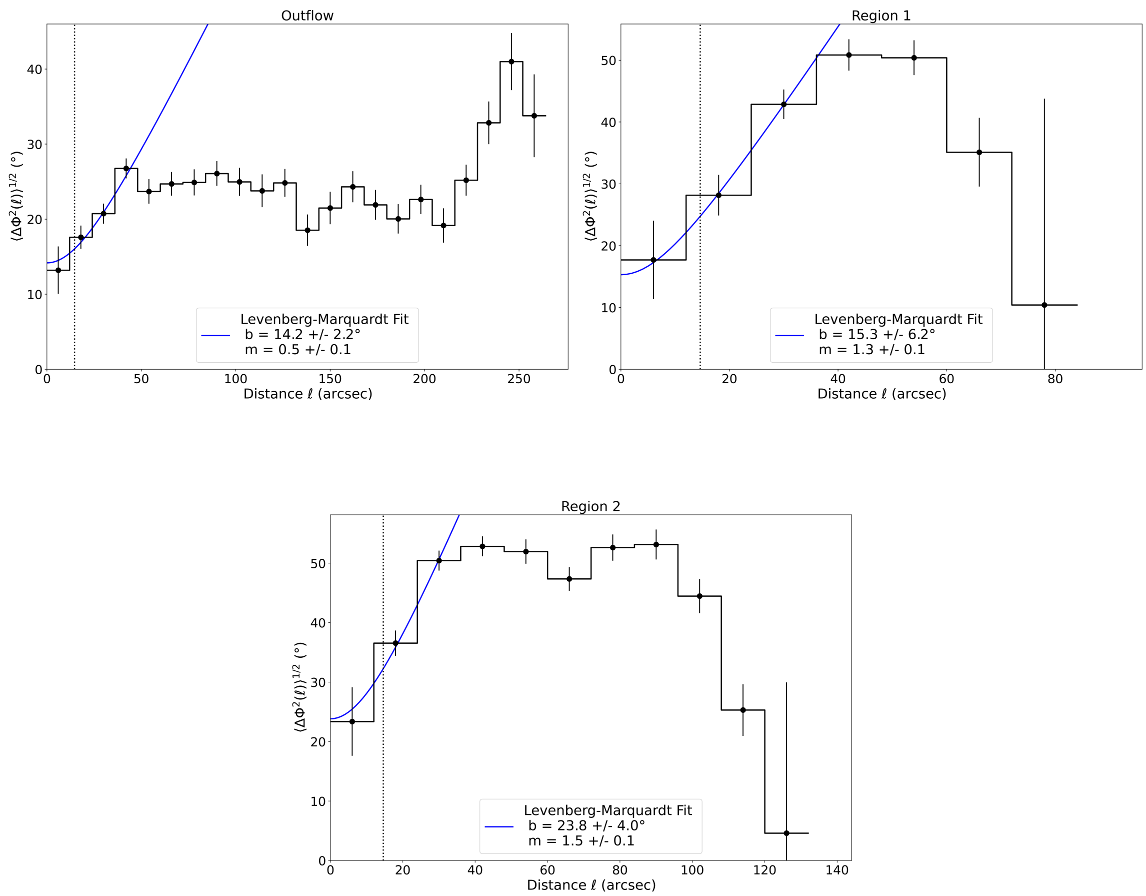

Figure 3.10: The angular dispersion function (ADF) histograms for various regions of interest in L43. All plots show fitting results when limiting the fit to the first three bins (36″). All fits were optimized with the Levenberg-Marquardt method and are weighted by the errors. Best-fit parameters are shown in the legend where b and m are from Eq 3.11. The JCMT beam size is plotted as a vertical dotted line in all three plots. *Top:* ADF results for the vectors spatially associated and aligned with the outflow. *Middle:* ADF results for vectors in Region 1 (see Fig. 3.8). *Bottom:* ADF results for vectors in Region 2 (see Fig. 3.8).

limited. This is because we do not generally apply the DCF method to regions interacting with outflows since we assume the deviations in the magnetic field to be small non-thermal gas motions in the region and an outflow is a much stronger disruptive force. In our case, we are arguing that some of the dense gas and dust has been affected by the outflow and hence that the outflow may have dragged the field (which is flux-frozen into the gas), aligning it with the outflow walls and giving us the low position angle dispersion. In that case, the low position angle dispersion may be due to a strong outflow rather than a strong field; although this would require more outflow modelling to determine if the outflow would preferentially align and order the field, or disorder the field. Additionally, we consider all the vectors spatially aligned with the outflow, but take just the dust density in the southern half of the L43 starless core. If we were to assume a much lower volume density, one that is more likely associated with outflow material, then our field strength would be lower.

We acknowledge the limitations of using the DCF method, especially when determining the position angle dispersion and acknowledge in such a low S/N environment, these uncertainties are increased. However, we do find magnetic field strengths that are on the order of strengths seen in other starless cores (Pattle et al., 2021; Karoly et al., 2020), including values which agree within error with those found in Crutcher et al. (2004).

3.4 Discussion

3.4.1 Contribution of the Magnetic Field

The mass-to-flux ratio λ (see Section 1.4) was estimated to quantify the importance of magnetic fields relative to gravity (Crutcher, 2004). It compares the critical value for the mass which can be supported by the magnetic flux to the observed mass and flux values. We have inferred the molecular hydrogen column density from dust flux

Table 3.2: DCF+ADF values of L43

Region	Outflow	Reg 1	Reg 2
$\langle\theta_B\rangle^a$ (°)	146(22)	140(25)	63(24)
RA (J2000)	16:34:34.9	16:34:41.7	16:34:35.6
DEC (J2000)	-15:47:30.0	-15:47:49.8	-15:46:37.1
a ($''$)	62.9	32.3	63.0
b ($''$)	17.4	24.8	28.8
PA^b (°)	130	0	120
c ($''$)	33.1	25.7	42.6
$N(H_2)$ ($\times 10^{21}$ cm^{-2})	33.0(7.0)	4.0(1.0)	52.0(9.0)
$n(H_2)$ ($\times 10^5$ cm^{-3})	4.0(0.9)	0.57(0.15)	4.9(0.8)
Δv_{NT} ^{c} (km s^{-1})	0.35(0.02)	0.35(0.02)	0.35(0.02)
b (°)	14.0(1.5)	15.3(6.2)	23.8(4.0)
σ_θ (°)	10.1(1.1)	11.0(4.5)	17.6(3.0)
B_{pos} (μG)	116(20) – 257(42)	40(17) – 88(38)	73(14) – 162(32)
$\mathcal{M}_A$	0.4(0.04) – 0.9(0.1)	0.4(0.2) – 1.0(0.4)	0.7(0.1) – 1.6(0.3)
v_A (km s^{-1})	0.3(0.04) – 0.7(0.1)	0.3(0.1) – 0.7(0.3)	0.2(0.03) – 0.4(0.1)
λ	-	0.3(0.2) – 0.8(0.4)	2.4(0.6) – 5.4(1.4)
E_B ($\times 10^{35}$ J)	0.5(0.2) – 2.6(0.9)	–	0.5(0.2) – 2.2(0.9)

a. Standard deviation of the Gaussian fit is in parentheses

b. PA of ellipses is counter-clockwise from North

c. Δv_{NT} values from Caselli et al. (2002a) observations and inferred magnetic field strength values from dust polarization and so can calculate the mass-to-flux ratios for the cores.

Using Equation 1.6, we calculate the mass-to-flux ratio to be 0.3–0.8 in the low-density periphery of the core, Region 1. We calculate a mass-to-flux ratio of 2.4–5.4 in the denser part of the core, Region 2. According to Crutcher (2004) these ratios can be overestimated due to geometric biases and they suggest it can be overestimated by a factor up to 3, although it is a statistical correction and its application to individual measurements is unclear. If we consider this statistical correction, the mass-to-flux ratios are ∼0.1–0.3 and ∼0.8-1.8 in Regions 1 and 2 respectively. These are then the lower limits for the mass-to-flux ratio in each region.

We also get Alfvén Mach numbers of 0.4–1.0 and 0.7–1.6 for Regions 1 and 2 respectively, suggesting that both regions are roughly trans-critical and magnetic field and turbulence may play equal parts in support. As noted previously, the velocity information we are using is for the main starless core which is near Region 2, but further from Region 1 which is the low-density area on the periphery of the main dense core, and it does not resolve individual parts of the molecular cloud. We also find Alfvén velocities in the range of 0.2–0.7 $\mathrm{km\,s^{-1}}$ throughout the cloud.

For the lower-density Region 1, the region is entirely magnetically sub-critical indicating that the region may still be sufficiently supported against gravitational collapse by the magnetic field. It is also slightly sub-Alfvénic, meaning the magnetic field may play the dominant role. In the denser Region 2, we obtain a more definitively supercritical mass-to-flux ratio (it should be noted the large uncertainties with this value, as well as the results of the statistical correction), with a lower limit approaching trans- to sub-critical. This gradient of a sub-critical envelope (Region 1) transitioning into a trans- to super-critical core (Region 2) at sufficient densities is described in Crutcher (2004). It does suggest that the magnetic field is not sufficiently strong to support against gravitational collapse in the main starless core. However, it is worth mentioning that there are still many other processes in the molecular cloud such as turbulence and the influence of the CO outflow that could prevent gravitational collapse into a stellar object. While we do not yet see a protostar forming, as mentioned in Section 3.3.1, we do see some possible fragmentation within the starless core where the densest part may be undergoing gravitational collapse.

Myers (2017) suggested from modelling that L43 has formed all of the stars it will form in its lifetime and does not contain sufficient amounts of dense gas for further star formation. However we find higher column density values than they use for their modelling and do see potential fragmentation in the core. Chen et al. (2009) finds that the main L43 starless core has observed DCO^+ and HCO^+ abundances that are higher and lower than modeled abundances respectively for an assumed amount of CO depletion. They suggest this indicates more CO depletion in the core and that the L43 starless core is spending a longer time at the higher density pre-protostellar core phase. If this is the case, additional supports such as turbulence may be needed to continue support against gravitational collapse in Region 2 since it seems to be moving beyond the stage where magnetic fields are critical. But findings of Region 2 in near equilibrium (within errors) also validates the long-lived age of the core that Chen et al. (2009) finds. The local magnetic field appears to still be significant in the more diffuse Region 1, but this region is beyond the area considered by Chen et al. (2009). Additionally, we must consider that the CO outflow has potentially altered the structure of the magnetic field in the cloud, even within the starless core, potentially weakening or strengthening the field.

3.4.1.1 Transition between magnetically- to matter-dominated material

In addition to consideration of the mass-to-flux ratio, the general relation between matter and magnetic dominated material outlined in Section 1.2.3 can be considered. As previously mentioned, on the large, filament-scale the orientation of the magnetic field relative to the filament transitions from parallel to perpendicular at a threshold density (Soler et al., 2013; Planck Collaboration et al., 2016b). Within the Ophiuchus region, the transition is thought to happen at $\sim 5\times10^{22}$ cm^{-2} (Planck Collaboration et al., 2016b), suggesting a dynamically important magnetic field on large scales up to this threshold column density. A global magnetic field strength in the region is given as 13-25 μG (derived with magnetic fields observed by Planck and the DCF method in Planck Collaboration et al., 2016b). We can see from Figure 3.2 that the large-scale field is parallel to the filamentary structure, despite densities in the main L43 core reaching up to that $\sim 5\times10^{22}$ cm^{-2} threshold.

On the cloud–core scale, there is a similar transition threshold, where the critical column density of the transition between magnetically- to matter-dominated phase can be calculated. This transition is when the cloud becomes gravitationally bound and begins to contract. This was first theorized by Mestel (1965, see his equation 85) where a relatively idealised case of a uniform magnetic field threading a uniform density cloud is considered, and the prediction of the relation between the critical surface density, Σ_c, and the magnetic field strength, B, at which the transition occurs, takes the form

$$\Sigma_c \,=\, (5/G)^{1/2}\,(B/3\pi) \tag{3.13}$$

which yields

$$[N(\mathrm{H}_2)/\mathrm{cm}^{-2}] \,\simeq\, 2\times10^{20}\,\times\,[B/\mu G]\,, \tag{3.14}$$

where N(H_2) is the H_2 column density. While an approximation, this equation provides a useful theoretical order-of-magnitude prediction.

In the magnetically-dominated phase, the material will mostly follow the magnetic field lines rather than alter them, i.e. flow along the field lines (though some material will still flow through). So in a cloud which is still magnetically-dominated, e.g. young, not yet dense enough or has a strong B-field, the local magnetic field may still trace the large-scale field. Then once the core or cloud has become sufficiently dense, it will start to alter the magnetic field. This has been seen in Ward-Thompson et al. (2023) and will be discussed further in Chapters 4 and 6.

In L43, the large-scale magnetic field is parallel to the filament (see Figure 3.2 and also Figure 3.1 for the whole region). In Figure 3.8, the 'blob' can be seen in the lower right of the image and the magnetic field vectors there, although only four of them, continue to trace the large-scale field. In addition, the lower plot of Figure 3.9 shows that there is a population of vectors in Region 2 which follow the Planck field orientation. In the upper plot of the same figure, those vectors can be seen on the periphery of the dense core, in the more diffuse regions. Meanwhile, in Region 1, which is similarly diffuse, the magnetic field appears to be perpendicular to the large-scale field.

We can use the column density map from Section 3.3.3 to estimate the column density in these regions. In the 'blob,' the upper periphery of Region 2, and then Region 1, the column density values are $\sim 1.4{\times}10^{21}$, $6{\times}10^{21}$ and $4{\times}10^{21}$ cm^{-2} respectively. All of these values are less than the transition density found by Planck Collaboration et al. (2016b). As mentioned above, in two of those cases, the field still traces the large scale field, but in Region 1, it is nearly perpendicular, suggesting that, as mentioned in Section 3.3.5, it may have been influenced by the nearby outflow. The upper edge of Region 2 is shielded from the outflow by the dense core and the 'blob' is far enough away.

The dense part of Region 2 which gives the second peak seen in the upper panel of Figure 3.9 has a column density of $\sim 5{\times}10^{22}$ cm^{-2} which is closer to the transition column density from Planck Collaboration et al. (2016b) and may indicate that the core of L43 has moved towards becoming matter-dominated. This would agree with Section 3.4.1 where Region 2 is magnetically super-critical towards the center but sub-critical in the lower density Region 1. However, each of these conclusions are using the Planck findings which is for the large-scale field and large-scale structure. It will be interesting to consider if this relationship is traced down to smaller scales and to investigate the relation to magnetic field strength.

If we use Equation 3.14 and substitute in the above column densities as the critical column densities, we get magnetic field strengths of 7, 30 and 20 μG in the 'blob,' the upper periphery of Region 2, and then Region 1. We would expect the 'blob' and the upper periphery of Region 2 to be near (but below) critical column densities because their magnetic fields still match the large-scale field. Region 1 has a different field orientation and would be a post-critical column density, but can be used to set a limit. Any field strength lower than these values would indicate the structure was gravitationally bound (if considering only magnetic field and gravity). Field strengths higher than this would suggest that the areas are not yet gravitationally bound and we might expect the magnetic field to still follow the large-scale structure, i.e. the flowing material is flowing preferentially along the lines and not across them due to contraction.

The magnetic field strength for Region 2 was calculated to be 73–162 μG, while for Region 1 it was 40–88 μG. In the case of Region 2, this calculation was done using a column density of 5×10^{22} cm^{-2}. If instead we use the above mentioned 6×10^{21} cm^{-2} for the periphery, we still get B=25–55 μG in Region 2. For the 'blob' we can consider the large-scale magnetic field strength which was 13-25 μG. In both of these regions, the field strength is roughly equal to or greater than the field strengths derived from the assumed critical densities. In addition, the column density in the core of Region 2 is $\sim8\times10^{22}$ cm^{-2} which yields a critical field strength of 400 μG from Equation 3.14. The calculated magnetic field strength in the core is nearly three times smaller which suggests that the core could be gravitationally bound and collapsing. As mentioned in Section 3.3.1, the main core does appear to have fragmented and from Section 3.4.1 it is magnetically super-critical, both of which would further support the conclusion of being gravitationally bound and collapsing.

Region 1 has a larger magnetic field strength than the critical value calculated from Equation 3.14 but the local field is nearly perpendicular to the large-scale field. We hypothesize two possible explanations for this:

1. As mentioned above it could be affected by the outflow which explains the magnetic field orientation being perpendicular to the large-scale field.

2. There is not a global, or even cloud-scale relation and the diffuse Region 1 may have transitioned to matter-dominated despite the envelope of Region 2 not transitioning. However, this somewhat contradicts the findings of Crutcher (2004).

We believe the first explanation is the most likely because of the very similar orientation to the outflow and the belief that the outflow does influence the rest of the L43 cloud, something which is discussed more in the next section. In addition, the region is at a very low density and unlikely to be collapsing to the point of rotating the magnetic field by nearly 90°.

Because the Planck magnetic field is parallel to the large scale structure and the column density of the structure is in general $<5\times10^{22}$, this isolated L43 filament appears to follow the general Ophiuchus trend. In addition, it appears that the L43 cloud follows the predicted critical column density of being gravitational bound as first suggested by Mestel (1965).

3.4.2 Interaction of the Magnetic Field with the Outflow

The spatial alignment (in the plane of sky) of the magnetic field in L43 with the outflow cavity walls can be seen in Figure 3.8, where the cyan outflow spatially overlaps with many of the magnetic field vectors. The magnetic field vectors that coincide with the CO outflow show a uniform distribution and strong peak at 146°. This coincides well with the outflow direction which we have taken to be ∼150±10° due to it curving slightly.

Weintraub et al. (1994) suggested that RNO 91 sits in the foreground of the general L43 molecular cloud and so the possibility exists that there is in fact no physical association between the magnetic field and outflow. However, as was mentioned in Sec. 3.3.1 and as can be clearly seen in Figure 3.2, the outflow appears to have carved a cavity out of the molecular cloud, indicating it is to some degree embedded. This was also suggested by Mathieu et al. (1988).

Alternatively, we may be tracing magnetic fields in the outflow cavity walls. In this case, as mentioned in Section 3.3.3, some of the Stokes I emission we see, especially in the regions coincident with the outflow cavity walls, may be CO features (Drabek et al., 2012), especially the isolated emission to the south of the main cloud. We expect some contribution to the measured Stokes I emission from CO but such contributions are typically less than 20% of the total emission observed (Drabek et al., 2012; Pattle et al., 2015; Coudé et al., 2016) and in our case, we see contributions of ∼5–15%. However, considering we do have some CO contribution, we cannot rule out the possibility that some fraction of the polarized emission in this region arises from CO polarization, polarized through the Goldreich-Kylafis effect (Goldreich & Kylafis, 1981, 1982). This would add a further ± 90° ambiguity on the magnetic field orientation.

On the other hand, we can assume the polarization and emission is not purely CO based as the emission features are also seen in all of the *Herschel* bands and persist after CO subtraction in 850 μm, indicating that there is a real dust feature present. A similar "hollow shell" morphology of dust emission in the presence of outflows is discussed in Moriarty-Schieven et al. (2006). Additionally, Bence et al. (1998) suggests that the mere presence of CO suggests some amount of dust shielding (from the UV field) in the outflow region. So we still consider it probable that we are tracing dust polarization in the outflow cavity walls.

Additionally, the relationship between magnetic fields with outflows has been observed on numerous occasions in other sources, on both JCMT and ALMA scales (see Hull et al. 2017; Hull et al. 2020). Hull et al. (2017), Hull et al. (2020) and Pattle et al. (2022) also see a similar alignment between the magnetic field and the cavity wall of the outflow to that which we see in L43/RNO 91. The benefit of our larger field of view here, when compared to ALMA, is that we can compare the magnetic field of the outflow to that in the surrounding regions and see that there is not just a preferential direction northwest to southeast, but rather that the magnetic field in the outflow region is actually different to that in the rest of the cloud. It should be noted that in regions observed by the JCMT, a preferred misalignment of 15–35° (this possibly increases to 50±15° when considering projection effects) between magnetic fields and outflows has previously been identified in a larger statistical sample (Yen et al., 2021). The outflow observations in that study are largely on envelope- or small-scales (i.e. tens of arcseconds) rather than large-scale outflows like we see here. So while there is a statistically preferred misalignment between magnetic fields as observed by JCMT and outflows, we do see a clear indication of this occurring in L43 but rather see good alignment between outflow and magnetic fields. This is perhaps because we have such distinct large-scale cavity outflow walls which is what JCMT may be preferentially tracing. RNO 91 would also be interesting to follow up with ALMA polarization observations since there are smaller scale outflows in the envelope as well (Lee & Ho, 2005; Arce & Sargent, 2006). This could be more directly compared to observations by Hull et al. (2017) and Hull et al. (2020) and to the statistical sample in Yen et al. (2021).

In RNO 91, the CO outflow was found to have a lower limit of its energy at $\approx 10^{29}$J (Bence et al., 1998). However this assumes a Class II source lifetime when considering how long the CO has been exposed to UV radiation, though a Class I lifetime would still be longer than the un-shielded CO lifetime of a few hundred years (Bence et al., 1998). So the CO outflow likely had a larger energy once and may have been able to influence the magnetic field orientation. Other studies have found the CO outflow energy to be $\sim 5\times10^{35}$J (Myers et al., 1988) and $\sim 1.4\times10^{35}$J (Arce & Sargent, 2006). These values are comparable to the magnetic energy values we see in L43, which is what we would expect. We can calculate the magnetic energy in Region 2 and the outflow region using Equation 1.5. Since we consider the outflow to have affected the dense gas and dust and dragged the magnetic field, we would expect the outflow energy to be at least equal to the magnetic energy. Assuming an ellipsoid shape when calculating the volume of both regions (see Table 3.2 for ellipse parameters), we find magnetic energies of $\approx$0.5–2.5$\times10^{35}$J. This suggests that we can help further place a lower limit on the outflow energy of $\approx$0.5–2.5$\times10^{35}$J, which is comparable to the values stated above, though we do remain cautious of the magnetic field strength derived in the outflow region as mentioned before.

3.4.3 Evolution of this isolated filament

One point of interest in this region is that there is a very clear evolutionary gradient from southwest to northeast. Initially there is the evolved T-Tauri star RNO 90 which is the oldest source and currently has no known large-scale outflows. It has also formed a protostellar disk (Pontoppidan et al., 2010). RNO 91, which is further along the filament, is a protostellar source which drives the now familiar CO outflow. Then finally the starless core sits $\approx$10,000 AU further along the filament.

The orientation of this filament is such that it extends roughly radially away from Sco OB2, with RNO 90 the closest to Sco OB2. The filament sits $\approx$42 pc away from Sco OB2 (in the plane-of-sky) assuming a general distance of 125 pc. While this may be merely a coincidence, it is interesting that the evolutionary track in such an isolated filament starts in the part of the filament pointing directly towards Sco OB2 (in the plane-of-sky). The Ophiuchus region and star formation within has previously been suggested to be shaped and driven by Sco OB2 (Loren, 1989).

Additionally, we can picture two evolutionary scenarios for the starless core, scenarios that with present observations we cannot distinguish between and that may very well be happening at the same time. The starless core L43 has formed with its long axis parallel to the outflow cavity wall. This could suggest that material has been funnelled down the filament which is also parallel with the large-scale Planck field and is building up on the outflow cavity walls. Build-up has not occurred so readily along the western wall of the outflow cavity because there is less material available for accretion to the west since RNO 90 has already been formed. However, it could also be the case that the dense core already existed and fragmented to form both the starless core and RNO 91 and the starless core has now been compressed along the filament orientation by the outflow. It is difficult to differentiate between these two scenarios and the possibility of course remains that they could both be true, with an initial fragmentation that has become denser over time. Kim et al. (2020) does suggest that the starless core is a 'late' or chemically-evolved, starless core as determined by a high $N(\mathrm{DNC})/N(\mathrm{HN^{13}C})$ ratio and line detection in $\mathrm{N_2D^+}$. So the core may have formed at a similar time to RNO 91 but has since had its evolution slightly delayed due to injected turbulence by RNO 91 as well as less readily available material to form a star with.

3.5 Summary

We presented polarization measurements of the infrared dark molecular cloud L43 at 850 μm made using JCMT/POL-2 as part of the JCMT BISTRO Survey. We found H_2 column densities on the order of 10^{22}-10^{23} cm^{-2}, which are typical values in dense starless cores. We measured a power law index of $\sim$ -0.85 when plotting polarization percentage as a function of total 850 μm intensity, indicating a possible decrease, but not complete loss, in grain alignment efficiency, deep within the molecular cloud. By rotating the polarization vectors by 90°, we inferred the magnetic field orientation in L43 and saw a complicated and multiple-component magnetic field.

We divided the magnetic field into three regions, with one region slightly offset from the dense submillimetre-bright core (Region 2), another region in the more diffuse region to the east (Region 1) and then vectors which spatially coincides in the plane of the sky with the CO outflow driven by RNO 91. We saw alignment between the magnetic field and the outflow cavity walls which is distinctly different from the magnetic field in the rest of the cloud. We calculated the magnetic field strengths of $\sim$40$\pm$20 to 90$\pm$40 μG in Region 1 and $\sim$70$\pm$15 to 160$\pm$30 μG in Region 2. We did calculate a magnetic field strength in the outflow region of $\sim$120$\pm$20 to 260$\pm$40 μG but advise caution with interpreting this value. Region 1 appeared to be magnetically sub- or trans-critical and but sub-Alfvénic. This suggested that the magnetic field is still important in comparison to gravity and turbulent motions. Region 2 is both magnetically super-critical and sub- to trans-Alfvénic so the magnetic field may not be playing a significant role. This is compounded by potential fragmentation in the main core, suggesting it could be heading towards forming a protostar. We also proposed an evolutionary gradient across the isolated filament starting with the most evolved source RNO 90 which is closest to the Sco OB2 association and moving away from Sco OB2 towards RNO 91 and then eventually the starless core.

Chapter 4

Magnetic fields in other star-forming regions

4.1 Overview

In this chapter, we present analysis of additional low-mass star-forming regions. The sources presented here (except for L1495A and L183, which I have been second and first author on respectively) have not been published and have all been reduced from the available raw data. To begin with, we introduce the BISTRO-3, and other, prestellar cores and their basic observed properties, including flux comparisons between $4''$ and $8''$ reductions when applicable. Then we will go through each source, introduce it and calculate magnetic field strengths and compare the magnetic field orientations with the large-scale B-field and where important, the core orientation.

Where possible, we take column density and velocity line-width values from published works. Many of these sources were observed as a part of the *Herschel* Gould Belt Survey (André et al., 2010) and we make use of their column density and temperature maps. We mostly use the three main tracers of dense material, NH_3, N_2H^+ and $C^{18}O$ (di Francesco et al., 2007) when measuring the velocity line width. Where possible, we use the structure function (see Section 3.3.6) on the cores. For each of the sources we also calculate Alfvén Mach numbers and the mass-to-flux ratio.

4.2 The Basic Properties of the Prestellar Cores

As can be seen in Figure 4.1, L183, L1544, L1517B and L1498 are all in rather isolated environments, similar to L43 seen in Chapter 3. Figure 4.2 shows the location of many of the objects relative to each other. These are all starless cores but are in varying stages of evolution as will be discussed below. It can be seen in Figure 4.1 that L1495 sits within the larger Taurus Molecular Cloud filament and is therefore a very chaotic environment on the large-scale. From the same figure, L1527 also sits within a more crowded environment on the larger-scale. Of the six sources, L1527 is the only source among these which has an embedded stellar object (an embedded Class 0/I protostar; van't Hoff et al., 2023). While not an extremely large sample size, this variety of pre- to proto-stellar objects (when including L43 as well) cover a range of evolutionary epochs and environments. In Chapter 6, we bring in additional sources from the literature to add to this list.

Luhman (2018) derived a series of distance measurements in the Taurus Molecular Cloud using Gaia DR2 data. Figure 4.2 shows the locations of the stars overlaid on the regions of interest, many of which are included in this chapter. They derive distances of 172, 159 and 128 pc for L1544, L1517B and L1495 respectively. These all agree with the approximate distance to Taurus of ≈140 pc (Roccatagliata et al., 2020) and agrees well with recent Gaia studies of the region (e.g. Gómez de Castro et al., 2024). The distance of L1527 is also determined to be 140 pc from a variety of studies (van't Hoff et al., 2023) and so we generally take the distance to these sources to be 140 pc, including L1498 which is in the Taurus Molecular Cloud complex but has no associated stars to probe distances with by Luhman (2018). The

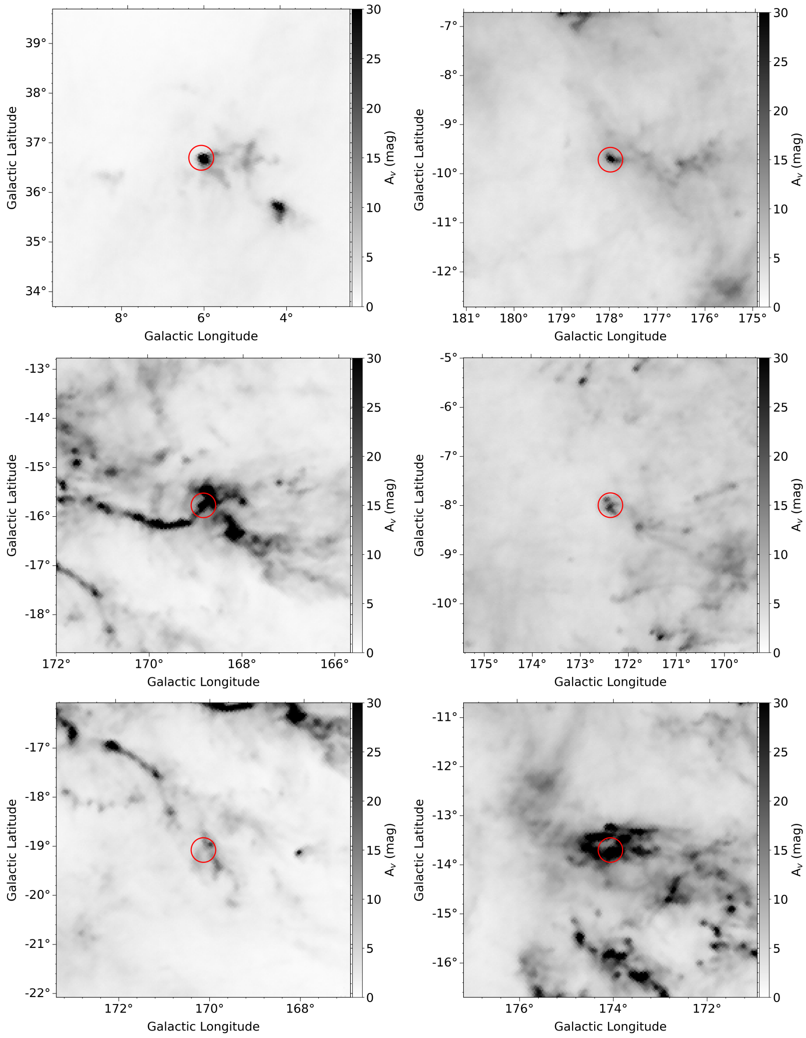

Figure 4.1: Planck A_V maps (Planck Collaboration et al., 2016a) of the various regions of interest. The starless, pre- or proto-stellar core locations are at the center and surrounded by a $15'$ radius red circle. *Upper Row:* L183, L1544 *Middle Row:* L1495, L1517B *Lower Row:* L1498, L1527.

distance to L183 is taken to be 110±10 pc (Franco, 1989).

The list of pre-stellar sources observed as a part of 'BISTRO-3' is shown in Section 2.2.1.1. In addition, we present observations of L1527 and L183, both of which were reduced from raw data that is available on the CADC archive. Figure 4.1 shows the general location of each of these sources using the Planck A_V extinction maps (Planck Collaboration et al., 2016a). It is from these images that we can identify these sources as being a part of a filamentary or isolated system, the first step towards identifying which mode of star formation they belong to (Seo et al., 2019, and see Figure 1.6).

Of the five prestellar cores observed by BISTRO-3, only three have their observations completed. L1495 was completed by BISTRO-3, building on top of BISTRO-2 observations. Then L43 and L1544 have both had all observations completed. L43 was presented in Chapter 3 while L1544 will be presented here. L1517B and L1498 are the two faintest cores and neither are fully observed, but preliminary maps are presented here and preliminary results are discussed.

L1498 was particularly difficult to observe with SCUBA-2/POL-2. Following methods from Lin et al. (2024), we used SCUBA-2 observations performed under Project IDs M21BP045 and M22BP041 to map the intensity of L1498. We then used that SCUBA-2 map as a mask to guide the map-maker towards the area of emission. We recovered some emission, but the signal-to-noise is still very small. L1517B is also a very dim core and so our vectors are rather low signal-to-noise. For the starless cores L1544, L1517B and L1495, we have reduced them using the $8''$ method discussed in Section 2.3.4. The data from L1495 were published by Ward-Thompson et al. (2023).

Table 4.1 lists the observed cores and their map statistics. For each of the cores, we extracted the central $3'$ region where noise is best characterized. None of the cores are large, extended structures and each was centered in the map, so the central

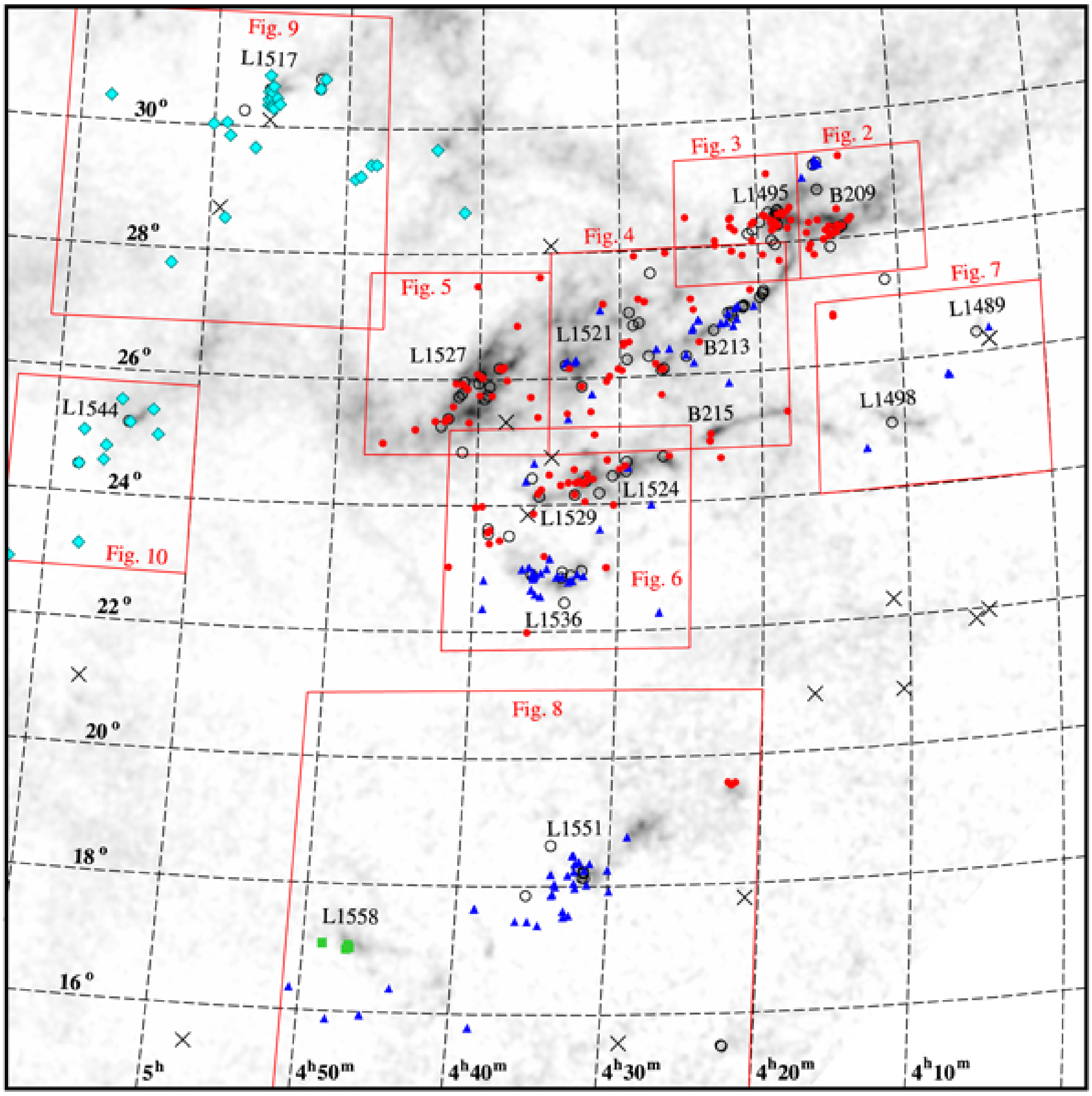

Figure 4.2: From Luhman (2018) showing the locations of many of the objects discussed in this chapter including L1527, L1498, L1495, B213 and L1544.

Source	Completed	Int. Time (hrs.)	4″ RMS (mJy/beam)	8″ RMS (mJy/beam)	8″ Peak FD (mJy/beam)
L1544	27/27	14.1	2.5±0.4	1.7±0.3	188
L1498[a]	9/27	4.7	4.0±0.2	–	35
L183	23/23	16.3[b]	3.1±0.2	1.7±0.1	189
L1517B	13/27	6.8	3.5±0.2	1.9±0.1	40
L1527[a]	9/9	5.0	5.4±0.2	–	900
L1495A	20/20	13.8	2.6±0.4	1.6±0.3	116

Table 4.1: List of the prestellar cores in this chapter and their map characteristics within the central 3′ region. The total integration time, and RMS for both the 4″ and 8″ maps, are given. The RMS values are the mean error value for the central 3′ area with standard deviation as the error. The peak flux density level is given from the 8″ maps.

a. The flux density values are taken from the 4″ map

b. This is a mosaic of 4 fields. Each field was observed for ≈4 hours.

3′ region was sufficient for getting the flux statistics as well. Table 4.1 shows the dependence of the noise level in the maps on pixel size. The noise level for the 8″ maps are lower by roughly a factor of $\sqrt{2}$. Section 2.3.4 predicted it should be lower by a factor of 2 (due to four times as many bolometers in a pixel and variance going as 1/N). If we apply the same factor we observe for the 8″, the noise level for 12″ vector catalogs would then be a factor of $\sqrt{3}$ lower than the 4″ catalogs. The original BISTRO observations wanted to achieve an RMS of 1.5 mJy beam^{-1} for 12″ catalogs, and it appears these prestellar cores have that depth after all observations are completed.

4.3 Magnetic Field Morphologies and Strengths

4.3.1 L1544

L1544 is considered to be one of the strongest infall candidates among prestellar cores and shows clear signs of gravitational collapse (Caselli et al., 2002b). It is most likely in the process of forming a star and gravity has begun to dominate the dynamics. The magnetic field of the L1544 core is shown in Figure 4.3 with the Planck vectors overlaid. The orientation of the large-scale magnetic field is $\approx 53°$ and is nearly perpendicular to the orientation of the core semimajor axis which is $\approx 150°$. The magnetic field in the core appears to also follow the large-scale magnetic field orientation, but it has begun to curve inward and actually displays the hourglass morphology associated with ambipolar diffusion (see panel d of Figure 1.5). This then suggests that gravitational collapse has indeed begun and the core has moved beyond the magnetically-dominated phase. It would appear that the core is in the stage of transitioning between Panel c and d from Figure 1.5.

We attempt to calculate a magnetic field strength in L1544 using the same method as Section 3.3.6. L1544 is in the Taurus Molecular Cloud complex but the column density maps have not been released by the HGBS group. We therefore made our own column density map following the method outlined in Section 3.3.3. However, the Hercshel maps have not been processed through the JCMT pipeline reduction and so they still contain much of the extended structure. An initial column density map was made for L43 with the unfiltered maps and so we can compare column density values derived from filtered and unfiltered maps. The column density maps made from the filtered Herschel images had column density values approximately 1.5$\times$ larger in the densest part of the cloud. The only other difference was the column density map with the unfiltered maps then had column density values outside of the main core in the extended regions. Since we only focus on the dense cores, this factor of nearly unity is manageable and with the uncertainties normally associated with column density values and calculations (up to 50%), it is acceptable. For L183, L1517B and L1498 we make column density maps with the unfiltered Herschel maps as well. For all regions, we use the Herschel-PACS 160 μm, Herschel-SPIRE 250, 350 and 500 μm and the SCUBA-2 850 μm intensity maps. We

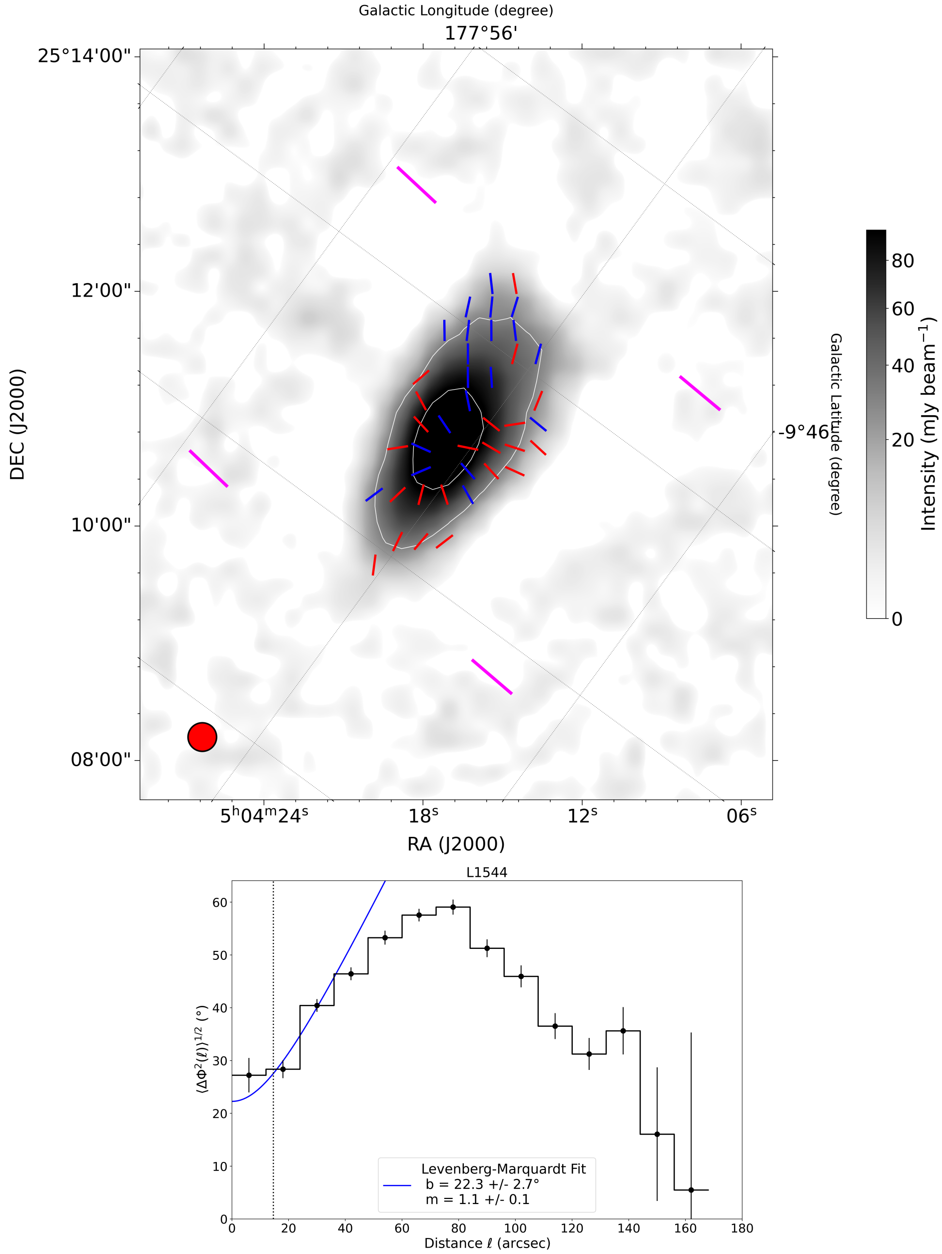

Figure 4.3: *Upper:* Plot of the magnetic field in L1544 (the polarization vectors have been rotated by 90°. The background greyscale is the 850 μm Stokes I emission. The large magenta vectors show the magnetic field inferred from Planck 353 GHz observations. Red vectors show polarization vectors with a signal to noise cut of I/DI>10 and P/dP>2 while blue vectors then show a slightly more stringent cut of P/dP>3. The JCMT beamsize is shown in the lower left corner. Vector lengths are all uniform. *Lower:* The ADF histogram with the best-fit parameters shown in the legends. The first three bins are fit. The beam size is shown with a vertical dashed line.

Table 4.2: Compiled and calculated properties of L1544

		L1544
Distance	(pc)	172
FWHM	($'' \times ''$)	60×24
θ	(°)	150
$N(H_2)$	($\times 10^{22}$ cm^{-2})	5.0±3.9
$n(H_2)$	($\times 10^{5}$ cm^{-3})	4.7±3.7
Δv_{NT}	(km s^{-1})	0.27±0.02
E_K	($\times 10^{35}$ J)	5.2±4.2
b		22.3±2.7
$\sigma\theta$	(°)	16.4±2.0
B_{pos}	(μG)	60(25)–132(55)
λ		2.9(2.5)–6.4(5.6)
$\mathcal{M}_A$		0.7(0.1)–1.5(0.2)
E_B	($\times 10^{34}$ J)	3.0(2.5)–15.0(12.0)

Δv_{NT} values taken from Lee, Myers & Tafalla (2001)

let temperature and column density vary to find the best fit. The errors reported are errors propagated through the fitting software.

The column density value of the core is given in Table 4.2 and we derive a volume density value using the geometric mean of the FWHM of the core. The Δv_{NT} is from N_2H^+ observations performed by Lee, Myers & Tafalla (2001) and have had the thermal contribution removed. The dispersion in position angle is calculated using the ADF method and the histogram is shown in the lower panel of Figure 4.3.

We calculate a magnetic field strength of 60–132 μG in L1544. The upper bound value agrees within error with the value found in Crutcher et al. (2004) of 140 μG which was calculated with a Q value of 0.5. The mass-to-flux ratio calculated is ≈3-6, which even accounting for the potential statistical correction of 1/3, gives a magnetically trans- to super-critical value. This is not surprising considering the hourglass morphology and the infall velocities.

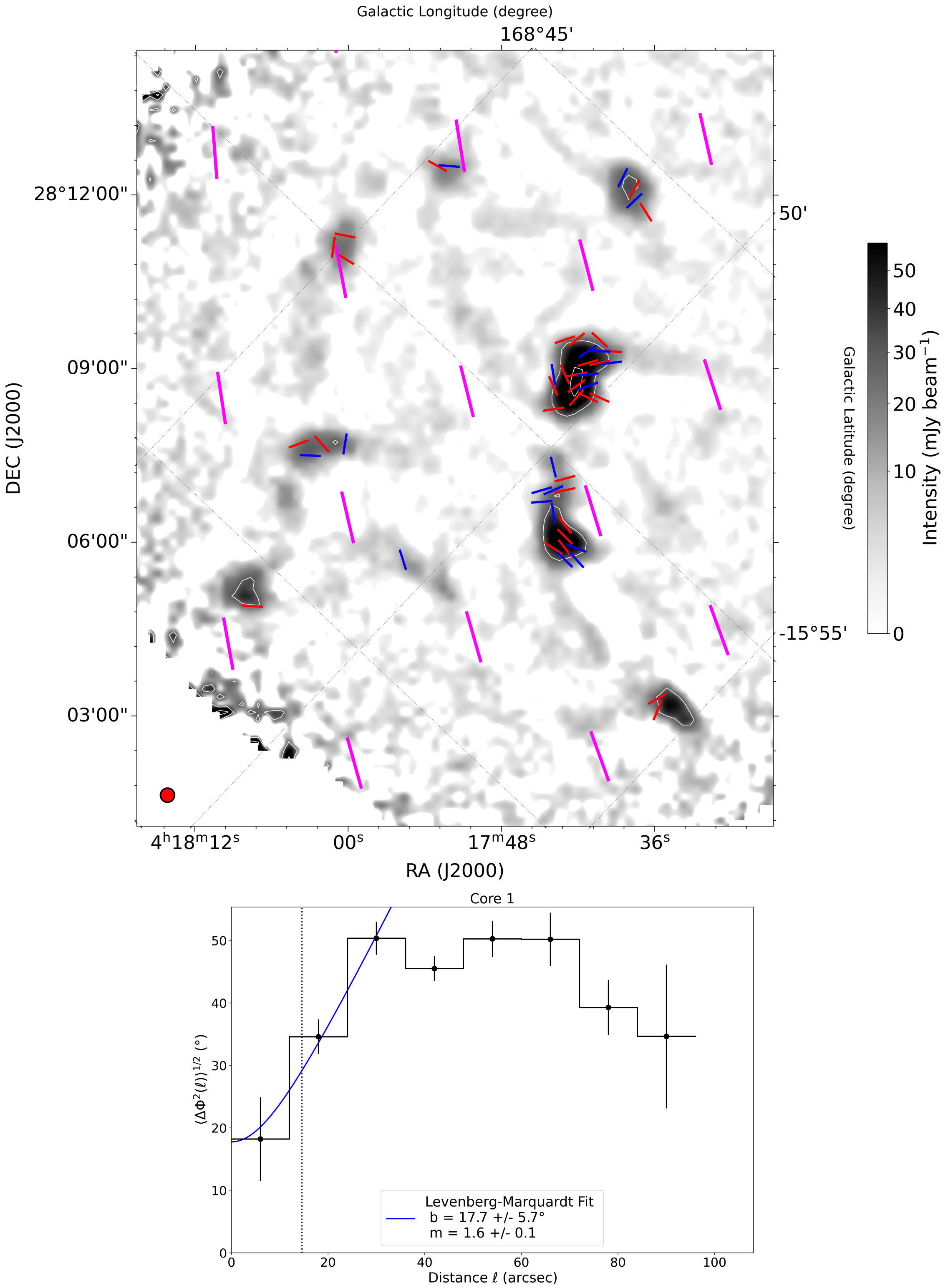

Figure 4.4: Same as Figure 4.3 but for L1495.

4.3.2 L1495A

As was seen above in Figure 4.1, L1495 is part of a larger filament and larger molecular cloud structure. Figure 4.4 shows the cores observed by SCUBA-2/POL-2 with the magnetic field vectors overlaid (Ward-Thompson et al., 2023). In Figure 4.5, the background is an RGB image with Herschel-SPIRE 500 and 250 μm shown as green and blue respectively and SCUBA-2 850 μm emission is shown as red. Here, the location of the embedded cores within a filamentary structure is better seen. Each of these cores are starless cores and candidate pre-stellar cores (Ward-Thompson et al., 2016; Howard et al., 2019).

We assign the cores numbers as shown in Figure 4.5. One core where we have detected polarization was not identified as a core by Ward-Thompson et al. (2016), as it was only detected very faintly in the earlier work. This is labelled on Figure 4.5 as core 4. We also note that core 2 appears to be split into two cores in the Stokes I image, which we here label 2N and 2S. Core 2 was not identified as a double core by Ward-Thompson et al. (2016) but they have very different polarization orientations so we treat them as separate. We therefore have a sample of 9 cores (Ward-Thompson et al., 2023).

Table 4.3 lists the cores detected in Ward-Thompson et al. (2023). We also state the core numbers assigned to them by Ward-Thompson et al. (2016), who fitted elliptical Gaussians to each of the cores and we list the properties of those ellipses also in Table 4.3. We note that core 21 from Ward-Thompson et al. (2016) is in our field of view, but no detectable polarized emission was observed at this position. For cores 2N, 2S and 4 we calculated the parameters of the elliptical Gaussians (Ward-Thompson et al., 2023).

Table 4.3 also lists the orientation of the local filament major axis at the position of each core, which we measure from Figure 4.5, and the core major axis orientation.

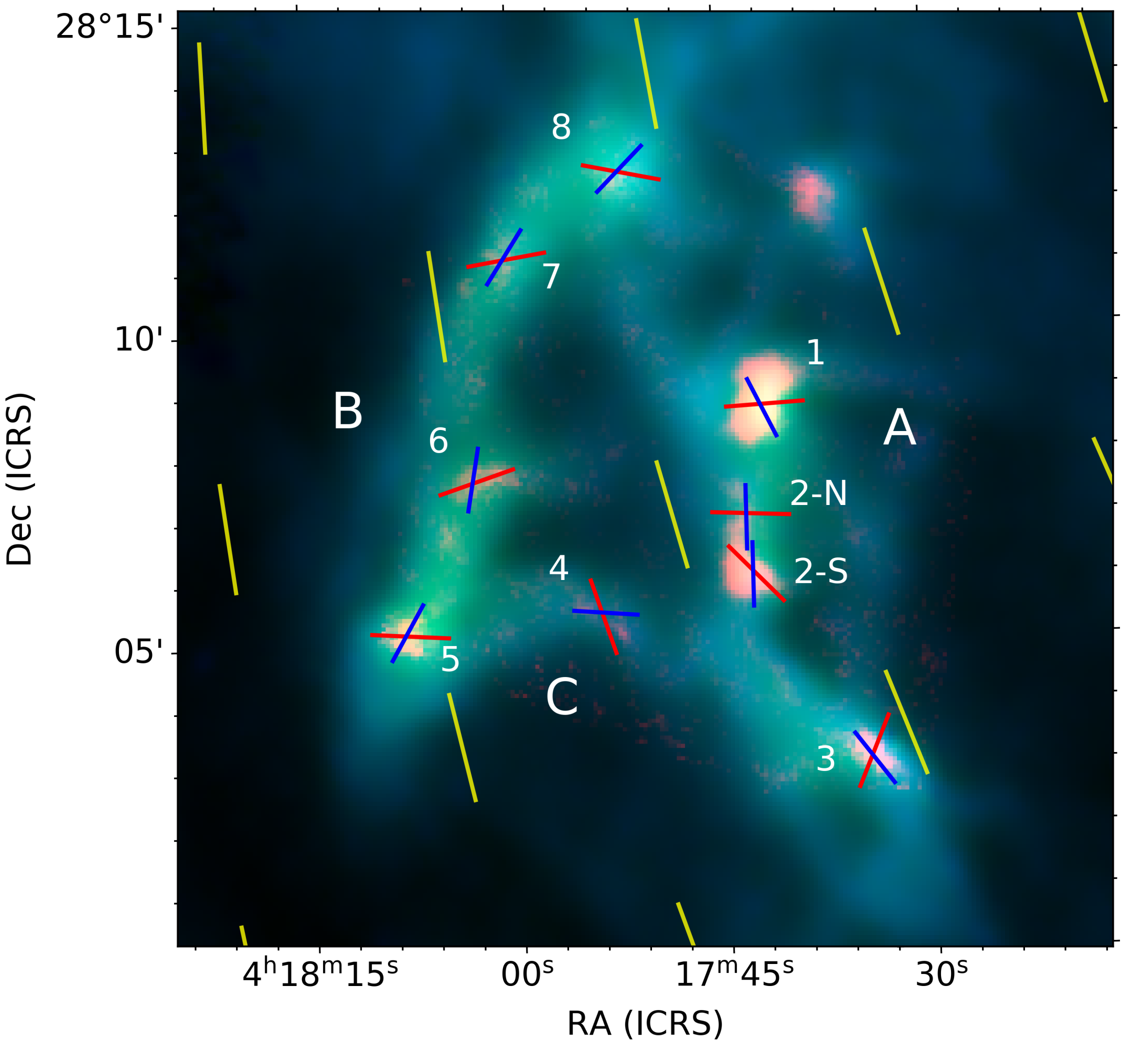

Figure 4.5: Image from Ward-Thompson et al. (2023). The background is an RGB image with Herschel-SPIRE 500 and 250 μm shown as green and blue respectively and SCUBA-2 850 μm emission is shown as red. The filaments seen in the original *Herschel* images are clearly seen and are labelled ‘A’, ‘B’ and ‘C’, as described in the text. The cores that we identify in this paper are numbered 1 to 8 as described in the text. The red vectors show the mean magnetic field orientation in each core from the POL-2 observations. The yellow vectors show the orientation of the large-scale magnetic field (over-sampled) from Planck observations (there are only about 4 independent Planck beams in this whole field of view). The blue half-vectors show the local filament major axis orientation (for core 8 we only show the axis of filament B). Each set of vectors in this image has a constant length for clarity.

Table 4.3: Core characteristics of L1495

Core no.[a]	FWHM[b] ($'' \times ''$)	$\theta^{b,c}_{core}$ (°)	$\theta^{c,d}_{fil}$ (°)	N(H_2)[e] ($\times 10^{21} cm^{-2}$)	n(H_2) ($\times 10^{5} cm^{-3}$)	θ^{c}_{pol} (°)
1 (2)	54.6 × 21.4	167	26	19.1 ± 7.6	2.0 ± 0.8	4 ± 2
2-N (7)	32.0 × 16.0	0	0	14.7 ± 5.9	2.4 ± 1.0	-3 ± 4
2-S (7)	32.4 × 20.7	45	0	15.7 ± 6.3	2.1 ± 0.8	-46 ± 3
3 (12)	55.2 × 20.3	53	37	15.3 ± 6.1	1.6 ± 0.6	68 ± 11
4 (−)	31.4 × 12.1	60	85	9.2 ± 3.7	1.7 ± 0.7	-72 ± 8
5 (5)	39.6 × 32.0	121	150	17.8 ± 7.1	1.8 ± 0.7	-4 ± 12
6 (11)	39.0 × 20.5	126	170	14.0 ± 5.6	1.8 ± 0.7	18 ± 5
7 (19)	45.0 × 22.2	165	147	14.4 ± 5.8	1.7 ± 0.7	9 ± 6
8 (14)	51.6 × 48.7	93	135 (15)	14.1 ± 5.6	1.0 ± 0.4	-13 ± 7

Table from Ward-Thompson et al. (2023)

a. Core number in parentheses from Ward-Thompson et al. (2016)

b. Values taken from Ward-Thompson et al. (2016)

c. All angle values are measured east of north

d. We adopt ±10° for the local filament angle except in cores 4 and 8 (see Section **??**)

e. Column density values from Gould Belt Survey (André et al., 2010)

Core 8 has two filament angles listed, because it sits at the junction of two filaments (Ward-Thompson et al., 2023). The value that is in brackets is for the western filament. We also list the temperature as measured by Ward-Thompson et al. (2016) and column density which was calculated by Palmeirim et al. (2013) using the *Herschel* bands at the resolution of SPIRE 250 μm. We calculate the volume number density in Table 4.3 using the column density values and the 850 μm core sizes from Ward-Thompson et al. (2016). We also list the weighted mean of the polarization position angle in each core from this work (note this is not magnetic field angle, it has not been rotated by 90°).

4.3.2.1 Magnetic Field Orientation of the Cores

Figure 4.5 shows the SCUBA2-POL2 polarization half-vectors overlaid in red, rotated by 90^o to indicate the orientation of the plane-of-sky magnetic field, within each dense core (Ward-Thompson et al., 2023). Each half-vector represents the

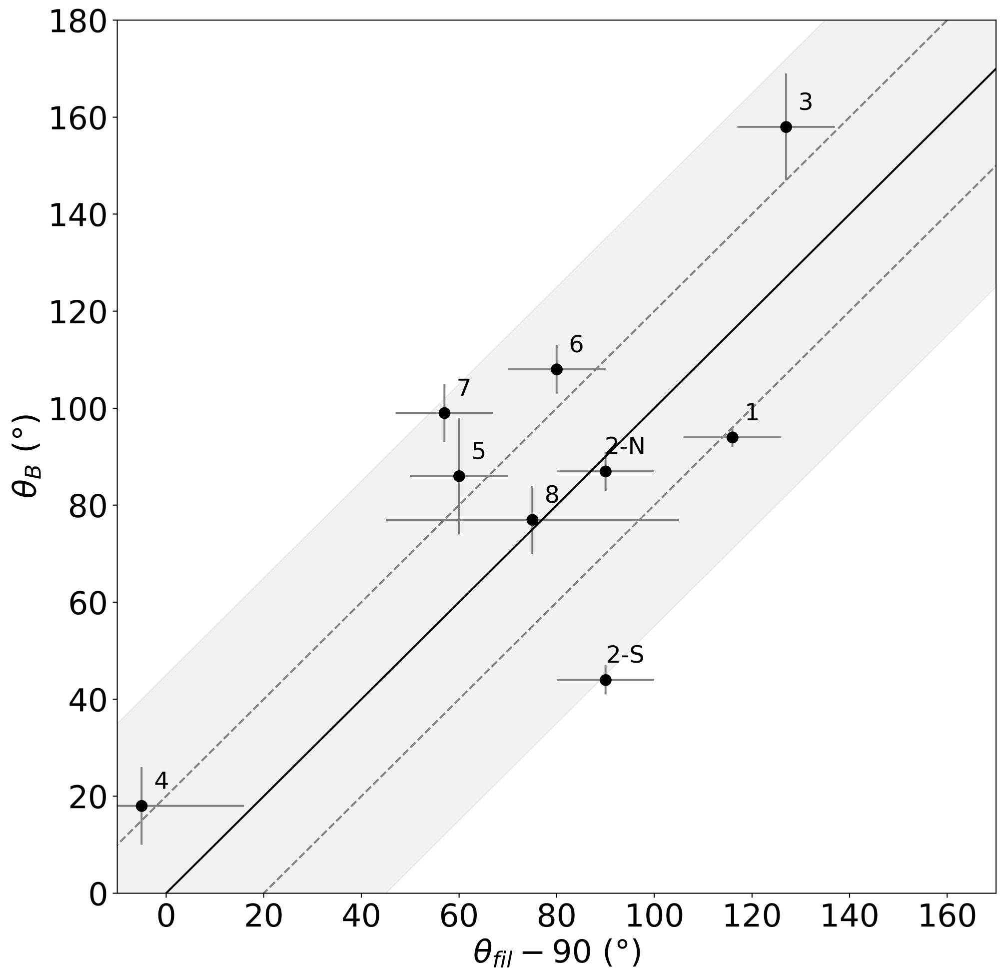

Figure 4.6: Image from Ward-Thompson et al. (2023). A plot of core magnetic field orientation for each core on the y-axis, versus 90^o minus its local filament major axis angle on the x-axis. The cores are numbered as in Figure 4.5. The solid line indicates a one-to-one correlation, which is where the points would be located if the B-field lay exactly orthogonal to the local filament orientation in every case. The two dashed lines represent $\pm 20^o$, roughly matching our predicted systematic angle error at our chosen signal-to-noise ratio cut-off. The shaded area is $\pm 45°$.

weighted mean polarization angle measured for each core respectively, rotated by 90^o. Also shown on Figure 4.5 in yellow are the half-vectors of the Planck measurements (over-sampled), also rotated by 90^o to indicate the large-scale plane-of-sky magnetic field orientation. Additionally, the blue vectors in each core indicate the local filament major axis as listed in Table 4.3.

Figure 4.5 shows that the magnetic field in cores 1, 2N and 3 lies roughly orthogonal to the local filament (Filament A) long axis. In core 2S the magnetic field is not orthogonal, but at this point the filament turns through 90^o, so it is difficult to uniquely define a filament orientation. Core 4 has a magnetic field orientation roughly orthogonal to the western half of Filament C, which turns somewhat at the position of core 4. The magnetic field orientations in cores 5, 6 and 7 also lie roughly orthogonal to their local filament (Filament B) major axis orientation. Core 7 is slightly further from orthogonal than the other two, although we note that here also the local filament orientation turns slightly. The magnetic field of core 8 is roughly orthogonal to filament B.

Figure 4.6 shows a plot of core magnetic field orientation for each core on the y-axis, versus 90^o minus its local filament major axis angle on the x-axis, in order to quantify the above discussion (Ward-Thompson et al., 2023). Any angle that lay between 180^o and 360^o has had 180^o subtracted from it and any angle that lay between 0^o and -180^o has had 180^o added to it due to the fact that both the magnetic field orientation and the filament orientation are half-vectors, as discussed above. The exception to this was core 4, whose error-bar overlaps the origin, so we extend the plot to slightly negative numbers to accommodate core 4. We took the error-bar in filament orientation to be $\pm 10^o$ as an indication of how accurately we could measure this orientation. For core 4 where the filament is curving we took the filament orientation to be the tangent to the curve and the error-bar to be the amount of curvature. For core 8, which lies at the junction of two filaments we took the local filament orientation to be that of filament B, which is denser. The error-bar used in the B-field orientation in each case is the standard deviation of the angles of the weighted mean half-vectors shown in Figure 4.5 and listed in Table 4.3.

If all B-field orientations lay exactly orthogonal to their respective filaments, then this plot would show a one-to-one correlation. This is shown by the solid line on Figure 4.6. We also plot two dashed lines, at $+20^o$ and -20^o from orthogonal. This is the typical systematic error that we would expect for a 2-σ detection of polarization (Naghizadeh-Khouei & Clarke, 1993), the value we chose for our cut, as described above. The shaded area represents $\pm 45°$.

It can be seen that there is a good degree of correlation in this plot, with most of the points consistent (including error bars) with lying between, or very close to, the dashed lines, and all lying within the shaded area. Hence we conclude that the magnetic fields that we have measured in these cores generally tend to lie closer to orthogonal than parallel to the local filament orientation in which the core is embedded. The core that lies furthest from the correlation line is 2S. This is one of the most dense cores and may have been affected by the proximity of core 2N or the effect of the filament changing orientation from the south to the north of core 2S.

It can be seen that the local field that we have measured in the starless cores within the filaments has totally dissociated from the large-scale field orientation seen by Planck, and there is no correlation between them. Qualitatively this can be seen by comparing the mean magnetic field angles. The mean large-scale B-field orientation is 16° east of north. Meanwhile, core 1 has a mean B-field orientation of ≈94°. Core 2 has an overall B-field orientation of ≈61° but that is split into the two populations of ≈87° and 44° for the north and south parts respectively. For the other cores, 90° can be added to the mean polarization values in Table 4.3 and it can be seen that none agree well with the 16° large-scale orientation.

The exception to the above statement is core 4, whose small-scale B-field that we have measured lies almost exactly parallel to the large-scale B-field orientation measured by Planck – see Figure 4.5. This may be a coincidence, because the B-field in core 4 also lies roughly perpendicular to its host filament. However, we note that core 4 and the filament in which it sits have the lowest column density of any of our cores by a factor of 1.5–2 (see Table 4.3), and thus it may be the youngest core.

We performed an approximate DCF analysis in core 1, where we have sufficient half-vectors to make this statistical analysis. We attempted to perform a DCF analysis using the ADF structure function on core 2 as well but there were not enough statistically significant vectors. For this DCF analysis, we followed the same method as in Section 3.3.6. We use ΔV_{NT}=0.206 km s^{-1} which is found from NH_3 velocity dispersion observations (Seo et al., 2015) and then removed the thermal component assuming a temperature of $\sim$10 K. We calculate a dispersion in the magnetic field position angle of 12.8$\pm$4.1^o using the ADF. The ADF histogram is shown in the lower panel of Figure 4.4. We then use the n(H_2) value of core 1 from Table 4.3. We obtained plane-of-sky magnetic field strength of 37$\pm$14 – 83$\pm$32 μG using Equation 3.8.

Using the N(H_2) value of core 1 from Table 4.3, we calculate a mass-to-flux ratio of 1.8$\pm$1.0 – 3.9$\pm$2.1. This core also has a magnetic energy less than both the kinetic and gravitational energies by a factor of $\sim$2 and $\sim$5 respectively. This all suggests that the main core we observe in L1495 is beyond the magnetically-dominated phase. It may have transitioned to the matter-dominated phase as discussed in Section 3.4.1.1. We discuss this further in Chapter 6 where we bring forward the analysis done in Section 3.4.1.1 and apply it to this region and the others in this section. This was also done in Ward-Thompson et al. (2023) and we will build on this as well.

4.3.3 L1498

L1498 and L1517B are the 'quieter' of the cores presented in this chapter, but L1498 is by far the quietest based on its flux distribution. L1498 is considered to be slightly less evolved than L1544 based on its lower deuterium fractionation, CO depletion factor and central H_2 density (Tafalla et al., 2004). It has also been identified as an infall candidate based on very significant blue excess in its asymmetric, double-peaked CS spectra (Lee, Myers & Tafalla, 2001). So despite the low flux density, the source may be more evolved, which is initially puzzling.

As mentioned above, it is very faint and difficult even for SCUBA-2/POL-2 to observe. The magnetic field in L1498 is plotted in Figure 4.7. The observations of this source are not complete and so we have very low signal-to-noise vectors and must relax our signal-to-noise cut requirements. The large-scale field observed by Planck is approximately 125° east of north and is shown with the magenta vectors. Meanwhile the L1498 core has an average magnetic field orientation of 178°, though there is significant scatter and field in the southeastern corner is the main component which is nearly 0 or 180°.

Kirk, Ward-Thompson & Crutcher (2006) found a transition of magnetic field orientation from the northwestern to the southeastern part of the core, going from $64\pm7°$ in the densest 'main' core in the northwest to $124\pm6°$ in the southeastern tail, but they appear to have detected more core structure than we do here (see left panel of Figure 4.8). Their magnetic field orientation in the diffuse tail matches the large-scale magnetic field orientation well (125°). The core magnetic field orientation is rotated by $\approx$60° to the large-scale field, although they also note that it is also roughly perpendicular to the major axis of the core which they found to be $\approx$135°. The difference of 20° between the core magnetic field orientation and major axis of the core is something they note is commonly seen in prestellar cores (Ward-Thompson et al., 2000).

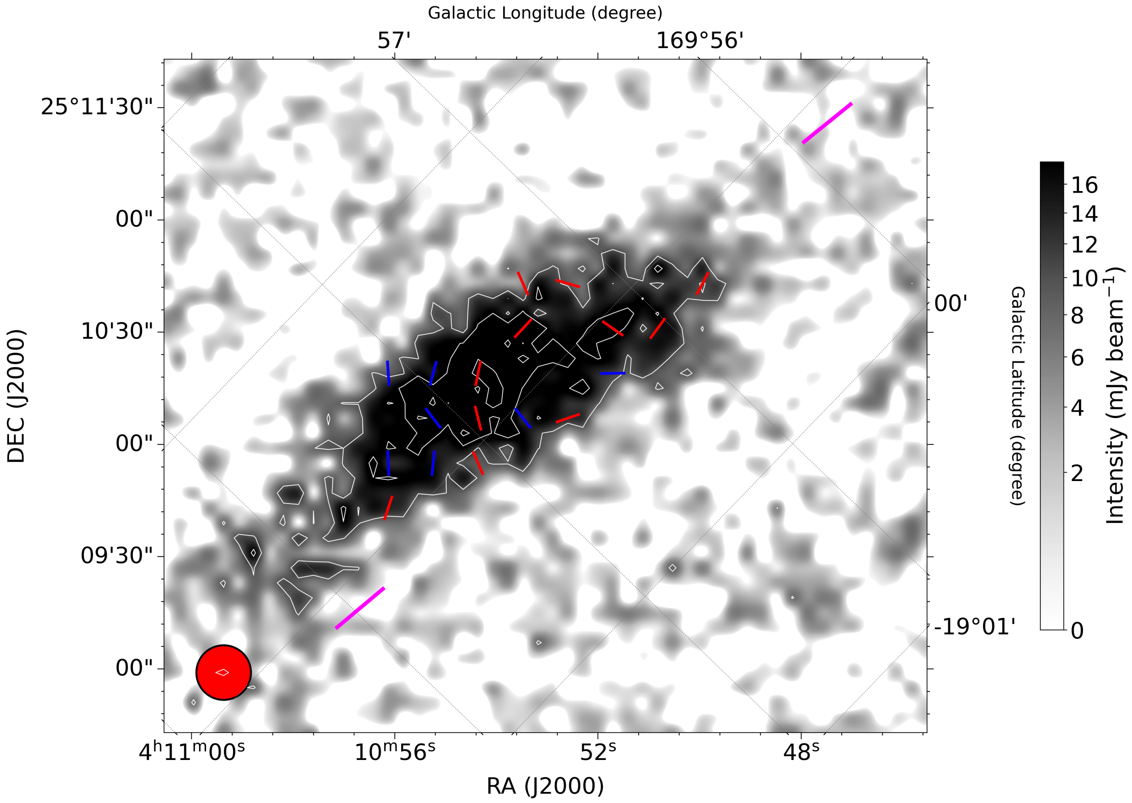

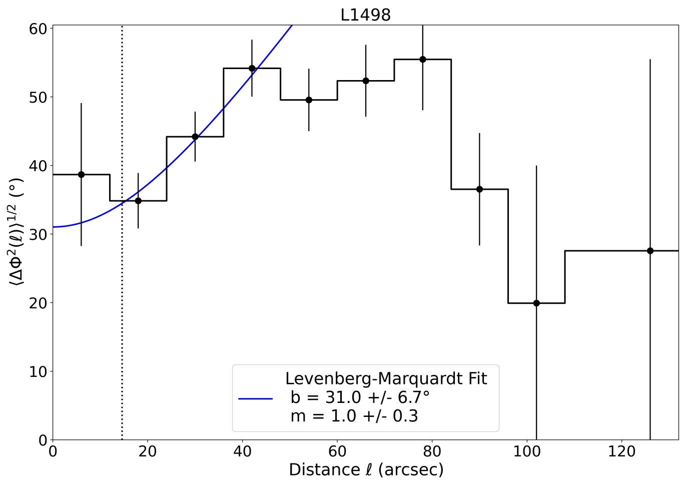

Figure 4.7: *Upper:* Plot of the magnetic field in L1498 (the polarization vectors have been rotated by 90°. The background greyscale is the 850 μm Stokes I emission. The large magenta vectors show the magnetic field inferred from Planck 353 GHz observations. Red vectors show polarization vectors with a signal to noise cut of I/DI>10 and P/dP>1 while blue vectors then show a slightly more stringent cut of P/dP>2. The JCMT beam size is shown in the lower left corner. All vector lengths are uniform. *Lower:* The ADF histogram with the best-fit parameters shown in the legends. The first three bins are fit. The beam size is shown with a vertical dashed line.

However, these early observations with the previous polarimeter on JCMT, SCUPOL, must be treated with caution. These sources are extremely dim and difficult to observe for POL-2, much less a previously less-sensitive instrument such as SCUPOL. In addition, the IP model was still under constant development, as well as the data reduction pipeline. In addition, there were different scanning patterns for SCUPOL and chopping was used (currently not using chopping). When SCUPOL was decommissioned, Matthews et al. (2009) used the most up-to-date data reduction software and IP models to reconstruct a legacy catalog of the SCUPOL observations, which included the L1517B and L1498 observations from Kirk, Ward-Thompson & Crutcher (2006). We show three plots in Figure 4.8 comparing the Stokes I structure and polarization vectors. It can be seen that the Stokes I structure in Matthews et al. (2009) matches well with the one observed by SCUBA-2/POL-2. In addition, the mean of the Matthews et al. (2009) vectors is $\approx 150^{\circ}$, more closely matching the average orientation of $\approx 178^{\circ}$ observed by POL-2 (versus 64° from Kirk, Ward-Thompson & Crutcher, 2006).

L1498 was one of the cores in which Lee, Myers & Tafalla (2001) found signs of infall motions with a double CS peak but single N_2H^+ peak. They find that the gas is moving from northwest to southeast and suggest that the core is a preprotostellar core on the verge of collapse. This gas motion is roughly along the semimajor axis of the core which means the motion is then preferentially perpendicular to the direction of the magnetic field lines, something which would suggest this core to have moved beyond the magnetically-dominated phase.

We follow the same method as in Section 4.3.1 to determine the column density of the region. The derived column density values have very large uncertainties which may be in part due to the low emission in the tail of the SED where the 850 μm contribution is. We calculate a volume density from these column density values and then get our N_2H^+ non-thermal velocity line widths from Lee, Myers & Tafalla

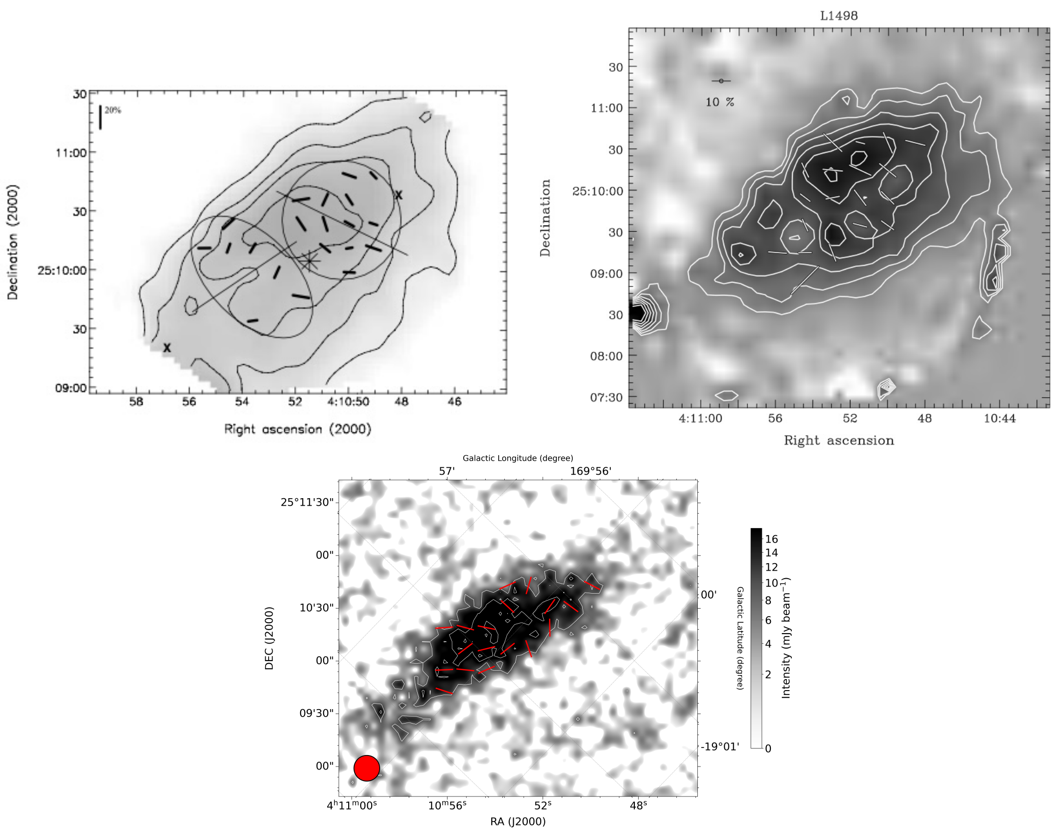

Figure 4.8: A comparison of the polarization observations in L1498. *Upper left:* Figure 1 from Kirk, Ward-Thompson & Crutcher (2006) which shows the background 850 μm dust emission with the magnetic field vectors (polarization rotated by 90°) plotted in black. Their two identified cores are shown with ellipses and a mean magnetic field orientation is shown as a long black line. *Upper right:* Figure 16 from Matthews et al. (2009) which shows polarization vectors in white overlaid on the background 850 μm dust emission. *Lower:* The same figure as Figure 4.7, but with all vectors plotted in red and rotated back by 90° to show polarization orientation.

Table 4.4: Compiled and calculated properties of L1498

		L1498
Distance	(pc)	140
FWHM	($'' \times ''$)	47.6×15.7
θ	($^\circ$)	125
$N(H_2)$	($\times 10^{22}$ cm^{-2})	2.9±2.4
$n(H_2)$	($\times 10^{5}$ cm^{-3})	3.8±3.1
Δv_{NT}	(km s^{-1})	0.19±0.01
E_K	($\times 10^{34}$ J)	7.6±6.3
b		31.0±6.7
$\sigma\theta$	($^\circ$)	23.7±5.2
B_{pos}	(μG)	26(12)–57(27)
λ		3.9(3.6)–8.6(8.0)
$\mathcal{M}_A$		1.0(0.2)–2.1(0.5)
E_B	($\times 10^{34}$ J)	0.21(0.1)–1.0(0.9)

Δv_{NT} values taken from Lee, Myers & Tafalla (2001)

(2001). All of these values are listed in Table 4.4.

We calculate a magnetic field strength of ≈25–60 μG. This is the lowest magnetic field strength calculated in this chapter, but that does agree well with results from Kirk, Ward-Thompson & Crutcher (2006) and Crutcher et al. (2004) where of the five prestellar cores observed, L1498 had the lowest magnetic field strength (10±7 μG). The calculated mass-to-flux ratio is magnetically supercritical, even when considering the statistical correction, though we should note the extremely large error bars (propogated through from column density values). The core is also approximately trans-Alfvénic at the lower limit and super-Aflvénic at the upper limit. These results do agree with the discussion above where the gas in the cloud is flowing inwards along the long axis and across the magnetic field lines.

4.3.4 L1517B

Despite L1517B appearing to be an isolated environment on the large scale (see Figure 4.1), it is slightly more chaotic since it consists of a series of quiescent filaments and starless cores, sitting near a stellar object (Hacar & Tafalla, 2011). This can be seen in Figure 4.9 which is adapted from Hacar & Tafalla (2011). The nearby stellar object is a pre-main sequence star called AB Aur which has a luminosity of $\sim$50 $L_\odot$ and mass of 2.4 $M_\odot$ (van den Ancker, de Winter & Tjin A Djie, 1998). The starless cores in L1517 (including L1517B) are thought to still be a part of the same system as AB Aur, but they show very few signs of interaction with the stellar object (Ladd & Myers, 1991). One theory is that they are remnants of the molecular cloud that AB Aur was formed from, but they are thought to be too quiescent for this to be the case (Ladd & Myers, 1991). Regardless, this could be a region in the very early stages of triggered star formation, a potential fourth mode of star formation to add to the Seo et al. (2019) model.

Hacar & Tafalla (2011) has suggested that the main dense cores seen above in Figure 4.9 have formed out of subsonic filaments in the region. They suggest that these subsonic, velocity-coherent filaments were formed from the turbulent ambient cloud. The cores then fragmented and inherited the kinematics of the filaments, suggesting it could be a slow-mode (see Figure 1.6) star-formation process, though the only core likely to form a star is L1517B. Even then, the core is not as evolved as others (it has poorer complex chemistry) like L1498 and L1544 (Lee, Myers & Tafalla, 2001; Megías et al., 2023). The core could be newly formed which could also explain why it still has the kinematics of the filament and has not yet been affected by the nearby AB Aur despite the believed association with the star (Ladd & Myers, 1991). L1517B also shows no significant blue excess and has a very small spread in the velocity dispersions (Lee, Myers & Tafalla, 2001).

The magnetic field in L1517B is plotted in Figure 4.10. As mentioned above, the observations of this source are not complete and so we have very low signal-to-noise vectors and must relax our signal-to-noise cut requirements. The large-scale field observed by Planck runs nearly entirely east-west which can be seen with the magenta

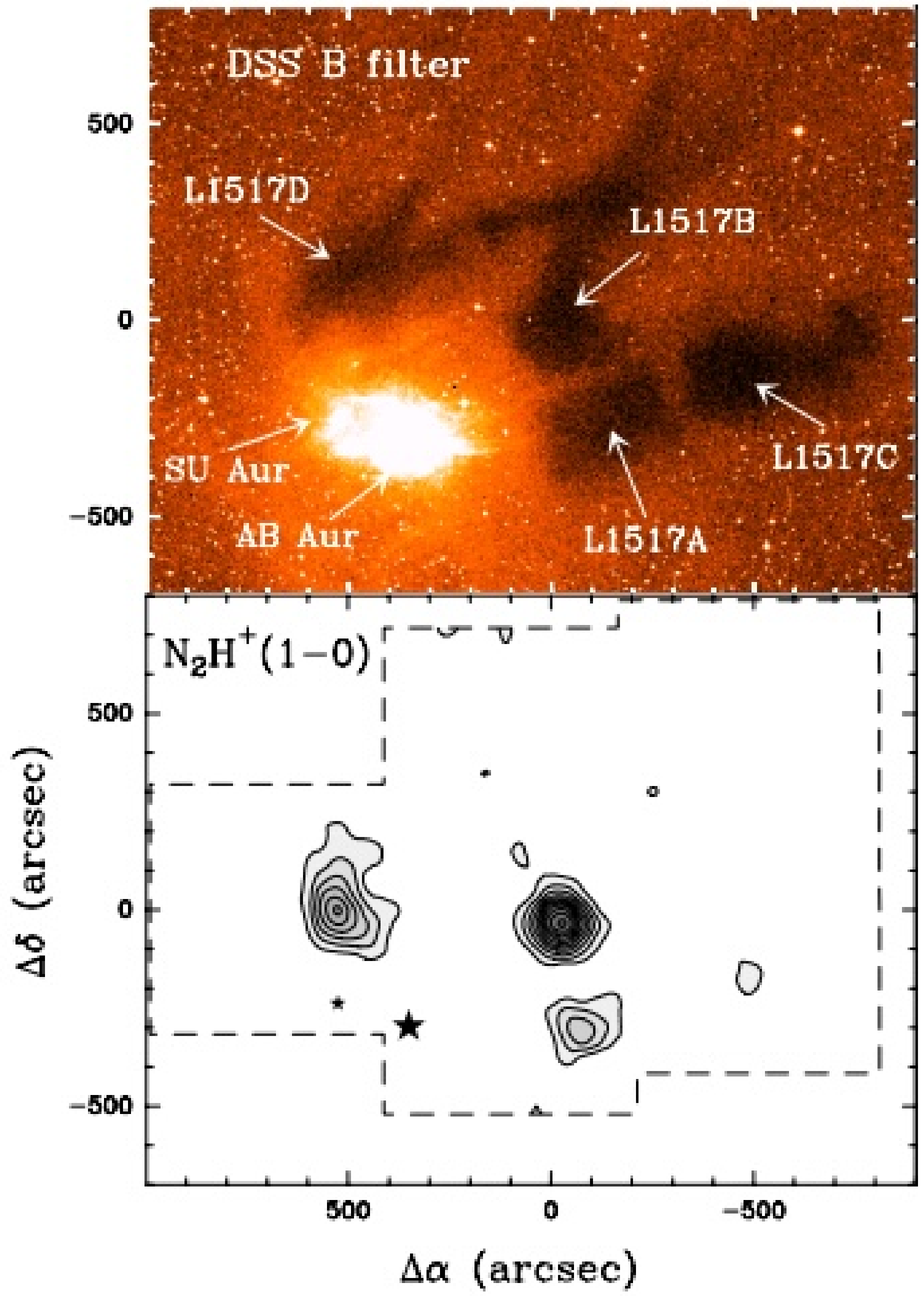

Figure 4.9: Figure 4 from Hacar & Tafalla (2011) showing the locations of the starless cores around the pre-main sequence stellar object AB Aur. The bottom panel shows the N_2H^+ (1-0) integrated intensity. The L1517B core is also well detected in 1.2 mm continuum observations.

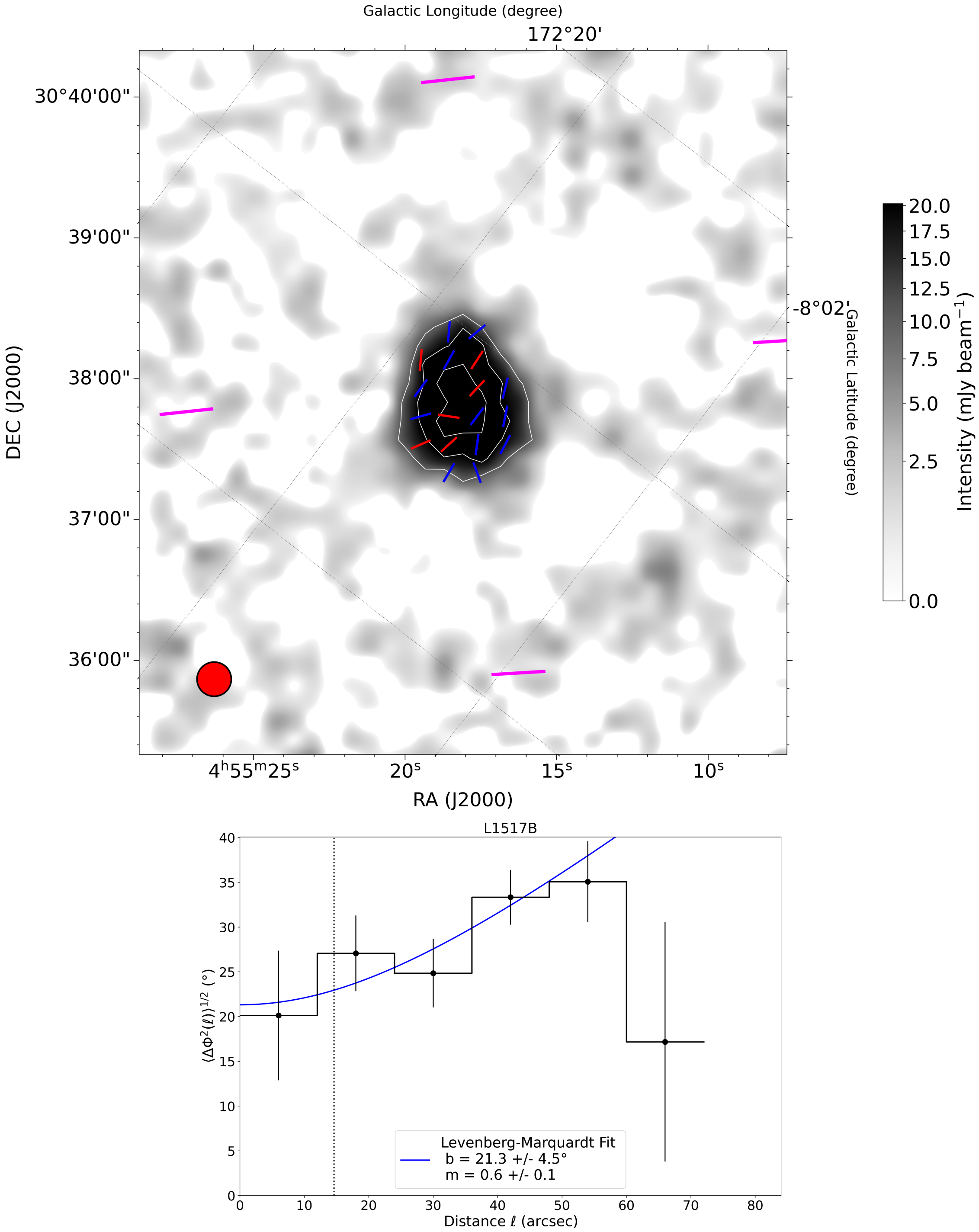

Figure 4.10: Same as Figure 4.7 but for L1517B. In addition, the observed fit of the ADF was better when fitting the first four bins, so this is was done.

vectors. Meanwhile the L1517B core has an average magnetic field orientation of ≈150°, though there is significant scatter. Kirk, Ward-Thompson & Crutcher (2006) found a transition of magnetic field orientation from the northern to the southern part of the core, going from 84° in the north to 156° in the south, but they appear to have detected more core structure than we do here. L1517B may be missing some Stokes I emission like L1498 and we have submitted SCUBA-2 proposals to observe L1517B like we did with L1498. Regardless, our core magnetic field orientation agrees with the southern area from Kirk, Ward-Thompson & Crutcher (2006). The L1517 molecular cloud was also observed using optical polarimetry and a similar east-west morphology was found (Sharma et al., 2022), suggesting the diffuse areas of the molecular clouds do still follow the large-scale field, and only on the core-scale does it deviate. The deviation is not completely perpendicular, closer to 60°.

Similar to L1498, following the disagreement between our POL-2 observations and the Kirk, Ward-Thompson & Crutcher (2006) maps, in both Stokes I and polarization, we turn to the SCUPOL legacy catalog of Matthews et al. (2009). Figure 4.11 shows the three magnetic field/polarization maps of Kirk, Ward-Thompson & Crutcher (2006), Matthews et al. (2009) and our POL-2 map. Both Matthews et al. (2009) and our own POL-2 map only observe the northern most core of Kirk, Ward-Thompson & Crutcher (2006). The Stokes I structure presented in Matthews et al. (2009) more closely matches the structure we see with SCUBA-2/POL-2. If we again compare mean magnetic field orientations, the mean magnetic field from Matthews et al. (2009) is ≈112° which is approximately halfway between our derived mean field of 150° and that from Kirk, Ward-Thompson & Crutcher (2006) of 84°. This is inconclusive when compared with L1498 where we saw better agreement in polarization angle between our work and Matthews et al. (2009). Again, we would tend to trust the newer observations due to a more sensitive detector and refined data reduction routine and IP model. In addition, L1517B may just be towards the

Table 4.5: Compiled and calculated properties of L1517B

		L1517B
Distance	(pc)	159
FWHM	($'' \times ''$)	27.1×18.1
θ	(°)	0
N(H_2)	($\times 10^{22}$ cm^{-2})	2.0±0.6
n(H_2)	($\times 10^{5}$ cm^{-3})	3.2±1.0
Δv_{NT}	(km s^{-1})	0.20±0.02
E_K	($\times 10^{34}$ J)	3.8±1.4
b		21.3±4.5
$\sigma\theta$	(°)	15.6±3.3
B_{pos}	(μG)	38(11)–84(24)
λ		1.8(0.8)–4.0(1.7)
$\mathcal{M}_A$		0.6(0.1)–1.4(0.3)
E_B	($\times 10^{34}$ J)	0.2(0.1)–1.2(0.7)

Δv_{NT} values taken from Lee, Myers & Tafalla (2001)

boundary of what instruments like SCUPOL or POL-2 can observe.

Similar to L1544, we did not have any HGBS data for this core. We had to create column density maps and we followed the same method described above in Section 4.3.1. The column density and subsequent volume density are given in Table 4.5. Interestingly, when we use the ADF on L1517B, the better fit of the data occurs when we fit the first 4 bins (up to a 48$''$ extent) rather than the first 3 bins as in the others. This could suggest that there is a slightly more coherent magnetic field structure across the whole core. Of the cores presented here, it is the least evolved and so perhaps the magnetic field is not so disturbed. The ADF histogram is shown in the lower panel of Figure 4.10 and the b-value and the dispersion in position angle is given in Table 4.5.

We calculated a magnetic field strength in L1517B of ≈40–85 μG. This is the second lowest magnetic field strength after L1498. Kirk, Ward-Thompson & Crutcher (2006) found a magnetic field strength of 30±10 μG so our lower bound agrees with this value within error. They also found the core to be highly supercritical, with a mass-to-flux ratio of 7±4 before correcting for any statistical effects. This is nearly

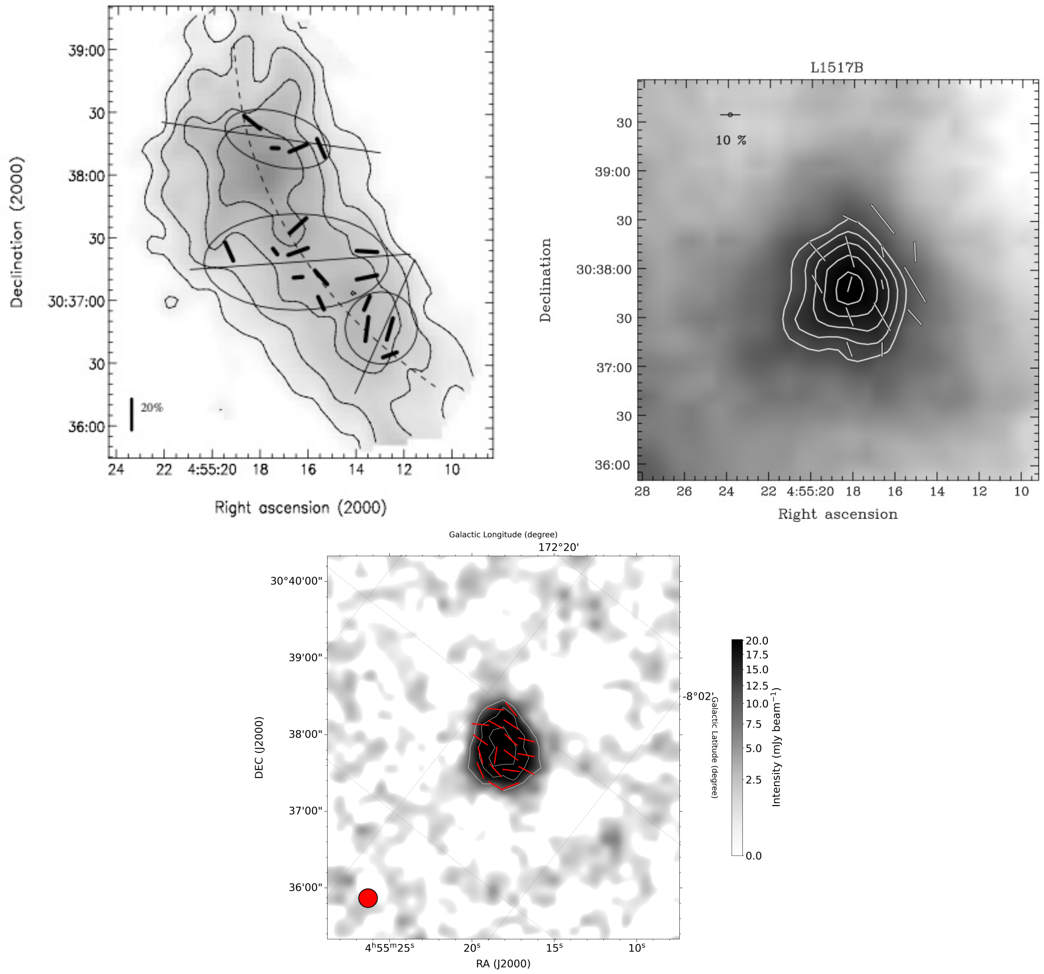

Figure 4.11: A comparison of the polarization observations in L1517B. *Upper left:* Figure 2 from Kirk, Ward-Thompson & Crutcher (2006) which shows the background 850 μm dust emission with the magnetic field vectors (polarization rotated by 90°) plotted in black. Their three identified cores are shown with ellipses and a mean magnetic field orientation is shown as a long black line. *Upper right:* Figure 20 from Matthews et al. (2009) which shows polarization vectors in white overlaid on the background 850 μm dust emission. *Lower:* The same figure as Figure 4.10, but with all vectors plotted in red and rotated back by 90° to show polarization orientation.

double our upper limit. They also found the mass to be greater than the critical mass supported by magnetic fields but less than the kinetic and total virial masses, though when attempting to account for the mass of the whole central region (not just the core), the ratio of virial to observed mass was closer to one. Sharma et al. (2022) derived a field strength of 23 μG though this was using ^{13}CO linewidths, a density of order 10^3 cm^{-3} and optical polarization, so this field strength is more for the larger-scale core envelope. They do get a mass-to-flux ratio of 0.73 which does support the magnetically sub-critical to super-critical transition from envelope to core (Crutcher, 2004).

L1517B appears to have moved beyond the stage at which magnetic fields can fully support against collapse. Similarly, the core itself no longer has an imprint of the large-scale magnetic field, suggesting it has moved beyond magnetically dominated. This can be explained as well by the fragmentation of the filament as suggested by Hacar & Tafalla (2011), where if the core is now already fully formed from the filament, it will have moved beyond magnetic dominated and we would expect the field to no longer follow the large-scale field. This is similar to other cores in L1495 (excluding core 4, see Section 4.3.2). The gravitational potential energy of L1517B is approximately 7×10^{34}J which is nearly double the kinetic energy and 7$\times$ the magnetic energy. If we calculate the thermal and non-thermal virial parameter (using Equation 1.2), we get $\alpha \approx$0.8, suggesting the core is gravitationally bound. L1517B and its lack of evolved star formation is an interesting case if neither magnetic nor kinetic pressures are able to support it at the moment. The nearby AB Aur may be preventing the core from contracting or done so in the past, but we would expect to see that in the kinematics of the surrounding cloud or core if it was due to stellar feedback.

4.3.5 L183

The L183 core is very chemically evolved, up to the point that a protostellar object would be expected but there is still nothing formed. It has tentatively been identified as an infall candidate based on very significant blue excess in its asymmetric, double-peaked CS spectra (Lee, Myers & Tafalla, 2001). It also has a $C^{18}O$ depletion level typically associated with chemically evolved cores (Tafalla, 2005a,b).

The large-scale magnetic field observed by Planck in L183 is largely in the east-west direction. This agrees well with optical polarization measurements which also trace a large scale east-west field through the diffuse material (Karoly et al., 2020). Interestingly, the magnetic field inferred with near-infrared polarization is slightly more curved and starts to match the submillimeter wavelength measurements which are nearly 90° offset from the large-scale magnetic field (Karoly et al., 2020). The fact that the magnetic field on the core scale no longer resembles the large scale field means that it could also have passed the point of being magnetically-dominated. In the initial publication of this source, they found all of the cores to be magnetically sub-critical (Karoly et al., 2020) which would contradict the above claim. However, they reduced the POL-2 data with a pixel size of $12''$ (and not using the method described in Section 2.3.4) and so the flux profile was much larger and there were perhaps arbitrarily large signal-to-noise vectors.

Here we have re-reduced the data using the method in Section 2.3.4. This data is shown in Figure 4.12 as blue and red pseudovectors (see Figure 4.12 description for more detail) and the Planck large-scale B-field is shown as magenta vectors. The magnetic field orientation in the two cores, the North and the South ones, appear similar to the orientation first derived in Karoly et al. (2020) but with a bit more scatter. This orientation, although very broadly scattered, peaks roughly perpendicular to the large-scale field. However, there is a small core to the west that has magnetic field vectors which are aligned with the large-scale field, something

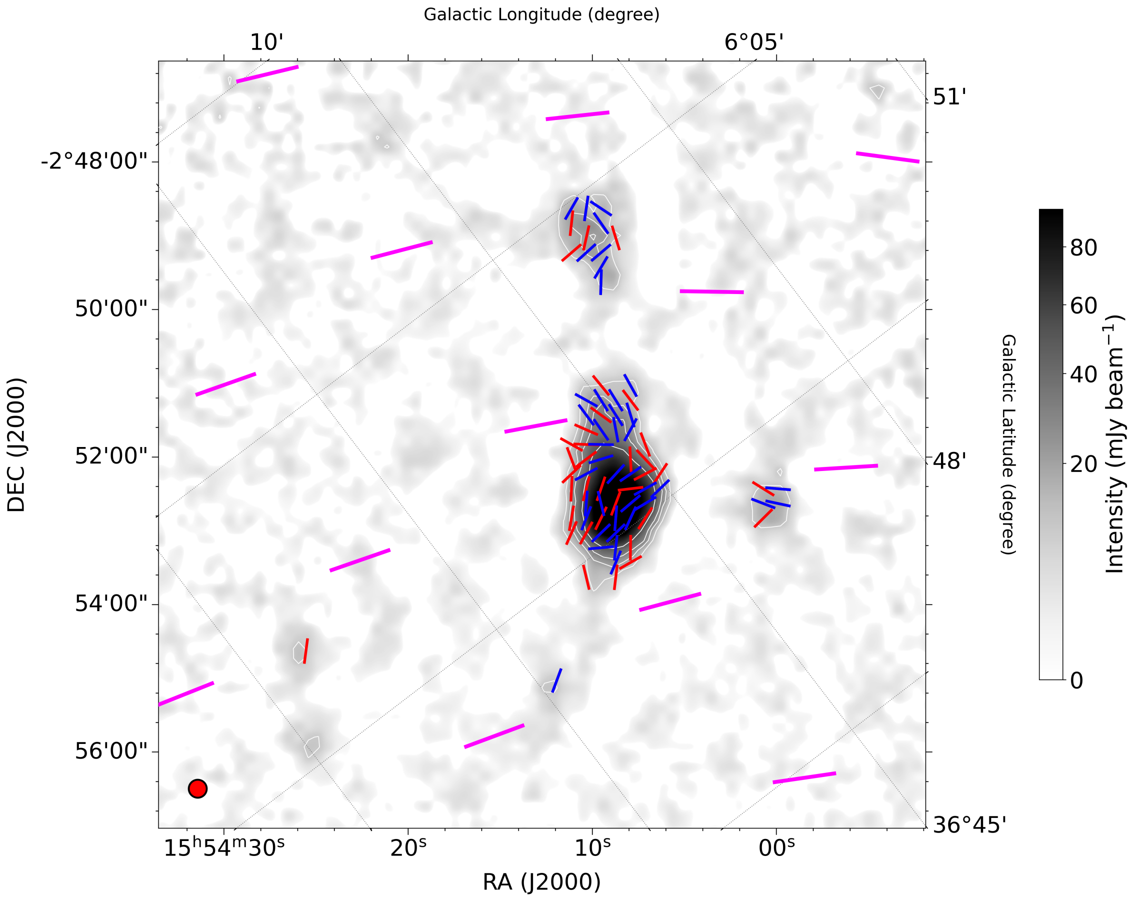

Figure 4.12: Same as Figure 4.7 but for L183.

Table 4.6: Physical properties of L183 cores

	Distance (pc)	FWHM ($'' \times ''$)	θ ($^\circ$)	N(H_2) ($\times 10^{22}$ cm^{-2})	Δv_{NT} (km s^{-1})	n(H_2) ($\times 10^5$ cm^{-3})	E_K ($\times 10^{34}$ J)	E_G ($\times 10^{34}$ J)
North	110	15.7×27.4	30	2.7±0.8	0.26±0.01	5.9±1.7	4.4±1.3	5.0
South	110	28.3×49.4	0	3.2±1.1	0.28±0.01	3.9±1.3	20.0±7.1	42.0
West	110	12.6×12.6	0	1.9±0.6	0.21±0.01	6.9±2.0	0.8±0.3	0.6

Δv_{NT} values taken from Lee, Myers & Tafalla (2001)

Table 4.7: Magnetic field properties of L183 cores

	North	South	West
b	26.3±6.4	21.0±3.1	–
$\sigma\theta$ ($^\circ$)	19.7±4.8	15.4±2.3	–
B_{pos} (μG)	51(15)–113(33)	58(13)–128(29)	–
λ	1.8(0.7)–4.0(1.6)	1.9(0.8)–4.2(1.7)	–
$\mathcal{M}_A$	0.8(0.2)–1.7(0.4)	0.6(0.1)–1.4(0.2)	–
E_B ($\times 10^{34}$ J)	0.2(0.1)–0.9(0.5)	1.3(0.6)–6.4(2.9)	–

similarly seen in L1495 (see Section 4.3.2).

The L183 core is very chemically evolved, up to the point that a protostellar object would be expected but there is still nothing formed. As mentioned in Chapter 1, the three main mechanisms for support would have to be thermal pressure, turbulent pressure or magnetic pressure. Assuming the results of Karoly et al. (2020) are correct, magnetic pressure would be the largest form of support, but the deviation from the large-scale field suggests that the core is no longer magnetically dominated, though perhaps the field strength is still strong enough to prevent collapse. We calculate a new field strength here with the updated reduction. We have also recalculated a column density and temperature map from the available Herschel data and the new L183 reduction. It should be noted that the Herschel data have not been filtered through the POL-2 pipeline as in Section 3.3.3, but we did use the same Equation 3.4 and same parameters, with β=1.8. However, with the addition of the Herschel/PACS 160 μm map, we let temperature be a free parameter with the column density and solved for both.

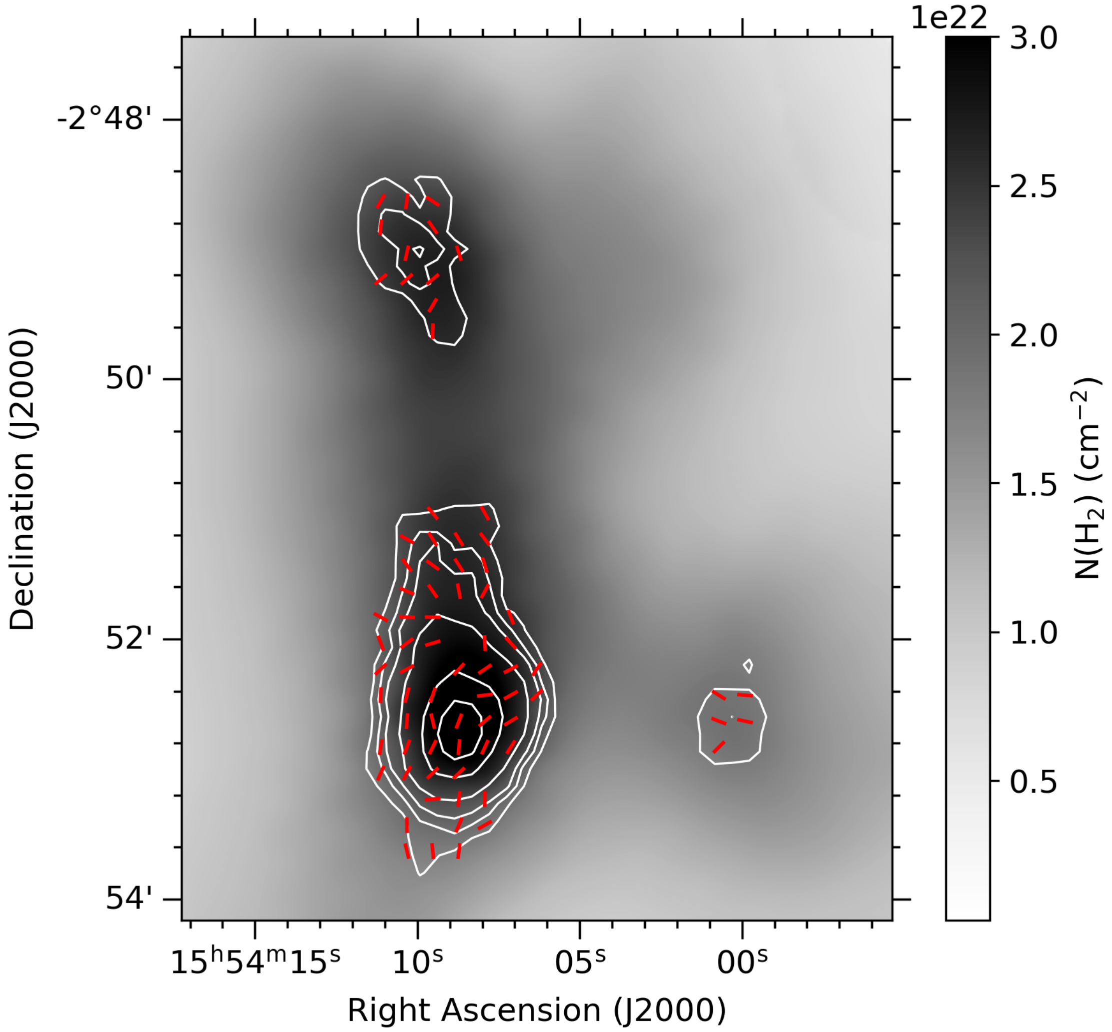

Figure 4.13: A plot of the H_2 column density calculated following the method in Section 3.3.3. The plotted contours are showing the 850 μm Stokes I emission. The levels are 10, 20, 30, 50, 100 and 150 mJy beam^{-1}. The magnetic field vectors are plotted in red. The three cores discussed in the text are identified with the contours and magnetic field lines. The north, south and west naming comes from their cardinal location.

The new column density map is plotted in Figure 4.13 with the vector from the three regions plotted on top. It is quite clear that the densest regions have the vectors which are most different from the large-scale field, while the more diffuse areas still have vectors parallel to the field. The mean of the magnetic field direction in the north and south core are both ≈160° which is preferentially perpendicular to the large-scale field which has an average orientation of 88°. The west core has a mean magnetic field direction of 80° which is then preferentially parallel to the large-scale field. The west core has too few vectors to meaningfully calculate a magnetic field strength and so no calculation is done, but the magnetic field strength is calculated in the north and south cores with the same method as in Section 3.3.6.

We use N_2H^+ (1-0) linewidths for each of the cores from Lee, Myers & Tafalla (2001, see also (Karoly et al., 2020)) and correct for the thermal contribution. The column density for each of the cores is given in Table 4.6 and a volume density is calculated using a geometric mean radius. We use the ADF method to calculate the dispersion in magnetic field angles and the resulting histograms are shown in Figure 4.14. The best-fit for both cores was with a fitting limit of 36″, similar to L43 (see Section 3.3.6) and both giving χ^2 <1. The results from the fit and the calculated dispersion in magnetic field angles is given in Table 4.7. We again calculate magnetic field strengths over a range of Q values. For this range, we also calculate the mass-to-flux ratio (λ), Alfvén Mach number ($\mathcal{M}_{\rm A}$), and magnetic field energy ($E_{\rm B}$) using Equations 1.6, 3.9, 3.10 and 1.5 respectively.

The new magnetic field strengths are lower than those calculated in Karoly et al. (2020) where the north core is their core 5 and the south core is their core 3. We calculate a magnetic field strength of 60–130 μG in the densest core (the south) and 50–110 μG in the slightly lower-density northern core. In both cases, the mass-to-flux parameter has a lower limit of ∼2, though as discussed before, there is the possibility in a statistically significant sample that the values may be overestimated by up to a value of 3 in which case the lower limits are ≈2/3. Both of the cores are roughly Alfvénically transcritical. These magnetic field strengths are lower than those found in Karoly et al. (2020) and our lower limit agrees with the value calculated in Crutcher et al. (2004). We also find higher mass-to-flux ratios which would suggest that the cores could be potentially contracting or at least at the stage where the magnetic field is no longer the primary method of resistance to gravitational collapse. Lee, Myers & Tafalla (2001) did find L183 as an infall candidate suggesting it could be evolving towards forming a stellar object.

4.3.6 L1527

As mentioned above in Section 4.2, L1527 is the most evolved of these sources. It has an embedded stellar object (an embedded Class 0/I protostar; van't Hoff et al., 2023), but still maintains a dusty envelope which can be well-observed in the sub-millimeter, but it drives a wide-angle outflow from within and already has a disc forming (van't Hoff et al., 2023). Aside from L1495, it is the other source which is not in a purely isolated environment (see Figure 4.1). The magnetic field as observed by SCUBA-2/POL-2 is shown in Figure 4.15. The overlaid Planck vectors show a large-scale magnetic field orientation of ≈46°. Meanwhile, the average core-scale magnetic field strength is ≈43°. The overall orientation of the semimajor axis of the sub-millimeter bright core is 133° east of north.

The outflow of the embedded protostar was observed by the JWST and an RGB image is plotted in Figure 4.16 with the magnetic field vectors overlaid. There is no clear relation between the outflow and the magnetic field vectors. There are a number of vectors which run perpendicular to the outflow, but these vectors are also perpendicular to the elongated axis of the dust emission. This is seen in Figure 4.17 where those vectors have been highlighted in white. The other vectors on the western periphery of the core do appear to be aligned with the outflow direction and could

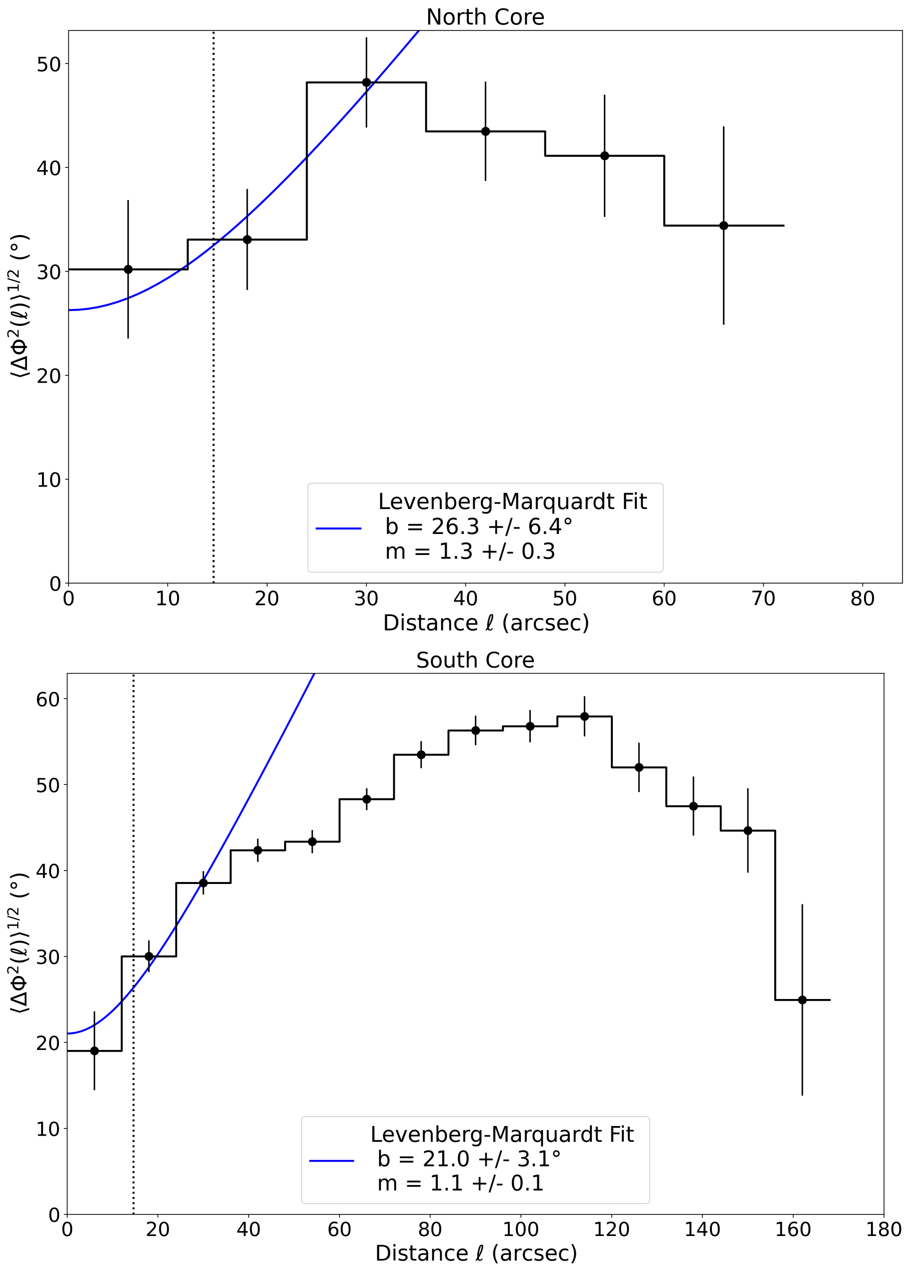

Figure 4.14: ADF histograms for two of the cores in L183. The best-fit parameters are shown in the legend. The first three bins are fit for each core. The beam size is shown with a vertical dashed line. *Left:* Histogram of the northern core. *Right:* Histogram of the southern core.

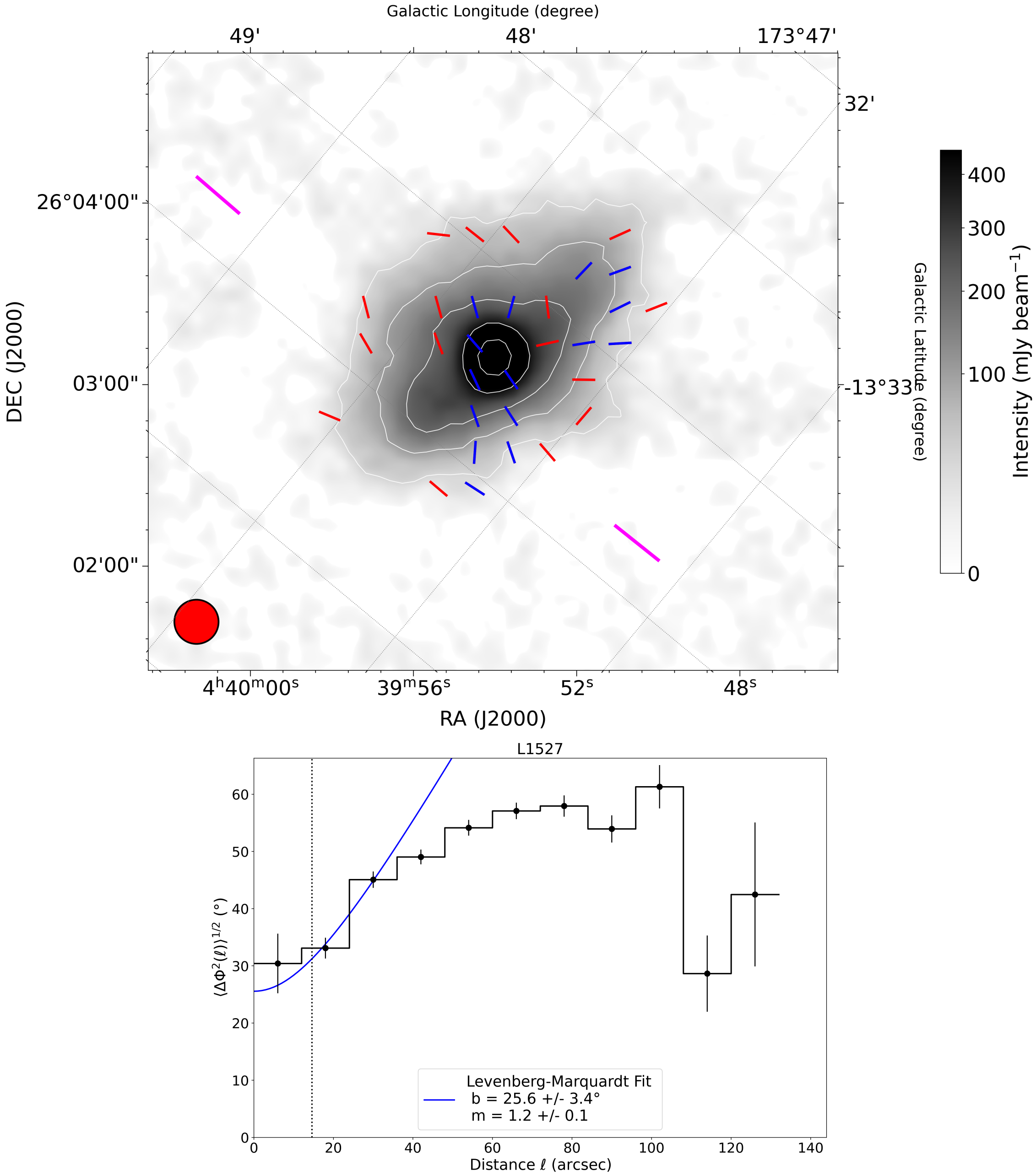

Figure 4.15: Same as Figure 4.3 but for L1527.

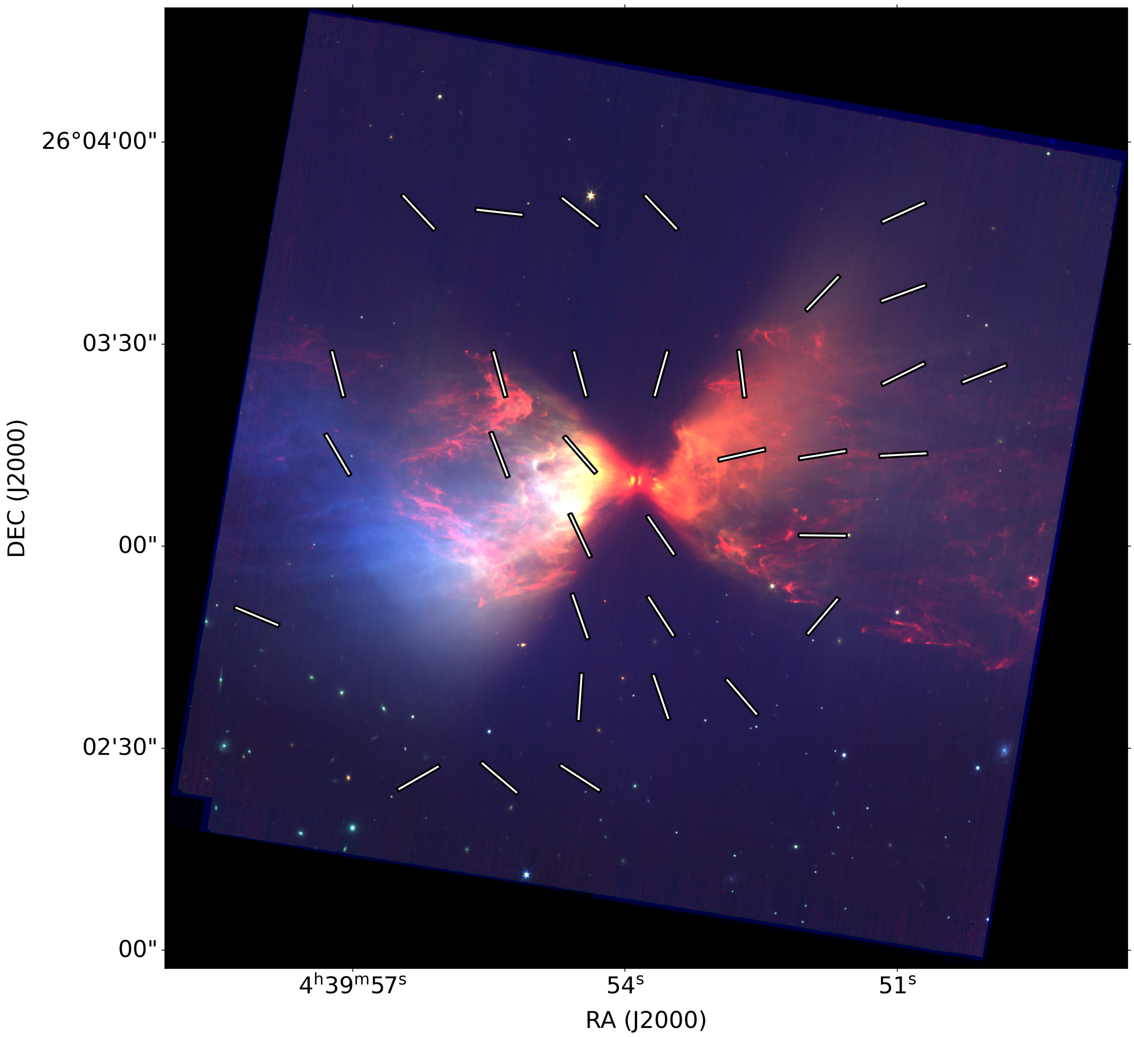

Figure 4.16: An RGB plot of L1527 from JWST. The f444W/f470N filter is shown as red, f335M filter as green and f200W filter as blue and shows the infrared bright bipolar outflow. Overlaid are the POL-2 vectors in white, showing the magnetic field information.

Table 4.8: Compiled and calculated properties of L1527

		L1527
Distance	(pc)	140
FWHM	($'' \times ''$)	40.1×20.1
θ	(°)	133
N(H_2)	($\times 10^{22}$ cm^{-2})	3.1±1.0
n(H_2)	($\times 10^{5}$ cm^{-3})	3.9±1.3
Δv_{NT}	(km s^{-1})	0.27±0.03
E_K	($\times 10^{34}$ J)	17±7
b		21.3±4.5
$\sigma\theta$	(°)	19.1±2.6
B_{pos}	(μG)	45(11)–100(24)
λ		2.3(1.0)–5.1(2.1)
$\mathcal{M}_A$		0.8(0.1)–1.7(0.2)
E_B	($\times 10^{34}$ J)	0.7(0.3)–3.5(1.7)

N(H_2) values from HGBS (André et al., 2010) map provided Kirk (priv. comm.)

Δv_{NT} values taken from Redaelli, Bizzocchi & Caselli (2020)

trace the foreground shell of the wide-angle outflow. The vectors on the eastern periphery appear to have no preferred orientation.

We attempted to calculate a magnetic field strength in L1527 using the same method as Section 3.3.6. L1527 is part of the Taurus Molecular Cloud complex and is a region which was observed as part of the HGBS (André et al., 2010). The region is not yet published, but the column density and temperature maps were provided by the lead of that paper, Dr. Jason Kirk (priv. comm.). The column density value of the core is given in Table 4.8 and we derive a volume density value using the geometric mean of the FWHM of the core. The Δv_{NT} is from N_2H^+ observations performed by Redaelli, Bizzocchi & Caselli (2020) and have had the thermal contribution removed. Considering the evolved source and the present outflow, this value may be higher, but we use the N_2H^+ observation to trace the dust. The outflow is better traced by ^{12}CO and ^{13}CO (Ohashi et al., 1997). The dispersion in position angle is calculated using the ADF method and the histogram is shown in the lower panel of Figure 4.15.

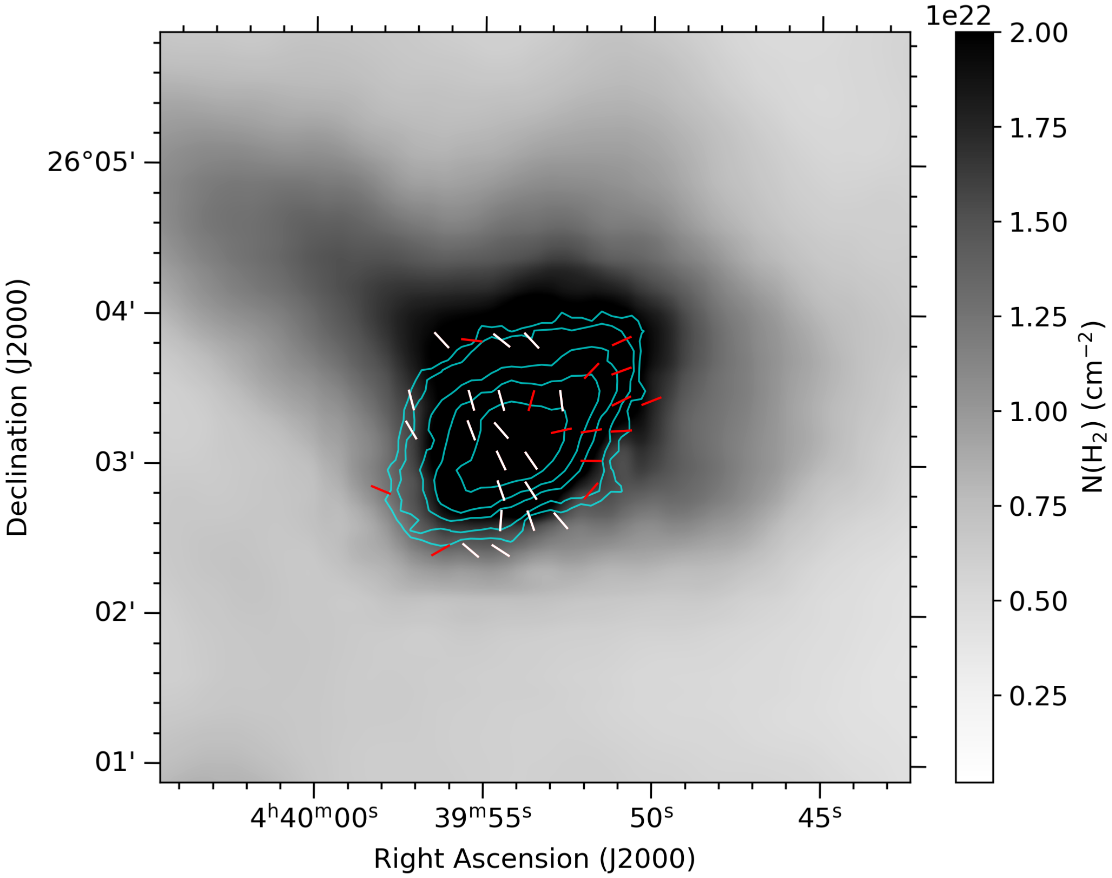

Figure 4.17: A plot of the H_2 column density from the HGBS (André et al., 2010) courtesy of Dr. Jason Kirk (priv. comm.). The plotted contours are showing the 850 μm Stokes I emission. The levels are 30, 50, 100, 150 and 250 mJy beam^{-1}. All of the magnetic field vectors plotted have the S/N cut of I/DI>10 and P/dP>2. Here we now plot vectors in white which we associate with being part of a population perpendicular to the core. The other vectors may be influenced by the outflow as well as seen in Figure 4.16.

Table 4.9: Summary of the magnetic field and core properties of all the sources

Source	θ_{Planck} (°)	$\theta_{\rm core}$ (°)	$\mu_{\theta,B}$ (°)	N(H_2) ($\times 10^{22}$ cm^{-2})	B_{pos} (μG)	λ
L1498	125	125	178	2.9(2.4)	26(12)–57(27)	3.9(3.6)–8.6(8.0)
L1517B	94	0	153	2.0(0.6)	38(11)–84(24)	1.8(0.8)–4.0(1.7)
L1544	53	150	7	5.0(3.9)	60(25)–132(55)	2.9(2.5)–6.4(5.6)
L1527	46	133	38	3.1(1.0)	45(11)–100(24)	2.3(1.0)–5.1(2.1)
L1495 (1)	16	167	98	1.9(0.8)	37(14)–83(32)	1.8(1.0)–3.9(2.1)
L1495 (2-N)	16	0	104	1.5(0.6)	–	–
L1495 (2-S)	16	45	43	1.6(0.6)	–	–
L183 North	88	30	164	2.7(0.8)	51(15)–113(33)	1.8(0.7)–4.0(1.6)
L183 South	88	0	166	3.2(1.1)	58(13)–128(29)	1.9(0.8)–4.2(1.7)
L183 West	88	0	80	1.9(0.6)	–	–

We derive a magnetic field strength of 45–100 μG and find that the core is overall magnetically supercritical. This does make sense considering the presence of a Class 0/I protostar. The interesting result from this object is that the magnetic field appears to still trace the dusty envelope and only at the edges has the outflow potentially affected the magnetic field. But the magnetic field is still perpendicular to the semimajor axis of the core, something which is quite common (Basu, 2000; Pattle et al., 2023). Interestingly, this magnetic field orientation is roughly parallel to the large-scale field, so although the core has obviously been matter-dominated for some extended period of time, the envelope magnetic field still follows the large-scale field.

4.4 Summary

The results from this chapter are summarized in Table 4.9. For each of the BISTRO-3 prestellar sources, we analyzed the magnetic field structure and its relative importance within the core. We also included data from two other sources, one prestellar in L183 and one with a formed protostar, L1527. In the prestellar cores, we calculate magnetic field strengths in the range of 30–130 μG which are of the same order seen in other prestellar cores. These magnetic field strengths generally yield magnetically super-critical cores indicating that the magnetic fields alone are not sufficient to provide support against collapse. Many of the sources are not affiliated with any sort of filamentary structure or larger molecular cloud and most have core-scale magnetic fields which have no imprint of the large-scale field remaining. This could indicate that many of these cores are more evolved and have become matter-dominated. L1498, L1544, L1495 and tentatively L183 are all strong infall candidates suggesting more evolved cores

One of the more evolved cores, L1544, has a highly structured magnetic field that also exhibits the hourglass morphology thought to be a key indicator of ambipolar diffusion and initially dynamically important magnetic fields. The other evolved source, L1527, has a two component magnetic field, one that appears to still be tied to the dusty envelope, with an orientation roughly perpendicular to the semi-major axis of the core and one associated with the bipolar protostellar outflow, similar to L43. L183 has already fragmented into three cores, two of which are magnetically super-critical. The least dense core appears to still have the morphology of the large-scale field associated with it. L1495 is a series of small filaments with a series of 9 cores forming within the filaments. A majority of these cores have mean magnetic field directions perpendicular to their local filament and with no imprint of the large-scale field. Only the least evolved, or least dense, core has a magnetic field similar to the large-scale field.

Chapter 5

Galactic Center

5.1 Overview

In this chapter, we present analysis of the Central Molecular Zone in the center of the Milky Way using SCUBA-2/POL-2 data observed as part of the BISTRO-3 survey. None of the BISTRO-3 data presented here have been published and I have reduced all of the available raw data. The observations are not yet complete but there is sufficient high signal-to-noise data to analyze the region. For the NH_3 data, we were provided reduced velocity data cubes, integrated intensity maps and velocity line width maps by Dr Jürgen Ott (priv. comm.) on behalf of the SWAG survey (Krieger et al., 2017).

This chapter focuses on two results in the CMZ. First we investigate if the magnetic field and the kinematics of the material in the CMZ correlate well on the larger scale. The second result we investigate is how strong the magnetic field is in individual molecular clouds in the CMZ and compare its influence with turbulent motions and gravity, following similar methods to Chapters 3 and 4.

5.2 The Central Molecular Zone

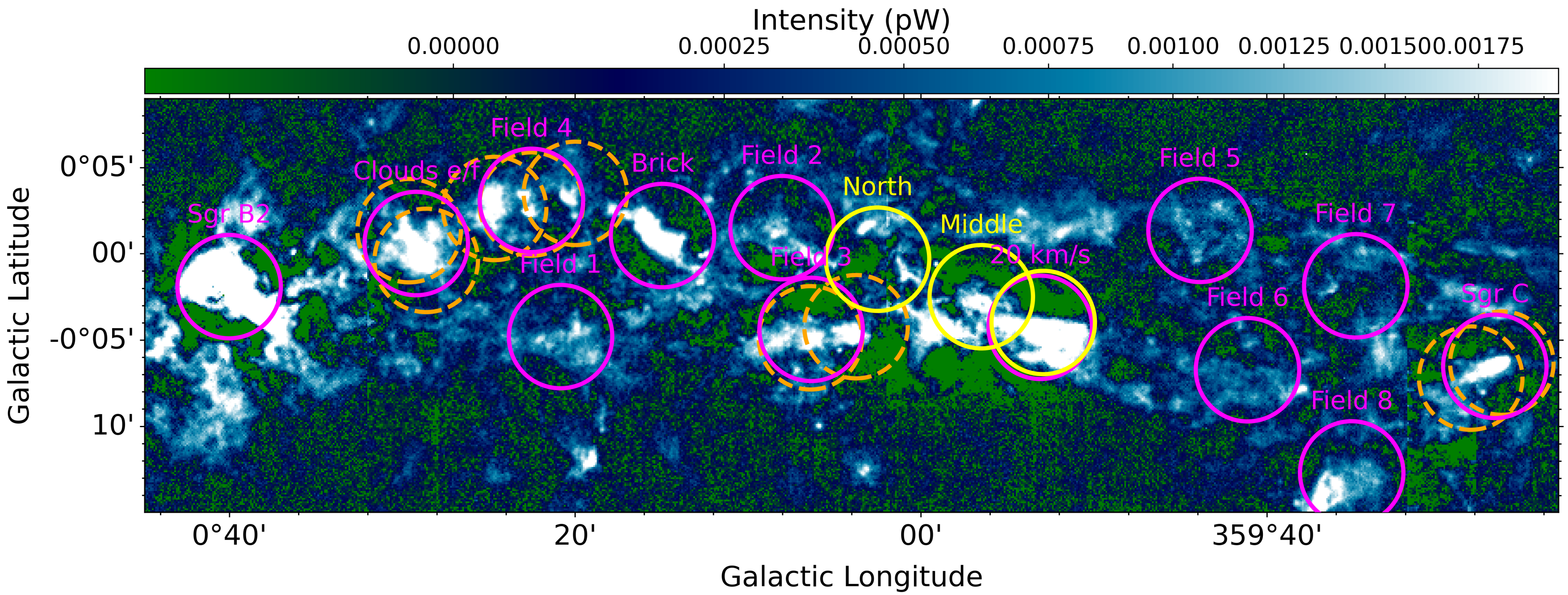

Figure 5.1: Background image is the 850 μm SCUBA-2 map from Parsons et al. (2018). This is a similar figure to Figure 2.10 but now in Galactic coordinates and with the SCUBA-2 (rather than SCUBA) map. Overlaid are the 6′ diameter circles showing the pointings observed towards the CMZ. The purple solid circles are the BISTRO-3 fields. The yellow solid circles are the three fields observed as part of M17AP074. The orange dashed circles are those fields observed as part of M20AP023. The field numbers correspond to Table 2.4.

CHAPTER 5

The Central Molecular Zone (CMZ) of the Galactic Centre is an extreme star-forming environment with large molecular clouds and complex kinematics. It consists of a total molecular gas mass of approximately $5 \times 10^7\,\mathrm{M}_\odot$ (Morris & Serabyn, 1996; Ferrière, Gillard & Jean, 2007) yet sees star-formation rates much lower than what is predicted, by about a factor of 10 (Barnes et al., 2017; Lu et al., 2019). Many mechanisms have been hypothesized to contribute to this reduced star formation rate, including, but not limited to, magnetic fields, turbulence, supernova feedback, episodic mass accretion and episodic star formation in general (Henshaw et al., 2023). The CMZ is highly turbulent with large velocity line-widths and many line-of-sight velocity components seen in a variety of CO and dense tracers (Eden et al., 2020; Krieger et al., 2017). Much of the mass is contained in a series of dense clouds which can be well-observed at sub-millimetre wavelengths (e.g. Pierce-Price et al., 2000; Parsons et al., 2018; Battersby et al., 2020). The most well-known clouds are Sagittarius B1 and B2, Clouds e/f (a part of the Dust Ridge), G0.253+0.016 (known more familiarly as the 'Brick'), the 20kms^{-1} and 50kms^{-1} clouds near Sagittarius A* and then Sagittarius C. These clouds are well observed at 850μm and can be seen in Figure 5.1.

Within the CMZ, the gravitational field is dominated by a variety of components, where the influence of each is determined by Galactocentric radius (Henshaw et al., 2023), but the overall potential is often referred to as the nuclear bulge (Launhardt, Zylka & Mezger, 2002). The orbital structure of the flow of gas is controlled by this gravitational potential. Beyond $\approx$300 pc radius, the current model of the Milky Way is that it contains a stellar bar which influences the gravitational field at that radius (see Figure 5.2a here or Figure 9 of Bland-Hawthorn & Gerhard (2016) for a schematic of our location in the Milky Way). Since the bar plays a role in feeding material to the CMZ through the dust lanes, it also affects the orbital structure of the CMZ (Henshaw et al., 2023). However, the primary gravitational components of the inner ∼100 pc area of the CMZ is the nuclear stellar cluster potential (up to ≈30 pc) and the nuclear stellar disc potential (≈30–300 pc) (Henshaw et al., 2023).

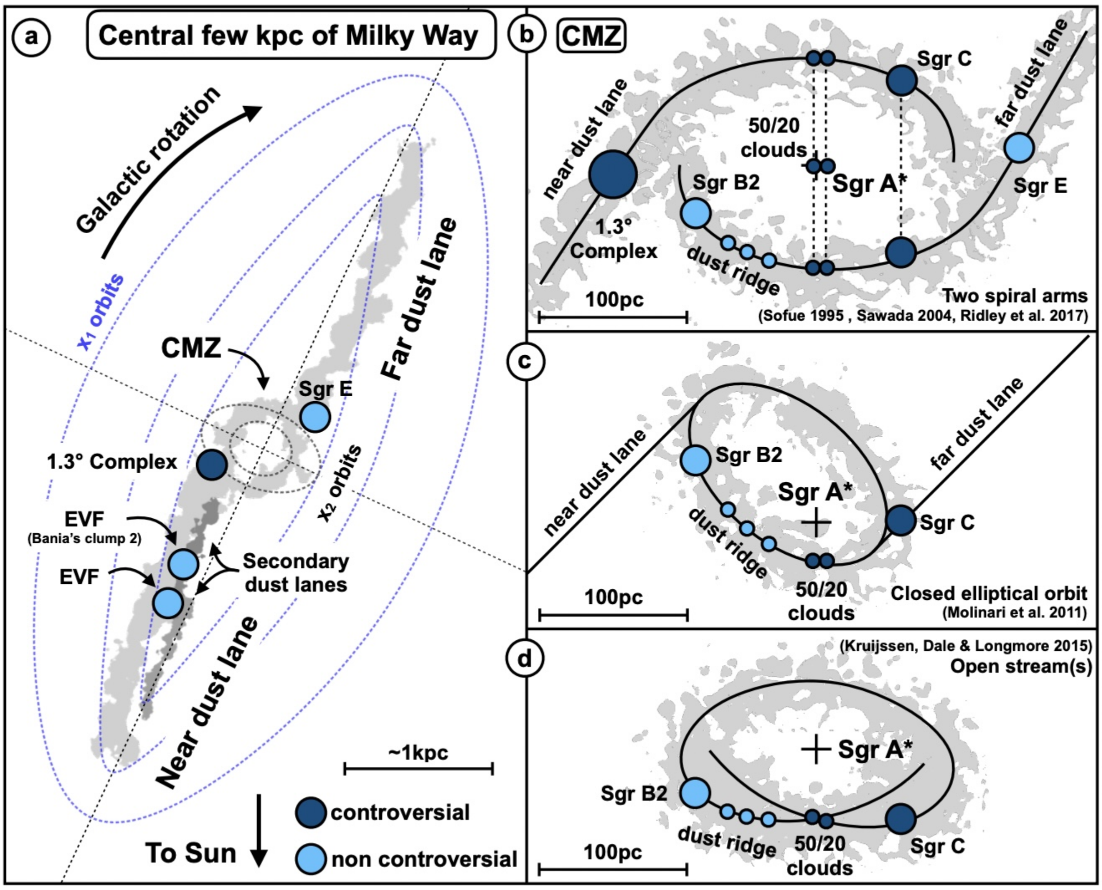

Figure 5.2: Figure 3 of Henshaw et al. (2023) showing the structure of the central few kpc of the Milky Way and then the various proposed orbital models mentioned in the text.

The orbital structure and geometry in the CMZ is not yet agreed upon. The three proposed models are plotted in Figure 5.2 in panels b, c and d. The first structure was suggested by Molinari et al. (2011) which was a closed elliptical orbit that looked like a figure-of-8 on the plane of the sky (a structure initially seen by Pierce-Price et al., 2000) that was inferred from Herschel and FRAO data (see panel c of Figure 5.2). This model was revisited and refined by Kruijssen, Dale

& Longmore (2015), where they used higher resolution velocity data and found a discontinuity in the velocity data which led them to model an open orbit, though still following the figure-of-8 like shape (see panel d of Figure 5.2). Ridley et al. (2017) conducted simulations to propose an orbital model to be explained by nuclear spiral arms feeding the material into the central area, but this model has different views of where the clouds in the CMZ are. Henshaw et al. (2016) compared the three models and found the model from Kruijssen, Dale & Longmore (2015) to fit the l, b, v data the best though it does not have a connection to the larger-scale features such as the dust lanes (see Figure 5.2 where panels b and c show how those orbital models might connect to the dust lanes and 1.3° Complex).

The CMZ is known to have a prevalent magnetic field, with a general global field strength of ∼50 μG on 400 pc scales (Crocker et al., 2010). Previous polarization studies have shown structured magnetic fields in the local clouds of the CMZ (Dotson et al., 2010; Matthews et al., 2009; Lu et al., 2024), though with magnetic field strengths approaching 10s of mG. The large-scale magnetic field observed by Planck and ACT is also well structured and runs largely east/west along the Galactic plane at 353 GHz (Guan et al., 2021). The magnetic field may play a variety of roles across the scales present in the CMZ, from preventing the global collapse of clouds to potentially being coupled to the orbit on which the clouds travel (Kauffmann et al., 2017).

We present here a complete, high resolution mosaic of the magnetic field of the CMZ observed by 850 μm dust emission polarization. With a beam size of $14\farcs1$, we can resolve the magnetic field of the molecular clouds at ∼0.5 pc which is close to the resolution of Planck in our nearby star-forming regions such as Ophiuchus, Perseus and Orion.

5.3 Observing Method

We observed the CMZ at 850 μm using SCUBA-2/POL-2 on JCMT. The observations of the CMZ consist of data from the BISTRO-3 large survey program (Project ID: M20AL018; P.I. Derek Ward-Thompson), data from Lu et al. (2024) (Project ID: M20AP023; P.I. Junhao Liu) and data from the CADC archive (Project ID: M17P074; P.I. Geoffrey Bower). The BISTRO observations were taken during a three year period from February 2020 up to most recently August 2023, the M20AP023 data were observed in June-July 2020 and the M17AP074 data were observed in March-April 2017. For a more detailed discussion of the observations, see Section 2.2.1.2.

The entire CMZ was observed in a total of 16 fields. The goal is to obtain a total coverage of ≈4 hours for each field (this is 8 repeats of ≈31 minutes). Figure 5.1 shows these 16 fields as well as identifying the pointings from M17AP074 and M20AP023. The Sgr A south field was a combination of data from BISTRO and M17AP074. Fields 3, 4, 9 (Sgr C) and Clouds E/F are a combination of data from BISTRO and M20AP023. Unfortunately due to time constraints, Fields 1-10 have not yet been fully observed to the desired 4 hours, but these are the additional fields to fill out the mosaic and do not center on any of the significant molecular clouds. The completed and still required time is summarised in Table 2.4. However, we have sufficient signal-to-noise ratio (SNR) across the whole CMZ and at least a repeat on enough fields so that we have an entire mosaic and can present the observations to date. The Stokes I, Q and U maps can also be seen in Figure 5.3.

5.3.1 Additional data reduction steps

In the first step, the raw bolometer timestreams are separated into separate Stokes I, Q and U timestreams for each individual field as described in Section 2.3.2 and initial auto-masked Stokes I maps are created. We then mosaic those initial Stokes

I maps to create a full coverage Stokes I map.

The second step of the reduction creates the final Stokes I, Q and U maps and we follow a similar method to the first step where each field is reduced separately. However, for each field, the mosaicked Stokes I map from step 1 is used as the template for masking, including the 'AST' and 'PCA' masks described in Section 2.3.3. We included the parameter *skyloop* (see Section 2.3.3) but decided against using *mapvar* (see Section 2.3.3) as each field only has eight repeats and so there are not enough repeats to characterize the noise well with *mapvar* (see Section 2.3.3). After each individual field is reduced, we mosaic the final Stokes I, Q and U maps of each field and then calculate a resulting polarization vector catalog. As described in the prior chapters, this vector catalog was then binned to $12''$ to increase S/N and attempt to compensate for the JCMT beam size.

5.4 Setting up the orbital model

5.4.1 The Stokes *I* map

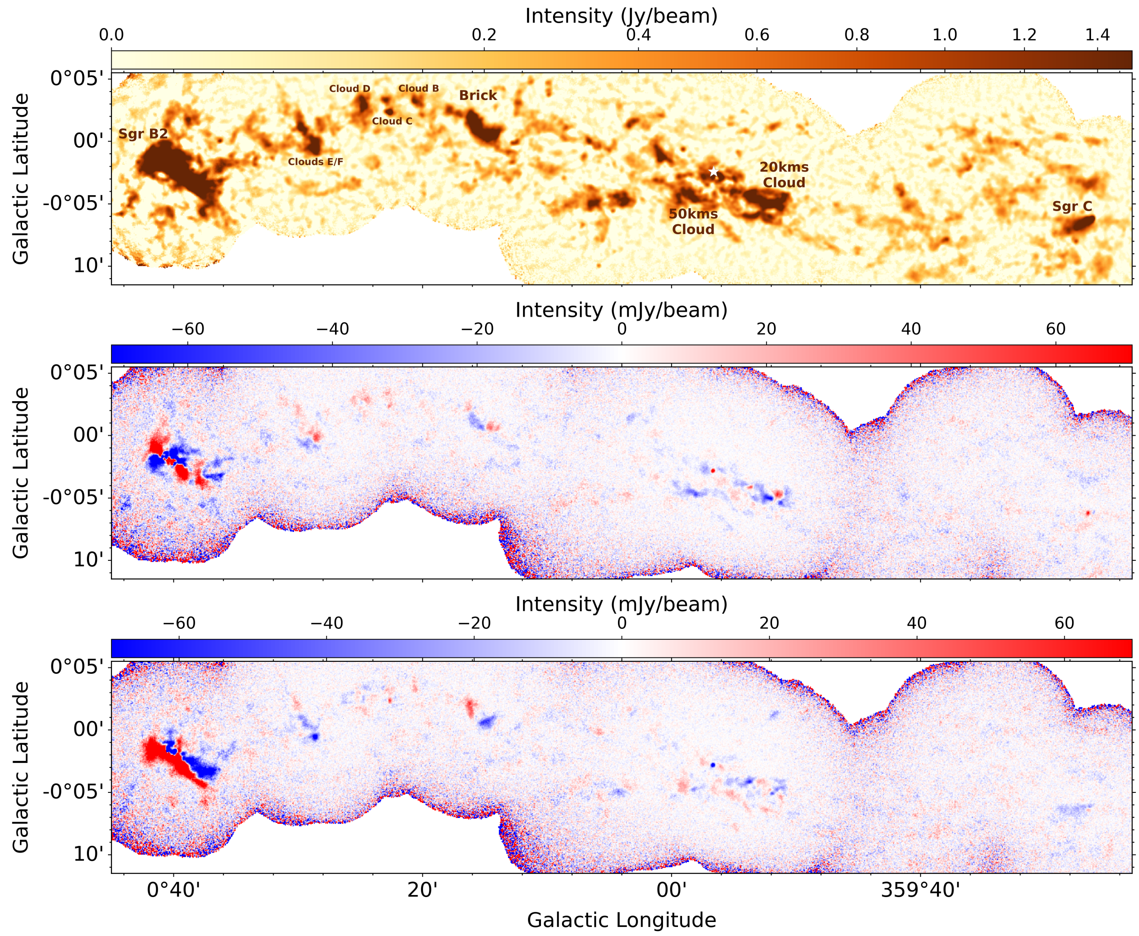

Figure 5.3: *Upper:* 850 μm Stokes I continuum. *Middle:* 850 μm Stokes Q continuum with the colormap spanning $\pm 10\,\delta Q_{RMS}$. *Lower:* 850 μm Stokes U continuum with the colormap spanning $\pm 10\,\delta U_{RMS}$. The main CMZ molecular clouds are labelled in the upper panel.

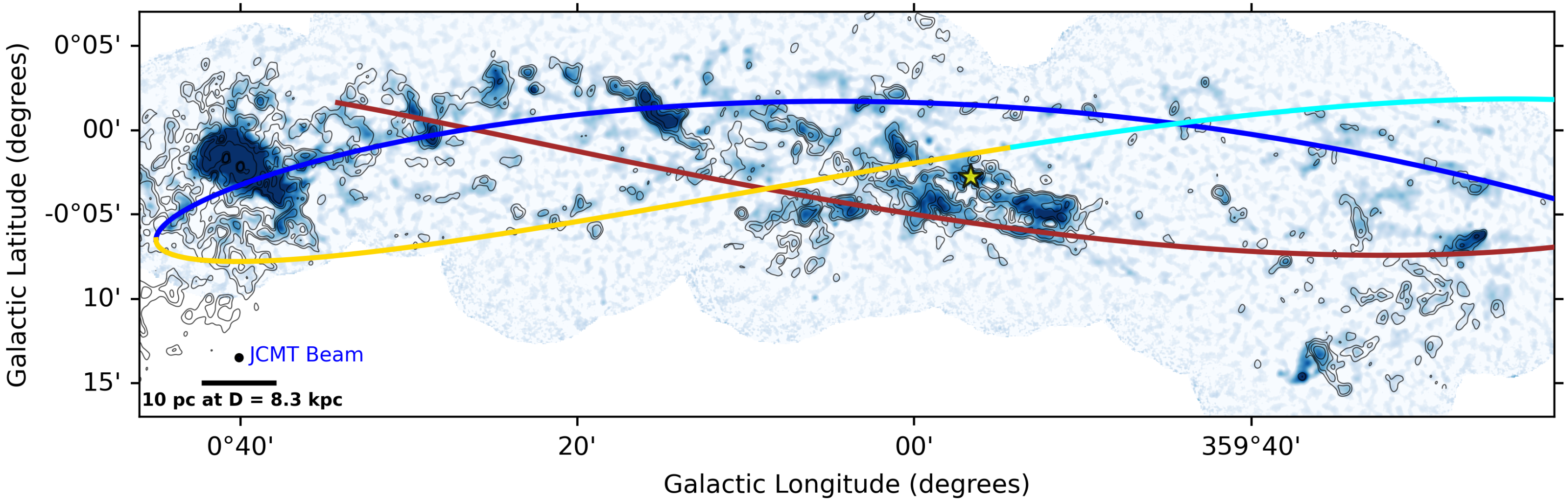

Figure 5.4: The orbital model from Kruijssen, Dale & Longmore (2015) is plotted over the 850 μm Stokes I dust emission from SCUBA-2/POL-2. The black contours trace the integrated SWAG NH_3 data. Sgr A* is marked with a yellow star.

Figure 5.4 shows the orbit from Kruijssen, Dale & Longmore (2015) plotted over the 850 μm dust emission form this work. Kruijssen, Dale & Longmore (2015) used the NH_3 data to determine where the dense structures were in the CMZ and they used the NH_3 velocity information to verify that their orbital model was physical. The NH_3 emission can be seen with the black contours in Figure 5.4 where the plotted orbit does trace many of the densest areas. It can also be seen that the NH_3 data traces the dense dust emission very well, justifying the fact that the NH_3 emission will trace dense areas. However, it can also be seen that the proposed orbit from Kruijssen, Dale & Longmore (2015) does not trace a lot of the dense structures we see at 850 μm.

We therefore use our 850 μm observations as the primary tracer of the dense material and require that our proposed orbit would trace as much of this material as possible. The model from Kruijssen, Dale & Longmore (2015) was a ballistic orbit model which theoretically shows the orbit of a particle placed in the CMZ based on a gravitational potential assumption and then this was checked with the velocity data along the orbit. We instead start with direct observations of the material and use it as a guide for what our orbital model will look like, and then aim to check our orbital model with similar gas kinematic data. We start the orbital model to the west at Sgr C and move east, following dense structures and their elongation where it appears to follow the general orbit. We do use the Kruijssen, Dale & Longmore (2015) model as a guide as well since it is known to be a good initial fit. However we do not have enough information to construct an entire orbit since we do not see a lot of emission in the southeastern quadrant of our map. We therefore refer now to our model as a stream which is more realistically a 'half-orbit.'

5.4.2 The magnetic field map

The second step was to use the magnetic field information to refine our guess of the stream. Figure 5.5 shows the orbital model from Kruijssen, Dale & Longmore (2015) but with our magnetic field vectors plotted as well (binned to 28″). Again, their orbit does not trace any of the magnetic field material very well, but this is perhaps not surprising because we already know that it does not trace all of the 850 μm dust material which is where the magnetic field information comes from. If the material was moving through the CMZ along an orbital model, we would expect to see some sort of preferential alignment, most likely parallel, with the magnetic field. This is because if the magnetic field is flux frozen in the material, then as the material moved it would drag the magnetic field lines and would preferentially drag it along the field lines rather than across them.

We selected our polarization vectors with strict SNR criteria, where $I/\delta I > 50$, P/δP >3, δP <2% and P<25%. This strict cut in Stokes I should ensure that we are tracing the high signal-to-noise regions and areas with the highest density. Since this initial fit is by-eye, we try and follow our 850 μm material while also choosing areas of emission which have magnetic fields that appear parallel to the orbit at that point. If we do see areas of a perpendicular magnetic field we try and avoid it, though not at the expense of missing the dense structure. This is most likely a biased method and we would expect to see alignment of the magnetic field and our orbit, but if this orbit is aligned with the magnetic field and is coherent in position-velocity space, then it would be a valid model.

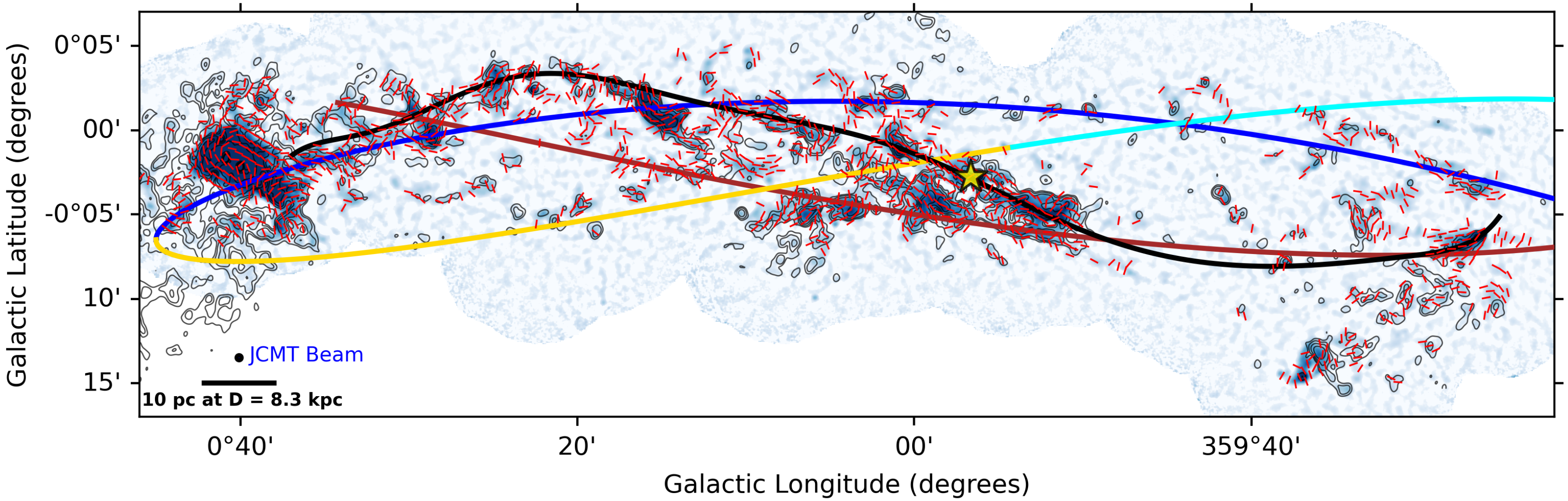

Figure 5.5: The orbital model from Kruijssen, Dale & Longmore (2015) is plotted with our proposed stream plotted in black. The background image is the 850 μm Stokes I dust emission from SCUBA-2/POL-2 and the red vectors represent the magnetic field orientation and the black contours trace the integrated NH_3 data.

We plot our model then in Figure 5.5, plotted against the orbit from Kruijssen, Dale & Longmore (2015). The influence of the dense material but also of the initial estimate from Kruijssen, Dale & Longmore (2015) can be seen in the right half of the image where our plotted stream follows theirs well up until Sgr A* and the 20 km/s cloud where we move our stream further north to both trace those dense clouds and the northeast–southwest magnetic field orientation at that point. The left half of the image is where our model deviates significantly as we try and connect the Dust Ridge clouds with our stream and trace that dense material closely. The left hand side of our stream may be closer to their dark blue 'Stream 2' but that is then not connected to their brown 'Stream 1' which is what our right half of the model traces well. We will investigate this possible discontinuity in Section 5.5.1 and we remain open to the idea that our traced model is in fact two separate streams and we investigate these two streams separately below. When viewed from above, the open orbital model from Kruijssen, Dale & Longmore (2015) looks like a pretzel (see Figure 5.2d and lower right panel of Figure 5.6) where Streams 1 and 2 both wrap around behind each other.

5.4.3 Velocity fitting

Previous studies determining the orbital structure in the CMZ for the most part relied largely on velocity information (see Molinari et al., 2011; Kruijssen, Dale & Longmore, 2015; Ridley et al., 2017; Sofue, 2022). Although we are approaching this from a B-field-first point of view, we must ensure that our proposed structure is coherent in velocity space. We used NH_3 (3-3) data (see Section 2.4.2) from the SWAG survey (Krieger et al., 2017) to probe the velocity structure because it is able to trace the dense structures that coincide with the material that is observed at 850 μm by SCUBA-2/POL-2 (see Figure 5.4).

The CMZ is incredibly chaotic when it comes to velocity data with different

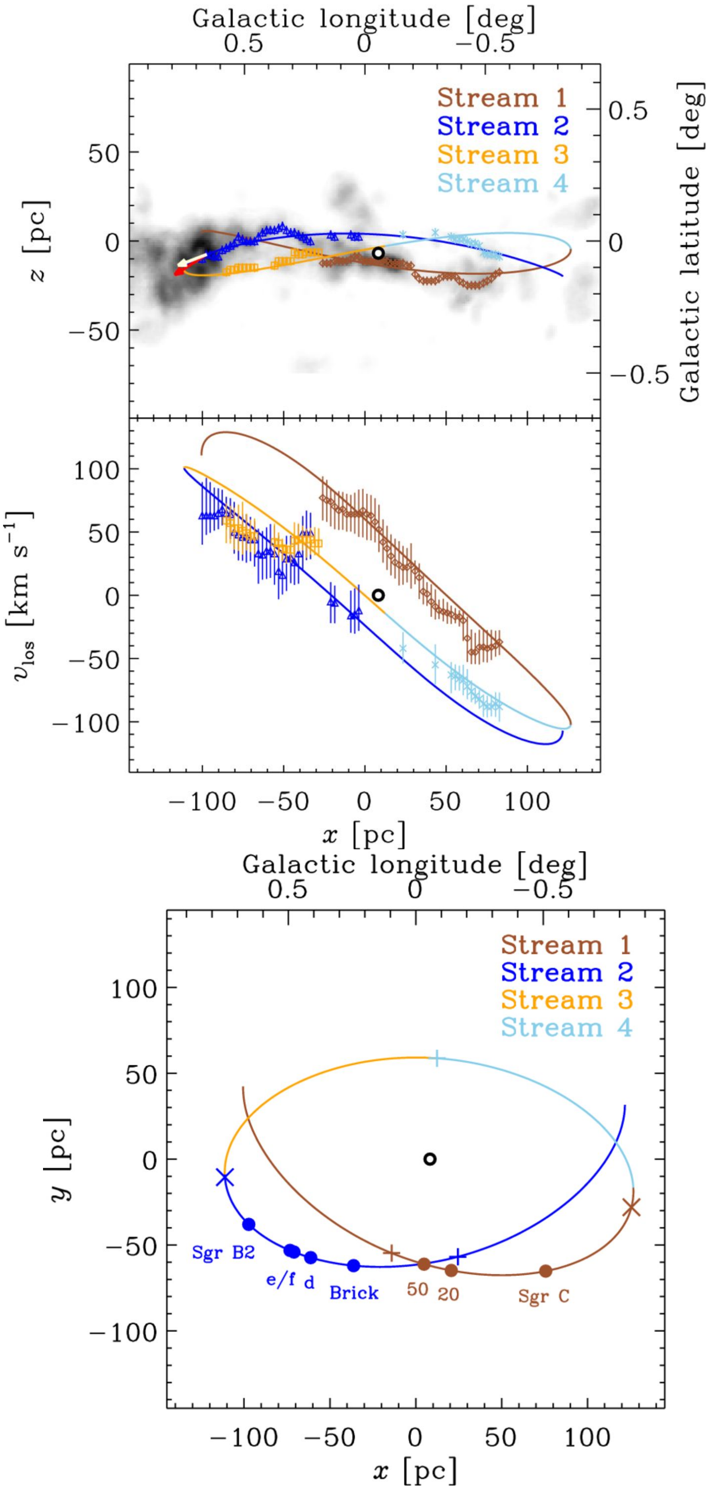

Figure 5.6: Figures 4 and 6 taken from Kruijssen, Dale & Longmore (2015) are shown. The upper panel is their orbit plotted on the integrated NH_3 greyscale and below it is the position-velocity diagram. The lower panel is a birds eye view of the orbit, illustrating the pretzel shape, with the observer in the negative y direction.

line-of-sights containing between one and five velocity peaks. This is seen in the NH_3 data (Krieger et al., 2017) as well as ^{12}CO, ^{13}CO and $C^{18}O$ data (priv. comm. David Eden; Eden et al., 2020). It can be very difficult to determine which of the peaks correspond with the same material we observe and further which of the peaks correspond to perhaps the larger orbital flow of the material. We show five NH_3 (3-3) spectra examples in Figure 5.7.

In order to evaluate the velocity data, we went pixel-by-pixel in the provided NH_3 (3-3) data cube and extracted the spectrum which goes from $\approx$-250 to 250 km/s. We determined a noise level from the baseline of the spectrum and set a requirement that a peak in the data would need to be above a SNR of 10. We used the python package *lmfit* (Newville et al., 2023) to set parameters and bounds for our Gaussian fits and performed the fitting by creating a single Gaussian and a double Gaussian model and then using the fit command. Examples of these spectra and the fitted Gaussians can be seen in Figure 5.7.

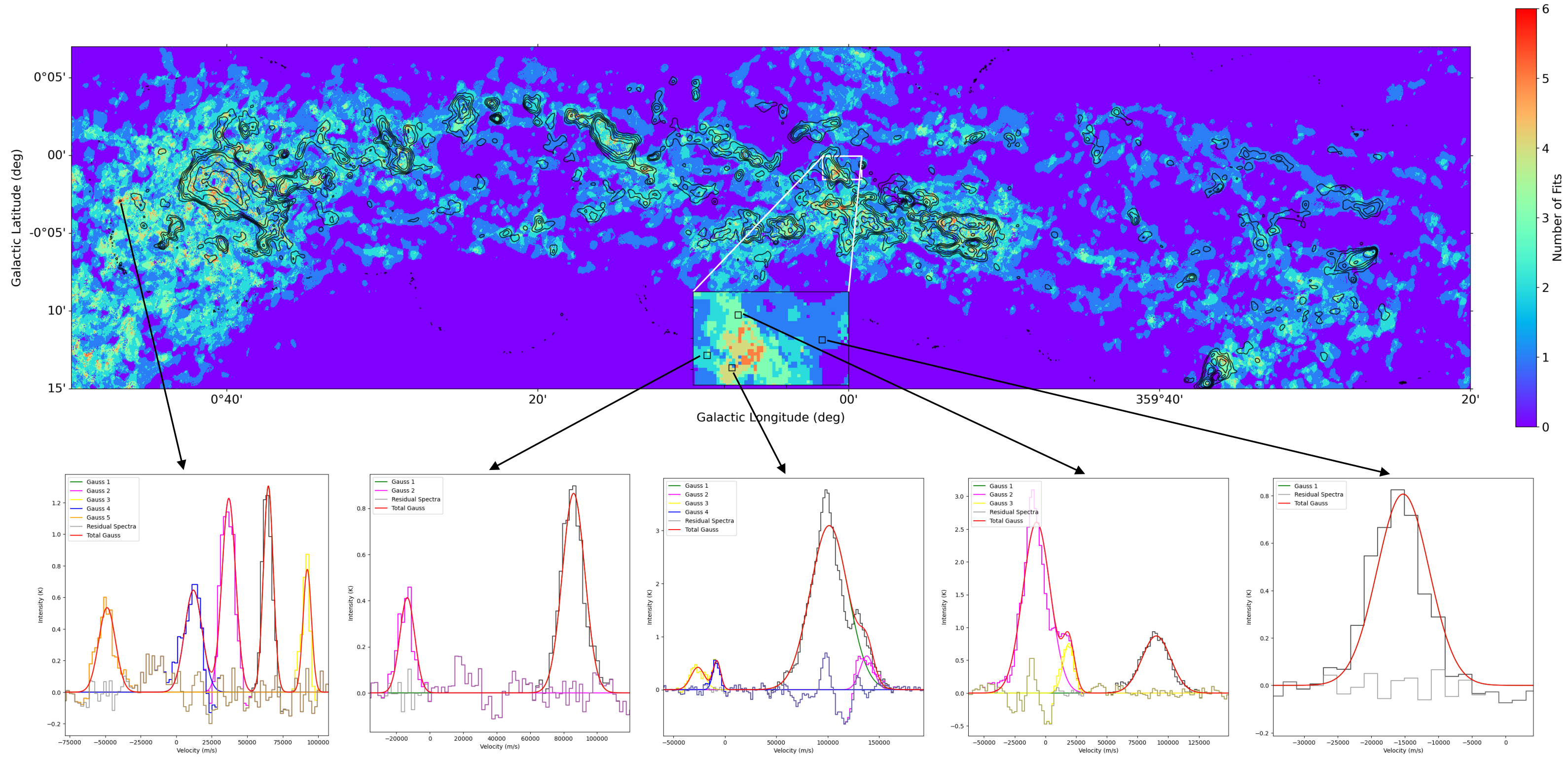

Figure 5.7: The background image shows the number of velocity components fit to the NH_3 data. The black contours trace the 850 μm dust emission from this work. The inset is of the square region and shows examples of areas of the clouds with one, two, three or four velocity components present. The fifth spectra taken from east of Sgr B2 shows 5 velocity components. The fit Gaussians are also overplotted with a red fit that is the sum of all the Gaussians. The residual spectra after all the Gaussians have been removed is plotted in grey.

We tried fitting both a single and double Gaussian each iteration. We determined which of the two were the best fit from two parameters, the Akaike information criterion (AIC) and the Bayesian information criterion (BIC). We checked first if either fit had the lowest values for both parameters at which point we took it to be the fit. If they had mixed results, we focused on which fitting parameters had the largest differences to try and figure out which fit was better. We provided bounds and initial fit estimates for each fit and safeguarded against the fitting routine failing to fit and simply using the bounds or initial guess as the 'best-fit.' Our code then determines which of the two fits is best, subtracts that fit from the spectrum and then tries to fit a spectrum again until it no longer finds peaks above the certain amplitude threshold which we set based on the noise level of the spectra. This routine worked well and many fits were checked by eye to ensure it was running properly. Figure 5.7 shows the number of fits found across the CMZ with five examples of the fit spectra. As an additional initial test of our fitting method, we checked our position-velocity plots made using the orbit from Kruijssen, Dale & Longmore (2015) to ensure we were identifying the correct peaks and we found the same velocity information along their orbital model as they did.

5.5 Comparison of the magnetic field and orbital structure

Figure 5.5 shows the orbit from Kruijssen, Dale & Longmore (2015) plotted over the Stokes I emission and magnetic field morphology. Figure 5.6 also shows the position-velocity diagram of the Kruijssen, Dale & Longmore (2015) orbit. We needed to ensure that our proposed stream would still fit the l, b, v data and as mentioned above, the model from Kruijssen, Dale & Longmore (2015) is suggested to do this the best. Most of the dense structures we are tracing are considered to be in the foreground of Sgr A* (see Section 4.3.2.2 of Henshaw et al., 2023). Because we do not have any magnetic field information of the orbit behind Sgr A*, we only aim to fit half of the elliptical orbit, hence getting our stream. In the context of the Kruijssen, Dale & Longmore (2015) model, we are ignoring Streams 3 and 4.

Having obtained a series of l, b coordinates from the by-eye fit, we then fit it with a polynomial to get an equation for the continuous stream through the CMZ. This way we can calculate the stream orientation at any position along it in order to compare it with magnetic field data. As mentioned above, this is most likely a biased fit in some regard since we focus on bright areas in the sub-millimeter and areas with many vectors as well as vectors that would follow that stream structure. The areas which are bright in the sub-millimeter also trace the cold dust, so our magnetic field information is only for some of the material in the CMZ. However, the velocity material we use to analyze the stream traces the dense material as well so we can be confident that we are tracing the kinematics of the same material we have magnetic field information for. Future analysis will be to develop a method for investigating a variety of potential streams and orbits to see which are best-aligned with the magnetic field and if that stream is still coherent in velocity space, and eventually agree with the gravitational potential models of the CMZ.

To determine the magnetic field structure along the stream, we start at the western end of the stream (at $\ell \approx$-0.58° or 359° 25′) and move along it in step sizes of 90″. At each point, we make a 90″×90″ box and then take the circular average of the magnetic field vectors within that area. This method does create the opportunity for vectors on the edge of those boxes to skew the circular mean. Future iterations will reduce the box size. We have already done so for step sizes and box sizes of 45″ and 45″×45″ respectively. These results show a similar trend to what we find with the 90″ bins. We then find the difference between the stream gradient at that point and the average magnetic field orientation. A value of 0 would then indicate that

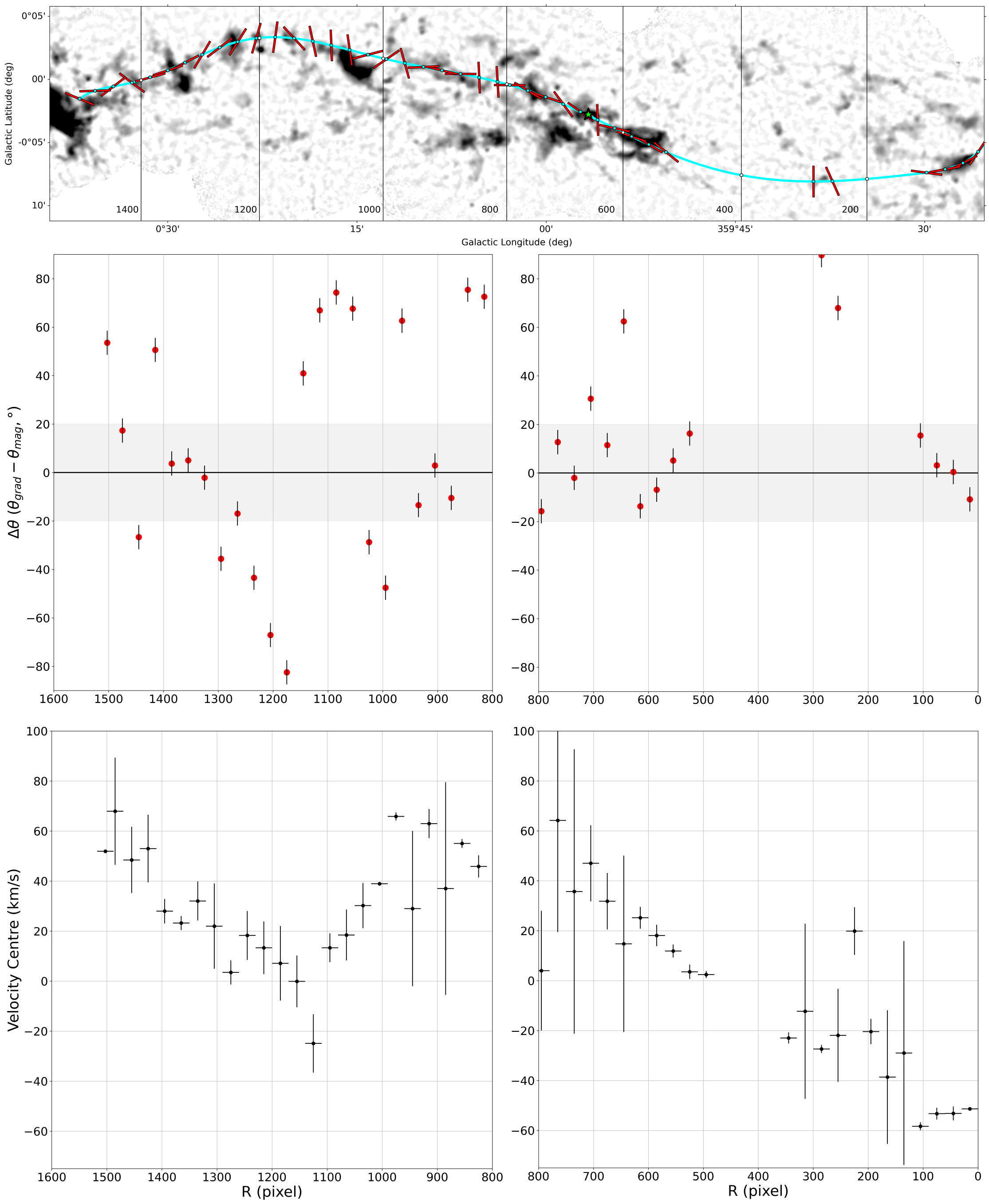

Figure 5.8: The stream is plotted as a cyan line on the 850 μm dust emission. The circular average of the magnetic field orientation is plotted as a red vector. Vertical lines show the location of distances along the stream in units of pixels (1 pixel is 3″). The second row shows the difference between the stream gradient and the local magnetic field orientation. The x-axis is distance along the stream which corresponds with the vertical lines drawn in the plot above. The choice for the two regions is discussed in Section 5.5.1. The lower row shows the 1st velocity component from the NH_3 data along the stream.

the magnetic field and stream are well-aligned.

As mentioned above, we started from a by-eye fit considering the dense clouds and the magnetic field, both traced at 850 μm. We therefore do expect some alignment. We check that our stream is still physical by investigating the kinematics along the stream, and we find that the stream is generally continuous in position-velocity space and it agrees well with what is found in Kruijssen, Dale & Longmore (2015).

5.5.1 Velocity structure

The bottom row of Figure 5.8 shows the identified velocity peaks along the stream. The velocity values along the stream have been binned to 30 pixels (which is 90" due to the 3" pixel size of the SWAG maps) in order to match the magnetic field information. The velocity points in these plots are the mean of the primary components within the 90$''$ box. The velocity structure along the first part and final part of the stream are well followed by our proposed stream, but the middle region between 700-1100 pixels shows significant scatter. When taking into account the other velocity peaks along this strema (i.e. not just the highest amplitude peak), there is a general trend from 25 km/s up to 75 km/s as we move along the stream in the middle region, but within the error bars it could also be a constant velocity. When considering the lower panel of Figure 5.6, this area, which is between 0 to -50 pc on the x-axis, coincides with where there is overlap between the tails of the open orbit and the part we are tracing.

Our velocity structure in the first part agrees well with what was found independently in Kruijssen, Dale & Longmore (2015). This part of our stream follows roughly their Stream 1 (see the brown stream in Figures 5.5 and 5.6). Their Stream 1 goes from ≈-50 km/s to +50 km/s though extends further towards positive longitudes than our first part. Our first part goes from ≈-50 km/s up to 40-50 km/s around the aptly named 20 and 50 km/s clouds near Sgr A (a little before the 600 mark in Figure 5.8). Our second part picks up at the ≈+50 km/s mark, but again as mentioned above, somewhat stagnates and decreases. We see then the trend continue from ≈+20 km/s around R=1200 up to nearly +80 km/s as we approach Sgr B2 (R≈1500). This is where our model differs from Kruijssen, Dale & Longmore (2015) where our second part coincides with their Stream 2 which is not connected to Stream 1. We propose that this can be reconciled by the projection of the orbit from our view on Earth. Again referring to the lower panel of Figure 5.6, the angle from which we are viewing this orbit means we have multiple streams along the line of sight. The 20 and 50 km/s cloud region is an area where the orbits cross which makes it difficult to decompose and then the region up to the Brick (R≈1100) is where Kruijssen, Dale & Longmore (2015) found a discontinuity in their orbit and where we struggle to reconcile this as well.

5.5.2 Magnetic field structure

The difference between the gradient of the stream and the local average magnetic field orientation (as explained above in Section 5.5) is shown in the middle row of Figure 5.8.

Due to the concept that the magnetic field is 'flux-frozen' into the gas (and therefore dust), the magnetic field will either follow the movement of the material or will direct the material. The magnetic field will resist charged material from flowing across it and so we expect the general flow of material to be parallel to the magnetic field lines. This may only be the case on the large-scale and in more diffuse areas where individual cloud gravity will not affect the magnetic field (i.e. no gravitational contraction will tangle the lines or move them to perpendicular to the material). This assumes that it is not gravitationally dominated, at which point the neutral material could collapse across magnetic field lines and bend them (Mestel,

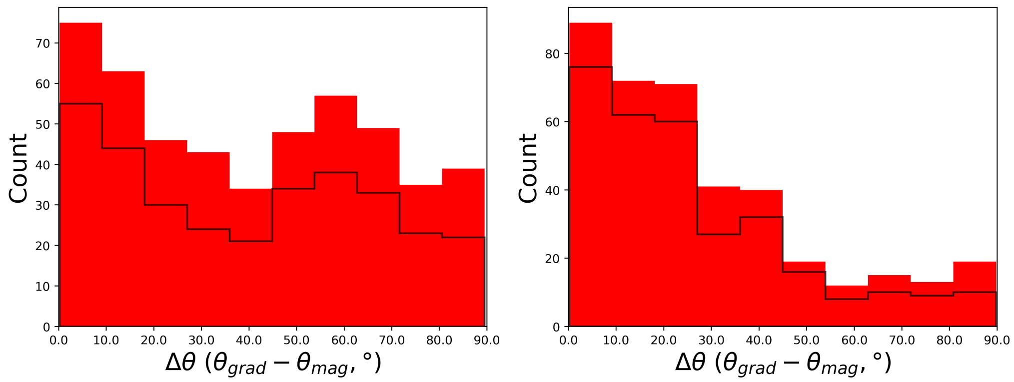

Figure 5.9: A histogram of the absolute value of the difference between the local gradient and the magnetic field orientation. The binning is 9° which corresponds to the approximate δ_θ signal-to-noise cut of our data. The left plot is 'part 2' where R>800 and the right plot is 'part 1' where R<800. The black histogram lines show the same distribution but with a cut in Stokes I of $I > 300$ mJ/beam.

1965).

The material that we are tracing at 850 μm is most likely not gravitationally dominated. This is because the star formation is much lower than is expected, meaning things are not collapsing. The CMZ is also incredibly turbulent and this is often the reason that is given for why the star formation rate is so low. As can be seen in Figure 5.5, the magnetic field is also very structured in these molecular clouds and this qualitatively suggests that some of the clouds have not undergone any large-scale gravitational contraction. However, there may be gravitational contraction on the smaller scales such as those probed by ALMA.

Given this scenario in the CMZ, we would expect the magnetic field lines to align with the orbital model. As can be seen in Figure 5.5, they do not align very well with the model from Kruijssen, Dale & Longmore (2015). The second row of Figure 5.8 shows that on the right side, the magnetic field does have a tendency to align with the stream we have plotted. When averaging magnetic field vectors within a 90″ box, 75% of the regions in the first part fall within $\Delta\theta$=0±20° while only 33% do in the second part. When averaging magnetic field vectors within a $45''$ box, 59% of the regions in the first part fall within $\Delta\theta$=0$\pm$20° while only 18% do in the second part. This is using all of the data points shown in Figure 5.8. However, there are two data points around the 300 pixel mark which are in a low signal to noise area and may be not associated with the stream. We also see other velocity components in this area, so those clouds may not be associated with the general stream. Without those two data points, only two others are preferentially not parallel. We may see this stream continue beyond the R=800 pixel mark into the three data points around R=900 pixel where this is the tail end of the Stream 1 from Kruijssen, Dale & Longmore (2015). This would suggest the magnetic field traces the Stream 1 very well, while everything on the left side, towards their (Kruijssen, Dale & Longmore, 2015) Stream 2 and beyond our 900 pixel mark is not well traced.

Another way to visualize this preferentially parallel behavior is to plot a general histogram of $\Delta\theta$. This is done in Figure 5.9. Again, $\Delta\theta$=0° indicates a parallel alignment and $\Delta\theta$=90° indicates a perpendicular alignment. Using the same error boundary as the middle plots of Figure 5.8, we use $\Delta\theta$ <20° to indicate 'preferentially parallel.' Both sides do show a preferential parallel nature, but the area R<800 (right plot of Figure 5.9) has a more distinct peak at $\Delta\theta$=0°.

If we apply a lower limit cut to Stokes I value where we require Stokes $I >$ 300 mJy/beam to ensure we are tracing the bright/dense stuff and replot the histograms in Figure 5.9, the peak at $\Delta\theta$=0° is more distinct for R<800. This is shown with the black histogram outline in Figure 5.9.

5.6 Magnetic field strengths and morphologies in the CMZ

5.6.1 Magnetic field strengths

For each cloud, we followed the same method as Section 3.3.6 to derive a magnetic field strength. To determine the volume density in each of the clouds, we used H_2 column density maps from the AzTEC survey (Tang, Wang & Wilson, 2021). The AzTEC maps are made with 160, 250, 350 and 500 μm *Herschel* maps as well as a 1.1 mm LMT map that was combined with Planck 353 GHz (850 μm) and CSO/Bolocam 1.1mm maps to recover the extended emission. To then calculate volume densities, we used a geometric mean radius of the regions to determine the depth of the cloud. This is a good approximation but can be an over-simplification if clouds are steeply inclined. For the non-thermal velocity line widths, we used the SWAG NH_3 maps (see Section 2.4.2, Krieger et al., 2017). We use the ADF method to calculate the dispersion in position angles. An example calculation is shown in Figure 5.11 for Sgr C. For most regions we fit only the first three bins as in previous chapters.

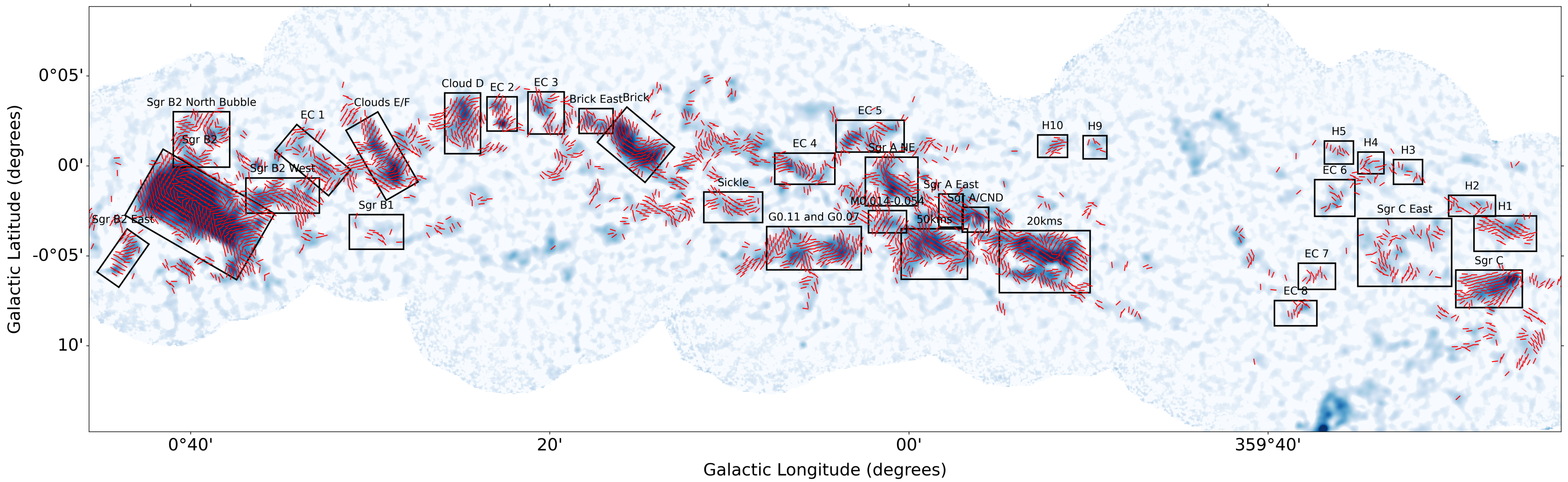

Figure 5.10: Background image is the 850 μm Stokes I dust emission from SCUBA-2/POL-2. Red line segments are plotted which show the magnetic field direction (polarization vectors rotated by 90° and binned to 14″). The regions in which we attempt to use the ADF method to calculate magnetic field strength are outlined in black boxes. 'EC' just stands for 'extra cloud,' which is a region with significant magnetic field detections that is not associated with a known cloud. The clouds which start with 'H' correspond to those found in Henshaw, Longmore & Kruijssen (2016).

For each of the clouds, we calculated the magnetic field strength assuming a Q value of 0.5 which is the approximation used (Ostriker, Stone & Gammie, 2001) when not using the range of values as in Chapters 3 and 4. We then also calculated the Alfvén Mach number and the mass-to-flux ratio. A histogram of these results are plotted in Figure 5.12. We were able to calculate values in 24 of the 34 regions shown in Figure 5.10. Overall there is a general trend of magnetic field strengths greater than 1 mG and the clouds being sub-alfvénic and magnetically sub-critical. This indicates that magnetic fields could be important on an individual cloud scale. Some nearby star-forming clouds also have similar ~mG field strengths, such as Orion A (Pattle et al., 2017) and Oph A (Kwon et al., 2018). While there are many factors which could contribute to suppressing star formation in the CMZ, the magnetic field strengths are strong enough to be considered as one of the primary suppressants.

5.6.2 Sagittarius C region

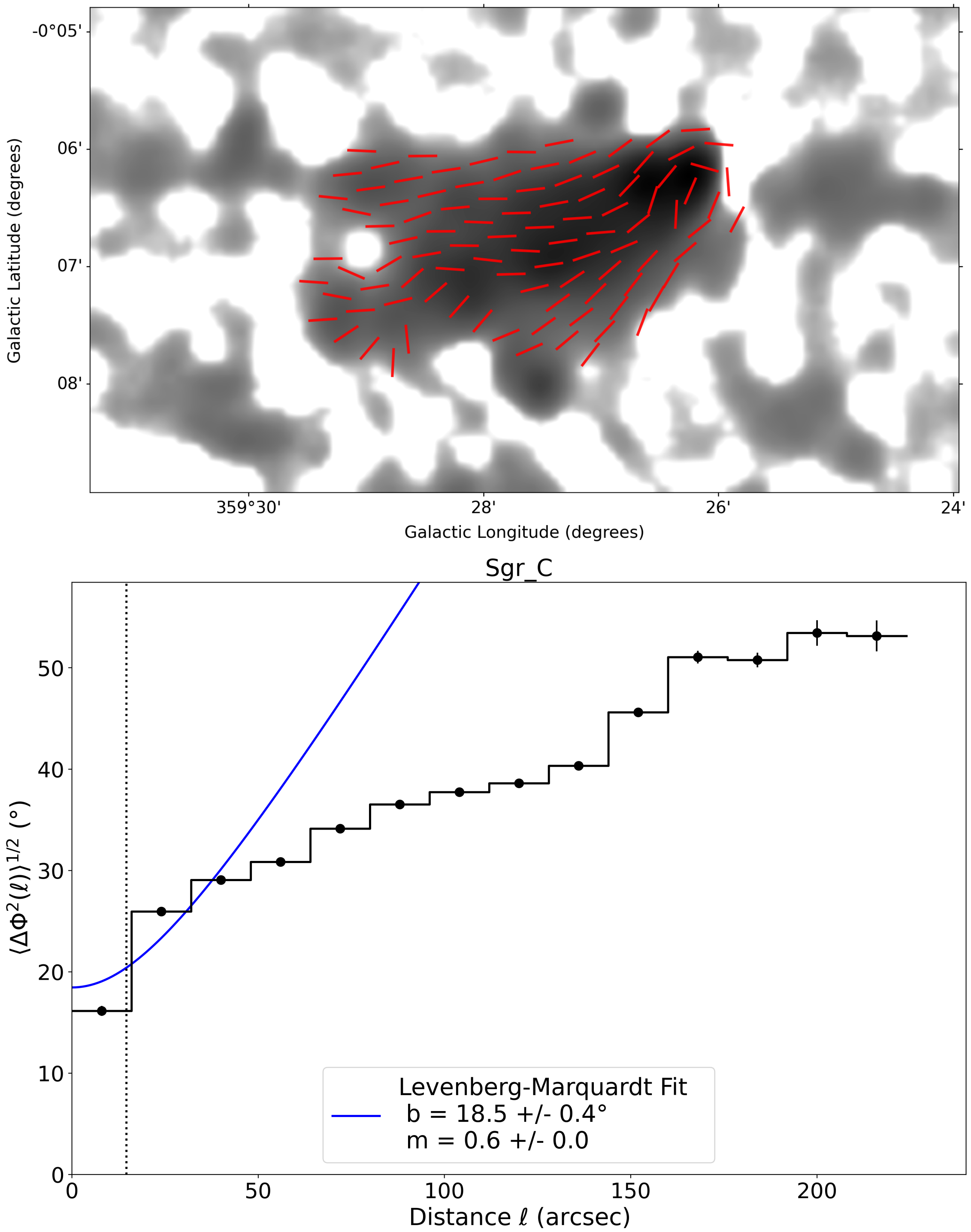

Figure 5.11: A zoom in of the Sgr C region from Figure 5.10. The ADF histogram is shown in the bottom panel. We performed the same method for each of the regions in Figure 5.10 if there were enough vectors.

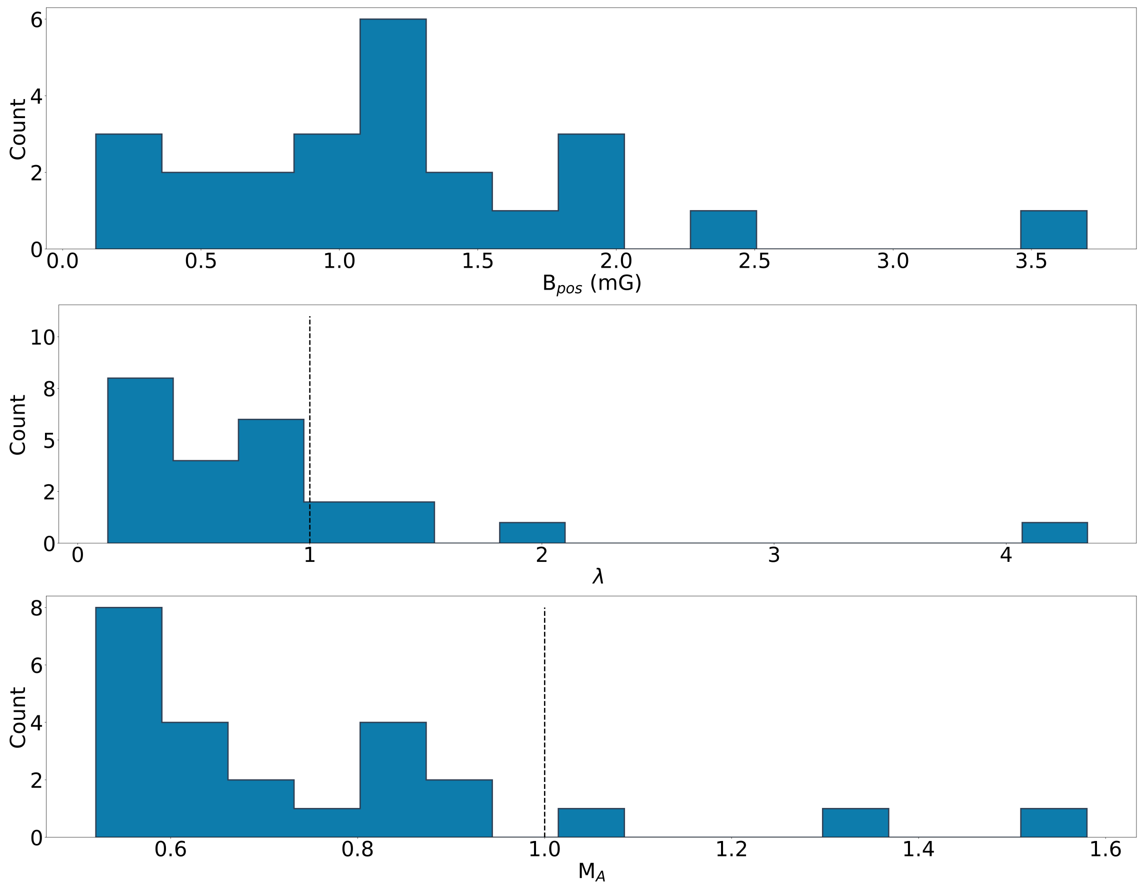

Figure 5.12: Histograms of the magnetic field strength (upper), mass-to-flux ratio (middle) and Alfvén Mach number (lower) for the regions in the CMZ. See Section 5.6 for more details.

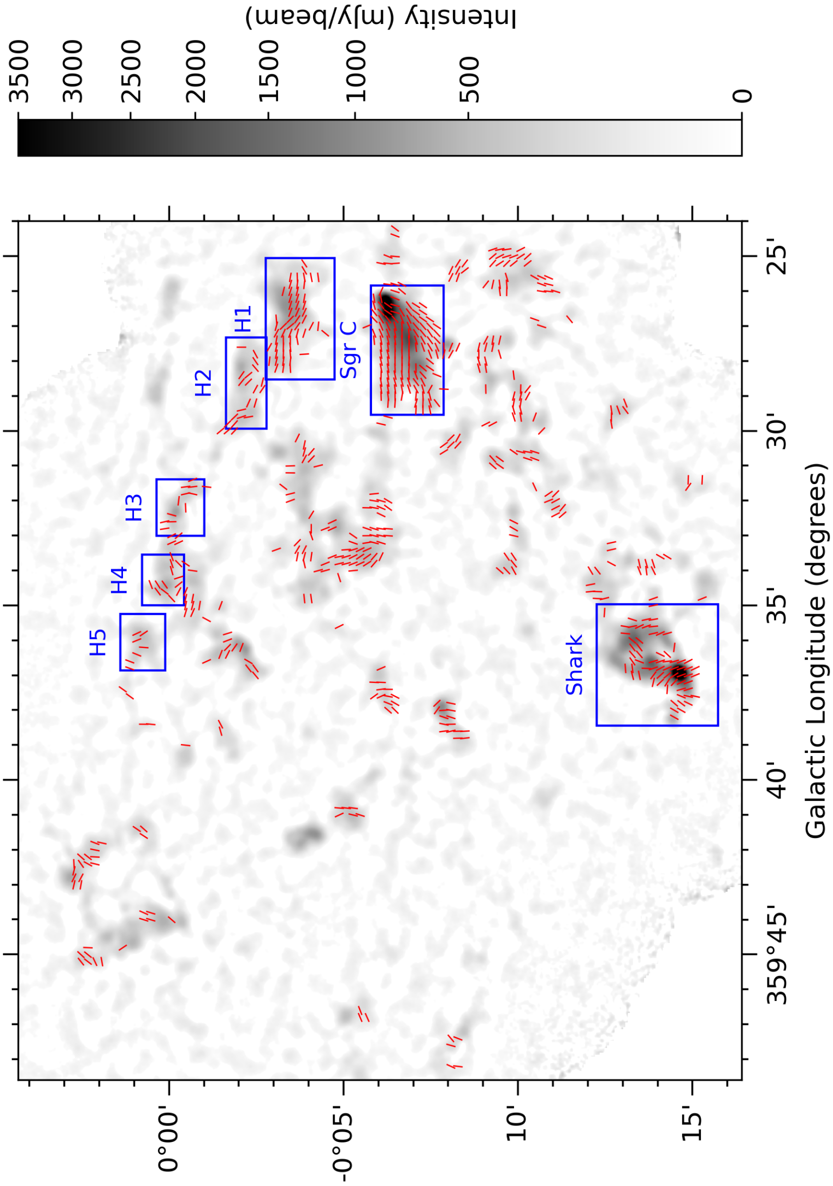

Figure 5.13: The region to the west of Sgr A* is plotted with the magnetic field vectors shown as uniform red line segments. The background is the 850 μm dust emission map. Regions of interest where there is either an ordered field or a known cloud are identified.

Roughly two thirds of the molecular gas and the distribution of star formation in the CMZ lie east of Sgr A* (Kendrew et al., 2013). To the west, there are not many massive molecular clouds, something which can be seen in Figure 5.13 with the lack of emission in the whole region. Sgr C is the largest molecular cloud west of Sgr A* and it accounts for most of the star formation (Kendrew et al., 2013).

There is another massive cloud to the south of the region around G359.62-0.24 which we designate 'the Shark' (see Figure 5.14). This cloud does have some active star formation, with a number of YSOs detected towards it (Yusef-Zadeh et al., 2009) as well as detections of masers at 6.7 GHz and 12.2 GHz (Song et al., 2022). There is also a cloud-cloud collision occurring which was originally thought to be an intermediate black hole candidate (Tanaka, 2018), so it is a very active star-forming site (though not compared to Sgr B2 or Sgr C). The magnetic field in the Shark has two primary components. One part of the magnetic field is in the head of the shark and runs almost directly galactic north-south. It also has a component to the east which appears to be perpendicular to the intensity structure. Then in the main body and tail of the Shark, the magnetic field appears to cross the other two bright sub-millimeter spots perpendicularly to the exterior lower-intensity structure. In Figure 5.14, the bright spot furthest west, just above the tail, is where the cloud-cloud collision is believe to be taking place. Then the bright spot to the east, the head of the Shark, contains one of the YSOs. There are also a series of X-ray candidates in the region.

The actual Sgr C molecular cloud has an extremely well-ordered field with what appears to be a single component, tracing the comet-like structure of Sgr C quite well. The field runs east-west in the diffuse region and then turns towards a northwest-southeast orientation at the head. There is a small second component which is in the south of the region and comes up at an $\approx 135^\circ$ angle to then join the east-west field. We calculated the magnetic field in Sgr C to be 540 μG and found

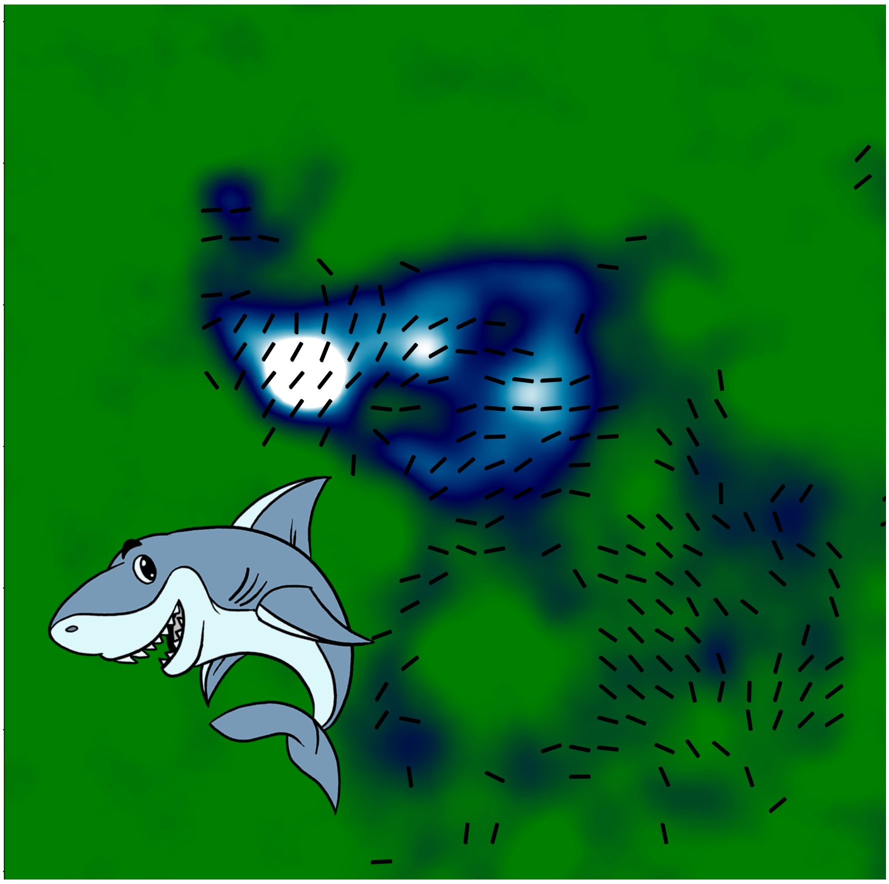

Figure 5.14: The sub-millimeter bright cloud which resides at around 359.62 -0.24 in Figure 5.13. A small cartoon illustration of a shark is shown to try and illustrate the resemblance.

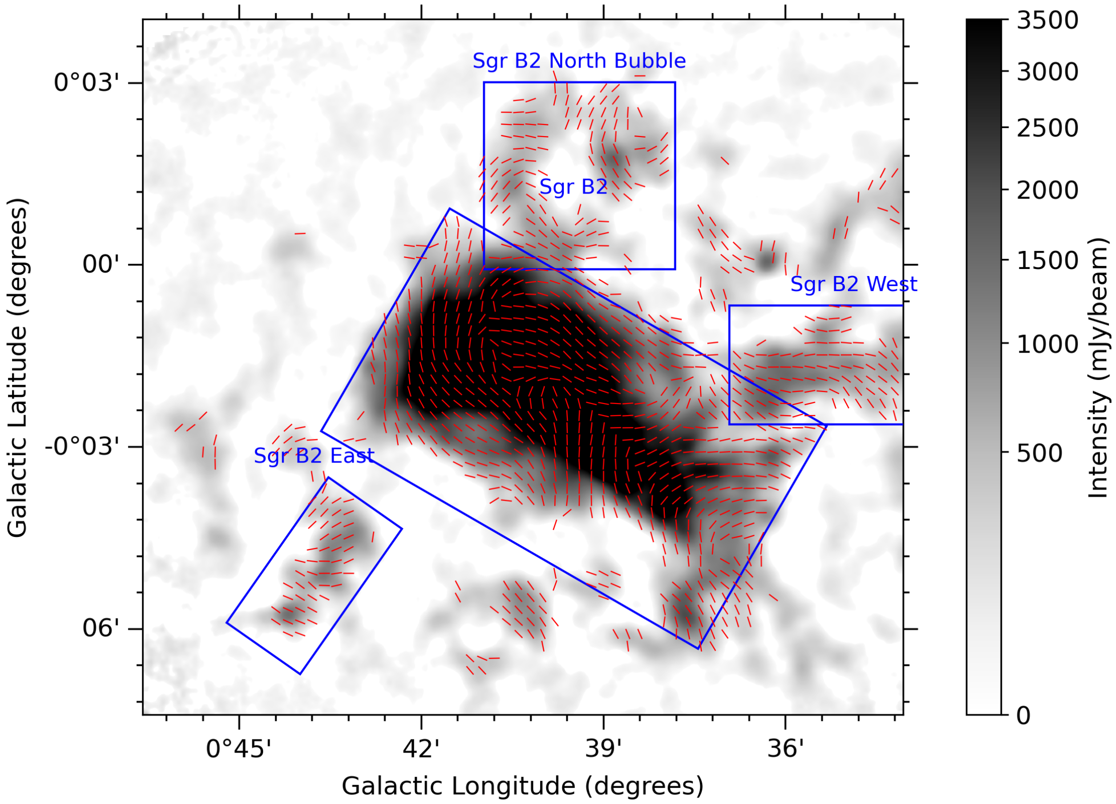

Figure 5.15: The Sagittarius B2 region is plotted with the magnetic field vectors shown as uniform red line segments. The background is the 850 μm dust emission map. Regions of interest where there is either an ordered field or a known cloud are identified.

it to be magnetically supercritical with λ=1.4. This would support the observation that this cloud is the most active star-forming cloud to the west of Sgr A*. We found the cloud to be sub-Alfvénic as well which makes sense considering the highly structured magnetic field.

5.6.3 Sagittarius B2 region

The Sagittarius B2 region is where a significant amount of gas mass in the CMZ is concentrated. The main Sgr B2 cloud which has a total mass of $> 10^6$ M$_\odot$ (Henshaw et al., 2023) and three main regions of star formation hotspots located in the dense center (Schmiedeke et al., 2016). From the 850 μm dust emission, we also identify a bubble/ring structure to the north of Sgr B2 which is labelled in Figure 5.15. Typically ring morphologies will have magnetic field vectors parallel to the edge of the ring (Könyves et al., 2021; Arzoumanian et al., 2021; Butterfield et al., 2024). These morphologies are often occurring when those rings are associated with expanding fronts and material is compressing along the edges and dragging the field. This ring morphology appears disconnected in the southwest corner and also does not have a single morphology around the edge, neither preferentially parallel or perpendicular the whole way around. Instead there appears to be a pinched field to the north which then curves off to a dense structure to the west, then near Sgr B2 the field is parallel to the bubble and then to the east the field is slightly perpendicular to the long edge. We are unsure what causes this ring or if it is fully continuous in line-of-sight or velocity space (a moment one map of the SWAG data does not provide anything conclusive). There are also two more structured magnetic field areas to the west and southeast of Sgr B2 which we have highlighted in Figure 5.15. To the southeast the magnetic field appears to be perpendicular to the structure while to the west it is parallel. The western cloud connects with other material towards the dust ridge and may be part of a larger flow of material while the southeastern dense region is rather isolated.

The magnetic field within the actual Sgr B2 cloud is extremely well-ordered but also complex. To the northeast, the magnetic field appears to spiral inwards slightly. Further down along the northeast-southwest diagonal from that point, the magnetic field meets at a triangular point from both sides of the ridge and this point relaxes to a more curved bow structure further to the southwest. This ridge is where the hotspot sites of star formation are occurring and that may be what is disrupting the field at those locations. Conversely, the density gradients in that region (shown later in Chapter 6, Section 6.3) all point inwards towards that ridge and so perhaps there is material flowing inwards towards the crest and feeding the star forming regions. Then the field may be dragged along by this flow or is controlling the flow towards the crest. The magnetic field strength in Sgr B2 was calculated to be ∼2.1 mG and be overall magnetically supercritical with λ=1.5. However, the material is then slightly sub-Alfvénic, so the magnetic field may be controlling the flow of material over turbulence, but it is still subject to the gravitational potential of this massive cloud.

5.6.4 Sagittarius A* region

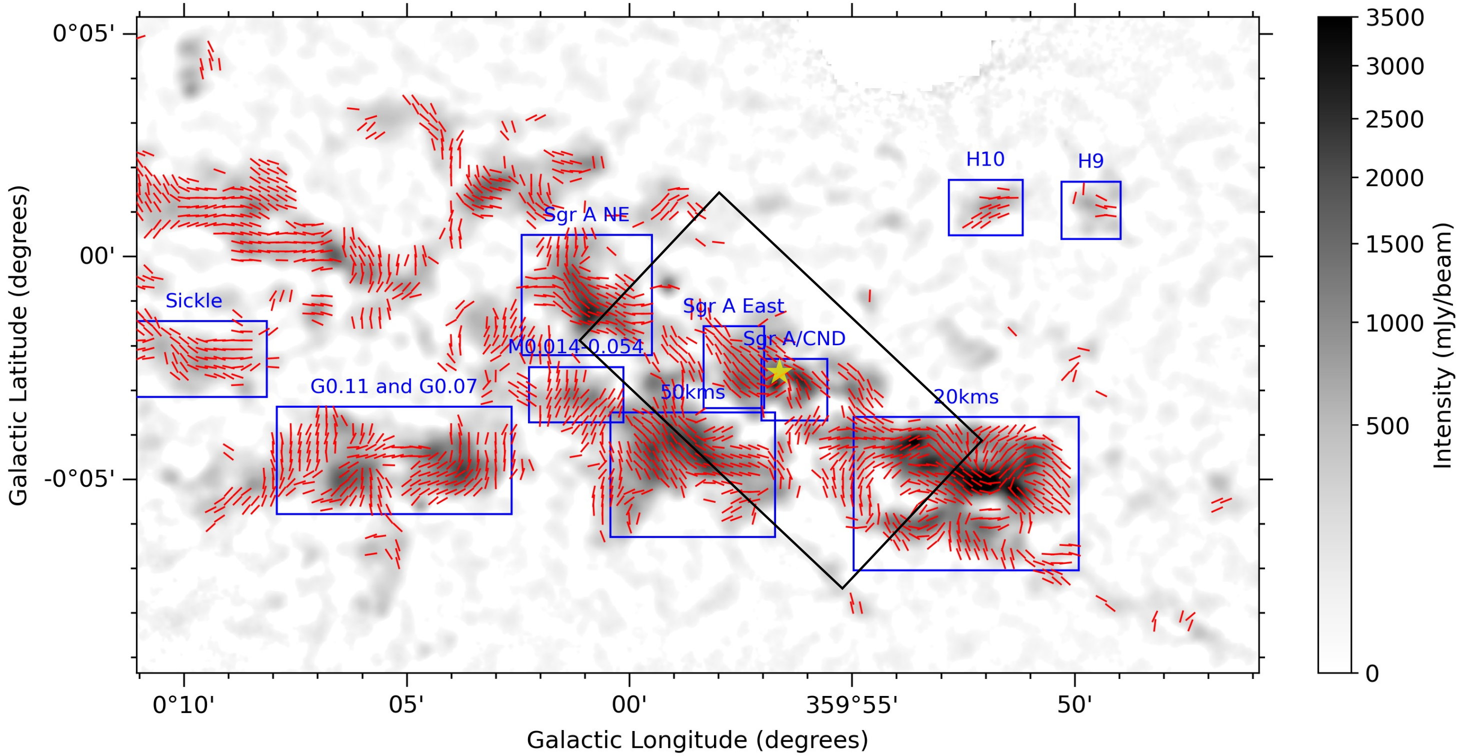

Figure 5.16: The Sagittarius A* region is plotted with the magnetic field vectors shown as uniform red line segments. The background is the 850 μm dust emission map. Regions of interest where there is either an ordered field or a known cloud are identified. A rotated black rectangle shows the area plotted in the left panel of Figure 5.17.

The Sgr A* region is perhaps the most chaotic region of the CMZ. It is where most of the proposed orbits cross and it forms the basis for a series of gravitational potentials. These gravitational potentials range in scale of influence, starting from the black hole Sgr A* (range of ∼1 pc), the nuclear stellar cluster (range between 1–30 pc) and the nuclear stellar disc (range between 30–300 pc) (Henshaw et al., 2023). The circumnuclear disc (CND) is the closest reservoir of dense molecular gas to Sgr A*, with a total mass of $\sim 3\times10^4$ $M_\odot$ and densities $\sim 10^5$–10^7 cm^{-3} (Henshaw et al., 2023). It is also an extreme region with dust temperatures greater than 100 K (Henshaw et al., 2023), compared to nearby molecular cloud dust temperatures of 10–20 K. The CND is labelled in Figure 5.16 where the rough ring structure can be seen with the brighter edge to the north. The right side of Figure 5.17 shows the magnetic field around the CND observed at both 53 μm (the LIC pattern) and 850 μm (red vectors). The 53 μm observations capture the detailed dust emission better than the 850 μm dust emission, but both magnetic field morphologies follow these observed dust lines, curling at the center of the CND. Guerra et al. (2023) found that the magnetic field observed at 53 μm is aligned with the ionized streamers falling onto Sgr A* and derived large magnetic field strengths, with medians in the range of 4.0–8.5 mG. Those same streamers appear to still be traced at 850 μm, though just not in as great of detail. The magnetic field from the 214 μm and 850 μm observations match very well (see left panel of Figure 5.17), appearing to trace similar material. However, there are some interesting deviations. In the left panel of Figure 5.17 around 17:45:45 -29:03:00, the magnetic field seen at 850 μm bows and splits into two populations while the 214 μm field continues in the north-south direction. In addition, the magnetic field at the center of the white rectangle, which is where the CND is, is nearly perpendicular between 214 and 850 μm. This area is where the magnetic field at 850 μm closely matches the morphology of the 53 μm field, curving and following the streamers onto Sgr A*. It is interesting and

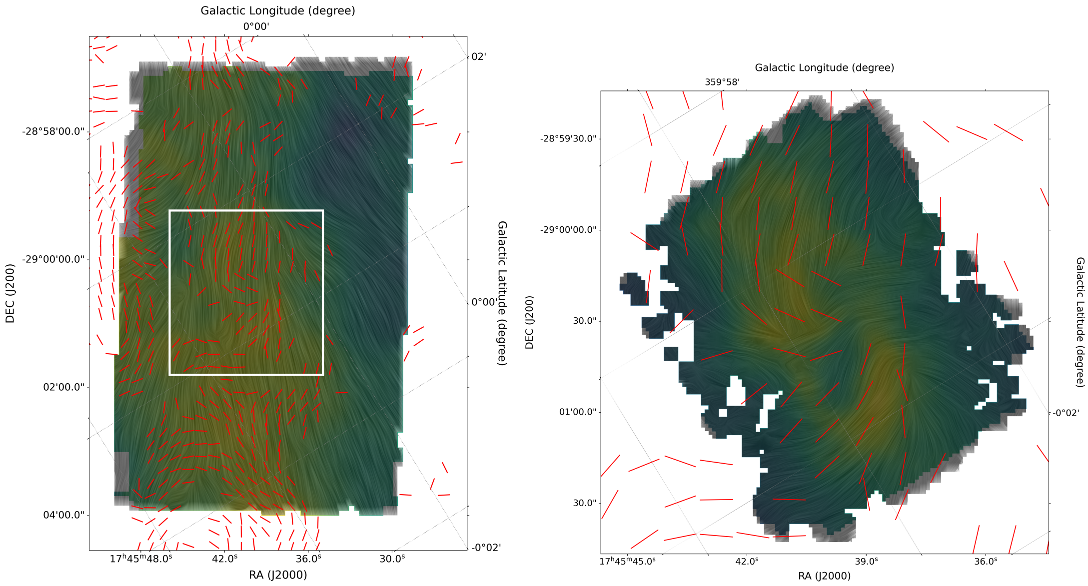

Figure 5.17: The left panel shows the area outlined by the black rectangle in Figure 5.16. The background is the HAWC+ 214 μm total intensity and the textured line integral convolution (LIC) shows the magnetic field orientation. The red line segments show the magnetic field inferred from 850 μm JCMT/POL-2 observations. The rectangle shows the area plotted in the right panel. On the right is the Sgr A* CND region observed with HAWC+ 53 μm.

not immediately clear why the 214 μm observations do not see this morphology. The beam sizes at 214 μm and 850 μm are nearly identical so it is unlikely due to beam smoothing.

The Sgr A* region is also home to two well known molecular clouds, the 20 km/s cloud and the 50 km/s cloud. They are named that for their distinctive velocity features across the cloud at those velocities. In both clouds, we see highly ordered fields. In the 50 km/s cloud, the magnetic field is roughly 45° and splitting what appears to be a bowed structure at the higher densities. The 20 km/s cloud has a very complex magnetic field that is highly structured but curves throughout the cloud and appears to follow the general density structures, for example forking off at 90° to each other to the western edge of the region shown in Figure 5.16. The magnetic field strengths in the 20 and 50 km/s clouds are 1.27 and 0.88 mG respectively. The 20 km/s is overall roughly magnetically transcritical and the 50 km/s is slightly magnetically sub-critical. Both clouds are slightly sub- to trans-Alfvénic.

There are many other regions with ordered magnetic fields in this region and all seem to have the ≈45° orientation through the dense regions. This is the case in the Sgr A East and Sgr A NE regions. This is the magnetic field morphology which we believe traces the orbit or motion of the material through that region. The G0.11 and G0.07 clouds have a more unique morphology, with seemingly three unique field structures within that region. To the west the field appears to again bow while to the center there is an almost pinched field morphology.

5.6.5 The Dust Ridge

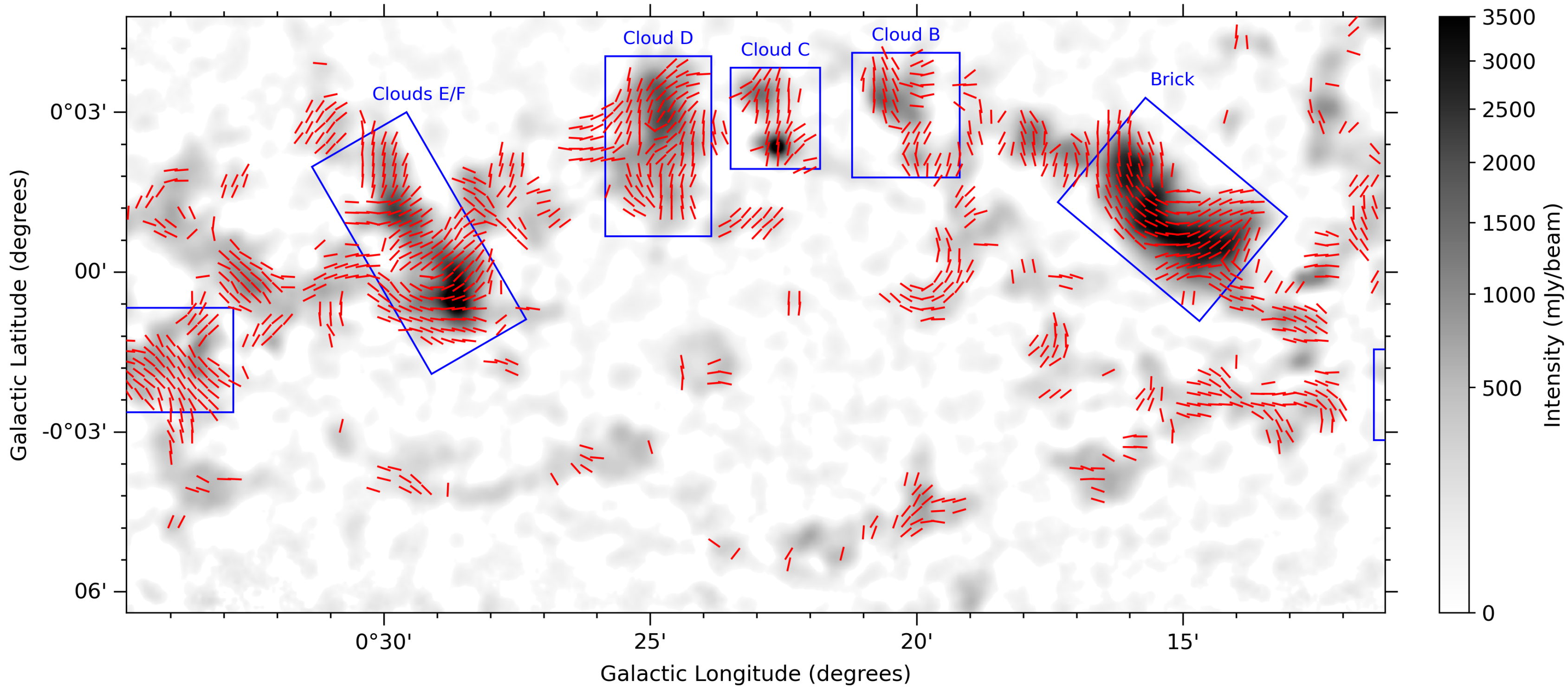

Figure 5.18: The Dust Ridge region is plotted with the magnetic field vectors shown as uniform red line segments. The background is the 850 μm dust emission map. Regions of interest where there is either an ordered field or a known cloud are identified.

The Dust Ridge is a series of dense molecular clouds which go from the 'Brick' (sometimes known as Cloud A) to Sgr B2. The 4 main clouds are Clouds E/F, Cloud D, Cloud C and Cloud B (see Figure 5.18). The magnetic field strengths of those four clouds are 1.93, 0.75, 1.08 and 1.17 mG respectively and all of the clouds are magnetically trans- or sub-critical and sub-Alfvénic. This is in contrast to the findings of Lu et al. (2024), but they found very high dispersions in magnetic field position angle despite the clearly well-ordered magnetic fields. They also use a different version of the ADF to the one we use. The magnetic field strength in the Brick is calculated to be 1.85 mG. This is significantly less than the magnetic field strength of 5.4 mG calculated by Pillai et al. (2015). However, we similarly find the Brick to be magnetically subcritical and sub-Alfvénic so the discretion may have been due to values of density and line widths used, but the highly-structured magnetic field morphologies follow the same orientation of running parallel to the observed curved intensity structure of the Brick.

Figure 5.19 shows a comparison of the Clouds E/F molecular cloud and the nearby Perseus molecular cloud as observed with *Herschel* and Planck. This comparison was picked out solely by eye due to the similar structure of the intensity and also then the similar structure of the magnetic field. The structure similarities are the bright massive core to the south and then a slight bottle neck opening up to another dense core to the north. Throughout most of the cloud, the magnetic field also runs perpendicular to the cloud. Taking the distance to Perseus to be 300 pc and the distance to the CMZ to be 8300 pc, the size of the two clouds is $\sim$12.3$\times$7.5 pc and $\sim$36.2$\times$24.3 pc for Clouds E/F and Perseus respectively. Clouds E/F have a dust mass $\sim$10$\times$ that in Perseus but is three times smaller (in the 2-D plane-of-sky) meaning it is roughly 100 times denser. However, with a higher density and similar magnetic field orientation, it is not forming stars as readily as Perseus. We also find a significantly higher magnetic field strength, 1.93 mG compared to 17-30 μG (Planck

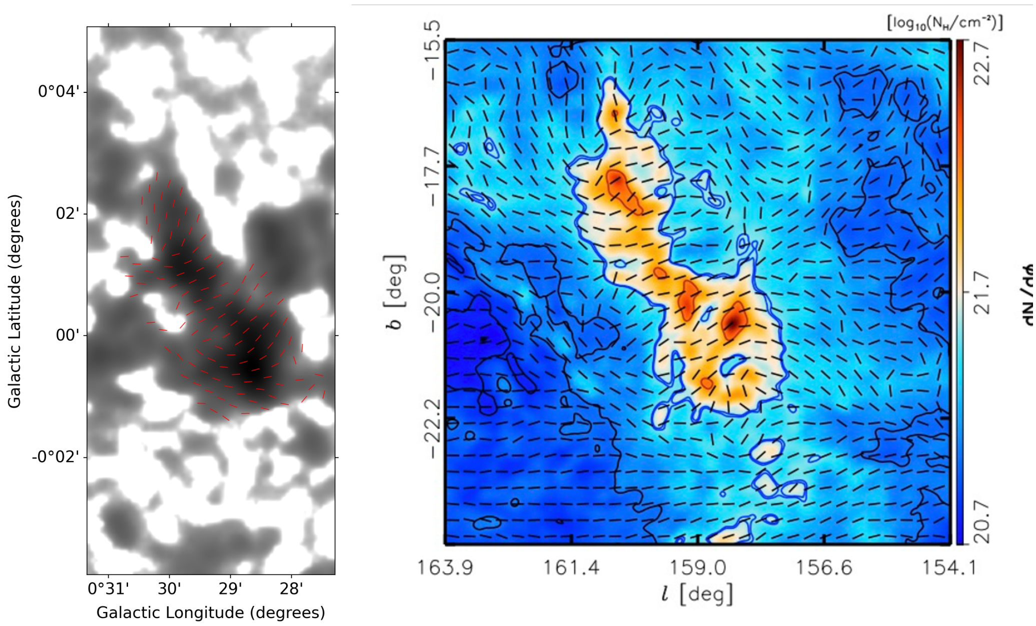

Figure 5.19: The magnetic field in the Clouds E/F is shown in the right panel. The left panel shows the *Herschel*/Planck observations of the Perseus molecular cloud (Planck Collaboration et al., 2016b).

Collaboration et al., 2016b). However this is most likely due to the densities being probed. The Planck-derived field strength is for a large-scale field strength and only goes up to $\sim 10^{22}$ cm^{-2} while the Clouds E/F have much higher column densities. The *Herschel*/Planck observations also traced the extended emission areas while we trace only the dense regions.

5.7 Summary

In this chapter we suggest a new partial orbital model (a 'stream') for the CMZ. We start from the 850 μm Stokes I emission which traces the dense structures in the CMZ. We require that our modeled stream passes through the dense structures. Then we add in the magnetic field information where we assume the field to be parallel to the stream and so we look for which dense structures our stream could go through to satisfy this. We do not drastically deviate from the previously derived orbital model of Kruijssen, Dale & Longmore (2015) because it has been shown to be continuous in many areas in position-velocity space. We then check the gas kinematics along our proposed stream using NH_3 observations from Krieger et al. (2017) to ensure that our new stream is still continuous in position-velocity space. We show that it is and that we also see a similar discontinuity between roughly Sgr A* and the Brick, similar to Kruijssen, Dale & Longmore (2015)

We then compare the magnetic field direction along the stream with the gradient of the stream. We find that on the western side of Sgr A* and the 20 km/s cloud, the magnetic field direction agrees well with the stream direction, aligning preferentially parallel to the stream. This is also the region that is best-defined in position-velocity space. On the eastern side, there is significantly more deviation of the magnetic field from the stream direction. There are many more molecular clouds on this side and a lot more velocity components. A majority of the mass in the CMZ is also in this eastern side and we think some of the individual cloud dynamics, whether turbulent or gravitational, could be affecting the observed magnetic field. Overall we have a preferentially parallel pattern of the magnetic field with our proposed partial orbital model and it is continuous in velocity space.

We then derive a CMZ-wide distribution of magnetic field strengths within the molecular clouds. For each cloud with significant magnetic field detections, we use the ADF method and $N(H_2)$ maps from Tang, Wang & Wilson (2021) and then line-widths from the NH_3 data. We find magnetic field strengths on the order of mG which is expected for the ordered magnetic field structure we see. We also derive mass-to-flux ratios and Alfvén Mach numbers, finding in both cases that the magnetic field within individual clouds appears to dominate, with a majority of clouds being both magnetically subcritical and sub-Alfvénic.

Chapter 6

How BISTRO Molecular Clouds Contribute to Star Formation Theory

6.1 Overview

In this chapter, we bring together the BISTRO sources presented in the previous chapters and include some of the literature BISTRO sources to investigate overall trends we find based on the magnetic field information. We approach this in two ways. First we investigate how magnetic fields play a role in, or are influenced by, the transition of material from magnetically-dominated to matter-dominated. In the nearby, low-mass star forming regions we investigate individual cores and use a theoretical relation from Mestel (1965) to compare measured values of column density and magnetic field with critical ones for a collapsing core. Further away, in the high-mass Central Molecular Zone (CMZ), we investigate the relation between the magnetic field orientation and the density structure of the CMZ using the histogram of relative orientation (HRO) method. Simulations suggest that a transition in magnetic field orientation within molecular clouds from lying parallel to perpendicular to density structure occurs only in the case where magnetic fields are dynamically important on large scales (e.g. Soler et al., 2013; Seifried et al., 2020). The second overall trend we investigate is how the magnetic field morphology looks in the different modes of star formation put forth by Seo et al. (2019).

6.2 Transition from magnetic- to matter-dominated

6.2.1 Nearby star-forming regions

We compiled a list of other star forming regions from BISTRO in Table 6.1 and list the derived magnetic field strengths and directions. We also list the core orientations and large-scale magnetic field orientation. Then for each region, given the column density value, we can calculate the critical magnetic field strength from Equation 3.14 which determines if the material is matter- or magnetically-dominated (see Section 3.4.1.1). Where magnetic field strengths are found, we also then calculate the critical column density, also from Equation 3.14. We do note that Equation 3.14 was derived for a spherical core, but many of the cores we investigate are circular in nature in our 2-D projection. If the calculated column density of the core is larger than the critical column density, the core is considered to be matter-dominated. If the column density is less than the critical column density than the core is magnetically-dominated. Similarly if we only have column density values, we can derive the critical magnetic field strength and compare it with other cores in the region or the large-scale field strength if they appear to follow the large-scale magnetic field. If the critical magnetic field strength is larger than the other cores or the large-scale field strength, then the core could be headed towards matter-dominated. If the critical magnetic field strength is less than other cores or the large-scale field strength, then the core may still be magnetically-dominated. What we have previously hypothesized is that matter-dominated cores will have magnetic fields which are dissimilar from the large-scale field while magnetically-dominated cores may still trace the large-scale magnetic field. This was tested in Ward-Thompson et al. (2023) and we discussed it in Chapter 3 in Lynds 43. Here we apply it to the range of BISTRO cores.

6.2.1.1 B213

The B213 region is a series of ∼0.05 pc cores that are embedded further along the L1495A/B213 filament in the Taurus region. The magnetic field observed with POL-2 is plotted in Figure 6.1 and the four main cores are labelled. East and West cores are both Class 0/I protostellar cores while the middle core and HGBS-1 are both prestellar cores (Eswaraiah et al., 2021). HGBS-1 was not really investigated in Eswaraiah et al. (2021) because many of the vectors are less than the stringent $P/\delta P=3$ cut. However if we lower that cut to $P/\delta P>2$, we recover more magnetic field vectors. However there is still an insufficient number to use the DCF method and so no B-field strength is derived. Instead, we calculate the critical magnetic field strength and compare it to the other cores and the large-scale field strength. To get a column density value we used the HGBS maps of the region (Palmeirim et al., 2013). The HGBS column density values are approximately 1.5× larger than the ones calculated in Eswaraiah et al. (2021) so we take this into account when determining the column density of the HGBS-1 core.

The derived critical magnetic field strength for HGBS-1 is then 50 ± 30 μG. This value is larger than the magnetic field strength of the other cores in the region, but also considering the large error bars, it could be smaller. The magnetic field orientation of the HGBS-1 prestellar core is ≈54° which is preferentially parallel to the

Table 6.1: Magnetic field and column density values of BISTRO-3 cores. The magnetic field strengths and critical column densities are in the format of $\text{value}_{\text{lowerlimit}}^{\text{upperlimit}}$ and otherwise uncertainties are given in parentheses.

Source	θ_{Planck} (°)	$\theta_{\rm core}$ (°)	$\mu_{\theta,B}$ (°)	N(H_2) (10^{22} cm^{-2})	B_{pos} (μG)	$N_{crit}(H_2)$ (10^{22} cm^{-2})	$B_{pos,crit}$ (μG)	Ref.
L43-1	63	0	140	0.4(0.1)	64_{23}^{126}	$1.3_{0.5}^{2.5}$	20(5)	1
L43-2	63	120	63	5.2(0.9)	118_{59}^{194}	$2.2_{1.2}^{3.9}$	260(45)	1
L43-2 edge	63	120	63	0.6(0.2)	40_{25}^{55}	$0.8_{0.5}^{1.1}$	30(10)	1
L43-blob	63	∼0	70	0.14(0.05)	–	–	7(2)	1
L1498	125	125	178	2.9(2.4)	42_{14}^{84}	$0.8_{0.3}^{1.7}$	145(120)	1
L1517B	94	0	153	2.0(0.6)	61_{27}^{108}	$1.2_{0.5}^{2.2}$	100(30)	1
L1544	53	150	7	5.0(3.9)	96_{35}^{187}	$1.9_{0.7}^{3.7}$	250(195)	1
L1527	46	133	38	3.1(1.0)	73_{34}^{124}	$1.5_{0.7}^{2.5}$	155(50)	1
L1495 (1)	16	167	98	1.9(0.8)	60_{23}^{115}	$1.2_{0.5}^{2.3}$	95(40)	1, 2
L1495 (2-N)	16	0	104	1.5(0.6)	–	–	75(30)	1, 2
L1495 (2-S)	16	45	43	1.6(0.6)	–	–	80(30)	1, 2
L1495 (4)	16	60	18	0.9(0.4)	–	–	45(20)	1, 2
L183 North	88	30	164	2.7(0.8)	82_{36}^{146}	$1.6_{0.7}^{2.9}$	135(40)	1
L183 South	88	0	166	3.2(1.1)	93_{45}^{157}	$1.9_{0.9}^{3.1}$	160(55)	1
L183 West	88	0	80	1.9(0.6)	–	–	95(30)	1
B213 East	28	126	121	1.1(0.6)	44_{28}^{60}	$0.9_{0.6}^{1.2}$	55(30)	3
B213 Middle	28	119	158	0.5(0.3)	12_{7}^{17}	$0.2_{0.1}^{0.3}$	25(15)	3
B213 West	28	127	48	1.0(0.6)	38_{24}^{52}	$0.8_{0.5}^{1}$	50(30)	3
B213 HGBS-1	28	20	54	1.0(0.6)	–	–	50(30)	3
FeSt 1-457	165	67	130	4.4^a	24_{12}^{36}	$0.5_{0.2}^{0.7}$	220(73)	5, 6
L1512	150	166	180(150)	0.8(0.5)	18_{11}^{25}	$0.4_{0.2}^{0.5}$	40(25)	7
Oph A (a)	11	170	54	15^b	5000_{500}^{5000}	100_{10}^{100}	750(250)	8
Oph A (d)	11		104	6.2^b	200_{20}^{200}	$4_{0.4}^{4}$	310(103)	8
Oph A (e)	11		100	4.5^b	800_{80}^{800}	$16_{1.6}^{16}$	225(75)	8
Oph-B1	33	148	131	$4.9(0.7)^b$	–	–	245(35)	9
Oph-B2	33	60	78	41(20)	630_{220}^{1040}	$12.6_{4.4}^{20.8}$	2050(1025)	9
Oph C	17	134	60(95)	10.5(6.2)	61_{27}^{108}	$1.2_{0.5}^{2.2}$	525(310)	10
L1689N	24	110	34	4.2(3.5)	366_{157}^{575}	$7.3_{3.1}^{11.5}$	210(175)	11
L1689 SMM-16	11	56	96	3.3(2.2)	284_{160}^{408}	$5.7_{3.2}^{8.2}$	165(110)	11
L1689B	1	75	8	1.0(0.8)	72_{12}^{132}	$1.4_{0.2}^{2.6}$	50(40)	11

a. Converted from A_V - see text for details

b. From HGBS (André et al., 2010)

References: 1. This work 2. Ward-Thompson et al. (2023) 3. Eswaraiah et al. (2021) 4. Coudé et al. (2019) 5. Alves et al. (2014) 6. Kandori et al. (2017) 7. Lin et al. (2024) 8. Kwon et al. (2018) 9. Soam et al. (2018) 10. Liu et al. (2019) 11. Pattle et al. (2021)

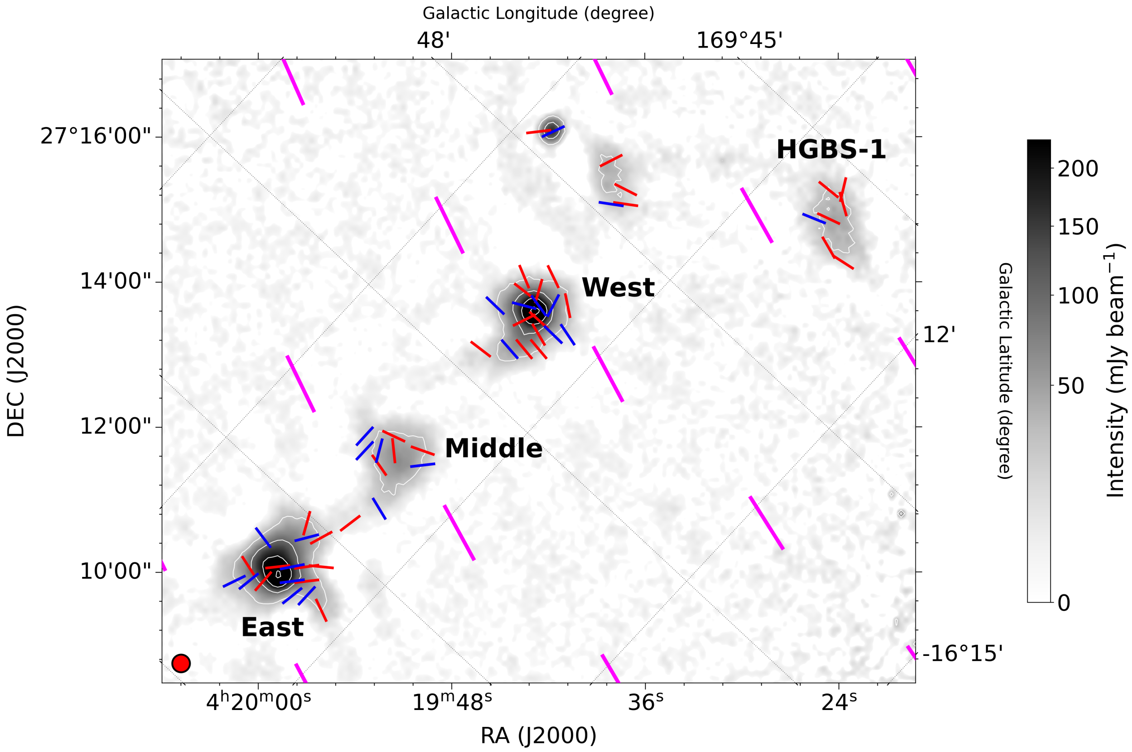

Figure 6.1: Plot of the magnetic field in B213 reproduced from Eswaraiah et al. (2021). The background is the 850 μm dust emission. POL-2 B-field vectors are plotted with I/δI>10 and then P/δP>2 in red and P/δP>3 in blue. The Planck B-field vectors are oversampled and plotted as purple lines. The JCMT beam-size is shown in the lower left corner. The regions corresponding to Table 6.1 are labelled.

Planck field orientation of ≈28°. This indicates the region may still be magnetically-dominated which would agree with the lower limits of the critical magnetic field strength. However, considering that two other cores in this filament, the West and the East cores, both have protostellar objects, it could be that HGBS-1 has transitioned to matter-dominated. The Middle core is the least dense of the four but with a very randomized magnetic field orientation. The West core is well-aligned with the Planck field but it is obviously matter-dominated since it has a protostellar object. Instead the protostellar object is known to drive an outflow and that outflow is oriented roughly parallel with the Planck field but slightly offset from the mean core magnetic field orientation from POL-2 (Eswaraiah et al., 2021). So the alignment of a matter-dominated core with the large-scale field may be due to the outflow and there is no connection to the large-scale field. There is no clear alteration to the dust structure of the core so it may be that the dust and therefore the magnetic field is not affected by the outflow, or we may be unable to resolve the alteration. If this is the case, then the magnetic field orientation of two of the four cores in B213 are aligned with the large-scale field, though with no clear indication of why it is the West and HGBS-1.

6.2.1.2 Ophiuchus - L1688

For Ophiuchus A (Oph A), we use column density values from HGBS to compare with the calculated critical column densities. The derived magnetic field strength for the central dense core (Region (a) in left panel of Figure 6.2), SM1 (Ward-Thompson et al., 1989) is 5 mG, though the authors note that this may be an overestimation due to using only the central densest bit of the core to calculate column and volume densities (Kwon et al., 2018). They also derive a very small angular dispersion which increases the derived field strength, but this is reasonable considering the very ordered field in that area. The only region of Oph A from Kwon et al. (2018)

that has a magnetic field parallel to the Planck field direction is their region (c) which has a mean magnetic field orientation of 16.5°. Nearly all of the other regions have mean magnetic field orientations $> 50^{\circ}$, nearly preferentially perpendicular to the large-scale field.

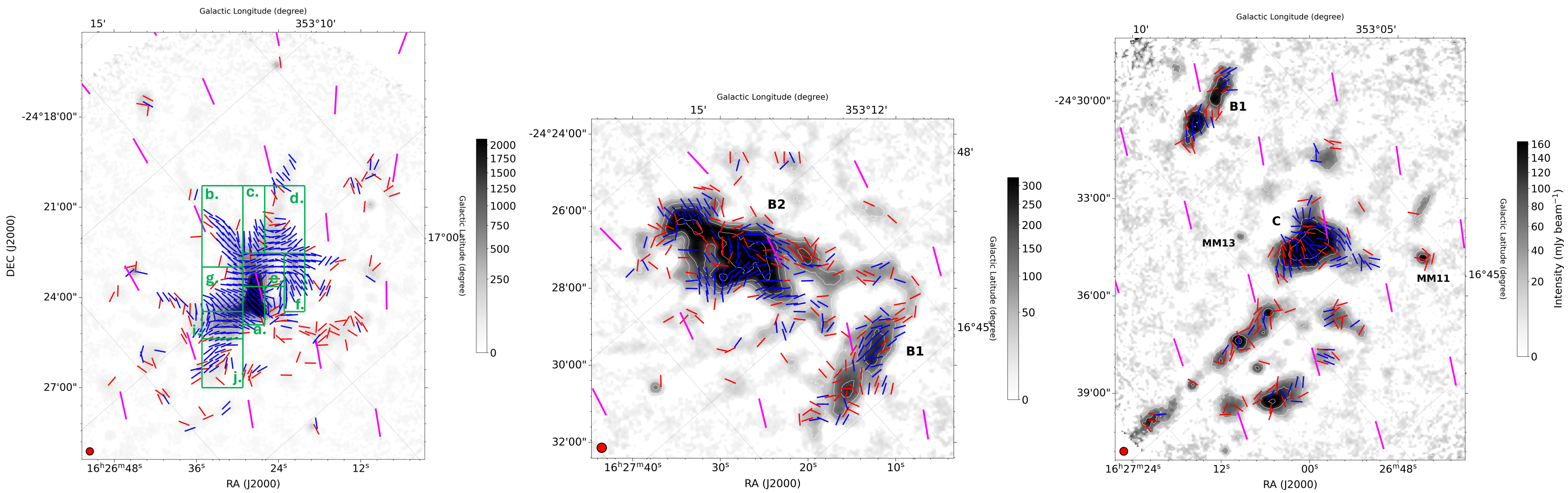

Figure 6.2: The magnetic field images are the same as Figure 6.1 but for Oph A (left), Oph B (center) and Oph C (right). They are reproduced from Kwon et al. (2018), Soam et al. (2018) and Liu et al. (2019) respectively.

For Ophiuchus B, the column density value for the B2 core came from Soam et al. (2018) which was ultimately inferred from 1.3 mm dust continuum observations, but for B1 we used HGBS data. As can be seen in Table 6.1, that column density value is an order of magnitude lower and in fact, HGBS values of B2 are of a similar order of magnitude as B1. This would scale down the derived magnetic field strength by $\sqrt{10}$ in B2. This would then scale down the critical column density by $\sqrt{10}$ as well, meaning the measured column density $\approx$ critical density. Oph B2 does appear to have some magnetic field vectors in the northeast corner of the core which are oriented roughly parallel with the large-scale field. This northeast corner is devoid of any protostellar sources with the YSOs located in the southwestern part of Oph B2 (see Figure 2 of Soam et al. (2018)). There is a prominent outflow associated with one of the YSOs located at the density peak around 16:27:30 -24:28:24 and its orientation agrees well with the northwest–southeast orientation of the vectors there. Using the HGBS column densities, B2 appears to be in the transition of magnetically- to matter-dominated, with half of the cloud appearing to have moved on beyond that transition and already contracted to form YSOs, while the other half still has no YSOs and has a magnetic field which follows the large-scale field.

Ophiuchus C is an extremely quiescent region in the L1688 complex. The tail to the south with knots in it seen in the right panel of Figure 6.2 begins to approach the Oph E complex. In the main Oph C core, there is a two component field, one at $\approx 60°$ and one at $\approx 95°$ (Liu et al., 2019). The $\approx 95°$ component looks to be on the edge of the cloud, both on the eastern edge and then some vectors on the northern edge. The main internal core has the field component which is northeast-southwest ($\approx 60°$). The core orientation is taken as the average of Cores MM3 and MM6A from Pattle et al. (2015). The magnetic field strength is given as the range of the different methods used by Liu et al. (2019). The main Oph C core is starless but there are two protostars in the vicinity, MM11 and MM13, found by Wilking, Gagné

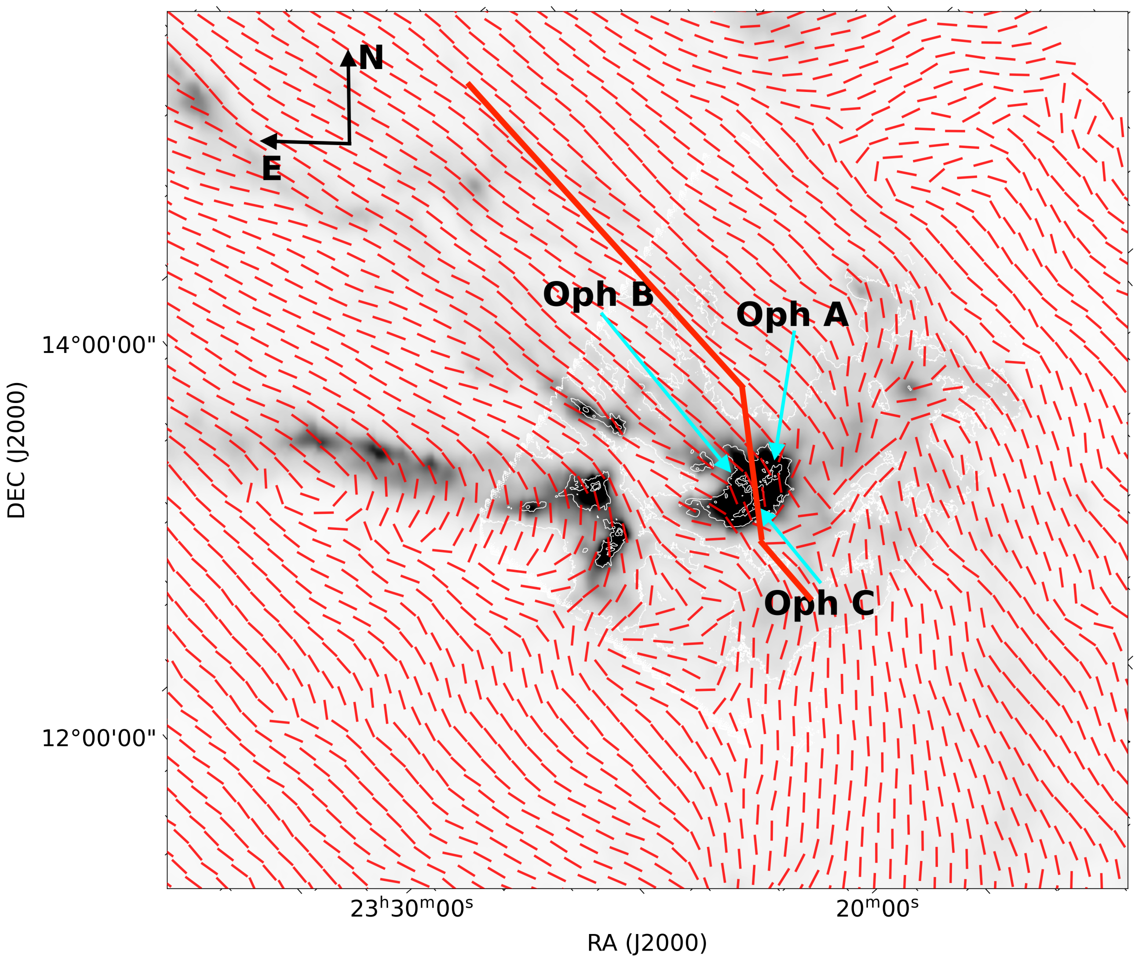

Figure 6.3: The Planck dust extinction map with the Planck magnetic field vectors overlaid in red. Column density contours are overlaid at 0.2, 0.6,1.8 and 3.6 $\times 10^{22}$ cm^{-2}. The three main cores are labelled. Three thick red lines are shown to emphasize the transition from 40–50° to ≈15° around Oph A, B and C and then back to 40–50°.

& Allen (2008) but not by Enoch et al. (2009). Liu et al. (2019) found that the Oph C orientation of 40–100 agreed well with the 40–100 orientation in Oph A and 50–80 orientation in Oph B. It is also consistent with $\sim$50° orientation in lower densities of the Ophiuchus cloud traced by NIR polarization (Kwon et al., 2015) and seen in Planck observations (see Figure 6.3).

As can be seen in the lower right panel of Figure 6.3 the large-scale field observed by Planck seems to change orientation in L1688 (the Oph A, B and C complex), transitioning from $\sim$40° in the surrounding Ophiuchus region to $\sim$10–20° where Oph A, B and C are located. In fact, this appears to happen in any of the dense regions where matter has accumulated. This could indicate that there is a larger scale transition occurring or has already occurred and the complex of Oph A, B and C has moved towards matter-dominated, hence altering the large-scale field orientation. In this case, while the parent cloud may be matter-dominated, the individual cores may still be magnetically supported as indicated by the large magnetic field strengths derived in Oph A, B and C. However we also know there is active star formation, with a protostar VLA 16235-2416 in Oph A (Ward-Thompson et al., 1989) and then numerous protostars in the vicinity of Oph C (Pattle et al., 2015), so some cores have overcome this support. In the case of Oph A, some of this star formation may be due to triggered star formation from its environment. As well, there are areas of the individual molecular clouds where the magnetic field still traces the large-scale $\sim$40–50° orientation and this generally occurs on the edge of clouds or in areas where no star formation has taken place. This would indicate that some cores may not have become matter-dominated, even though their derived column densities are higher than calculated critical column densities.

6.2.1.3 Ophiuchus - L1689

Figure 6.4 shows the magnetic field within three main regions of L1689, L1689N, SMM-16 and L1689B. L1689B is a prestellar core candidate while SMM-16 is a gravitationally bound prestellar clump, fragmented into three smaller cores (Pattle et al., 2021). L1689N is the most evolved clump with a multiple system of Class 0 protostars, IRAS 16293-2422, and then also a starless core IRAS 16293E (Pattle et al., 2021). L1689B is considered to be undergoing large-scale infall while SMM-16, although currently identified as starless, has begun fragmenting. This suggests that all three regions are evolved and or evolving and most likely headed towards the matter-dominated phase, if not there already. The right side of the Figure 6.4 shows that each of these regions is also connected to a series of filaments which may also play a role in their evolution. In the case of L1689B, the large-scale magnetic field from Planck is perpendicular to the filament, but it is then parallel to the SMM-16 filament and parallel to two of the L1689N filaments while perpendicular to one. In all three regions, the core-scale magnetic field appears to be perpendicular to the filament, where in the L1689N, this only happens in the southeastern part, while the two vertical filaments to the west are parallel to the core magnetic field at those points.

Both L1689N and L1689B trace the large-scale Planck field well. In L1689N, the large scale field is oriented at 24° while the core magnetic field orientation is ≈34° when removing the vectors associated with the protostellar system. In L1689B the large-scale and core-scale magnetic field orientations are 1° and 8° respectively. The magnetic field strengths for the three regions calculated by Pattle et al. (2021) are 366±209, 284±124 and 72±40 μG for L1689N, SMM-16 and L1689B respectively. We use these values to calculate the critical column density, and get 7.3, 5.7 and 1.4×10^{22} cm^{-2} for L1689N, SMM-16 and L1689B respectively. For each of the three regions, the calculated critical column densities are greater than the measured ones

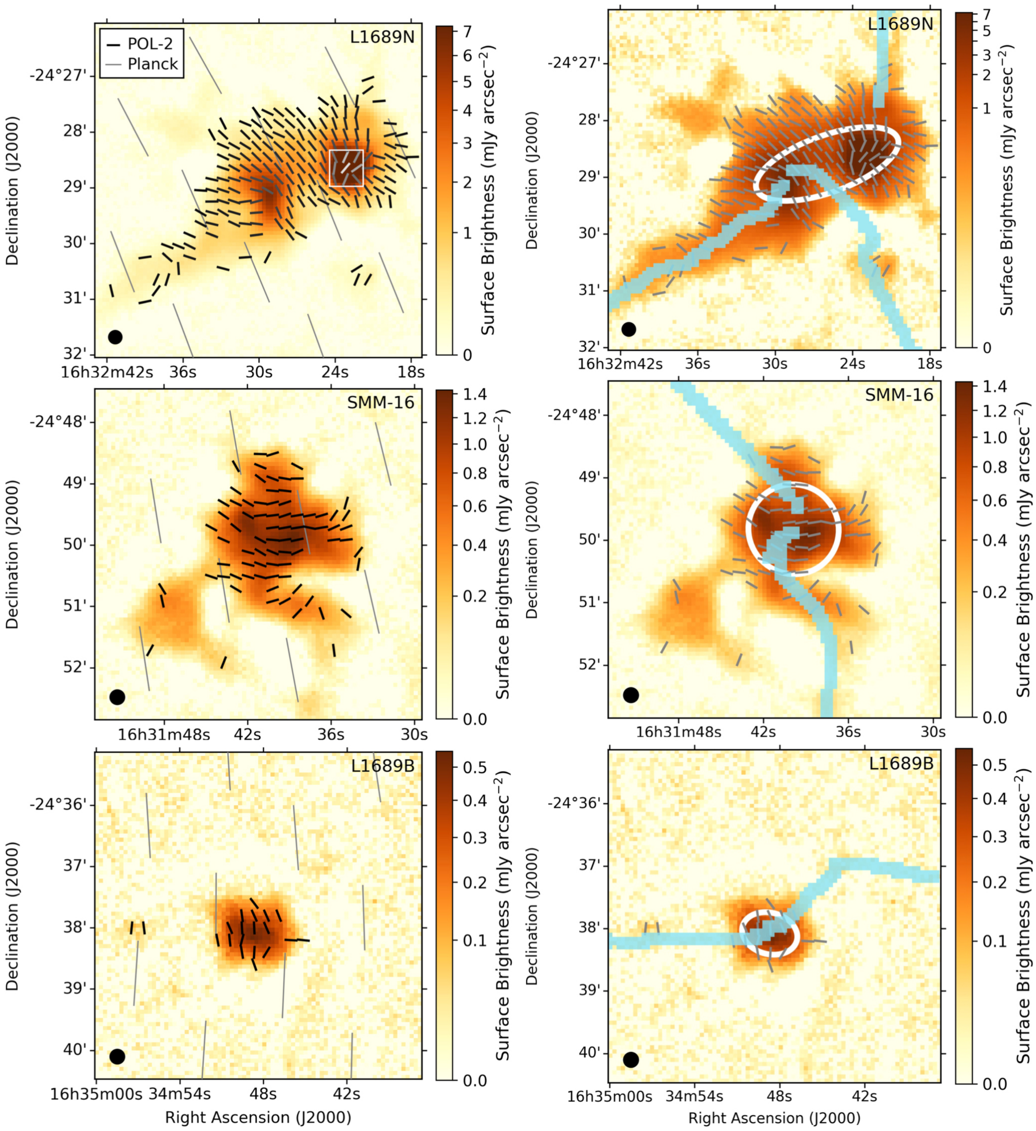

Figure 6.4: Figures 4 and 6 taken from Pattle et al. (2021). On the left the POL-2 vectors are shown in black and the large-scale (oversampled) Planck vectors are shown in grey. The right panel shows the POL-2 vectors as grey lines now and the white overlaid ellipses are the best-fit core orientations derived from the Stokes I emission. The blue lines are the filaments observed by Herschel.

and so each of the regions would be considered to be magnetically-dominated. The measured column density value of L1689N was found with masking the emission around the protostellar system. If instead it was included, the column density increases to 7.9×10^{22} cm^{-2} and then L1689N would be considered in the stage of transitioning from magnetically-dominated to matter-dominated. This would make more sense considering the protostars in that region. L1689B has no prestellar object yet and the magnetic field traces the Planck field well which agrees with what we think happens in the magnetically-dominated phase. Since the infall is only detectable along the line-of-sight, it is not possible to determine if infall is also happening from the filament on either side, at which point it would be going across the magnetic field lines, suggesting we should see an hourglass morphology or that the core is then matter-dominated. SMM-16 however, although still magnetically-dominated and starless, does not follow the Planck field well.

6.2.1.4 FeSt 1-457 and L1512

The large-scale magnetic field for FeSt 1-457 is found from the optical and are plotted in light grey in the upper left panel of Figure 6.5. NIR observations are plotted in a darker grey in the upper left panel and in yellow in the upper right panel. The NIR observations show a roughly north south orientation and may show an hourglass orientation in the envelope (Kandori et al., 2017). The large-scale magnetic field is oriented at approximately 165° and the NIR observations of Alves et al. (2014) follow this orientation as well, where the hourglass is not observed. The core scale magnetic field was observed at 870 μm using the polarimeter PolKa on the APEX telescope. We derive the column density value shown in Table 6.1 from the visual extinction value of ≈40 mag (Alves et al., 2014) using the relation $N(H_2)\approx1.1\times10^{21}(\mathrm{cm}^{-2}\mathrm{mag}^{-1})A_V$ (Güver & Özel, 2009). Previous studies have shown that the core is no longer held stable against gravitational collapse by thermal or turbulent pressures (Kandori et al., 2005), however there is no associated stellar or protostellar object and the core is still starless. This could suggest that the magnetic field is playing a significant role, although we find that the column density of the core is higher than the critical column density derived from its magnetic field strength. This would suggest the core is matter-dominated. The magnetic field of the core is still preferentially parallel to the large scale magnetic field with an orientation of $\approx$130°. This is also approximately perpendicular to the core orientation of 67° which itself is nearly perpendicular to the large-scale magnetic field, whether traced by optical or NIR polarimetry. This could suggest that the core has formed within magnetically-dominant material where material fell along the field lines to accumulate with a major-axis perpendicular to the field lines and now that it has transitioned to matter-dominated, it is slowly reshaping the magnetic field at the core level.

L1512 has approximately a north-south orientation in the main core that then then rotates to $\approx$150° in the south. The large-scale magnetic field in this region is also oriented approximately 150° and so the core appears to still have an imprint of the large-scale field in the diffuse edges. The core does sit within a larger filament and may have material falling inward along this filaments from the north and south, hence influencing the nearly 180° (north-south) magnetic field orientation. The critical column density calculated from the magnetic field strength derived by Lin et al. (2024) is slightly less than the observed column density. However, within error bars they are approximately equal. If this is the case, similar to FeSt 1-457, L1512 may be in the process of transitioning from magnetically-dominated to matter-dominated. However, it could also be that the change in magnetic field orientation comes from the infalling material rather than any gravitational contraction of the core itself. The core orientation is such that the material may not be falling perpendicularly onto the core as suggested in FeSt 1-457, but instead perhaps from the filaments as

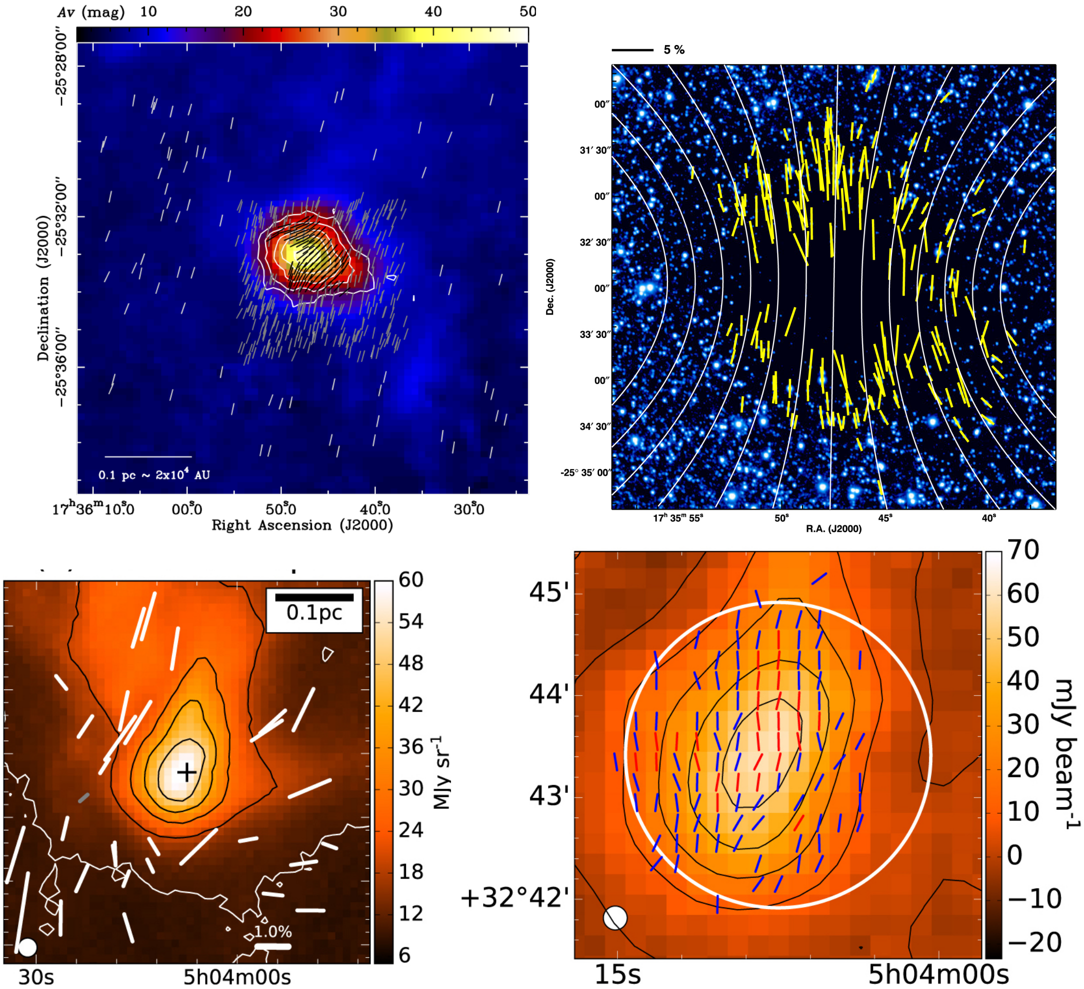

Figure 6.5: Plots of the magnetic field in FeSt 1-457 and L1512 taken from Alves et al. (2014); Kandori et al. (2017) and Lin et al. (2024) respectively. The upper panel shows plots of the magnetic field of FeSt 1-457 inferred from sub-mm (870 μm from APEX/PolKa) on the left in black and NIR (H-band from IRSF/SIRPOL) observations on the right. The inferred hourglass magnetic field model from Kandori et al. (2017) is plotted in the right image. The lower panel has the magnetic field of L1512 inferred by Mimir H-band polarization observations on the left and by JCMT/SCUBA-2/POL-2 on the right. The backgrounds are Herschel 500 μm on the left and SCUBA-2 850 μm on the right.

mentioned above, and so parallel to the core elongation.

6.2.1.5 L1495A

It can be seen that the local field that we have measured in the starless cores within the filaments of L1495A has totally dissociated from the large-scale field orientation seen by Planck (see Figure 4.5), and there is no correlation between them. Planck Collaboration et al. (2016b) find a significantly sub-critical mass-to-flux ratio of $\sim 0.2 - 0.4$ on large scales in Taurus, while Soler (2019) find from *Planck* observations that in the L1495/B213 filament (just to the south of the region studied here), a transition from preferentially parallel to preferentially perpendicular occurs at $N_{\rm H} \sim 10^{21.5}\,{\rm cm}^{-2}$ (3.1×10^{21} cm^{-2}). The balance of evidence suggests that the cloud is still magnetically-dominated on large scales, but we show that is maybe not the case on small scales.

For the cores 1 and 2, the mean field orientation is roughly perpendicular to the Planck field, though in the south part of core 2, it is only $\approx$30° offset. However, in core 4, the magnetic field direction is parallel to the large-scale Planck field. We investigate this further, considering this to be an indicator of the transition between magnetically- to matter-dominated material. Figure 4.6 showed that there is a preferential tendency for the local field to be perpendicular to the filament direction, an orientation which, at least on the large scales, is suggested to mean the material is matter-dominated (Planck Collaboration et al., 2016b).

In the four cores listed above in Table 6.1, there were only enough magnetic field vectors to calculate a magnetic field strength in core 1. The calculated magnetic field strength was $\approx$60 μG. The calculated critical column density value using that magnetic field strength is 1.2×10^{22} cm^{-2} which is slightly less than the measured column density value, further suggesting a transition to matter-dominated. In cores 2 and 4, we could not calculate a magnetic field strength, but we were able to use the measured column density value to calculate a critical magnetic field strength. In core 2, that critical field strength is 75–80 μG. We can compare these field strengths with the one calculated in core 1 and the large-scale magnetic field strength derived from Planck and NIR observations. There are literature values of 25–77 μG from optical and NIR observations (Chapman et al., 2011) for L1495A-B10 and the equivalent Planck value is 13–32 μG (Planck Collaboration et al., 2016b) for the large-scale field around the Taurus region as a whole. The calculated critical field strengths of core 2 are higher than any of the measured field strengths and would therefore further support the conclusion that core 2 has transitioned to matter-dominated. Then for core 4, the hypothesized scenario from Ward-Thompson et al. (2023) is that core 4 may be the youngest core and still undergoing the transition from magnetically- to matter-dominated phase, and it would lead us to set the critical column density N(H_2) at around 9.2×10^{21} cm^{-2} (Ward-Thompson et al., 2023). Inserting this value into Equation 3.14 predicts a magnetic field strength in L1495A-B10 of $\sim$45μG. If core 4 has passed the critical point of the intermediate phase, then this B-field value is an upper limit (Ward-Thompson et al., 2023). This critical field strength is less than the measured strength in core 1 and is of order the field strength from NIR observations, though slightly higher than Planck observations.

Considering the transition of preferentially parallel to preferentially perpendicular occurs at $\approx$3.2$\times$10^{21} cm^{-2} on large scales in Taurus, there may be a separate transition at small scales which is explained by the Mestel (1965) relation, where in L1495A it is 9.2$\times$10^{21} cm^{-2}. This is further explored in Section 6.2.1.9.

6.2.1.6 L43

In L43, the large-scale magnetic field is parallel to the filament (see Figure 3.2 and also Figure 3.1 for the whole region). In Figure 3.8, the ‘blob’ can be seen in the lower right of the image and the magnetic field vectors there, although only four of them, continue to trace the large-scale field. In addition, the lower plot of Figure 3.9 shows that there is a population of vectors in Region 2 which follow the Planck field orientation. In the upper plot of the same figure, those vectors can be seen on the periphery of the dense core, in the more diffuse regions. Meanwhile, in Region 1, which is similarly diffuse, the magnetic field appears to be perpendicular to the large-scale field.

We estimated the column density in these regions and found they are $\sim 1.4{\times}10^{21}$, $6{\times}10^{21}$ and $4{\times}10^{21}$ cm^{-2} for the 'blob,' the upper periphery of Region 2, and Region 1 respectively. All of these values are less than the transition density found by Planck Collaboration et al. (2016b) in Ophiuchus which is $\sim 5{\times}10^{22}$ cm^{-2}. As mentioned above, in two of those cases, the field still traces the large scale field, but in Region 1, it is nearly perpendicular, suggesting that, as mentioned in Section 3.3.5, it may have been influenced by the nearby outflow. The upper edge of Region 2 is shielded from the outflow by the dense core and the 'blob' is far enough away. The dense part of Region 2 which gives the second peak seen in the upper panel of Figure 3.9 has a column density of $\sim 5{\times}10^{22}$ cm^{-2} which is closer to the transition column density from Planck Collaboration et al. (2016b) and may indicate that the core of L43 has moved towards becoming matter-dominated. This would agree with Section 3.4.1 where Region 2 is magnetically super-critical towards the center but sub-critical in the lower density Region 1.

We used Equation 3.14 and substituted in the above column densities as the critical column densities to get magnetic field strengths of 7, 30 and 20 μG in the 'blob,' the upper periphery of Region 2, and then Region 1. We expected the 'blob' and the upper periphery of Region 2 to be near (but below) critical column densities because their magnetic fields still match the large-scale field. Region 1 has a different field orientation and would be a post-critical column density, but can be used to set a limit. The magnetic field strength in the periphery of Region 2 was calculated to be 25–55 μG, while for Region 1 it was 40–88 μG. The critical magnetic field strength is within the range of field strengths for Region 2 but in Region 1, the critical field strength is much lower than the calculated value (which means it should still be heavily magnetically-dominated). For the 'blob' we can consider the large-scale magnetic field strength which was 13-25 μG. In Region 2 and the 'blob', the measured field strength is roughly equal to or greater than the critical field strengths derived from the assumed critical densities and so consider them to be still magnetically dominated.

6.2.1.7 L183

From Figure 4.13, it was quite clear that the densest regions have the vectors which are most different from the large-scale field, while the more diffuse areas still have vectors parallel to the field. The mean of the magnetic field direction in the north and south core are both $\approx$160° which is preferentially perpendicular to the large-scale field which has an average orientation of 88°. The west core has a mean magnetic field direction of 80° which is then preferentially parallel to the large-scale field. The west core has too few vectors to meaningfully calculate a magnetic field strength and so no calculation was done, but the magnetic field strength is calculated in the north and south cores with the same method as in Section 3.3.6. In both cases, the calculated magnetic field strength is lower than the critical magnetic field strength calculated from the column density using Equation 3.14. This supports the idea that they are matter-dominated which we suggest is why the magnetic field orientations are so different from the large-scale.

Meanwhile in the west core, the magnetic field aligns nearly perfectly parallel with the Planck field. If we apply a similar reasoning as in Section 6.2.1.5, this core is therefore the youngest and not yet transitioned into the matter-dominated phase. The core is quite dense, and the calculated critical magnetic field strength determined from the column density is 95 μG. It is approximately twice as dense as the core 4 in L1495A and so there may not be a global critical column density threshold where the transition from magnetically- to matter-dominated occurs. This is shown by Equation 3.14 where it does scale by the magnetic field strength (though as mentioned before, this omits any thermal and turbulent pressures). This critical magnetic field strength is of the order the field strength in the other L183 cores and so this west core may be right at the transition.

6.2.1.8 L1544, L1517B, L1498 and L1527

L1544, L1517B and L1498 all have core-scale magnetic fields which no longer trace the large-scale magnetic field. L1544 very clearly has moved beyond the magnetically-dominated stage because it is exhibiting the class hourglass structure which is theorized to occur once the core starts contracting and is able to have significant material fall perpendicular to the magnetic field lines. For each of these cores, the calculated magnetic field strength is less than the critical field strength calculated from their column densities. This would suggest each is matter-dominated which is supported by their magnetic fields not resembling the large-scale fields. However, despite being matter-dominated none have an embedded protostellar object yet. As discussed in Chapter 4, some of these cores are more evolved than others, while cores like L1517B may be influenced by their surroundings. In fact, the mean field direction of L1517B is roughly parallel to the projected direction to the AB Aur star which should be interacting with the L1517 molecular cloud (though it has not been shown to be). Similar to outflows affecting the field orientation in L43 or Oph B2, the L1517B core could still be magnetically-dominated compared to the gravitational pressures but perhaps stellar winds or external radiation are what is affecting the magnetic field direction.

L1527 meanwhile has a two component magnetic field, one which is perpendicular to the major axis of the dusty envelope and one which is aligned with the outflow direction. The dusty envelope magnetic field is preferentially parallel to the large-scale magnetic field, but in this case, the core has clearly evolved beyond magnetically-dominated because there is an embedded protostar. This is further supported by the fact that the critical magnetic field strength is nearly twice that of the calculated magnetic field strength. So the relation of Mestel (1965) still explains this scenario, but there has not been the change in field orientation from the large-scale field which we have seen in other cores.

6.2.1.9 Overall trends

In order to evaluate any overall trends in our sample of cores, we choose to compare a few key metrics. Our goal is to show that the relation of Mestel (1965) holds in these nearby star forming regions and molecular clouds. We show this in two ways. Figure 6.6 is a plot of the magnetic field strength versus column density. We plot a dashed line which represents Equation 3.14 (Mestel, 1965) to divide the plot into two regions. Above the line would be cores where the calculated column densities are less than the critical column densities derived from calculated magnetic field strengths (using Equation 3.14). Below the line would be cores where the calculated column densities are greater than the critical column density values. In the former case, this would mean those cores above the line are magnetically-dominated while in the latter case, those cores below the line are matter-dominated. We plot each source from Table 6.1 and color code them according to the difference between the mean magnetic field ($\mu_{\theta,B}$) in that source and the large-scale magnetic field (traced by Planck, θ_{Planck}). A low difference would indicate the magnetic field in the source still traces the large-scale magnetic field and has not become matter-dominated. We would then expect these points to lie above the dashed line in Figure 6.6 and be colored purple according to the colorbar in the figure. Then a high difference (colored yellow) would indicate the magnetic field of the source has been altered from the large-scale field, here assumed to be due to gravity and the movement of matter across field lines, hence bending them. These points would be expected to lie below the line, in the matter-dominated region.

We also show this expected behavior using Figure 6.7. Here we plot $N(H_2)/N_c$ on the x-axis versus the difference between the mean magnetic field ($\mu_{\theta,B}$) in that source and the large-scale magnetic field (traced by Planck, θ_{Planck}). We plot a vertical dashed line to divide the plot where left would be magnetically-dominated sources and to the right would be matter-dominated sources. We further divide the plot with a horizontal line which divides the plot into sources where the large scale field is similar to the mean magnetic field in the bottom region and in the top are sources where the two magnetic field orientations are different. Here we would expect all of the sources to fall in either the lower left or upper right quadrant if following the relation of Mestel (1965). This would represent sources where they are magnetically-dominated with similar large-scale and core-scale magnetic fields (lower left quadrant) and sources which are matter-dominated with core-scale magnetic fields that no longer trace the large-scale magnetic field.

We differentiate sources from this work and from literature using circles and squares, respectively. Across our sample of cores, there does not appear to be a general trend. A majority of the cores do lie below the dotted line in Figure 6.6 which indicates their calculated column densities are higher than the critical column density derived using the calculated magnetic field strength in the core. That would suggest that a majority of the cores are matter-dominated. However, matter dominated does not mean it is due to start forming stars imminently. The calculation of magnetic- to matter-dominated only considers the magnetic field and gravity. Many of these cores might have large turbulent motions or in the case of a region like

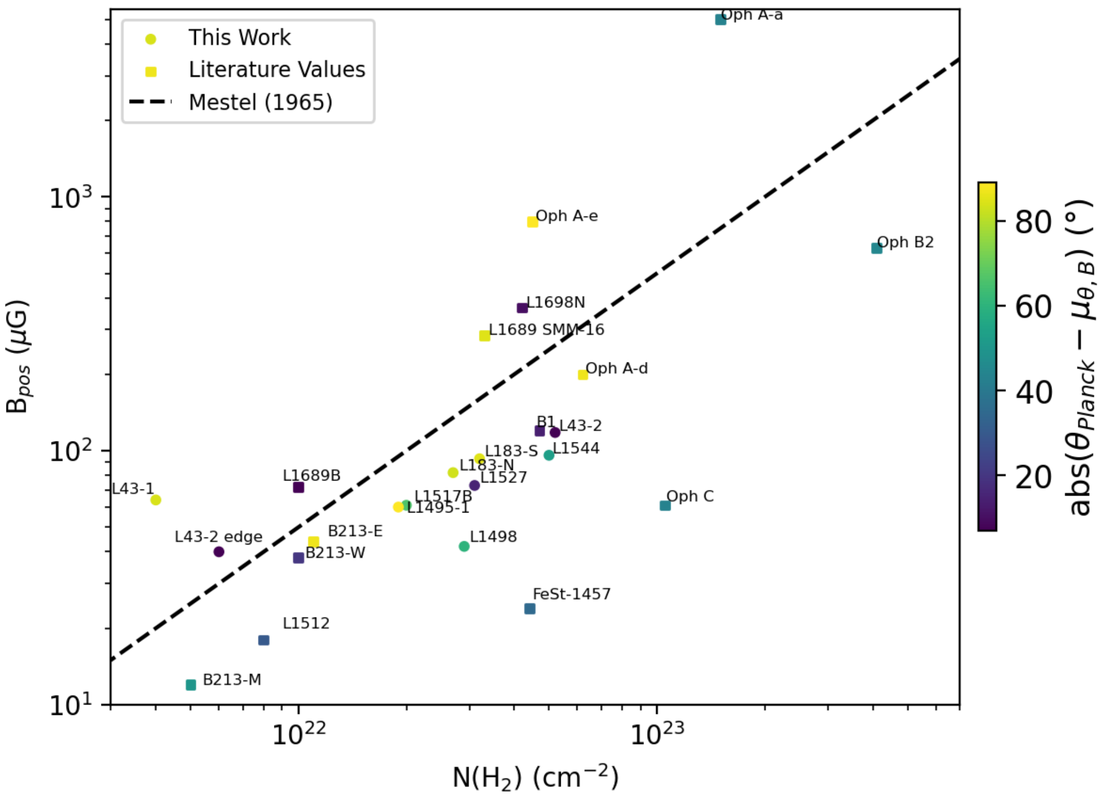

Figure 6.6: A log-log plot of B_{pos} versus H_2 column density for all of the cores listed in Table 6.1 which have magnetic field strengths. The line is from Equation 3.14 (Mestel, 1965). Circles represent sources from this work while squares represent sources taken from literature (see Table 6.1 for references).

Oph A or L1517B, they are influenced by their surroundings. While triggered star formation may take place, the influence of the young surrounding stars may also hinder the formation of dense enough cores. This conclusion is also shown with a majority of the cores to the right of the vertical line in Figure 6.7.

The other question we want to answer from this plot is if the core scale magnetic field orientation still traces the large-scale field in matter dominated cores. We had predicted that cores which are still magnetically-dominated would have field orientations similar to the large-scale field in which they are embedded (Ward-Thompson et al., 2023). Conversely, once a core was matter-dominated, the matter

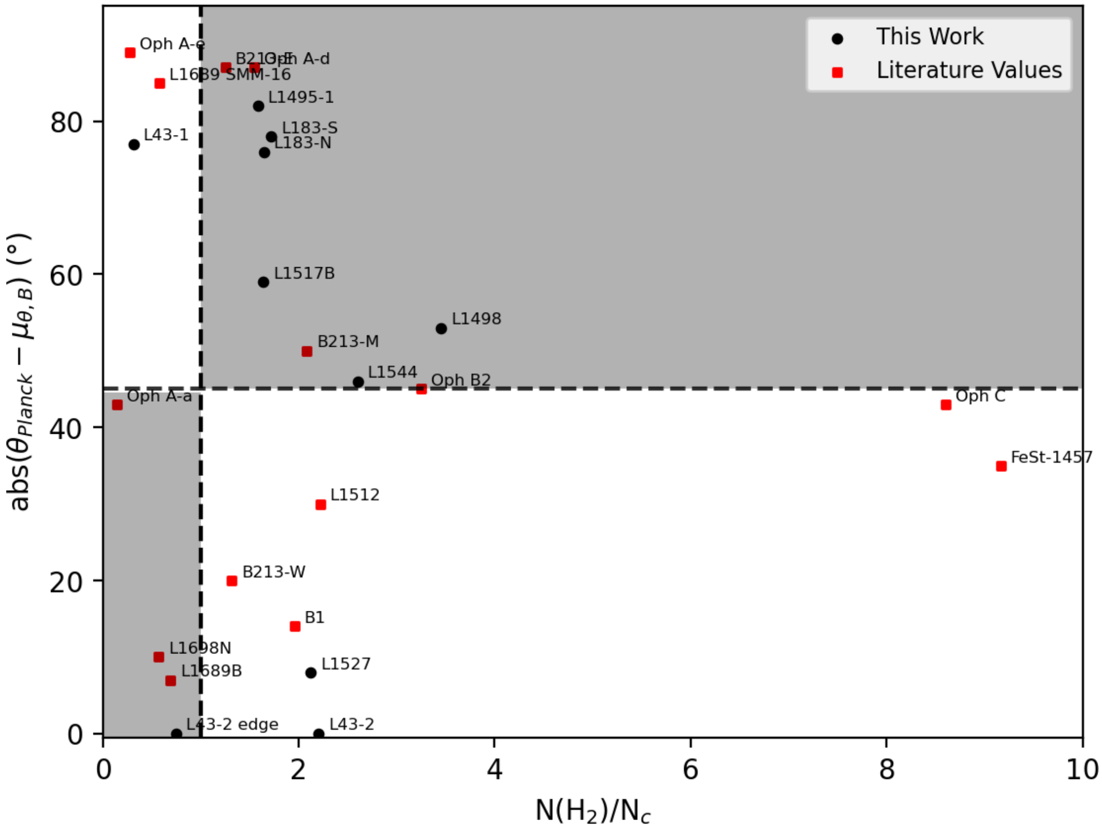

Figure 6.7: A plot of difference in large scale magnetic field angle (θ_{Planck}) and source mean magnetic field angle ($\mu_{\theta,B}$) vs the ratio of observed column density (N_{H_2}) to critical density (N_c). The vertical dashed line shows the separation between magnetic (left) and matter (right) dominated sources. The horizontal dashed line breaks the plot into agreement between large- and core-scale magnetic fields (below) and disagreement (above). The two regions which follow the Mestel (1965) relationship are shaded in. Black circles represent sources from this work while red squares represent sources taken from literature (see Table 6.1 for references)

would be able to flow across the field lines and twist/bend them so the core scale field would not have a similar orientation to the large-scale field. What we would expect then is that Figure 6.6 would show a population of cores above the dotted line which have low $abs(\theta_{Planck} - \theta_B)$ values. Conversely we expect the population of cores under the dotted line to have high $abs(\theta_{Planck} - \theta_B)$ values. Instead we do not see a clear trend in either direction. Similarly, in Figure 6.7, there are some sources which fall into the two shaded quadrants, but many lie outside of those two shaded quadrants. The shaded quadrants represent the two cases mentioned above. In both plots we can see the instances where the relation holds, and of the five magnetically-dominated cores, three have core magnetic field orientations similar to Planck. When including the Oph A regions, Oph A (a) has a $\Delta\theta = 43°$ and Oph A (e) has a $\Delta\theta = 89°$, so Oph A (a) has no preferential alignment while (e) is nearly perpendicular. The matter-dominated side is more spread out and no firm conclusion can be drawn from them. Instead, there must be other factors influencing why the magnetic field changes from large-scales down to small-scales. Overall, we can break Figure 6.7 into sources within the quadrants and sources outside of them. Overall, there are 14 sources inside the shaded quadrants and 10 sources outside of them. So a majority of our sources which have measured magnetic field strengths do show what we would expect from the relation of Mestel (1965).

6.2.2 The Central Molecular Zone

6.2.2.1 Magnetic field and density structures - histograms of relative orientation

In nearby star-forming regions, a combination of Planck and Herschel data revealed a general trend of magnetic fields transitioning from parallel to intensity structures to perpendicular to them (Planck Collaboration et al., 2016b). Herschel was used to observe the large-scale structures of the molecular cloud complexes and Planck was used to observe the magnetic field. The method used to test the transition is called the histogram of relative orientation (HRO; Soler et al., 2013; Soler et al., 2017). It is fundamentally a way of visualizing the comparison between the density structure and the magnetic field orientation. The angle of the 2D-density contours is given by

$$\psi = tan^{-1}(\frac{\partial\Sigma/\partial x}{\partial\Sigma/\partial y}) \ , \tag{6.1}$$

where $\partial\Sigma/\partial x$ and $\partial\Sigma/\partial y$ are the projected column density gradients in the x- and y-directions respectively (Soler et al., 2013). This angle ψ will be perpendicular to the density gradient direction. The difference between the magnetic field vector and the contour orientation vector is then given by ϕ which is the angle of relative orientation (Soler et al., 2013) in the range of $abs(\phi) < 90°$. A histogram of ϕ is then made and it is split into three sections, $\phi < 22.5°$, $\phi > 67.5°$ and then $22.5° < \phi < 67.5°$ which represent preferentially parallel alignment, preferentially perpendicular and no preferred orientation respectively.

To then determine how the alignment of the magnetic field with the material changes at different densities, we then split the map into a series of either column density or intensity bins and for each bin, construct the histogram of the angle differences. We then define a shape parameter ξ,

$$\xi = \frac{A_{\mathrm{c}} - A_{\mathrm{e}}}{A_{\mathrm{c}} + A_{\mathrm{e}}} \ , \tag{6.2}$$

where A_{c} is the area of the histogram where $\phi < 22.5°$ (preferentially parallel) and A_{e} is the area where $\phi > 67.5°$ (preferentially perpendicular).

If $\xi < 0$ there is a preferential perpendicular alignment between the density structure and the magnetic field (so density gradients are parallel to B-field) and if $\xi > 0$ there is preferential parallel alignment between the magnetic field direction and the density structure (density gradients are then perpendicular to B-field). This is illustrated in Figure 6.8. The white vectors in that image show the density gradient direction which is perpendicular to the density structure contours. These density

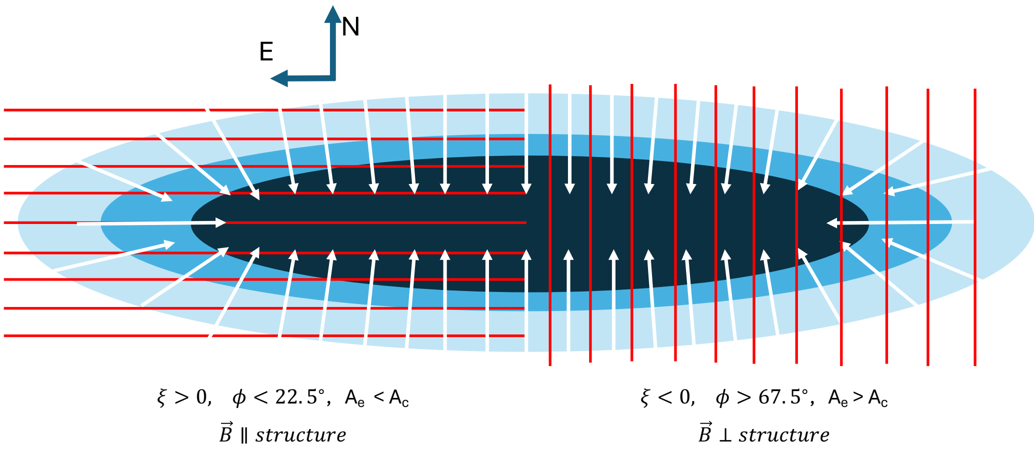

Figure 6.8: A cartoon image illustrating various parameters of the HROs and their physical meaning. The blue ellipsoids represent material with the darker colors representing higher densities. The white arrows are the column density gradients which is ψ+90°. The magnetic field is represented with red lines. The two extreme situations are shown. On the left the magnetic field is parallel to the structure contours and hence ϕ < 22.5°, ξ >0 (see Eq. 6.2) and the area where ϕ > 67.5° ($A_{\rm e}$) is less than the area where ϕ < 22.5° ($A_{\rm c}$). On the right the magnetic field is perpendicular to the structure contours and hence ϕ > 67.5°, ξ <0 and $A_{\rm e}$ > $A_{\rm c}$.

gradient vectors are plotted as blue lines in the left column of Figure 6.10 and so where they are perpendicular to the red lines (which represent the magnetic field orientation), the magnetic field is actually parallel to the density structure which would give a $\xi > 0$, and vice versa for $\xi < 0$.

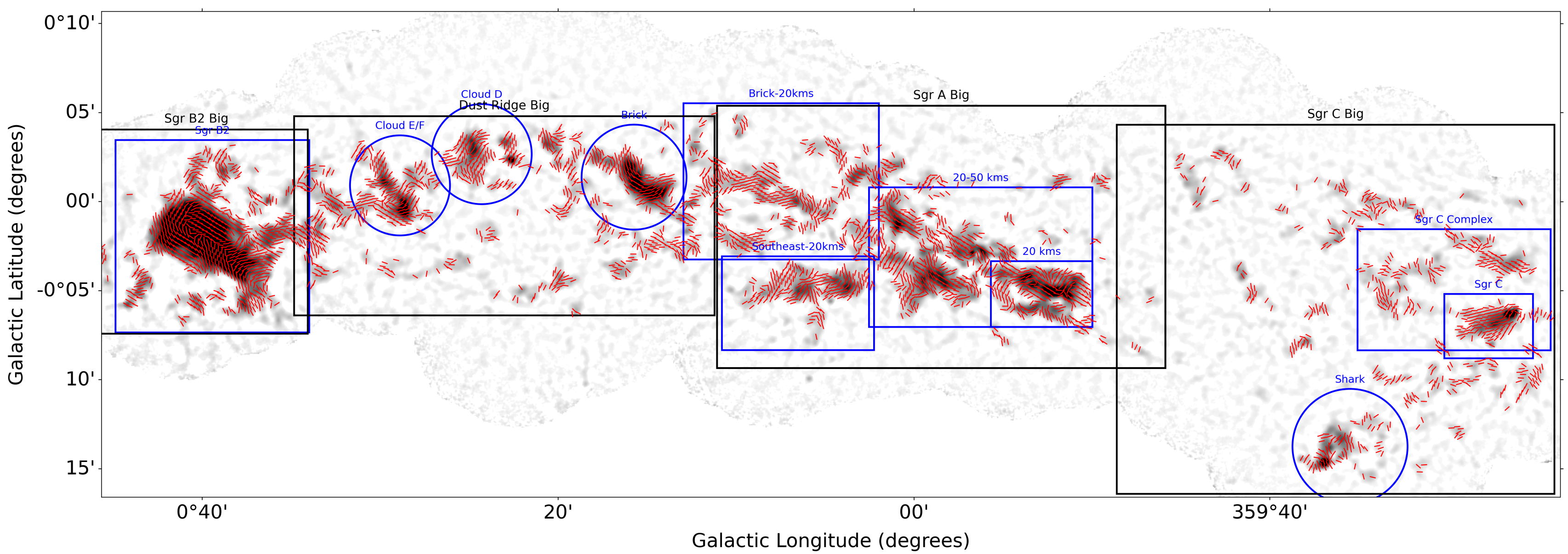

Figure 6.9: Background image is the 850 μm Stokes I dust emission from SCUBA-2/POL-2. Red line segments are plotted which show the magnetic field direction (polarization vectors rotated by 90° and binned to 14″. Overlaid are the regions corresponding to Figures 6.10, 6.11 and 6.13.

If our results were to follow the same trend from Planck Collaboration et al. (2016b); Soler et al. (2017), we would expect to see ξ decrease from positive values to negative values as column density (or intensity as a proxy for column density) increases. We present HRO plots in Figures 6.10, 6.11 and 6.12 of Sgr B2, the set of regions from Figure 6.9 and the entire CMZ respectively. We used three different data sets to determine different density gradients. We try with our own 850 μm dust continuum map, with the 250 μm Hi-GAL *Herschel*/SPIRE dust map and then with the same AzTEC column density map used in Section 5.6. The magnetic field observed at 850 μm will trace the same structure as our 850 μm maps and so that means we will be biased towards the densest structures and not trace extended, low-density structure and therefore may miss the transition. The *Herschel* map will show the extended structure, but we may not be able to trace the magnetic field in those regions. The AzTEC maps will be similar to the 250 μm maps which will contain extended structure but no magnetic field in those regions. The AzTEC maps stop just west of Sgr B2 so there is no column density information for that region and we investigate only the orientation relative to the 250 and 850 μm maps (see Figure 6.10).

6.2.2.2 Column density transition threshold

As can be seen by Figure 6.10, in the case of the 250 μm emission, there is no distinct transition from parallel to perpendicular or vice versa. The shape factor is <=0 across the intensity bins, suggesting that the magnetic field either has not distinct orientation to the structure or is slightly preferentially perpendicular to the structure of the Sgr B2 cloud. The magnetic field orientation in Sgr B2 is very complex and exhibits a curling pattern to the northeast and to the southwest an arced field that does actually cross perpendicular to the general northeast-southwest orientation of Sgr B2. This occurs at the higher intensities within the third to last

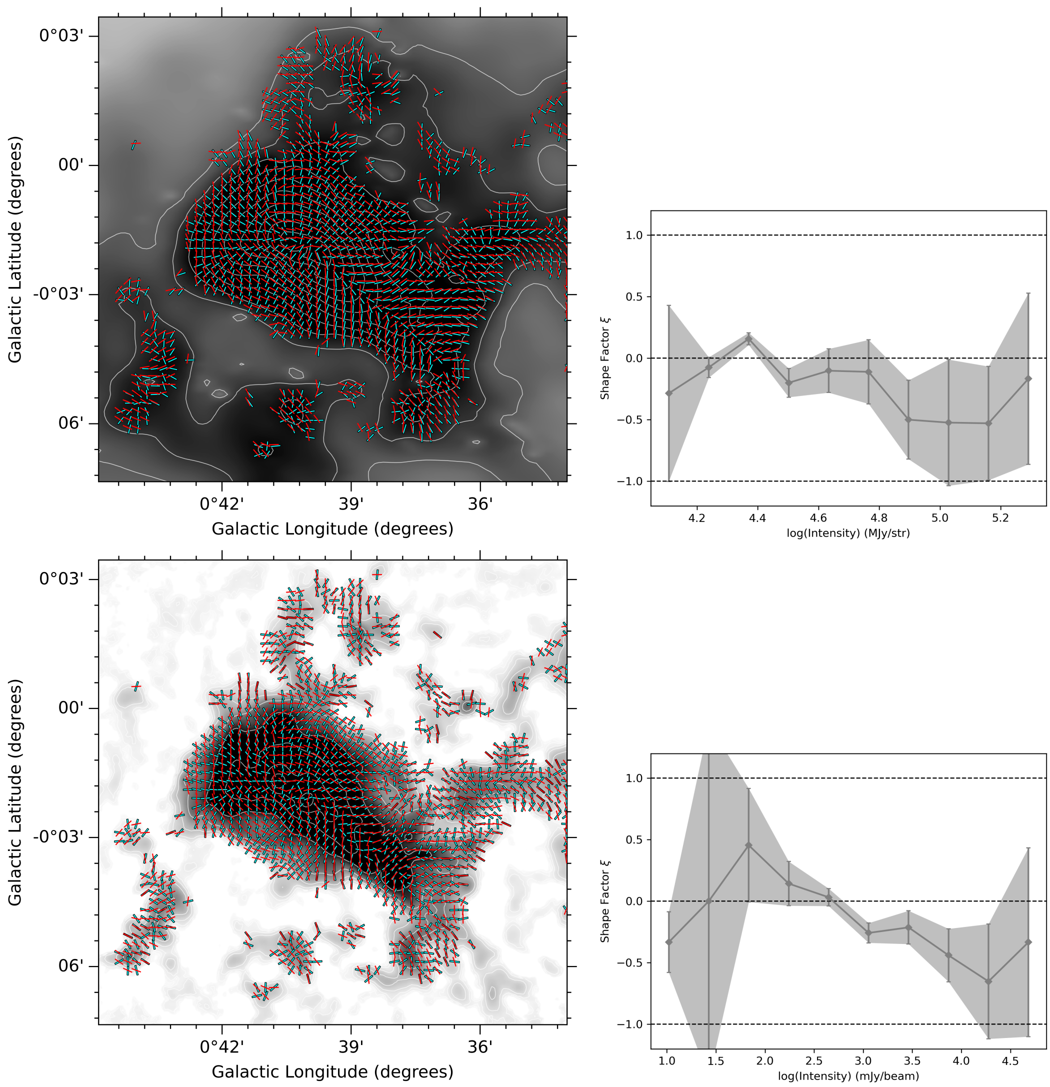

Figure 6.10: A series of HRO and vector plots for Sgr B2. The upper left panel uses *Herschel*/SPIRE 250 μm maps to calculate the density gradient. The lower left panel is made using SCUBA-2/POL-2 850 μm maps to calculate the density gradient. The cyan vectors in the panels show the column density gradient (perpendicular to the structure) and the red vectors show the magnetic field orientation. The contours correspond to the bins used in the histograms to the right. The right panel is the two HRO plots with the Herschel data on the top and JCMT on the below.

contour which does show a shape factor of ≈-0.5. In the lower density sides of the cloud, the magnetic field lines run parallel to the contours which also follows the transition seen in Planck Collaboration et al. (2016b). This transition is seen with the 850 μm comparison where the HRO shows that the magnetic field starts out either perpendicular or no preferred orientation to the structure and then becomes slightly parallel before becoming perpendicular again at higher intensities (and therefore densities). Overall there appears to be a general overall trend of preferentially perpendicular alignment. As we mentioned above, we might be tracing the densest material since we observe at 850 μm and from under the atmosphere (losing the extended structure) so we will be biased towards tracing the material which has already transitioned to perpendicular orientation between the magnetic field and density structures.

We performed the same analysis for Sgr B2 for each of the regions shown in Figure 6.9. We try and investigate if the transition can be seen at the individual cloud level with the smaller regions versus the four largest areas shown with black squares in Figure 6.9. These HROs are shown in Figure 6.11 and the region names match those in Figure 6.9. The figure illustrates that for nearly all of the regions, there is no obvious transition threshold where the magnetic field orientation transitions from parallel to the density structure to perpendicular. Instead, most of the intensity and column density bins have preferentially perpendicular alignments (ξ <0). This could again be due to the general bias of our observations. While Planck and Herschel both flew above the atmosphere and could match extended structure observations, hence tracing the lower column density and intensity regions, we cannot.

Figure 6.12 shows a series of three HROs which encompass the entire CMZ and all the magnetic field information we have within our mosaic. We performed the HRO analysis for the three different density and intensity maps mentioned in Section 6.2.2.1. The 250 and 850 μm HROs both show that the alignment of the

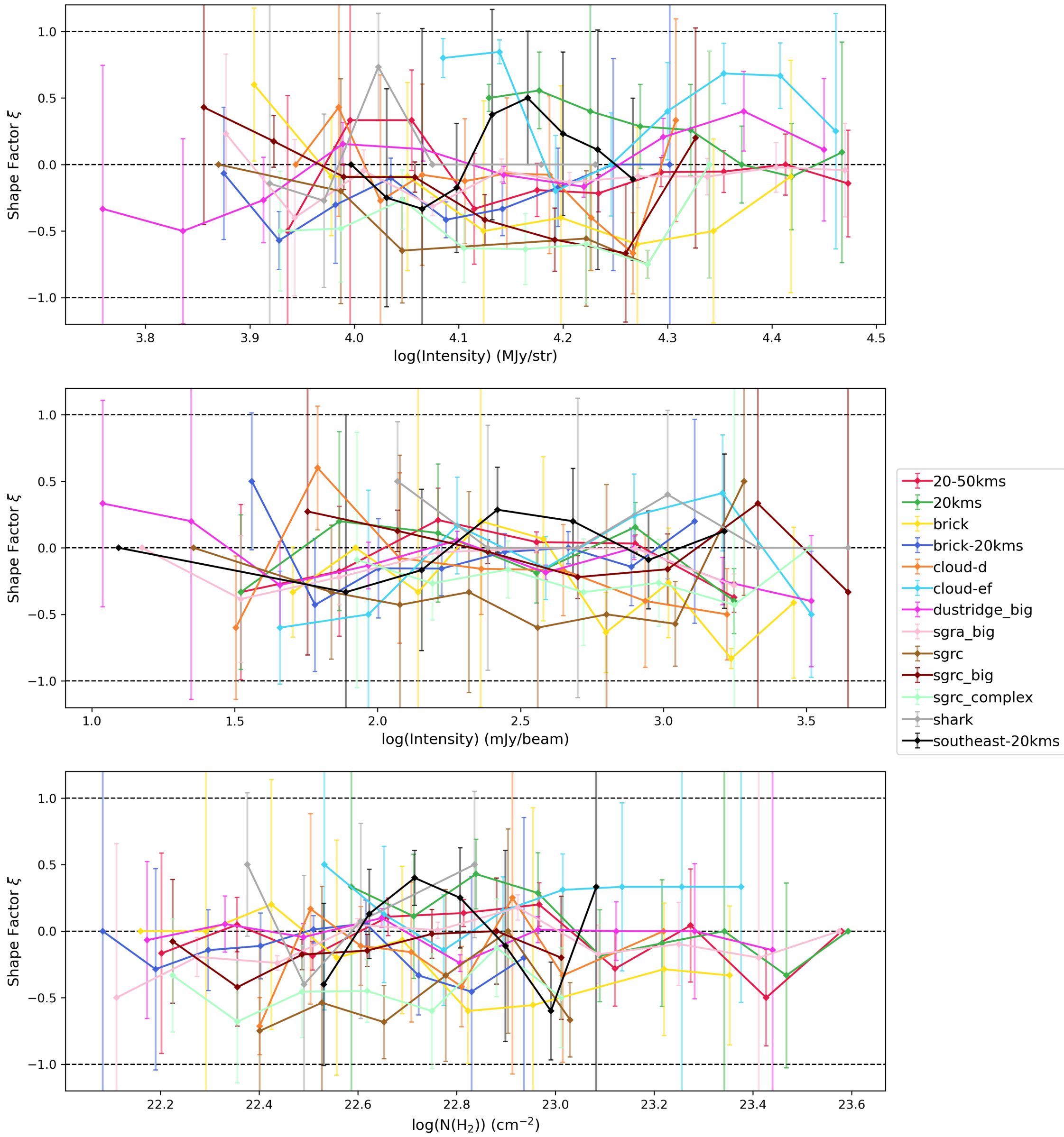

Figure 6.11: A plot showing the HROs for each of the regions shown in Figure 6.9. The Sgr B2 region is shown as an example in Figure 6.10 and is not included in these plots because it is significantly brighter and skews the axes to the right. The upper plot is made using *Herschel*/SPIRE 250 μm maps to calculate the density gradient. The center plot is made using SCUBA-2/POL-2 850 μm maps to calculate the density gradient. The lower plot is made using the AzTEC H_2 column density plots to calculate the density gradient.

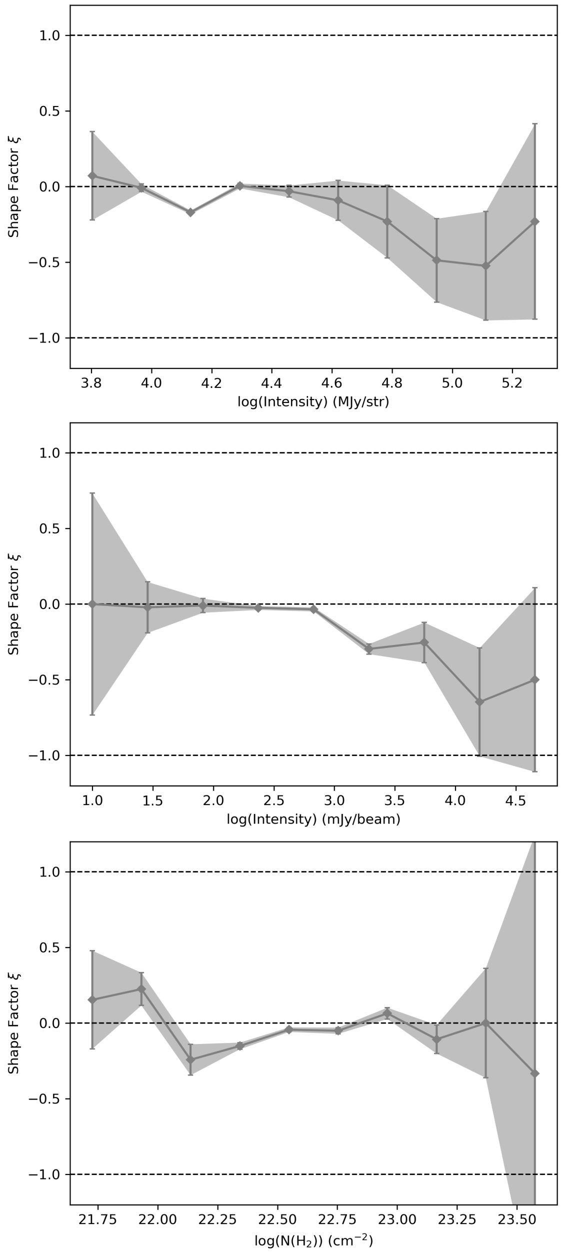

Figure 6.12: Three HROs for the entire CMZ. Upper panel is the HRO constructed with the 250 μm *Herschel*/SPIRE map. Centre panel is the HRO constructed with the 850 μm SCUBA-2/POL-2 map. Lower panel is the HRO constructed with the AzTEC H_2 column density map. Note that the AzTEC analysis does not include Sgr B2 as mentioned in the text.

magnetic field goes from unaligned to then preferentially perpendicular to the structure at higher intensities. As mentioned before, this follows the same trend seen in Planck Collaboration et al. (2016b); Soler et al. (2017). The HRO constructed with the AzTEC map appears to remain around ξ=0 up to high densities. This global pattern of no alignment into preferentially perpendicular alignment suggests that we either do not trace the diffuse material and therefore do not see the stage of the magnetic field directing the material, or within the CMZ, the magnetic field is not the dominant mechanism for shaping the material. We do know from Section 5.6 that the magnetic field on individual cloud scales is very strong and the mass-to-flux ratios suggest an important magnetic field. However, the magnetic field may still be dragged along with the material or is being shaped by external factors such as feedback or the large-scale kinematics of the region. This may be why we see the magnetic field perpendicular to structures but still playing a role on individual cloud scales. The same is true for nearby regions, where the transition of parallel to perpendicular alignment occurs on the large-scale, but even in regions where the large-scale magnetic field is perpendicular to the structure, on small, individual cloud-scale, the magnetic field is suppressing star formation.

Figure 6.13 tells a similar story of preferential perpendicular alignments. For each of the regions we calculate the total shape factor, not varying with column density or intensity bins. Nearly all of the regions have an overall $\xi < 0$ with all three of the density/intensity maps, though for a majority the shape factor is >-0.2 and in some clouds there is $\xi >0$.

6.3 The Different Modes of Star Formation

As mentioned in Chapter 1, Seo et al. (2019) suggests three different modes for star formation. They make this framework based on the L1495-B218 filament in the Taurus Molecular Cloud (see upper panel of Figure 1.3). Figure 1.6 shows the three

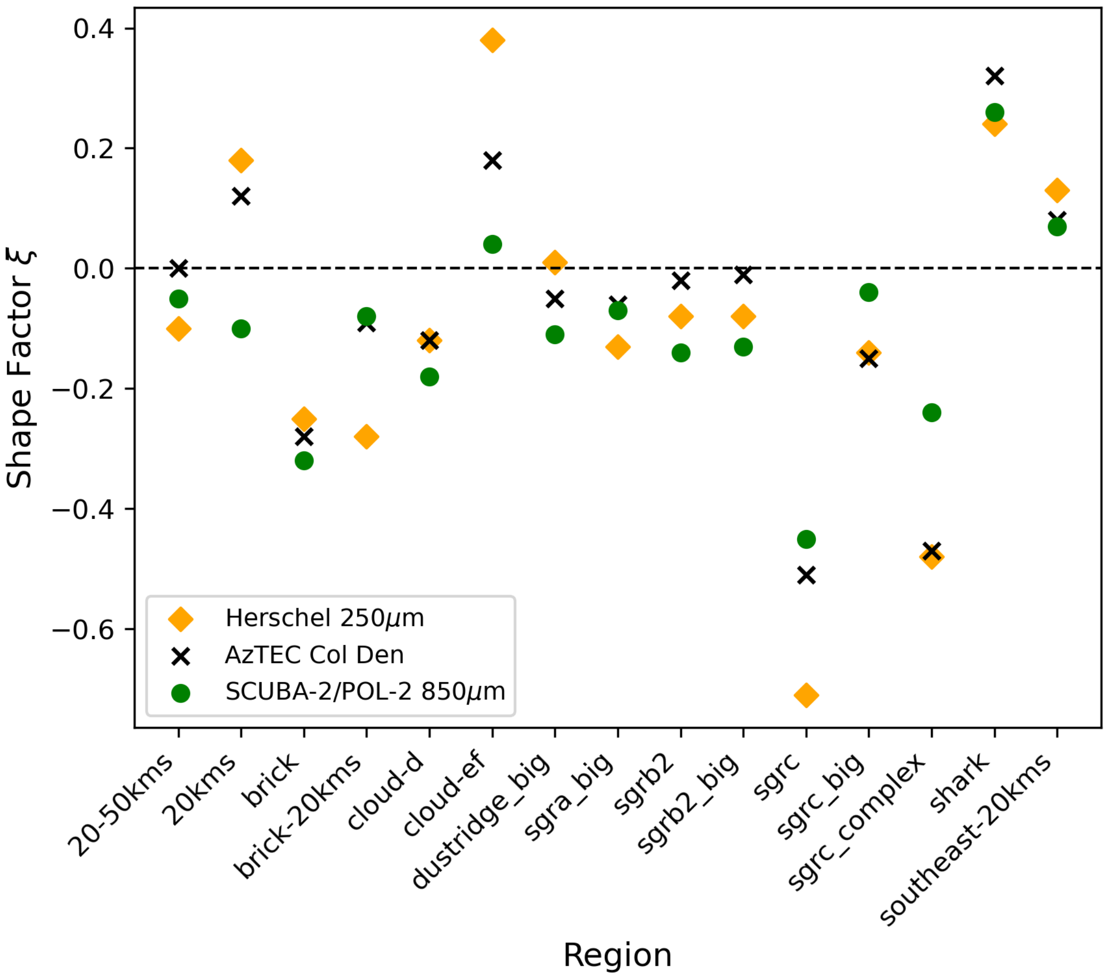

Figure 6.13: A summary of the overall shape factor for each of the regions shown in Figure 6.9. These overall shape factors were not calculated in bins and represent just a general trend in the region of preferentially perpendicular or parallel orientation between the magnetic field and the structure.

modes, each of which are divided into three steps which we simply label as a, b and c. The fast mode of star formation is one that can lead to the formation of clusters (Seo et al., 2019). In this fast mode, filaments feed a central hub or central filament, accreting material until a dense region is formed where core formation can take place. Enough mass is centrally located that numerous cores and eventually stars can form, hence the clustering, or perhaps, a high-mass core and star can form. The slow mode was suggested due to the observation of a number of dense cores within the Taurus filament. Some of the dense cores were gravitationally bound while some were confined by the pressure of the surrounding filament. However, the eventual formation of a star does not seem to be influenced by any large scale nature of the filament or previous dynamics. The large scale flow of the filament is important for creating the dense cores and 'feeding them' but not eventual star formation (Seo et al., 2019). The isolated mode was suggested to account for an isolated dense core to the southeast of the L1495A/B10 region which was not associated with any velocity-coherent filaments or any other identified filaments. A majority of dense cores are thought to be formed in filaments (André et al., 2010), so this isolated mode is not considered to be the dominant source of star formation (Seo et al., 2019).

With the plethora of regions observed with BISTRO-1, BISTRO-2 and BISTRO-3, we attempt to look for these modes of star formation in these other regions. Then, once we establish the mode of star formation occurring, we look at the magnetic field in that region and see if there is a common pattern across the different modes for how the magnetic field looks or how strong it is. The study by Seo et al. (2019) made use of very detailed kinematic observations (many species and at high resolution) to trace the velocity coherence of filaments and large scale inflows. This is not the case for many of the BISTRO regions and we instead rely on the more general identification of these modes, where a central hub formation is indicative of the fast mode, an extended, coherent filament with multiple cores is indicative of the slow mode and a regular molecular cloud in ambient material is the isolated mode. A majority of the sources presented above fit into the slow and isolated modes and so we bring in additional published BISTRO sources which demonstrate the fast mode of star formation.

6.3.1 Magnetic fields in the fast mode of star formation

There have been a variety of intermediate-mass star-forming regions observed by BISTRO, many of which involve a hub-filament system (HFS). As mentioned above, with the lack of comprehensive kinematic data for each of these regions, we rely on the existence of a HFS to indicate if the region is forming stars via the fast mode. We then split the fast mode into the three stages, where filaments are first coming together to accrete material into a central hub (a), then that hub starting to fragment into cores (b) and then finally the existence of many low-mass or a few high-mass stars already existing in the hub.

The most common magnetic field morphology we see in the fast mode is pinched magnetic fields at the hub locations. This seems to occur towards the later stages of the fast mode, where generally the magnetic field is perpendicular to the density structure, which is normally a clump or large filament, as the hub is forming. Prior to the hub formation, the magnetic field is then a mixture of perpendicular and parallel to the density structure depending on how the matter is flowing into the hub.

Some of the most pronounced pinched magnetic field morphologies are in the DR 21 filament (see Figure 6.14) and in the Orion A filament at the south end (see Figure 6.15). In both of these hub systems, there are massive stars which have been formed and are driving large outflows (Pattle et al., 2017; Ching et al., 2022). This pinching of the magnetic field is similar to the idea of ambipolar diffusion but

Table 6.2: Similar to Table 6.1 but here we also assign a mode of star-formation to each core from Seo et al. (2019). The (a), (b) and (c) correspond to the columns in Figure 1.6.

Source	$\theta_{large-scale}$ (°)	$\theta_{\rm core}$ (°)	$\mu_{\theta,B}$ (°)	N(H_2) (10^{22} cm^{-2})	B_{pos} (μG)	Environment
L43-2	63	120	63	5.2(0.9)	118_{59}^{194}	Isolated (c))
L1498	125	125	178	2.9(2.4)	42_{14}^{84}	Isolated (a/b)
L1517B	94	0	153	2.0(0.6)	61_{27}^{108}	Isolated (b)*
L1544	53	150	7	5.0(3.9)	96_{35}^{187}	Isolated (b)
L1527	46	133	38	3.1(1.0)	73_{34}^{124}	Isolated (c)
L1495 (1)	16	167	98	1.9(0.8)	60_{23}^{115}	Slow (b)
L1495 (2-N)	16	0	104	1.5(0.6)	–	Slow (b)
L1495 (2-S)	16	45	43	1.6(0.6)	–	Slow (b)
L1495 (4)	16	60	18	0.9(0.4)	–	Slow (a)
L183 North	88	30	164	2.7(0.8)	82_{36}^{146}	Isolated (b)
L183 South	88	0	166	3.2(1.1)	93_{45}^{157}	Isolated (b)
L183 West	88	0	80	1.9(0.6)	–	Isolated (a)
B213 East	28	126	121	1.1(0.6)	44_{28}^{60}	Slow (c)
B213 Middle	28	119	158	0.5(0.3)	12_{7}^{17}	Slow (b)
B213 West	28	127	48	1.0(0.6)	38_{24}^{52}	Slow (c)
B213 HGBS-1	28	20	54	1.0(0.6)	–	Slow (b)
FeSt 1-457	165	67	130	4.4^{a}	24_{12}^{36}	Isolated (b)
L1512	150	166	180(150)	0.8(0.5)	18_{11}^{25}	Isolated (b)
Oph A	11	170	54	15^{b}	5000_{500}^{5000}	Isolated/slow (c)*
Oph B	33	60	78	41(20)	630_{220}^{1040}	Isolated/slow (b/c)
Oph C	17	134	60(95)	10.5(6.2)	61_{27}^{108}	Isolated/slow (b)
L1689N	24	110	34	4.2(3.5)	366_{157}^{575}	Slow (c)
L1689 SMM-16	11	56	96	3.3(2.2)	284_{160}^{408}	Slow (b)
L1689B	1	75	8	1.0(0.8)	72_{12}^{132}	Slow (b)
DR 21[1]	≈90	–	–	∼10	630–1040	Fast (c)
IC 5146[2]	28	–	37	5.5	0.5(0.2)	Fast (b/c)
Orion A[3]	122	–	116	36(28)	6600(4700)	Fast (c) and Slow (b/c)
NGC 6334[5]	130	–	∼130	∼10	100–820	Fast (a/b) and Slow (c)
Mon R2[6]	∼165	–	–	∼10	1000(60)	Fast (c)

* Potential triggered star formation mode

References: 1. Ching et al. (2022) 2. Wang et al. (2019) 3. Pattle et al. (2017) 4. Arzoumanian et al. (2021) 5. Hwang et al. (2022)

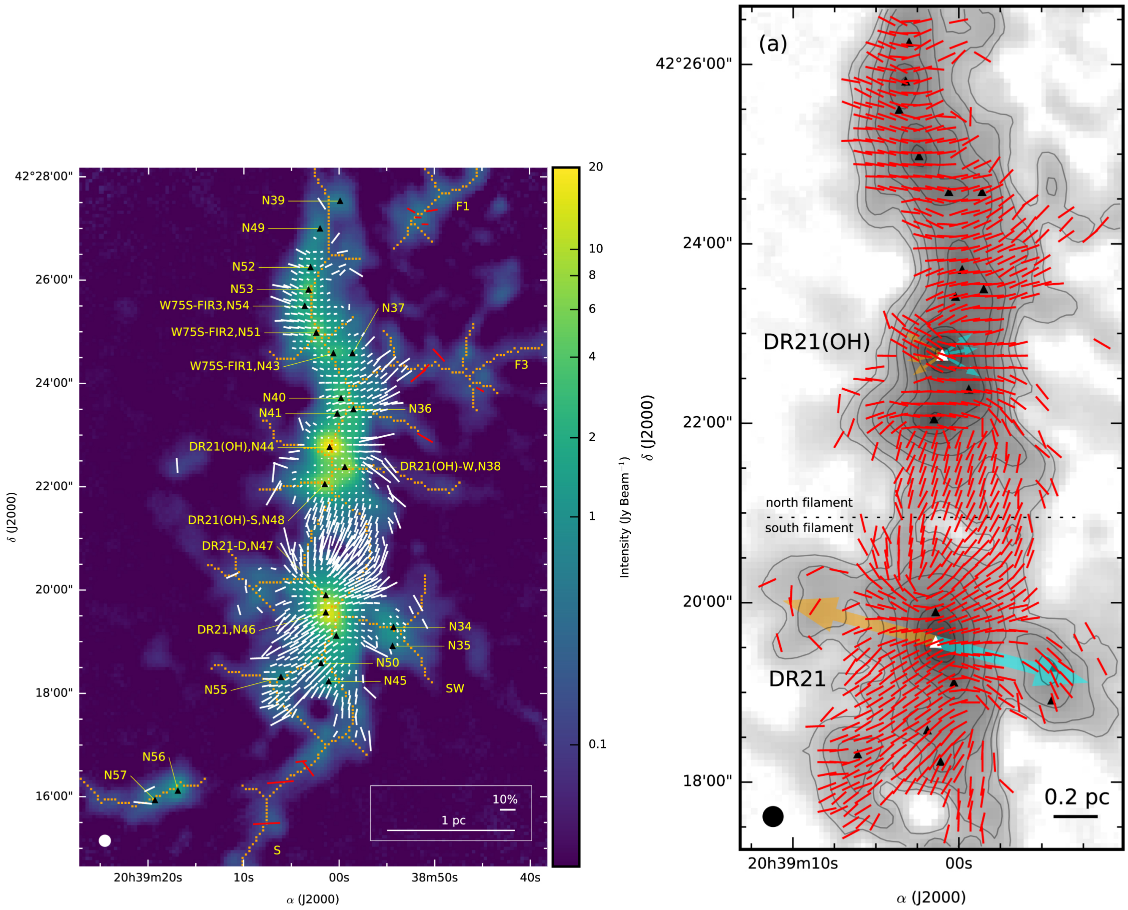

Figure 6.14: Figures 1 and 2 from Ching et al. (2022). On the left is the dust polarization map from JCMT/POL-2 at 850 μm with filaments shown with orange dots along the crests. 24 massive cores are labeled with black triangles. On the right is a zoomed in figure of the magnetic field plotted on the Stokes I map with the same massive core locations shown. Now the redshifted (orange arrows) and blueshifted (blue arrows) outflows from DR21(OH) to the north and DR21 to the south are shown.

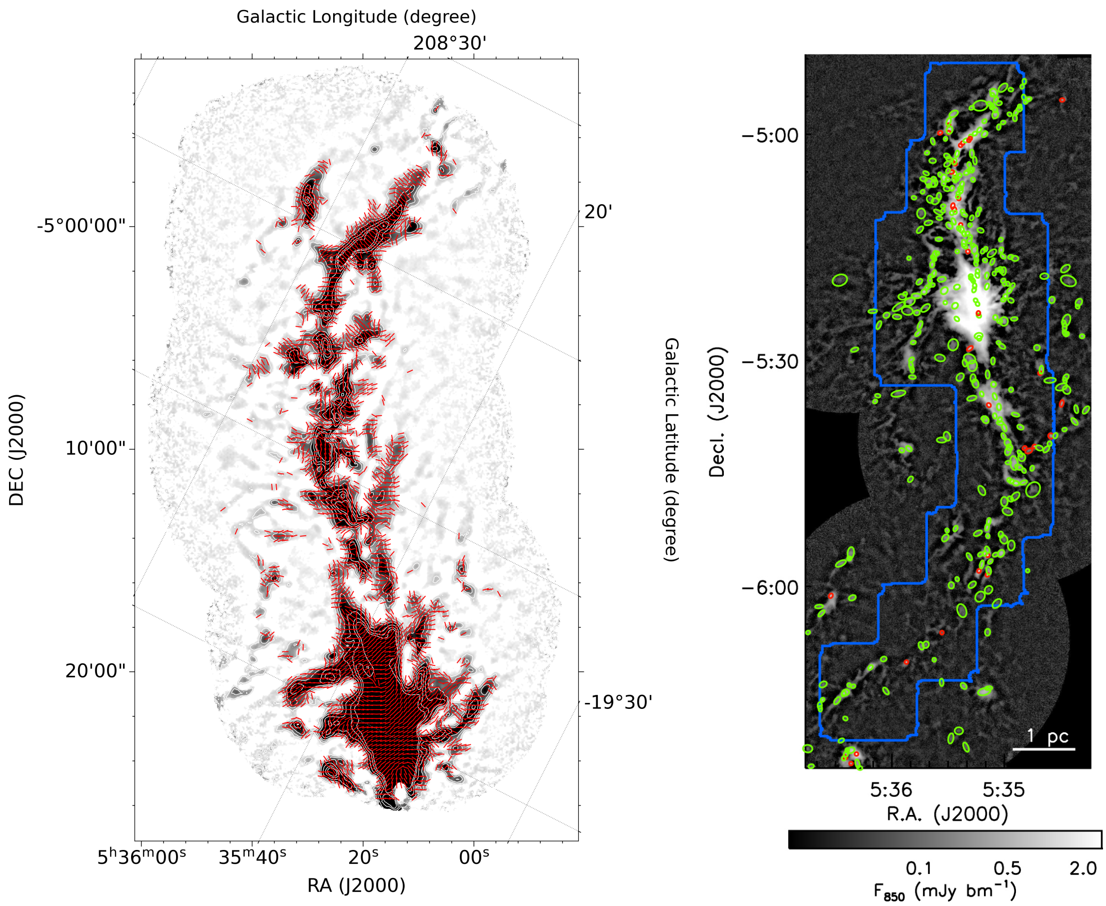

Figure 6.15: On the left is the magnetic field of the whole Orion A filament observed with JCMT/SCUBA-2/POL-2 as part of BISTRO-2. The lower third of the map was published in Pattle et al. (2017). The background image is the 850 μm dust emission. On the right is the Figure 1 from Kirk et al. (2017) which shows identified starless cores in green and protostellar cores in red. The image on the left is approximately the upper half of the image on the right.

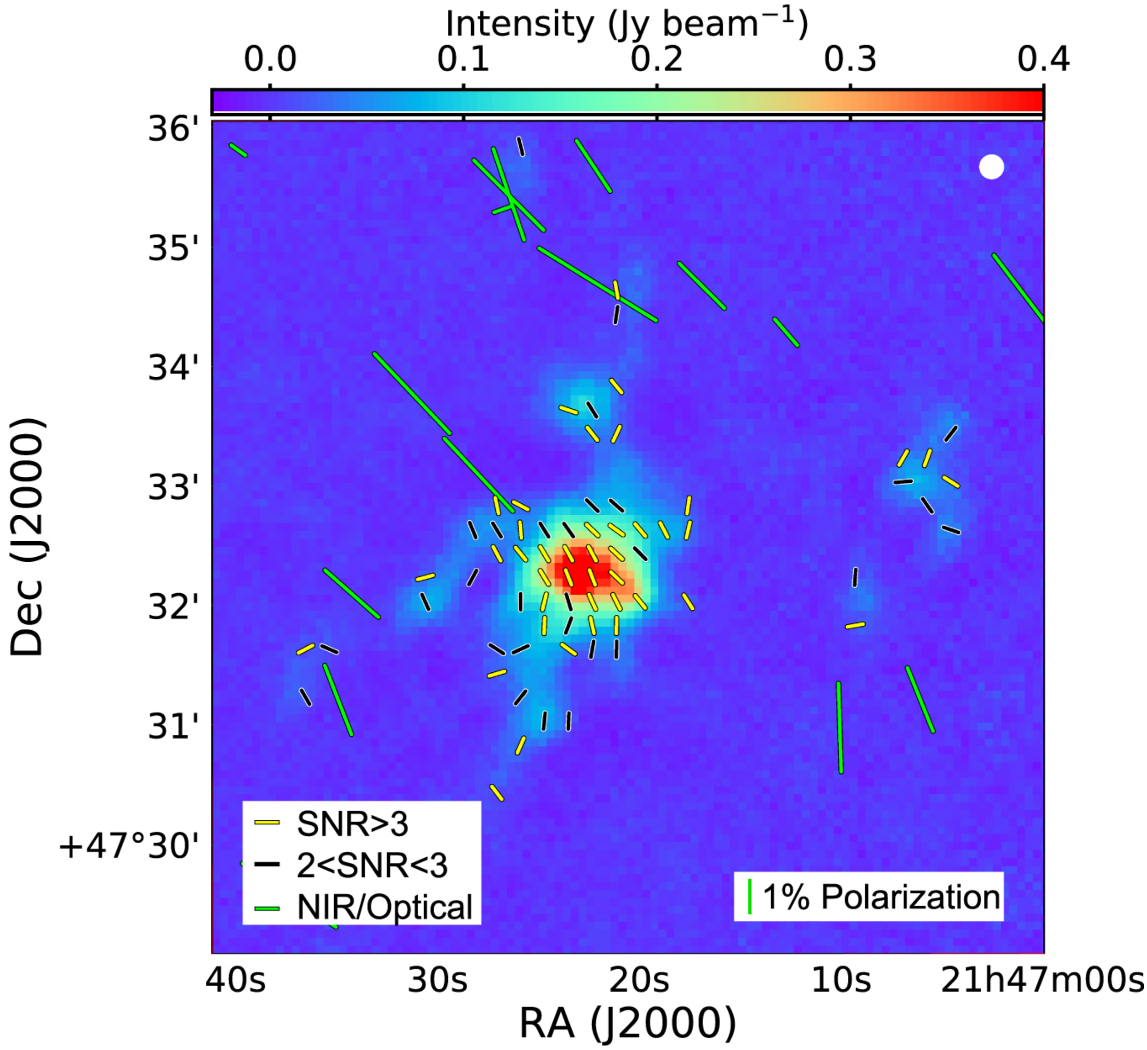

Figure 6.16: Figure 3 of IC 5146 from Wang et al. (2019). The magnetic field orientation from JCMT/POL-2 is plotted as yellow and black vectors on the 850 μm dust continuum map. The large-scale magnetic field traced by H-band polarization are shown in green. The orientation of the large-scale filament is such that it traces a line between the main dense core and the small clump to the northwest.

on a much larger scale. Since the magnetic fields are normally perpendicular to the filament and hub structures, as material flows into the hub system from along the filaments, once the hub becomes massive enough and gravitational contraction occurs, then the magnetic field will be dragged along by the material and hence exhibit this pinched morphology. Because both of the aforementioned Orion A and DR 21 have the massive stars already formed in their hub system, they are classed as being in the (c) stage of the fast mode. As will be discussed later, the Orion A filament most likely has slow mode star formation occurring further to the north where there are no hubs, but the filamentary structures are still prevalent and many cores are forming (see right panel of Figure 6.15). In DR 21 we also see a magnetic field which is parallel to the filament between DR 21 and DR 21(OH) which may be explained by motions of the gas in that location, or Ching et al. (2022) suggest the more massive DR 21 is dragging the field lines.

IC 5146 is not as massive as Orion A or DR 21. Instead it is more of a core-scale HFS which sits at the head of an east-west filament. It contains a few young protostars and so we class it is transitioning from the fast (b) star formation mode into the fast (c) mode. The magnetic field is starting to exhibit a pinched morphology to the east, but those magnetic field vectors also trace the large-scale field which itself is roughly perpendicular to the filament. We suggest in NGC 6334, there are multiple modes of star formation like in Orion A. As we will discuss later, there is slow (c) star formation along the main ridge to the south in filaments 3 and 2. This slow mode is creating massive cores then which differentiates it from other slow star formation modes such as in L1495A (see Section 6.3.2). However, NGC 6334 does have a HFS at the northeast end. A wide range of magnetic field orientations are found, but there is a predominantly perpendicular (to the filament) magnetic field structure. Lower on down the filament, there are also other areas of perpendicular orientation, but in some areas, parallel too.

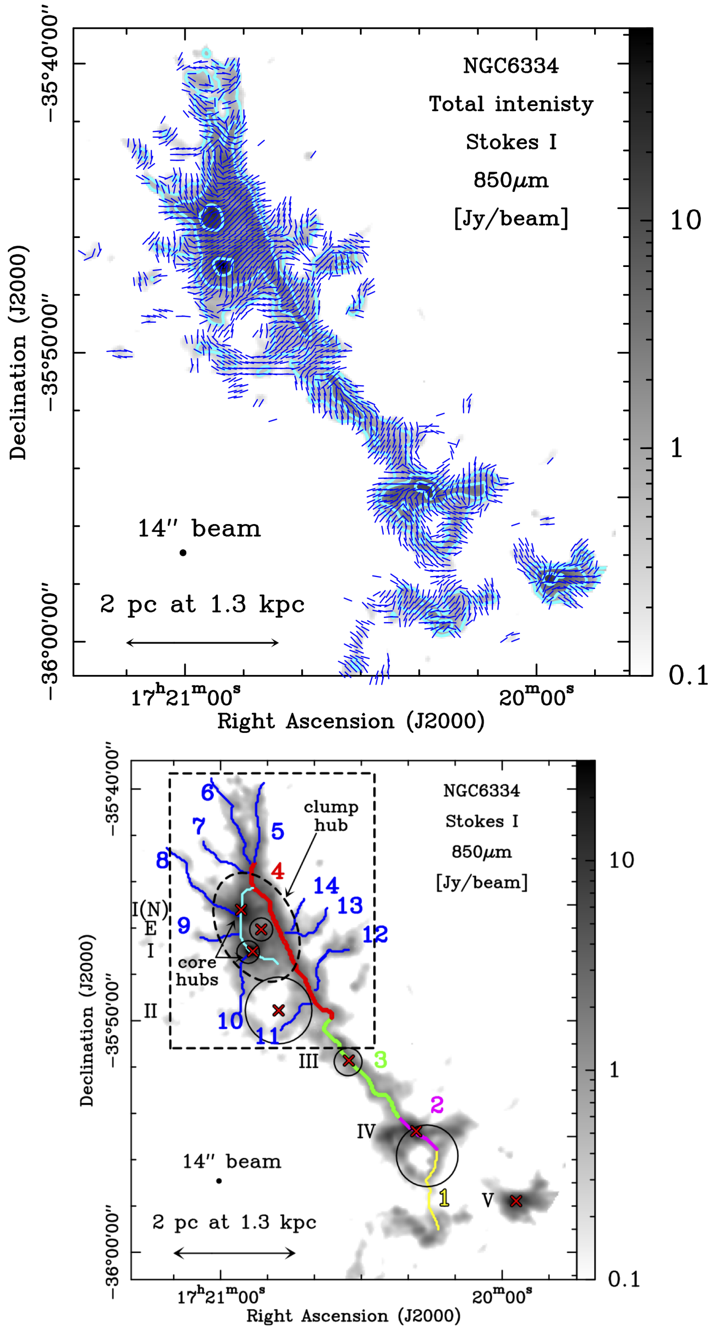

Figure 6.17: Figures 3 and 10 of NGC 6334 from Arzoumanian et al. (2021). The upper panel is the 850 μm Stokes I continuum with blue lines showing the magnetic field orientation overplotted. The lower panel shows the filaments and sub-filaments of NGC 6334. The main ridge filaments are labeled as 1–4. The filaments 2 and 3 contain high-mass star forming cores. The northeast area is where the filaments and sub-filaments converge into the hub system.

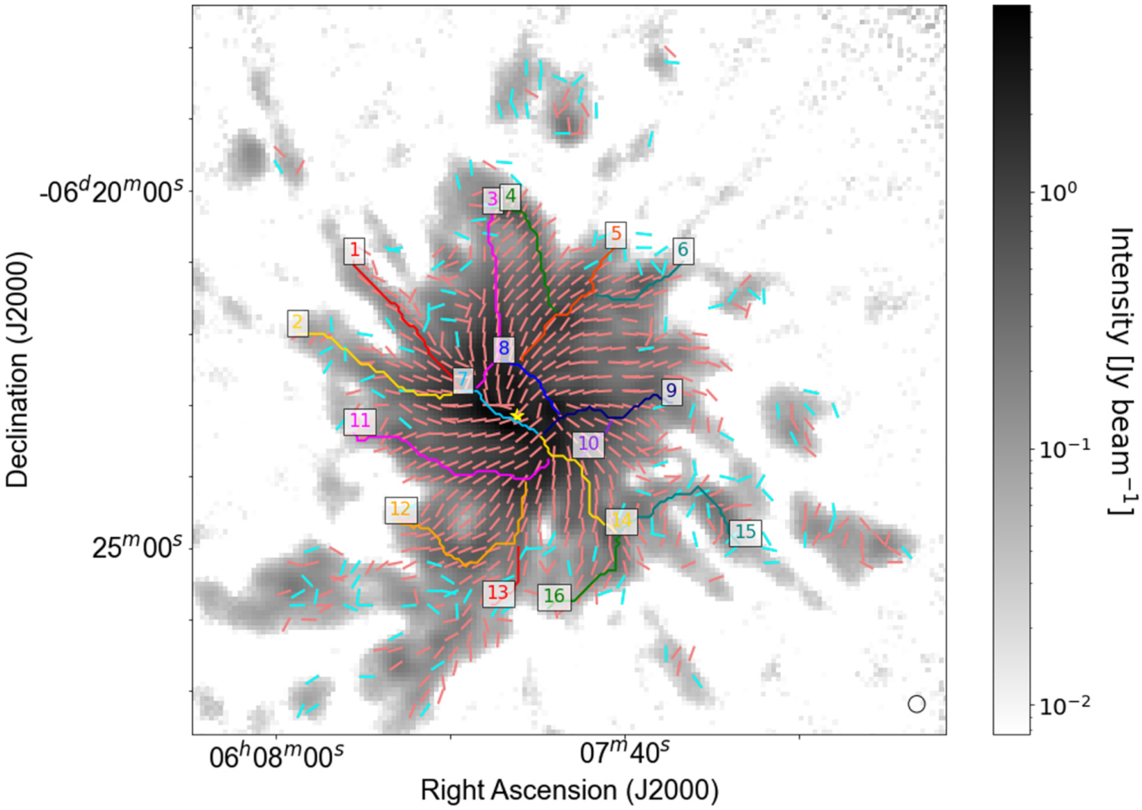

Figure 6.18: Figure 4 of Monoceros R2 from Hwang et al. (2022). The background image is the 850 μm Stokes I continuum. The pink and blue vectors represent the magnetic field direction observed with POL-2 with the pink just having a stricter S/N cut. The skeletons of the filaments are shown as colored lines. The central source IRS 1, a 10 $M_\odot$ star driving a HII region, is shown as a yellow star.

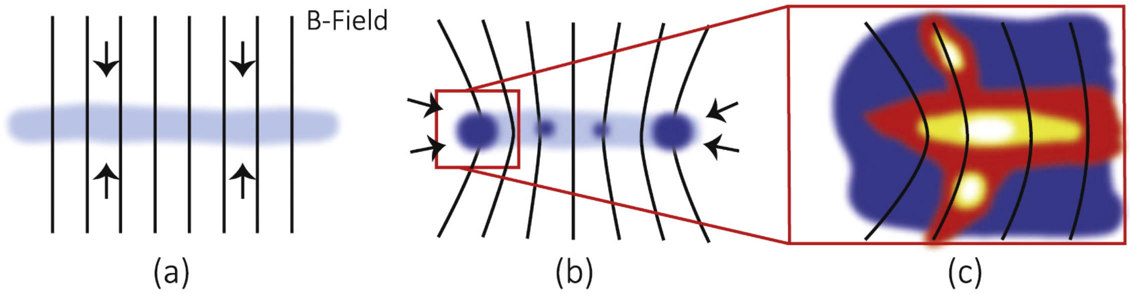

Figure 6.19: Schematic of IC 5146 evolution from Figure 13 of Wang et al. (2019). It shows the evolution of a HFS like IC 5146 with the magnetic field lines shown as black lines and the material in blue, with darker blue indicating higher densities.

Monoceros R2 is a very interesting source because it does not show as explicit of a pinching morphology. Instead, Hwang et al. (2022) found a spiral structure that spiraled in towards the center of the hub. Physically, the fields cannot all spiral to one point, but they may become tangled inside the hub. We suggest that the magnetic field also shows a slightly more pinched morphology. The right side of the pinched field traces the area to the north of filament 9 which is oriented east-southeast and curves down towards filament 12 where it changes to primarily a southeast orientation. The left side of the pinched field then follows filament 5 at approximately a southeast orientation and then below filament 7, it curves back to northeast-east. Considering the star formation occurring within the center of Mon R2, we designate is undergoing the fast (c) mode of star formation.

Figure 6.19 illustrates what occurs in IC 5146 (Wang et al., 2019), but we also see this pattern of the first two steps (a and b) throughout the sources presented here. There is a predominantly perpendicular orientation of the magnetic field to the filament and where hub systems have formed, we see pinched magnetic field lines. The filaments are formed with dynamically important magnetic fields and the filaments are initially magnetically subcritical. Then filaments further accrete mass along the magnetic field lines or from other colliding filaments or sub-filament

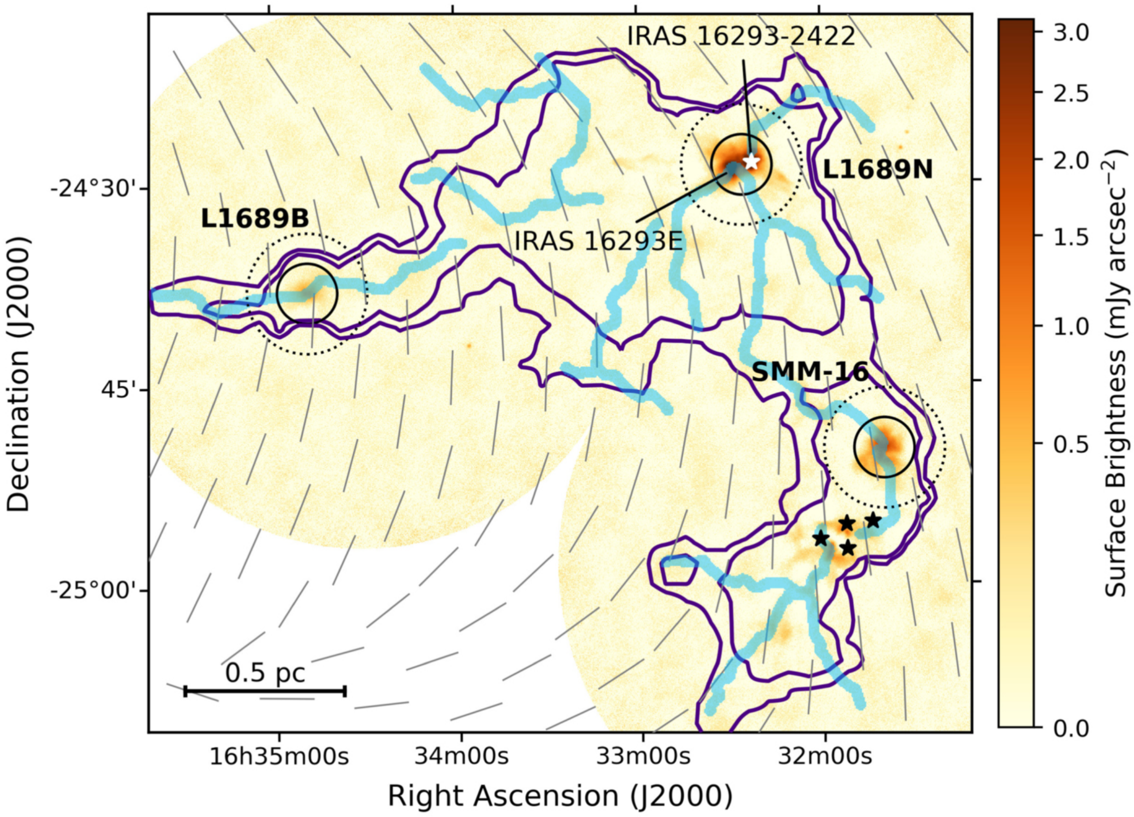

Figure 6.20: Figure 2 from Pattle et al. (2021). It shows the filaments seen with *Herschel* and the location of the L1689 cores within them. The large scale magnetic field is also overplotted.

systems. Once enough mass is accreted they will be supercritical and bend the magnetic fields. This is a similar scenario to what is described in Pattle et al. (2017). The final stage is then fragmentation of the massive core along field lines, but we are not able to resolve that in many of these sources.

6.3.2 Magnetic fields in the slow mode of star formation

The slow mode of the star formation is clearly visible in L1495A (see Figure 4.5) and B213 (see Figure 6.1) where distinct filaments seen by Herschel have embedded cores and in the case of B213, some of those cores have evolved to become protostars. The less obvious candidates for the slow mode of star formation are the cores in L1689.

They sit within a system of filaments (see Figure 6.4 and 6.20) but the cores are not within the same filament. This might motivate them to be a part of the isolated star formation model. L1689N is also fed by a series of filaments and has undergone star formation already. It is not nearly as massive as the cores being created and fed in the fast mode of star formation, but it is perhaps just a smaller-scale of that process. It also has a magnetic field that exhibits less of a pinching morphology and it only is perpendicular to one of the filaments feeding it.

The general picture for the slow mode is that the large-scale magnetic field will be perpendicular to the filaments since that is how filaments form in a strong, dynamically important, magnetic field. For the three youngest cores in their respective regions, core 4 in L1495A, L1689B in L1689 and HGBS-1 in B213, the magnetic field is parallel to the large-scale field, suggesting that when they are first formed, the cores in the filament inherit the large-scale field. This places them at the slow (a) stage where other cores have increased in density and as they evolve, the cores affect the magnetic field which is why SMM-16, the Middle core in B213 and many of the cores in L1495A have field orientations different from their filament. This places those cores at the slow (b) stage. Then any of the cores which have formed stars, such as the East and West cores in B213 and L1689N, the field can be different from the filament, but other dynamics, such as outflows (West core of B213) can affect the magnetic field orientation then.

6.3.3 Magnetic fields in the isolated mode of star formation

A majority of the cores discussed in Chapter 4 and in Section 6.2 we consider to be undergoing isolated star formation. In isolated mode, we get a variety of fields, often times tracing large-scale magnetic field or core-scale dynamics. We include sources which are themselves isolated but which may form multiple cores and stars. For example, with L43, which sits inside a small filament, the relative location of the cloud in the Ophiuchus region places it as a rather isolated molecular cloud (see Figure 3.1). This filament has formed multiple protostars and prestellar cores. In this filament, the magnetic field of RNO 90, the oldest protostellar object, is oriented roughly 0° (see Figure 3.8). Interestingly, the few vectors around RNO 91, the younger protostellar source, are also roughly 0° (see Figure 3.8). In both cases, these orientations are offset from the filament orientation by 67°. Meanwhile, the magnetic field in the final dense core is roughly parallel to the large-scale field. This core was formed from the original molecular cloud rather than ambient material.

L183 is another molecular cloud with multiple cores (see Figure 4.3.5), though in this case none of them have any protostellar objects. Here the two more evolved and denser cores have magnetic field orientations not following the large-scale and so they are in the isolated (b) stage. However the youngest core still has a magnetic field similar to the large-scale field and may therefore be closer to the isolated (a) mode. L1544, L1498, L1517B, FeSt 1-457 and L1512 are all along varying stages of evolution, but none show signs of a formed protostellar source and so they sit at the isolated (b) stage. Their magnetic fields are varying, compared to both the core orientation and the large-scale field, with no clear pattern. It may be that cores which form out of the ambient material will have random field directions, associated more with the initial turbulence of the area and how that turbulence may have affected the orientation of the core-scale magnetic field, rather than any large-scale field or density structure.

The Ophiuchus cores are difficult to classify as undergoing isolated versus slow mode star formation. All of the cores sit within the larger L1688 cloud complex. However, the dense cores which we can observe at 850 μm are each relatively isolated from each other. They also vary in the stages of isolated mode star formation. Oph B2 has a protostellar object so is most likely undergoing isolated (a) mode star formation. This is similar to Oph A which also has the VLA 1623 source embedded.

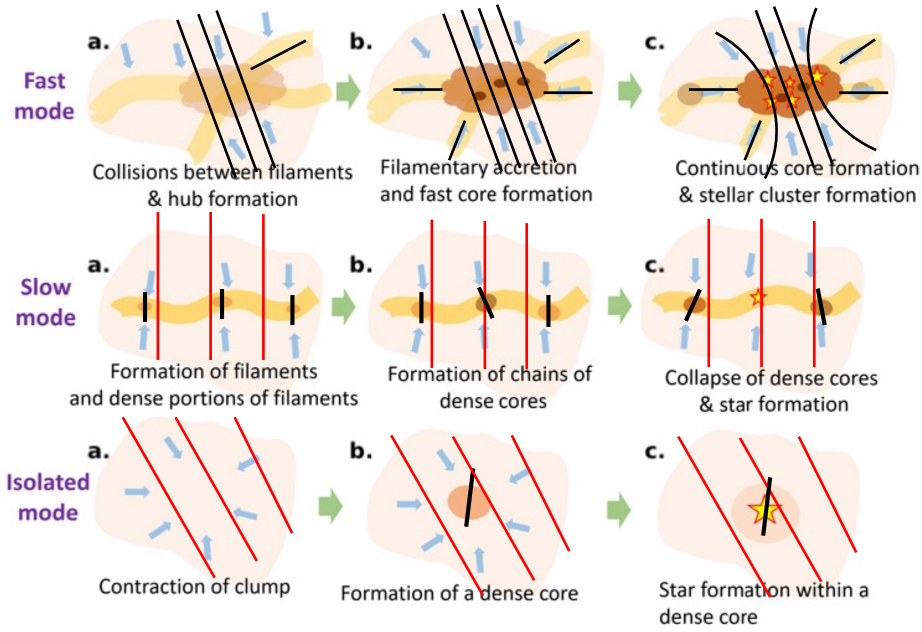

Figure 6.21: The cartoon star formation model taken from Seo et al. (2019). Overlaid are the magnetic field directions for each of the modes of star formation. The red lines represent large-scale magnetic fields (such as those observed with Planck) and the black lines represent core-scale magnetic fields (such as those observed with JCMT/POL-2).

Oph A may also be undergoing triggered star formation from a nearby B1 star. Oph C is an isolated prestellar core, though may be undergoing some fragmentation with multiple smaller cores found in Pattle et al. (2015). It is most likely sitting at the isolated (b) stage. If these sources were considered to be undergoing slow mode star formation, they would be between the (b) and (c) stages where many dense cores have been formed and some protostellar objects are beginning to be formed.

6.3.4 The whole magnetic field picture

Figure 6.21 shows the diagram from Seo et al. (2019) but with the magnetic field lines overlaid. These magnetic field lines are based on what we have observed in the BISTRO sources and reflect the most common orientation we see. In the fast mode, the magnetic fields are initially perpendicular to a majority of the filaments and therefore perpendicular to the elongated hub formation. Then as the hub starts to accrete material, there will be a magnetic field component still perpendicular, but there will also be components parallel to the filaments that are feeding the hub (Arzoumanian et al., 2021). Finally, when stars and more cores have formed, whether multiple or one massive, the gravitational contraction will begin to pinch the magnetic field lines which were originally perpendicular. DR 21 exhibits this perfectly where to the north of the filament, the field lines are still perpendicular to the filament but in the two massive cores of DR 21(OH) and DR 21, the perpendicular magnetic field now appears pinched. The illustration from Wang et al. (2019) in IC 5146, which is shown in Figure 6.19, illustrates this transition well.

In the slow mode, we have a large-scale magnetic field (red lines in Figure 6.21) which is initially perpendicular to the filament as the filament accretes material from along the field lines. Then individual cores begin to form in the filament and they initially form as magnetically-dominated material and their magnetic field still resembles the large-scale field. Then once these cores start to gravitationally contract and become matter-dominated, their core magnetic field orientations deviate from the parent large-scale field. In the case of L1495A, we showed that these field orientations will be preferentially parallel to the embedded filament, but in the case of B213, there are some of the cores which do not have field orientations perpendicular to the filament. This orientation may ultimately depend on the internal kinematics of the core.

Finally in the isolated mode, we initially just have a large-scale magnetic field in the ambient material. When material starts to contract and a dense core is formed, this dense core could initially still maintain the large-scale field orientation. The contraction of the core occurs in areas where turbulence will have dissipated so that core formation can occur. Less turbulence means the magnetic field will be less-disrupted and will therefore still follow the large-scale field. Or, the core magnetic field may have been disrupted by turbulence, and once the turbulence dissipated, the remaining magnetic field is different from the large-scale field, but with no turbulence, the core can form. Once the dense core moves to matter-dominated, the magnetic field orientation may differ as the core dynamics and gravitational pressure alter the magnetic field orientation. When the actual star is formed, there will still be a magnetic field in the dusty envelope, but protostellar outflows may have altered the magnetic field in areas that interact with this outflow (such as in L43).

6.4 Summary

In this chapter we have amassed the data and results presented in Chapters 3, 4 and 5 of this work to focus on how these data can contribute to global understanding of how magnetic fields contribute to the star formation process. In the first part of this chapter, we investigated how the magnetic field of individual cores changed based on magnetic field strength and column density. We compared calculated column density and magnetic field strength values with critical values derived from the theoretical model of Mestel (1965) on when cores switch from magnetically-dominated to matter-dominated. We find that a majority of our cores are already matter-dominated if considering just the magnetic field strength and gravitational pressure. We only find seven cores to be magnetically-dominated still. We also theorized that those magnetically-dominated cores might still contain an imprint of the large-scale magnetic field, but nearly half had different core-scale magnetic fields than the large-scale field. In addition, of the matter-dominated cores, there was not a clear pattern of cores having significantly different field orientations from the large-scale field.

Then we moved towards the CMZ where we investigated how the orientation of the magnetic field changes at different densities. We are unable to resolve core-scale magnetic field properties in the CMZ and so rely on large-scale relations such as those found by *Herschel* and Planck in the nearby star forming regions. We find that nearly all of the molecular clouds in the CMZ already have preferentially perpendicular alignment or no alignment between the magnetic field and the density structures. Visually this would mean that magnetic fields are parallel to the minor axes of clouds and filaments. Planck found that there is a transition column density where magnetic fields go from preferentially parallel to preferentially perpendicular in nearby star forming regions. We may miss this transition because the magnetic field traced by the JCMT/POL-2 is not sensitive to the extended, low density structure. So the material we are observing may all be past the critical column density threshold.

Finally we have attempted to add an extra parameter to the three modes of star formation suggested by Seo et al. (2019). For each of the modes and each of the stages within each mode, we look for patterns in the magnetic field strengths of BISTRO sources that fit within the different modes/stages. We find that clouds which undergo fast-mode star formation begin with a perpendicular magnetic field to the majority of the filaments in the region and that remains the case until the hub system which forms begins to evolve and gravitationally contract or undergo heavy inflow, at which point the magnetic field will become pinched. Regions that undergo slow mode of star formation will similarly have magnetic fields perpendicular to the initial filaments forming. When cores form along the filament and begin to contract, they may alter the direction of the magnetic field within those cores and there will be a disconnect from the original large-scale field. We found in L1495A that there is a preference for cores to have magnetic field orientations roughly perpendicular to the local filament orientation, but the ultimate field direction most likely relies on internal dynamics of the cores. For clouds undergoing isolated mode star formation, we find no real pattern about how the magnetic field will look other than they appear to be ordered within these cores. We suggest that the cores form in areas without turbulent motions and the magnetic fields here may then be ordered with the turbulence gone, but have been shaped by the turbulence to have a random orientation.

Chapter 7

Conclusions and Future Work

In this thesis we have presented magnetic field observations from the JCMT/POL-2 across a variety of spatial scales, focusing on the earlier stages of star formation. We have presented detailed work on the Lynds 43 molecular cloud and then extended that work towards a series of other prestellar cores, investigating their magnetic field morphologies and strengths. We then brought all of newly presented observations together with literature observations to investigate any global trends we could see in the early stages of star formation. We also added characteristic magnetic field observations to the modes of star formation presented by Seo et al. (2019), offering another metric by which to judge how star formation is taking place in molecular clouds. To extend the spatial scales of our observations, we observed the Central Molecular Zone of the Galactic Center and investigated if the magnetic field plays a role on the large scale, influencing the orbital structure of the CMZ. We also presented the highly structured magnetic fields of the individual clouds and find that most are magnetically sub- or trans-critical and also primarily have magnetic fields which are perpendicular to their intensity structures.

7.1 Chapter 2: Instrumentation, observations and data reduction

In this chapter, we presented how the polarimeter and bolometer camera on JCMT operate. We also summarized the data reduction process so explain how we obtain our polarization maps and catalogs. We presented a new data reduction method for the JCMT/POL-2 data when dealing with low-SNR sources. The new reduction, which involves reducing with larger pixels, increases the signal-to-noise for the vector catalogs while appearing not to compromise the validity of the data. This method will need additional investigation which we plan to do with the other prestellar cores.

7.2 Chapter 3: Lynds 43

In this chapter, we presented BISTRO-3 observations of the Lynds 43 molecular cloud. L43 is an isolated, $\sim$0.4 pc long dense filament near the Ophiuchus region. It has two formed protostars and a sub-millimeter bright dense core. We plot the large-scale outflow from the youngest protostar, which is still an embedded source, and find that it spatially perfectly matches with a dust cavity seen by *Herschel*. We show that part of the magnetic field observed in L43 has most likely been influenced by this outflow because the dust and the magnetic field observed in the dust are both aligned with the outflow cavity walls. This magnetic field morphology is also distinct from the rest of the cloud, where the magnetic fields in the envelopes of the two protostars are roughly north-south and the magnetic field in the dense core is parallel to the filament and the large-scale magnetic field. We find magnetic field strengths in the range of 70–160 μG which give magnetically super-critical values in the main core. This is supported based on potential fragmentation we see in the core and we suggest that this core could be next to form a star along the filament. We also point out that the star formation gradient in this filament follows other theories that star formation in Ophiuchus is triggered by the Sco OB2 association. We also investigated how theoretical predictions from Mestel (1965) about transition of material in a star forming core from magnetically- to matter-dominated played out in L43 and again that the main core of L43 is most likely matter-dominated, suggesting it could contract because the magnetic field is no longer strong enough to solely support the collapse.

7.3 Chapter 4: Magnetic fields in other star-forming regions

For each of the BISTRO-3 prestellar sources, we analyzed the magnetic field structure and its relative importance within the core. We also included data from two other sources, one prestellar in L183 and one with a formed protostar, L1527. In the prestellar cores, we calculate magnetic field strengths in the range of 30–130 μG which are of the same order seen in other prestellar cores. These magnetic field strengths generally yield magnetically super-critical cores indicating that the magnetic fields alone are not sufficient to provide support against collapse. Many of the sources are not affiliated with any sort of filamentary structure or larger molecular cloud and most have core-scale magnetic fields which have no imprint of the large-scale field remaining. This could indicate that many of these cores are more evolved and have become matter-dominated. L1498, L1544, L1495 and tentatively L183 are all strong infall candidates suggesting more evolved cores

One of the more evolved cores, L1544, has a highly structured magnetic field that also exhibits the hourglass morphology thought to be a key indicator of ambipolar diffusion and initially dynamically import magnetic fields. The other evolved source, L1527, has a two component magnetic field, one that appears to still be tied to the dusty envelope, with an orientation roughly perpendicular to the semi-major axis of the core and one associated with the bipolar protostellar outflow, similar to L43. L183 has already fragmented into three cores, two of which are magnetically supercritical. The least dense core appears to still have the morphology of the large-scale field associated with it. L1495 is a series of small filaments with a series of 9 cores forming within the filaments. A majority of these cores have mean magnetic field directions perpendicular to their local filament and with no imprint of the large-scale field. Only the least evolved, or least dense, core has a magnetic field similar to the large-scale field.

7.4 Chapter 5: The Galactic Center

In this chapter we suggest a new partial orbital model for the CMZ. We start from the 850 μm Stokes I emission which traces the dense structures in the CMZ. We require that our modeled orbit passes through the dense structures. Then we add in the magnetic field information where we assume the field to be parallel to the orbit and so we look for which dense structures our orbit could go through to satisfy this. We do not drastically deviate from the previously derived orbital model of Kruijssen, Dale & Longmore (2015) because it has been shown to be continuous in many areas in position-velocity space. We then check the gas kinematics along our proposed orbit using NH_3 observations from Krieger et al. (2017) to ensure that our new orbit is still continuous in position-velocity space. We show that it is and that we also see a similar discontinuity between roughly Sgr A* and the Brick, similar to Kruijssen, Dale & Longmore (2015)

We then compare the magnetic field direction along the orbit with the gradient of the orbit. We find that on the western side of Sgr A* and the 20 km/s cloud, the magnetic field direction agrees well with the orbital direction, aligning preferentially parallel to the orbit. This is also the region that is best-defined in position-velocity space. On the eastern side, there is significantly more deviation of the magnetic field from the orbit direction. There are many more molecular clouds on this side and a lot more velocity components. A majority of the mass in the CMZ is also in this eastern side and we think some of the individual cloud dynamics, whether turbulent or gravitational, could be affecting the observed magnetic field. Overall we have a preferentially parallel pattern of the magnetic field with our proposed orbital model and the orbital model is continuous in velocity space.

We then derive a CMZ-wide distribution of magnetic field strengths within the molecular clouds. For each cloud with significant magnetic field detections, we use the ADF method and N(H_2) maps from (Tang, Wang & Wilson, 2021) and then line-widths from the NH_3 data. We find magnetic field strengths on the order of mG which is expected for the ordered magnetic field structure we see. We also derive mass-to-flux ratios and Alfvén Mach numbers, finding in both cases that the magnetic field within individual clouds appears to dominate, with a majority of clouds being both magnetically subcritical and sub-Alfvénic.

7.5 Chapter 6: How BISTRO molecular clouds contribute to star formation theory

In this chapter we have amassed the data and results presented in Chapters 3, 4 and 5 of this work to focus on how these data can contribute to global understanding of how magnetic fields contribute to the star formation process. In the first part of this chapter, we investigated how the magnetic field of individual cores changed based on magnetic field strength and column density. We compared calculated column density and magnetic field strength values with critical values derived from the theoretical model of Mestel (1965) on when cores switch from magnetically-dominated to matter-dominated. We find that a majority of our cores are already matter-dominated if considering just the magnetic field strength and gravitational pressure. We only find seven cores to be magnetically-dominated still. We also theorized that those magnetically-dominated cores might still contain an imprint of the large-scale magnetic field, but nearly half had different core-scale magnetic fields than the large-scale field. In addition, of the matter-dominated cores, there was not a clear pattern of cores having significantly different field orientations from the large-scale field.

Then we moved towards the CMZ where we investigated how the orientation of the magnetic field changes at different densities. We are unable to resolve core-scale magnetic field properties in the CMZ and so rely on large-scale relations such as those found by *Herschel* and Planck in the nearby star forming regions. We find that nearly all of the molecular clouds in the CMZ already have preferentially perpendicular alignment or no alignment between the magnetic field and the density structures. Visually this would mean that magnetic fields are parallel to the minor axes of clouds and filaments. Planck found that there is a transition column density where magnetic fields go from preferentially parallel to preferentially perpendicular in nearby star forming regions. We may miss this transition because the magnetic field traced by the JCMT/POL-2 is not sensitive to the extended, low density structure. So the material we are observing may all be past the critical column density threshold.

Finally we have attempted to add an extra parameter to the three modes of star formation suggested by Seo et al. (2019). For each of the modes and each of the stages within each mode, we look for patterns in the magnetic field strengths of BISTRO sources that fit within the different modes/stages. We find that clouds which undergo fast-mode star formation begin with a perpendicular magnetic field to the majority of the filaments in the region and that remains the case until the hub system which forms begins to evolve and gravitationally contract or undergo heavy inflow, at which point the magnetic field will become pinched. Regions that undergo slow mode of star formation will similarly have magnetic fields perpendicular to the initial filaments forming. When cores form along the filament and begin to contract, they may alter the direction of the magnetic field within those cores and there will be a disconnect from the original large-scale field. We found in L1495A that there is a preference for cores to have magnetic field orientations roughly perpendicular to the local filament orientation, but the ultimate field direction most likely relies on internal dynamics of the cores. For clouds undergoing isolated mode star formation, we find no real pattern about how the magnetic field will look other than they appear to be ordered within these cores. We suggest that they cores form in areas without turbulent motions and the magnetic fields here may then be ordered with the turbulence gone, but have been shaped by the turbulence to have a random orientation.

7.6 Future work

The most promising area of future research stemming from this work is the Galactic Center. SOFIA/HAWC+ recently released a legacy full mosaic of the magnetic field in the Galactic Center at similar resolutions but at 214 μm. We showed in Chapter 5 that although some of the magnetic field morphology does agree between 214um and 850um, there are areas in the CMZ where the magnetic field structure does not agree between the two wavelengths. This could be due to different dust populations or other polarimetry properties that would be very interesting to investigate. In addition, there has not been any work done towards a large-scale magnetic field influence through the region, so that is an area I hope to build upon. The goal is to develop a method for testing multiple orbits and also checking that they do not violate constraints placed by the gravitational potentials in the CMZ. It may be ultimately difficult to discern if the magnetic field is 'controlling' the orbit or if it is being dragged around the CMZ with the flow of material.

CHAPTER 7

One of the other directions this research could go is investigating further Sections 6.2 and 6.4. Section 6.2 essentially found no explicit preference for core-scale magnetic fields to follow their parent large-scale fields. This was true across a variety of criticality stages. Further work could be done to investigate how these cores differ and if other metrics, such as core rotation, infall velocity, turbulence levels or core chemistry might influence why the magnetic field looks like it does. In Section 6.4, Orion A is the most promising candidate to do a full-scale investigation similar to Seo et al. (2019) but this time with full magnetic field information. The Taurus molecular cloud has the magnetic field information we have presented but it is not clear if the fast-mode star formation in the L1495/B213 filament has associated magnetic field observations. Orion A has the hub area to the south, extended filaments with numerous prestellar cores and then isolated clouds throughout. It may also be a test-bed for investigating a fourth mode of triggered star formation.

We have already attempted to follow up observations in L43 with an ALMA proposal to observe RNO 90 and RNO 91 at the envelope scale to investigate the magnetic field. We believe this presents a very unique opportunity of two young protostars forming from the same isolated molecular cloud, but along different stages in their protostellar lifetimes. We also see the magnetic field align with the large-scale outflow cavity walls, but are curious to see how the magnetic field actually aligns with the outflows at the envelope scales. RNO 90 has been observed by ALMA before and seen to still have small-scale bipolar outflows. The main L43 core would also be interesting to observe just in continuum with a higher resolution telescope to investigate if the fragmentation is really occurring and following up with kinematic information to do a proper virial analysis of the cores.

Bibliography

Abbas M. M. et al., 2004, ApJ 614, 781

Alves F. O., Frau P., Girart J. M., Franco G. A. P., Santos F. P., Wiesemeyer H., 2014, A&A 569, L1

Andersson B. G., Lazarian A., Vaillancourt J. E., 2015, ARA&A 53, 501

André P., 1994, in The Cold Universe, Montmerle T., Lada C. J., Mirabel I. F., Tran Thanh Van J., eds., p. 179

—, 1995, Ap&SS 224, 29

André P., Di Francesco J., Ward-Thompson D., Inutsuka S. I., Pudritz R. E., Pineda J. E., 2014, in Protostars and Planets VI, Beuther H., Klessen R. S., Dullemond C. P., Henning T., eds., pp. 27–51

André P. et al., 2010, A&A 518, L102

Andre P., Montmerle T., 1994, ApJ 420, 837

Andre P., Ward-Thompson D., Barsony M., 1993, ApJ 406, 122

André P., 2017, Comptes Rendus Geoscience, 349, 187

Arce H. G., Sargent A. I., 2006, ApJ 646, 1070

Arzoumanian D. et al., 2011, A&A 529, L6

—, 2021, A&A 647, A78

Bailer-Jones C. A. L., Rybizki J., Fouesneau M., Mantelet G., Andrae R., 2018, AJ 156, 58

Barnes A. T., Longmore S. N., Battersby C., Bally J., Kruijssen J. M. D., Henshaw J. D., Walker D. L., 2017, MNRAS 469, 2263

Barnett S. J., 1915, Physical Review, 6, 239

Bastien P., 1983, A&A 119, 109

Basu S., 2000, ApJL 540, L103

Battersby C. et al., 2020, ApJS 249, 35

Beattie J. R., Federrath C., 2020, MNRAS 492, 668

Beckwith S. V. W., Sargent A. I., Chini R. S., Guesten R., 1990, AJ 99, 924

Bence S., Padman R., Isaak K., Wiedner M., Wright G., 1998, MNRAS 299, 965

Benson P. J., Myers P. C., 1989, ApJS 71, 89

Bland-Hawthorn J., Gerhard O., 2016, ARA&A 54, 529

Blandford R. D., Payne D. G., 1982, MNRAS 199, 883

Bonnor W. B., 1956, MNRAS 116, 351

Brandenburg A., Lazarian A., 2013, Space Sci. Rev. 178, 163

Butterfield N. O. et al., 2024, arXiv e-prints, arXiv:2401.01983

Caselli P., Benson P. J., Myers P. C., Tafalla M., 2002a, ApJ 572, 238

Caselli P., Walmsley C. M., Zucconi A., Tafalla M., Dore L., Myers P. C., 2002b, ApJ 565, 331

Chandrasekhar S., Fermi E., 1953, ApJ 118, 116

Chapin E. L., Berry D. S., Gibb A. G., Jenness T., Scott D., Tilanus R. P. J., Economou F., Holland W. S., 2013, MNRAS 430, 2545

Chapman N. L., Goldsmith P. F., Pineda J. L., Clemens D. P., Li D., Krčo M., 2011, ApJ 741, 21

Chen J.-H., Evans N. J., Lee J.-E., Bourke T. L., 2009, ApJ 705, 1160

Ching T.-C. et al., 2022, ApJ 941, 122

Clarke S. D., Whitworth A. P., 2015, MNRAS 449, 1819

Cohen M., 1980, AJ 85, 29

Cooper B. F. C., Price R. M., 1962, Nature 195, 1084

Coudé S. et al., 2019, ApJ 877, 88

—, 2016, MNRAS 457, 2139

Crocker R. M., Jones D. I., Melia F., Ott J., Protheroe R. J., 2010, Nature 463, 65

Crutcher R. M., 2004, Ap&SS 292, 225

—, 2012, ARA&A 50, 29

Crutcher R. M., Kemball A. J., 2019, Frontiers in Astronomy and Space Sciences, 6

Crutcher R. M., Nutter D. J., Ward-Thompson D., Kirk J. M., 2004, ApJ 600, 279

Crutcher R. M., Wandelt B., Heiles C., Falgarone E., Troland T. H., 2010, ApJ 725, 466

Cui C., Bai X.-N., 2021, MNRAS 507, 1106

Currie M. J., Berry D. S., 2014, KAPPA: Kernel Applications Package

Currie M. J., Berry D. S., Jenness T., Gibb A. G., Bell G. S., Draper P. W., 2014, Astronomical Society of the Pacific Conference Series, Vol. 485, Starlink Software in 2013, Manset N., Forshay P., eds., Astronomical Society of the Pacific, p. 391

Davis L., 1951, PhRv, 81, 890

de Geus E. J., de Zeeuw P. T., Lub J., 1989, A&A 216, 44

de Korte P. A. J. et al., 2003, Review of Scientific Instruments, 74, 3807

di Francesco J., Evans, N. J. I., Caselli P., Myers P. C., Shirley Y., Aikawa Y., Tafalla M., 2007, in Protostars and Planets V, Reipurth B., Jewitt D., Keil K., eds., p. 17

Dolginov A. Z., Mitrofanov I. G., 1976, Ap&SS 43, 291

Dotson J. L., Vaillancourt J. E., Kirby L., Dowell C. D., Hildebrand R. H., Davidson J. A., 2010, ApJS 186, 406

Drabek E. et al., 2012, MNRAS 426, 23

Draine B., 2010, Physics of the Interstellar and Intergalactic Medium, Princeton Series in Astrophysics. Princeton University Press

Ebert R., 1955, ZA 37, 217

Eden D. J. et al., 2020, MNRAS 498, 5936

Enoch M. L., Evans, Neal J. I., Sargent A. I., Glenn J., 2009, ApJ 692, 973

Eswaraiah C. et al., 2021, ApJL 912, L27

Federrath C., 2015, MNRAS 450, 4035

Federrath C., Klessen R. S., 2012, ApJ 761, 156

Fehér O. et al., 2022, ApJS 258, 17

Ferrière K., Gillard W., Jean P., 2007, A&A 467, 611

Forbrich J., Wiesemeyer H., Thum C., Belloche A., Menten K. M., 2008, A&A 492, 757

Franco G. A. P., 1989, A&A 223, 313

Friberg P., Bastien P., Berry D., Savini G., Graves S. F., Pattle K., 2016, Society of Photo-Optical Instrumentation Engineers (SPIE) Conference Series, Vol. 9914, POL-2: a polarimeter for the James-Clerk-Maxwell telescope, Society of Photo-Optical Instrumentation Engineers, p. 991403

Friberg P., Berry D., Savini G., Bintley D., Dempsey J., Graves S., Parsons H., 2018, in Society of Photo-Optical Instrumentation Engineers (SPIE) Conference Series, Vol. 10708, Millimeter, Submillimeter, and Far-Infrared Detectors and Instrumentation for Astronomy IX, Zmuidzinas J., Gao J.-R., eds., p. 107083M

Gaia Collaboration et al., 2021, A&A 649, A1

Garufi A. et al., 2022, A&A 658, A137

Girart J. M., Patel N., Vlemmings W. H. T., Rao R., 2012, ApJL 751, L20

Girart J. M., Rao R., Marrone D. P., 2006, Science, 313, 812

Girichidis P., Seifried D., Naab T., Peters T., Walch S., Wünsch R., Glover S. C. O., Klessen R. S., 2018, MNRAS 480, 3511

Goldreich P., Kylafis N. D., 1981, ApJL 243, L75

—, 1982, ApJ 253, 606

Gómez de Castro A. I., de la Fuente Marcos R., Canet A., Beitia-Antero L., Yáñez-Gestoso J., Carlos Vallejo J., 2024, A&A 681, A72

Guan Y. et al., 2021, ApJ 920, 6

Guerra J. A., Lopez-Rodriguez E., Chuss D. T., Butterfield N. O., Schmelz J. T., 2023, AJ 166, 37

Güver T., Özel F., 2009, MNRAS 400, 2050

Hacar A., Clark S. E., Heitsch F., Kainulainen J., Panopoulou G. V., Seifried D., Smith R., 2023, in Astronomical Society of the Pacific Conference Series, Vol. 534, Protostars and Planets VII, Inutsuka S., Aikawa Y., Muto T., Tomida K., Tamura M., eds., p. 153

Hacar A., Tafalla M., 2011, A&A 533, A34

Hall J. S., 1949, Science, 109, 166

Heiles C., Troland T. H., 2005, ApJ 624, 773

Hennebelle P., Inutsuka S.-i., 2019, FrASS, 6, 5

Henshaw J. D., Barnes A. T., Battersby C., Ginsburg A., Sormani M. C., Walker D. L., 2023, in Astronomical Society of the Pacific Conference Series, Vol. 534, Protostars and Planets VII, Inutsuka S., Aikawa Y., Muto T., Tomida K., Tamura M., eds., p. 83

Henshaw J. D., Longmore S. N., Kruijssen J. M. D., 2016, MNRAS 463, L122

Henshaw J. D. et al., 2016, MNRAS 457, 2675

Herbst W., Warner J. W., 1981, AJ 86, 885

Hildebrand R. H., 1983, QJRAS 24, 267

Hildebrand R. H., Kirby L., Dotson J. L., Houde M., Vaillancourt J. E., 2009, ApJ 696, 567

Hiltner W. A., 1949, Science, 109, 165

Hodapp K.-W., 1994, ApJS 94, 615

Holland W. S. et al., 2013, MNRAS 430, 2513

Howard A. D. P., Whitworth A. P., Marsh K. A., Clarke S. D., Griffin M. J., Smith M. W. L., Lomax O. D., 2019, MNRAS 489, 962

Huang K.-Y., Kemball A. J., Vlemmings W. H. T., Lai S.-P., Yang L., Agudo I., 2020, ApJ 899, 152

Hull C. L. H. et al., 2017, ApJ 847, 92

Hull C. L. H., Gouellec V. J. M. L., Girart J. M., Tobin J. J., Bourke T. L., 2020, ApJ 892, 152

Hwang J. et al., 2022, ApJ 941, 51

Hwang J., Pattle K., Parsons H., Go M., Kim J., 2023, AJ 165, 198

Inutsuka S.-I., Miyama S. M., 1992, ApJ 388, 392

Irwin K. D., 1995, Applied Physics Letters, 66, 1998

Jeans J. H., 1902, Philosophical Transactions of the Royal Society of London Series A, 199, 1

Jijina J., Myers P. C., Adams F. C., 1999, ApJS 125, 161

Kandori R. et al., 2005, AJ 130, 2166

—, 2017, ApJ 845, 32

Karoly J., Soam A., Andersson B. G., Coudé S., Bastien P., Vaillancourt J. E., Lee C. W., 2020, ApJ 900, 181

Karoly J. et al., 2023, ApJ 952, 29

Kauffmann J., Pillai T., Zhang Q., Menten K. M., Goldsmith P. F., Lu X., Guzmán A. E., Schmiedeke A., 2017, A&A 603, A90

Kendrew S., Ginsburg A., Johnston K., Beuther H., Bally J., Cyganowski C. J., Battersby C., 2013, ApJL 775, L50

Kim G. et al., 2020, ApJS 249, 33

Kirk H. et al., 2017, ApJ 846, 144

—, 2018, ApJS 238, 8

Kirk H., Myers P. C., Bourke T. L., Gutermuth R. A., Hedden A., Wilson G. W., 2013, The Astrophysical Journal, 766, 115

Kirk J. M., Ward-Thompson D., Crutcher R. M., 2006, MNRAS 369, 1445

Könyves V. et al., 2021, ApJ 913, 57

Krieger N. et al., 2017, The Astrophysical Journal, 850, 77

Kruijssen J. M. D., Dale J. E., Longmore S. N., 2015, MNRAS 447, 1059

Krumholz M. R., Federrath C., 2019, FrASS, 6

Kwon J. et al., 2018, ApJ 859, 4

Kwon J., Tamura M., Hough J. H., Nakajima Y., Nishiyama S., Kusakabe N., Nagata T., Kandori R., 2015, ApJS 220, 17

Ladd E. F., Myers P. C., 1991, in Astronomical Society of the Pacific Conference Series, Vol. 16, Atoms, Ions and Molecules: New Results in Spectral Line Astrophysics, Haschick A. D., Ho P. T. P., eds., p. 241

Larson R. B., 1969, MNRAS 145, 271

—, 1981, MNRAS 194, 809

—, 1985, MNRAS 214, 379

Launhardt R., Zylka R., Mezger P. G., 2002, A&A 384, 112

Lazarian A., Hoang T., 2007, MNRAS 378, 910

—, 2011, in Astronomical Society of the Pacific Conference Series, Vol. 449, Astronomical Polarimetry 2008: Science from Small to Large Telescopes, Bastien P., Manset N., Clemens D. P., St-Louis N., eds., p. 116

Lee C.-F., Ho P. T. P., 2005, ApJ 624, 841

Lee C.-F., Li Z.-Y., Ching T.-C., Lai S.-P., Yang H., 2018, ApJ 854, 56

Lee C.-F., Mundy L. G., Stone J. M., Ostriker E. C., 2002, ApJ 576, 294

Lee C. W., Myers P. C., Tafalla M., 2001, ApJS 136, 703

Li H.-b., Houde M., Lai S.-p., Sridharan T. K., 2010, ApJ 718, 905

Lin S.-J. et al., 2024, ApJ 961, 117

Liu J. et al., 2019, ApJ 877, 43

Liu J., Zhang Q., Qiu K., 2022, FrASS, 9, 943556

Loinard L., Torres R. M., Mioduszewski A. J., Rodríguez L. F., 2008, ApJL 675, L29

Loren R. B., 1989, ApJ 338, 902

Lu X. et al., 2024, ApJ 962, 39

—, 2019, ApJS 244, 35

Luhman K. L., 2018, AJ 156, 271

Lyo A. R. et al., 2021, ApJ 918, 85

Mac Low M.-M., 1999, ApJ 524, 169

Machida M. N., 2017, arXiv e-prints, arXiv:1711.00384

Mairs S. et al., 2021, AJ 162, 191

—, 2015, MNRAS 454, 2557

Masson J., Chabrier G., Hennebelle P., Vaytet N., Commerçon B., 2016, A&A 587, A32

Masson J., Teyssier R., Mulet-Marquis C., Hennebelle P., Chabrier G., 2012, ApJS 201, 24

Mathieu R. D., Benson P. J., Fuller G. A., Myers P. C., Schild R. E., 1988, ApJ 330, 385

Mattern M., Kainulainen J., Zhang M., Beuther H., 2018, A&A 616, A78

Matthews B. C., McPhee C. A., Fissel L. M., Curran R. L., 2009, ApJS 182, 143

McKee C. F., Ostriker J. P., 1977, ApJ 218, 148

Megías A., Jiménez-Serra I., Martín-Pintado J., Vasyunin A. I., Spezzano S., Caselli P., Cosentino G., Viti S., 2023, MNRAS 519, 1601

Mestel L., 1965, QJRAS 6, 265

—, 1966, MNRAS 133, 265

Molinari S. et al., 2011, ApJL 735, L33

Montier L., Plaszczynski S., Levrier F., Tristram M., Alina D., Ristorcelli I., Bernard J. P., Guillet V., 2015, A&A 574, A136

Moriarty-Schieven G. H., Johnstone D., Bally J., Jenness T., 2006, ApJ 645, 357

Morris M., Serabyn E., 1996, ARA&A 34, 645

Mouschovias T. C., 1979, ApJ 228, 475

Myers P. C., 2017, ApJ 838, 10

Myers P. C., Heyer M., Snell R. L., Goldsmith P. F., 1988, ApJ 324, 907

Naghizadeh-Khouei J., Clarke D., 1993, A&A 274, 968

Nakano T., Nakamura T., 1978, PASJ 30, 671

Newville M. et al., 2023, lmfit/lmfit-py: 1.2.2

Ohashi N., Hayashi M., Ho P. T. P., Momose M., 1997, ApJ 475, 211

Ostriker E. C., Stone J. M., Gammie C. F., 2001, ApJ 546, 980

Padovani M., Galli D., Glassgold A. E., 2009, A&A 501, 619

Padovani M., Ivlev A. V., Galli D., Caselli P., 2018, A&A 614, A111

Palmeirim P. et al., 2013, A&A 550, A38

Parsons H. et al., 2018, ApJS 234, 22

Pattle K., Fissel L., Tahani M., Liu T., Ntormousi E., 2023, in Astronomical Society of the Pacific Conference Series, Vol. 534, Protostars and Planets VII, Inutsuka S., Aikawa Y., Muto T., Tomida K., Tamura M., eds., p. 193

Pattle K. et al., 2021, ApJ 907, 88

Pattle K. et al., 2019, ApJ 880, 27

Pattle K. et al., 2022, MNRAS 515, 1026

—, 2017, ApJ 846, 122

—, 2015, MNRAS 450, 1094

Pierce-Price D. et al., 2000, ApJL 545, L121

Pillai T., Kauffmann J., Tan J. C., Goldsmith P. F., Carey S. J., Menten K. M., 2015, ApJ 799, 74

Planck Collaboration et al., 2016a, A&A 586, A132

—, 2016b, A&A 586, A138

—, 2016c, A&A 594, A28

Plaszczynski S., Montier L., Levrier F., Tristram M., 2014, MNRAS 439, 4048

Pon A., Toalá J. A., Johnstone D., Vázquez-Semadeni E., Heitsch F., Gómez G. C., 2012, ApJ 756, 145

Pontoppidan K. M., Salyk C., Blake G. A., Käufl H. U., 2010, ApJL 722, L173

Price S. D., Egan M. P., Carey S. J., Mizuno D. R., Kuchar T. A., 2001, AJ 121, 2819

Purcell E. M., 1979, ApJ 231, 404

Redaelli E., Bizzocchi L., Caselli P., 2020, A&A 644, A29

Rice S. O., 1945, The Bell System Technical Journal, 24, 46

Ridley M. G. L., Sormani M. C., Treß R. G., Magorrian J., Klessen R. S., 2017, MNRAS 469, 2251

Roccatagliata V., Franciosini E., Sacco G. G., Randich S., Sicilia-Aguilar A., 2020, A&A 638, A85

Roy A. et al., 2014, A&A 562, A138

Sadanari K. E., Omukai K., Sugimura K., Matsumoto T., Tomida K., 2023, MNRAS 519, 3076

Sadavoy S. I. et al., 2013, ApJ 767, 126

Schmiedeke A. et al., 2016, A&A 588, A143

Schnee S. et al., 2010, ApJ 708, 127

Schwörer A. et al., 2019, A&A 628, A6

Segura-Cox D. M., Looney L. W., Stephens I. W., Fernández-López M., Kwon W., Tobin J. J., Li Z.-Y., Crutcher R., 2015, ApJL 798, L2

Seifried D., Walch S., 2015, MNRAS 452, 2410

Seifried D., Walch S., Weis M., Reissl S., Soler J. D., Klessen R. S., Joshi P. R., 2020, MNRAS 497, 4196

Seo Y. M. et al., 2019, ApJ 871, 134

—, 2015, ApJ 805, 185

Sharma E., Gopinathan M., Soam A., Lee C. W., Seshadri T. R., 2022, MNRAS 517, 1138

Shirley Y. L., Nordhaus M. K., Grcevich J. M., Evans, Neal J. I., Rawlings J. M. C., Tatematsu K., 2005, ApJ 632, 982

Simon A., 1955, Phys. Rev., 98, 317

Soam A. et al., 2018, ApJ 861, 65

Sofue Y., 2022, MNRAS 516, 907

Soler J. D., 2019, A&A 629, A96

Soler J. D. et al., 2017, A&A 603, A64

Soler J. D., Hennebelle P., Martin P. G., Miville-Deschênes M.-A., Netterfield C. B., Fissel L. M., 2013, ApJ 774, 128

Song S.-M. et al., 2022, ApJS 258, 19

Stamatellos D., Whitworth A. P., Bisbas T., Goodwin S., 2007, A&A 475, 37

Stephens I. W. et al., 2014, Nature 514, 597

—, 2017, ApJ 851, 55

Stone J. M., Gardiner T. A., Teuben P., Hawley J. F., Simon J. B., 2008, ApJS 178, 137

Stone J. M., Tomida K., White C. J., Felker K. G., 2020, ApJS 249, 4

Tafalla M., 2005a, in IAU Symposium, Vol. 231, Astrochemistry: Recent Successes and Current Challenges, Lis D. C., Blake G. A., Herbst E., eds., pp. 17–26

—, 2005b, in Cores to Clusters, Kumar M. S. N., Tafalla M., Caselli P., eds., Springer New York, New York, NY, pp. 31–46

Tafalla M., Myers P. C., Caselli P., Walmsley C. M., 2004, A&A 416, 191

Tahani M., Plume R., Brown J. C., Kainulainen J., 2018, A&A 614, A100

Tanaka K., 2018, ApJ 859, 86

Tang Y., Wang Q. D., Wilson G. W., 2021, MNRAS 505, 2377

Teixeira P. S., Takahashi S., Zapata L. A., Ho P. T. P., 2016, A&A 587, A47

Teyssier R., 2002, A&A 385, 337

Tielens A. G. G. M., 2005, The phases of the ISM, Cambridge University Press, p. 265–316

Tomida K., Tomisaka K., Matsumoto T., Hori Y., Okuzumi S., Machida M. N., Saigo K., 2013, ApJ 763, 6

Tsukamoto Y. et al., 2023, in Astronomical Society of the Pacific Conference Series, Vol. 534, Protostars and Planets VII, Inutsuka S., Aikawa Y., Muto T., Tomida K., Tamura M., eds., p. 317

van den Ancker M. E., de Winter D., Tjin A Djie H. R. E., 1998, A&A 330, 145

van't Hoff M. L. R. et al., 2023, ApJ 951, 10

Vaytet N., Commerçon B., Masson J., González M., Chabrier G., 2018, A&A 615, A5

Verschuur G. L., 1968, Phys. Rev. Lett. 21, 775

Walch S. et al., 2015, MNRAS 454, 238

Wang J.-W. et al., 2019, ApJ 876, 42

Ward-Thompson D. et al., 2007, PASP 119, 855

—, 2023, ApJ 946, 62

Ward-Thompson D., Kirk J. M., Crutcher R. M., Greaves J. S., Holland W. S., André P., 2000, ApJL 537, L135

Ward-Thompson D. et al., 2016, MNRAS 463, 1008

Ward-Thompson D., Robson E. I., Whittet D. C. B., Gordon M. A., Walther D. M., Duncan W. D., 1989, MNRAS 241, 119

Ward-Thompson D., Whitworth A. P., 2011, An Introduction to Star Formation. Cambridge University Press

Wardle J. F. C., Kronberg P. P., 1974, ApJ 194, 249

Weintraub D. A., Tegler S. C., Kastner J. H., Rettig T., 1994, ApJ 423, 674

Wilking B. A., Gagné M., Allen L. E., 2008, in Handbook of Star Forming Regions, Volume II, Reipurth B., ed., Vol. 5, p. 351

Wilking B. A., Lada C. J., Young E. T., 1989, ApJ 340, 823

Wurster J., Bate M. R., Price D. J., 2019, MNRAS 489, 1719

Yang Y.-L. et al., 2018, ApJ 860, 174

Yen H.-W. et al., 2021, ApJ 907, 33

Yen H.-W., Koch P. M., Takakuwa S., Krasnopolsky R., Ohashi N., Aso Y., 2017, ApJ 834, 178

Yoon S.-Y., Lee J.-E., Lee S., Herczeg G. J., Park S., Mace G. N., Lee J.-J., Jaffe D. T., 2021, ApJ 919, 116

Young C. H., Bourke T. L., Young K. E., Evans, Neal J. I., Jørgensen J. K., Shirley Y. L., van Dishoeck E. F., Hogerheijde M., 2006, AJ 132, 1998

Yuan L. et al., 2020, A&A 637, A67

Yusef-Zadeh F. et al., 2009, ApJ 702, 178

Zeeman P., 1897, The London, Edinburgh, and Dublin Philosophical Magazine and Journal of Science, 44, 55

Zier O., Springel V., Mayer A. C., 2024, MNRAS 527, 1563

Zuckerman B., Evans, N. J. I., 1974, ApJL 192, L149